Experimental characterization of helium plasma jets

Marlous Hofmans

▶ To cite this version:

HAL Id: tel-03080479

https://theses.hal.science/tel-03080479

Submitted on 17 Dec 2020

Experimental characterization of helium plasma jets

Thèse de doctorat de l'Institut Polytechnique de Paris
préparée à l'Ecole polytechnique et Eindhoven University of Technology

École doctorale n°626 École Doctorale de l'Institut Polytechnique de
Paris (ED IP Paris)
Spécialité de doctorat: Physique

Thèse présentée et soutenue à Eindhoven, Pays-Bas, le 15 octobre 2020, par

MARLOUS HOFMANS

Composition du Jury :

Dr. S. Starikovskaia
École Polytechnique (LPP), France   Président

Prof.dr. D. O'Connell
University of York, Royaume-Uni   Rapporteur

Prof.dr. U. Cvelbar
Jožef Štefan Institute, Slovénie   Rapporteur

Dr. R.A.H. Engeln
Eindhoven University of Technology (PMP), Pays-Bas   Examinateur

Dr. O.Y.N. Guaitella
École Polytechnique (LPP), France   Directeur de thèse

Prof.dr.ir. G.M.W. Kroesen
Eindhoven University of Technology (EPG), Pays-Bas   Directeur de thèse

Dr.Dipl.-Ing. A. Sobota
Eindhoven University of Technology (EPG), Pays-Bas   Co-directeur de thèse

Experimental characterization of helium plasma jets

PROEFSCHRIFT

ter verkrijging van de graad van doctor aan de Technische Universiteit Eindhoven, op gezag van de rector magnificus, prof.dr.ir. F. P. T. Baaijens, voor een commissie aangewezen door het College voor Promoties, in het openbaar te verdedigen op 15 oktober 2020 om 16:00 uur.

door

Marlous Hofmans

geboren te Zoetermeer

Dit proefschrift is goedgekeurd door de promotoren en de samenstelling van de promotie-commissie is als volgt:

voorzitter:	prof.dr.ir. E. J. E. Cottaar
promotor:	prof.dr.ir. G. M. W. Kroesen
copromotoren:	dr. O. Y. N. Guaitella (École Polytechnique)
	dr.Dipl.-Ing. A. Sobota
leden:	dr. S. Starikovskaia (École Polytechnique)
	dr. R. A. H. Engeln
	prof.dr. D. O'Connell (University of York)
	prof.dr. U. Cvelbar (Jožef Štefan Institute)

Experimental characterization of helium plasma jets

Marlous Hofmans

Summary

Experimental characterization of helium plasma jets

Plasma jets have a broad range of applications, such as treating tumors and stimulating wound healing in plasma medicine, stimulating seed and plant growth in plasma agriculture and modifying polymer fibres in surface treatments. Although a plasma jet may look simple, it is in fact a transient discharge that propagates in a flow of a rare gas (such as helium) inside a dielectric capillary, where it is produced following the principle of a dielectric barrier discharge, after which it continues propagating outside through the ambient air, following the streamer mechanism, until it impacts on the target for the applications. For all applications it is important to understand the dynamics in the plasma jet. This thesis studies an atmospheric pressure helium plasma jet that is powered by positive, unipolar pulses. Experiments are performed that focus on the propagation dynamics, flow structure and temperature in a freely expanding jet, as well as the influence of a metallic target on the plasma.

A Stark polarization spectroscopy setup is built to measure the electric field in the ionization front along the axis of the jet. Values of 10 kV/cm are obtained inside the capillary, while in the plasma plume an increase in electric field is measured up to 20 kV/cm. With a variation of the amplitude and duration of the applied voltage pulse, the same values for the electric field are obtained, while the length of the plasma plume changes. Comparison with the results of a two-dimensional fluid model show an excellent agreement on the propagation distance and velocity of the ionization wave, that are obtained in the experiments from intensified high speed imaging. The electric field comparison shows a maximum difference of 11 %, but the same increase in the plasma plume. From the simulations, the potential in the ionization front can be assessed, which depends on the potential that is transferred from the powered electrode and on the potential difference induced by the local charge separation. It is found that the potential in the ionization front that is needed to sustain propagation is proportional to the local oxygen concentration, which increases along the axis of the jet. Therefore, a higher electric field is necessary when the oxygen concentration increases and thus an increase in the electric field is measured for increasing positions in the plasma plume.

The densities of N_2 and O_2 in the plasma jet are measured with rotational Raman scattering and yield, starting in the center of the jet at the exit of the capillary, an increase in air fraction of 60 % over 2 mm in radial direction and 20 % over 22 mm in axial direction. These values correspond to an increase in the potential needed in the front to sustain propagation of 5 kV and 1.7 kV, respectively, which is why the propagation in radial direction is limited. For distances up to 10 mm from the exit of the capillary it is found that the air fractions in the jet are independent of the shape of the applied voltage pulse and even of whether the plasma is on or off. In the same setup, Thomson scattering is used to determine the electron density and the electron temperature in the plasma jet. Values in the order of 10^{19} m^{-3} and a few eV, respectively, are measured. The electron density is found to increase with axial position, while the electron temperature decreases. Comparison with results from the same simulations as before shows that the position

in the jet where Thomson scattering measures is actually right after the ionization front and not inside it. This explains then the behavior of the electron density and temperature: because the electron density is high behind the front, the losses of electron energy through collisions are higher and thus the electron temperature is lower. Decreasing the amplitude of the applied voltage by one third leads to a decrease in electron density of around 14 %.

The results of the pulsed jet of this thesis are also compared to published results of a jet with the same geometry and gas flow rate, but with a sinusoidal (AC) applied voltage at a six times higher frequency and a three times lower voltage amplitude. From the results of the air fractions in the pulsed jet, it is estimated that the flow composition of the pulsed jet and the AC jet are the same. The electric field in both jet is found be be the same, which may seem surprising, but can be explained by the similar potential in the front that is needed to sustain propagation, since the flow composition is the same. On the other hand, the plasma plume is two to three times shorter in the AC jet than in the pulsed jet. The difference in dissipated power is two orders of magnitude and is thus not proportional to the plume length. Although the electric field is the same, the electron density is expected to be much lower in the AC jet due to the lower voltage amplitude, and therefore the difference in plume length is probably caused by the difference in the amount of produced electrons. This can then also explain the higher gas temperature in the pulsed jet, as measured with rotational Raman scattering and a temperature probe, with respect to the AC jet.

As could be expected, the temperature of the gas in the plasma jet is found to increase, with around 12 °C, when the voltage is applied to the jet as to when only the gas flow is applied. Increasing the amplitude, pulse duration and frequency of the applied voltage pulses has a positive effect on the gas temperature, which corresponds to the measured energy per pulse that is dissipated in the plasma.

The voltage pulses also have an influence on the flow structure of the jet, as is visualized by schlieren imaging. For different rates of the applied helium flow, the flow structure in the jet is shown to be different at plasma Off and plasma On. Turbulent structures are seen at all flow rates when the plasma is applied and only at the highest flow rate when the plasma is off. These turbulences can be induced by an increase of the gas flow velocity, which can be caused by the gas heating of the plasma or the electric wind from momentum transfer between charged and neutral particles in the form of the electrohydrodynamic force. Equations from literature are used with the measured values for most parameters such as the electric field, electron density and temperature, gas temperature and velocity to estimate which of these two mechanisms dominates. It is found that the gas heating of 12 °C induces an increase in the gas velocity of an order of magnitude lower than the initial gas velocity, while the electric wind causes a doubling of the gas velocity. Therefore, the main mechanism that induces turbulences in the jet of this thesis is estimated to be the electrohydrodynamic force.

Placing a metallic target at 1 cm from the exit of the capillary is shown to accelerate the ionization wave towards the target, with respect to the behavior of the ionization wave in the free jet, when the target is grounded. When the metallic target is at floating potential, the ionization wave only propagates faster in the last 5 mm before the target. The gas temperature increases with up to 25 °C in the channel between the capillary and the floating target. In all cases, however, the electric field is measured to be approximately the same. With both targets, a return stroke has been observed after the impact of the ionization wave on the target that propagates from the target back towards the powered electrode, through the channel that is already ionized. Comparison with results from the same simulations as for the free jet, but adapted to the case of the targets, shows an agreement on all these observations. Furthermore, the simulations show the return stroke as an electrical redistribution of the powered electrode and the target and they

also show another redistribution at the end of the voltage pulse between the powered electrode that is now grounded and the positive plasma. This redistribution is also in the experiments visible as another ionization wave propagating from the capillary to the target, with an intensity that is higher in the case of a floating than with a grounded target.

In the case of a floating target, the time evolution of the potential in the target is measured and shows an increase from the moment of impact until the end of the applied voltage pulse, after which it decreases until it reaches zero again. It is shown that the amplitude and duration of the applied voltage pulse determine the maximum potential that is reached in the target. Right after the impact, the potential in the target is still low (close to grounded), while it can increase to half of the applied voltage at the end of the pulse, which is why the return stroke is similar for the floating and grounded target. Results from the simulations show that for a grounded target the electric field and electron temperature remain high and the electron density increases during the voltage pulse, while this does not happen for a floating target. For the floating target, both experiments and simulations show that the electric field, electron density and temperature increase after the end of the voltage pulse. The increase in electron density is for both targets attributed to electron emission from the metallic surfaces and charge transport in the plasma.

Thus, this thesis characterizes a pulsed atmospheric pressure plasma jet, using different optical (emission and laser) and electrical diagnostics as well as results from simulations to deepen the understanding of the dynamics in plasma jets.

Résumé

Caractérisation expérimentale de jets de plasma d'hélium

Les jets de plasma ont une large gamme d'applications, allant du traitement des tumeurs et la stimulation de la cicatrisation des plaies en médecine par plasma, à la stimulation de la croissance des graines et des plantes en agriculture assistée par plasma ou encore la modification des fibres polymères dans les traitements de surface. Bien qu'un jet de plasma puisse paraître simple, il s'agit en fait d'une décharge transitoire complexe qui se propage dans un écoulement de gaz rare (tel que l'hélium). Ils sont initiés à l'intérieur d'un capillaire diélectrique suivant le principe d'une décharge à barrière diélectrique, puis continuent leur propagation à l'extérieur du capillaire dans l'air ambiant en se développant selon un mécanisme de streamer, jusqu'à ce qu'ils impactent éventuellement une cible pour les applications. La compréhension de la dynamique du jet de plasma est essentielle pour toutes les applications. Cette thèse porte sur l'étude d'un jet de plasma d'hélium à pression atmosphérique qui est alimenté par des impulsions positives unipolaires. Les mesures réalisées adressent à la fois la dynamique de propagation du plasma, la structure de l'écoulement de gaz et la température dans un jet en expansion libre, ainsi que l'influence d'une cible métallique sur le plasma.

Un dispositif de spectroscopie Stark polarisée a été conçu pour mesurer le champ électrique dans le front d'ionisation le long de l'axe du jet. Des valeurs de 10 kV/cm sont observées à l'intérieur du capillaire, tandis que dans la plume de plasma en sortie de capillaire, une augmentation du champ électrique jusqu'à 20 kV/cm est mesurée. Les mêmes valeurs de champ électrique sont obtenues en variant l'amplitude et la durée des pulses de tension appliquée, alors que la longueur de la plume de plasma change. La comparaison avec les résultats d'un modèle de fluide bidimensionnel montre un excellent accord sur la distance de propagation et la vitesse de l'onde d'ionisation obtenus par imagerie rapide avec une caméra CCD intensifiée. La comparaison du champ électrique montre quant à elle une différence maximale de 11 %, tout en reproduisant fidèlement la longeur d'extension de la plume de plasma. Les simulations numériques permettent d'évaluer le potentiel dans le front d'ionisation qui dépend à la fois du potentiel appliqué à l'électrode haute tension et transféré à la plume ainsi que de la différence de potentiel induite par la séparation de charge locale. On constate que le potentiel du front d'ionisation nécessaire pour entretenir la propagation est proportionnel à la concentration locale en oxygène, qui augmente le long de l'axe du jet. Par conséquent, un champ électrique plus élevé est nécessaire lorsque la concentration en oxygène augmente et donc une augmentation du champ électrique est mesurée pour des positions croissantes le long de la plume de plasma.

Les densités de N_2 et O_2 dans le jet de plasma sont mesurées par diffusion Raman rotationnelle et donnent, à partir du centre du jet à la sortie du capillaire, une augmentation de la fraction d'air de 60 % sur 2 mm en direction radiale et 20 % sur 22 mm en direction axiale. Ces valeurs correspondent à une augmentation du potentiel dans le front d'ionisation nécessaire pour soutenir la propagation de 5 kV et 1,7 kV respectivement, expliquant pourquoi la propagation en direction radiale est limitée. Pour des distances allant jusqu'à 10 mm de la sortie du capillaire,

on constate que les fractions d'air dans le jet sont indépendantes de la forme de l'impulsion de tension appliquée, et même du fait que le plasma soit allumé ou éteint. Dans la même configuration, la diffusion Thomson est utilisée pour déterminer la densité électronique et la température électronique dans le jet de plasma. Des valeurs de l'ordre de 10^{19} m^{-3} et de quelques eV respectivement, sont mesurées. On constate que la densité électronique augmente avec la position axiale, tandis que la température électronique diminue. La comparaison avec les résultats des mêmes simulations fluides que précédemment montre que la position dans le jet à laquelle la diffusion Thomson permet réellement d'effectuer les mesures se trouve en réalité juste après le front d'ionisation, et non au centre du front. Cela explique les densités électroniques élevées observées ainsi que les températures électroniques relativement basses par rapport à ce qui serait attendu dans le front. Une diminution de l'amplitude de la tension appliquée d'un tiers entraîne une diminution de la densité électronique d'environ 14 %.

Les résultats du jet pulsé de cette thèse sont également comparés aux résultats publiés d'un jet avec la même géométrie et le même débit de gaz, mais alimenté avec une tension sinusoïdale (AC) à une fréquence six fois plus élevée et une amplitude de tension trois fois plus faible. A partir des résultats des fractions d'air dans le jet pulsé, on estime que la composition du flux du jet pulsé et du jet AC sont les mêmes. Le champ électrique dans les deux jets se révèle être le même, ce qui peut sembler surprenant, mais peut s'expliquer par le potentiel nécessaire en amont du jet pour entretenir la propagation est controlé principalement par la composition du gaz à une position donnée, qui reste inchangée quelque soit le plasma jet. En revanche, la plume de plasma est deux à trois fois plus courte dans le jet AC que dans le jet pulsé. La différence de puissance dissipée est de deux ordres de grandeur et n'est donc pas proportionnelle à la longueur de la plume. Bien que le champ électrique soit le même, la densité électronique devrait être beaucoup plus faible dans le jet AC en raison de l'amplitude de tension plus faible. Par conséquent la différence de longueur de la plume est probablement causée par quantité plus faible d'électrons produits. La même cause peut alors aussi expliquer la température du gaz plus élevée observée dans le jet pulsé par rapport au jet AC, comme mesuré à la fois par diffusion Raman rotationnelle et avec une sonde de température optique.

Comme on pouvait s'y attendre, la température du gaz dans le jet de plasma augmente, d'environ 12 ºC, lorsque la tension est appliquée au jet par rapport au flux de gaz seul. L' augmentation de l'amplitude, de la durée d'impulsion ou de la fréquence des impulsions de tension appliquées augmente la température du gaz, comme attendu de part la plus grande dissipée dans le plasma.

Les impulsions de tension ont également une influence sur la structure de l'écoulement de gaz dans le jet, comme le montre l'imagerie schlieren. Pour différents débits d'hélium, la structure d'écoulement dans le jet se révèle différente selon que le plasma est allumé ou éteint. Des structures turbulentes sont visibles à tous les débits lorsque le plasma est appliqué et uniquement au débit le plus élevé lorsque le plasma est éteint. Ces turbulences peuvent être induites par une augmentation de la vitesse d'écoulement du gaz, qui peut être provoquée soit par l'échauffement du gaz, soit par du"vent ionique" induit par le transfert d'impulsion entre particules chargées et neutres sous la forme de la force électrohydrodynamique. Des équations de la littérature sont utilisées avec les valeurs mesurées pour la plupart des paramètres tels que le champ électrique, la densité électronique et la température électronique, la température et la vitesse du gaz pour estimer lequel de ces deux mécanismes domine. On constate que le chauffage du gaz d'environ 12 ºC induit une augmentation de la vitesse du gaz d'un ordre de grandeur inférieur à la vitesse initiale du gaz, tandis que le vent électrique provoque un doublement de la vitesse du gaz. On estime donc que le principal mécanisme induisant des turbulences dans le jet de cette thèse est la force électrohydrodynamique.

Lorsque le jet impacte une cible métallique placé à 1 cm de la sortie du capillaire, la propagation de l'onde d'ionisation accélère en se rapprochant de la cible par rapport au comportement de l'onde d'ionisation dans le jet libre. Cette accélération est notable tout au long de la propagation lorsque la cible est mise à la terre, mais si la cible métallique est à un potentiel flottant, l'onde d'ionisation n'accélère que dans les 5 derniers mm avant la cible. La température du gaz augmente jusqu'à 25 ºC dans le canal entre le capillaire et la cible flottante. Dans tous les cas, cependant, le champ électrique est mesuré être approximativement le même que dans le jet libre. Avec les deux cibles, une onde de"rebond" a été observée après l'impact de l'onde d'ionisation sur la cible, se propageant de la cible vers l'électrode alimentée, à travers le canal déjà ionisé. La comparaison avec les résultats des mêmes simulations que pour le jet libre, mais adaptées au cas des cibles, montre un excellent accord sur toutes ces observations. De plus, les simulations montrent que l'onde de retour résulte d'une redistribution électrique du potentiel de l'électrode haute tension et de la cible. Une autre redistribution est également mise en évidence à la fin de l'impulsion de tension entre l'électrode alimentée, qui est maintenant reliée à la terre et le plasma positif. Cette redistribution est également visible dans les expériences comme une autre onde d'ionisation se propageant du capillaire à la cible, avec une intensité plus élevée dans le cas d'une cible flottante qu'avec une cible mise à la terre.

Dans le cas d'une cible flottante, l'évolution temporelle du potentiel dans la cible est mesurée et montre une augmentation à partir du moment de l'impact jusqu'à la fin de l'impulsion de tension appliquée, après quoi elle diminue jusqu'à atteindre à nouveau zéro. On montre que l'amplitude et la durée de l'impulsion de tension appliquée déterminent le potentiel maximum qui est atteint dans la cible. Juste après l'impact, le potentiel de la cible est encore faible (proche de la terre), alors qu'il peut augmenter jusqu'à la moitié de la tension appliquée à la fin de l'impulsion, c'est pourquoi le rebond de l'onde d'ionisation est similaire pour une cible flottante ou connectée à la terre. Les résultats des simulations montrent que pour une cible mise à la terre, le champ électrique et la température des électrons restent élevés, et la densité électronique augmente pendant l'impulsion de tension, alors que cela ne se produit pas pour une cible flottante. Pour la cible flottante, les expériences et les simulations montrent que le champ électrique, la densité électronique et la température augmentent après la fin de l'impulsion de tension. L'augmentation de la densité électronique en présence d'une cible métallique peut être attribuées à la fois à l'émission d'électrons de la surface et au transport de charge dans le plasma.

Ainsi, cette thèse caractérise un jet de plasma à pression atmosphérique pulsée, à l'aide de différents diagnostics optiques (emission et laser) et électriques ainsi que des résultats de simulations pour approfondir la compréhension de la dynamique des jets de plasma.

Samenvatting

Experimentele karakterisatie van helium plasma jets

Plasma jets hebben een breed scala aan toepassingen, zoals het behandelen van tumoren en het stimuleren van wondgenezing in de plasmageneeskunde, het stimuleren van de groei van zaden en planten in de plasmalandbouw en het modificeren van polymeervezels bij oppervlaktebehandelingen. Hoewel een plasma jet er misschien eenvoudig uitziet, is het in feite een voortbewegende elektrische ontlading die zich voortplant in een stroom van een edelgas (zoals helium). Deze ontlading wordt opgewekt in een diëlektrisch capillair buisje, volgens het principe van een diëlektrische barrièreontlading, waarna deze zich verder naar buiten voortplant door de omgevingslucht, volgens het streamer-mechanisme, totdat de ontlading het doelwit van de toepassingen bereikt. Voor alle toepassingen is het belangrijk om de dynamische processen in de plasma jet te begrijpen. Dit proefschrift bestudeert een helium plasma jet onder atmosferische druk die wordt aangedreven door positieve, unipolaire pulsen. Er zijn experimenten uitgevoerd die zich richten op de voortplantingsdynamiek, de structuur van de gasstroom en de temperatuur in een vrij expanderende plasma jet, evenals de invloed van een metalen doelwit op het plasma.

Een Stark-polarisatiespectroscopie-opstelling is gebouwd om het elektrische veld in het ionisatiefront langs de lengteas van de jet te meten. Waardes van 10 kV/cm zijn waargenomen in het capillaire buisje, terwijl in de plasmapluim een toename van het elektrische veld wordt gemeten tot 20 kV/cm. Bij een variërende amplitude en duur van de aangelegde spanningspuls zijn dezelfde waarden voor het elektrische veld verkregen, terwijl de lengte van de plasmapluim verandert. Vergelijking met de resultaten van een tweedimensionaal vloeistofmodel laat een uitstekende overeenkomst zien in de voortplantingsafstand en de snelheid van de ionisatiegolf, welke in de experimenten worden verkregen uit hogesnelheidsbeeldvorming met een geïntensiveerde CCD camera. De vergelijking van het elektrische veld laat een maximaal verschil zien van 11 %, maar de toename van het elektrische veld in de plasmapluim is hetzelfde. Uit de simulaties kan de potentiaal in het ionisatiefront worden verkregen, welke afhangt van de potentiaal die wordt overgedragen vanaf de elektrode waar de spanningspuls wordt aangelegd en ook van het potentiaalverschil dat wordt geïnduceerd door lokale ladingsscheiding. Het is gebleken dat de potentiaal in het ionisatiefront die nodig is om de voortplanting in stand te houden evenredig is met de lokale zuurstofconcentratie, die toeneemt langs de as van de jet. Daarom is een hoger elektrisch veld nodig wanneer de zuurstofconcentratie toeneemt en dus wordt een toename van het elektrische veld gemeten voor toenemende posities in de plasmapluim.

De dichtheden van N_2 en O_2 in de plasma jet worden gemeten met rotationele-Raman-verstrooiing en laten, beginnend in het midden van de jet bij de uitgang van het capillaire buisje, een toename in de luchtfractie van 60 % over 2 mm in radiale richting en 20 % over 22 mm in axiale richting zien. Om de voortplanting in stand te houden bij dergelijke N_2 en O_2 concentraties, zijn potentiaal toenames van respectievelijk 5 kV en 1,7 kV nodig. De voortplanting in radiale richting is daarom beperkt. Voor afstanden tot 10 mm vanaf de uitgang van het capillaire buisje blijkt dat de luchtfracties in de jet onafhankelijk zijn van de vorm van de aangelegde span-

ningspuls en zelfs van of er wel of geen plasma gemaakt wordt. In dezelfde opstelling wordt Thomson-verstrooiing gebruikt om de elektronendichtheid en de elektronentemperatuur in de plasma jet te bepalen. Hierbij worden waarden met een ordegrootte van respectievelijk 10^{19} m^{-3} en enkele eV gemeten. De elektronendichtheid blijkt toe te nemen met de axiale positie, terwijl de elektronentemperatuur afneemt. Vergelijking met resultaten van de eerder besproken simulatie laat zien dat de Thomson-verstrooiings methode eigenlijk direct na het ionisatiefront meet en niet erin. Dit verklaart dan het gedrag van de elektronendichtheid en temperatuur: doordat de elektronendichtheid achter het front hoog is, verliezen de elektronen meer energie door botsingen en dus is de elektronentemperatuur lager. Wanneer de amplitude van de aangelegde spanning met een derde verlaagd wordt, neemt de elektronendichtheid met ongeveer 14 % af.

De resultaten van de door pulsen aangedreven jet uit dit proefschrift worden ook vergeleken met de gepubliceerde resultaten van een jet met dezelfde geometrie en gasstroomsnelheid, maar met een sinusvormige (AC) aangelegde spanning met een zes keer hogere frequentie en een drie keer lagere spanningsamplitude. Op basis van de gemeten luchtfracties in de gepulseerde jet wordt geschat dat de samenstelling van de gasstroom van de gepulseerde jet en de AC-jet dezelfde zijn. Het elektrische veld in beide jets blijkt hetzelfde te zijn, wat misschien verrassend lijkt, maar kan worden verklaard door de vergelijkbare potentiaal in het golffront die nodig is om de voortplanting in stand te houden, aangezien de samenstelling van de gasstroom hetzelfde is. Aan de andere kant is de plasmapluim twee tot drie keer korter in de AC-jet dan in de gepulseerde jet. Het gedissipeerd vermogen is twee ordegroottes kleiner en is dus niet evenredig met de lengte van de pluim. Hoewel het elektrische veld hetzelfde is, wordt verwacht dat de elektronendichtheid veel lager is in de AC-jet vanwege de lagere amplitude van de aangelegde spanning, en daarom wordt het verschil in pluimlengte waarschijnlijk veroorzaakt door het verschil in de hoeveelheid geproduceerde elektronen. Dit zou dan ook de hogere gastemperatuur in de gepulseerde jet verklaren, zoals gemeten met rotationele-Raman-verstrooiing en een temperatuursonde, ten opzichte van de AC-jet.

Zoals te verwachten was, blijkt de temperatuur van het gas in de plasma jet te stijgen, met ongeveer 12 °C, wanneer de spanning op de jet wordt aangezet ten opzichte van wanneer alleen de gasstroom wordt aangezet. Het verhogen van de amplitude, pulsduur en frequentie van de aangelegde spanningspulsen heeft een positief effect op de gastemperatuur, wat overeenkomt met de gemeten energie per puls die in het plasma wordt gedissipeerd.

De spanningspulsen hebben ook invloed op de structuur van de gasstroom in de jet, zoals is gevisualiseerd door middel van schlieren-beeldvorming. Voor verschillende snelheden van de gebruikte heliumstroom wordt getoond dat de structuur van de gasstroom in de jet afhangt van de aanwezigheid van het plasma. Wanneer er een plasma is, worden turbulente structuren gezien bij alle stroomsnelheden en alleen bij de hoogste stroomsnelheid wanneer het plasma is uitgeschakeld. Deze turbulenties kunnen worden geïnduceerd door een toename van de gasstroomsnelheid, die kan worden veroorzaakt door de opwarming van het gas in het plasma of door de elektrische wind door impulsoverdracht tussen geladen en neutrale deeltjes in de vorm van de elektrohydrodynamische kracht. Gebruikmakende van gemeten waardes voor het elektrische veld, elektronendichtheid en temperatuur, gastemperatuur en snelheid wordt een afschatting gemaakt op basis van theoretische uitdrukkingen om te bepalen welk van de twee processen de meeste invloed heeft op de gasstroomsnelheid. Uit die afschatting blijkt dat de toename in gastemperatuur van 12 °C een toename van de gassnelheid veroorzaakt die een ordegrootte lager is dan de aanvankelijke gassnelheid, terwijl de elektrische wind een verdubbeling van de gassnelheid veroorzaakt. De elektrohydrodynamische krant wordt dan ook beschouwd als de belangrijkste bron van turbulentie voor de jet die in dit proefschrift bestudeerd wordt.

Bij het plaatsen van een metalen doelwit op 1 cm van de uitgang van het capillaire buisje

blijkt de ionisatiegolf naar het doelwit te versnellen wanneer deze geaard is, ten opzichte van het gedrag van de ionisatiegolf in de vrije jet. Wanneer het metalen doelwit zich op zwevende potentiaal bevindt, plant de ionisatiegolf zich alleen in de laatste 5 mm voor het doelwit sneller voort dan in de vrije jet. De gastemperatuur stijgt met maximaal 25 ºC in het kanaal tussen het capillaire buisje en het doelwit op zwevende potentiaal. In alle gevallen wordt echter ongeveer hetzelfde elektrische veld gemeten. Bij beide doelwitten is een teruggaande golf waargenomen na de impact van de ionisatiegolf op het doelwit die zich voortplant vanaf het doelwit terug naar de aangedreven elektrode, door het kanaal dat al is geïoniseerd. Deze waarnemingen zijn in overeenstemming met de resultaten van dezelfde simulaties als voor de vrije jet, maar aangepast aan de situatie met doelwitten. Verder laten de simulaties zien dat de teruggaande golf zorgt voor een elektrische herverdeling van de aangedreven elektrode en het doelwit, en ook laten ze een vergelijkbare herverdeling zien aan het einde van de spanningspuls tussen de aangedreven elektrode die nu geaard is en het positieve plasma. Deze herverdeling is ook in de experimenten zichtbaar als een andere ionisatiegolf die zich voortbeweegt van het capillaire buisje naar het doelwit, met een intensiteit die bij een doelwit op zwevende potentiaal hoger is dan bij een geaard doelwit.

In het geval van een doelwit op zwevende potentiaal wordt de tijdsevolutie van de potentiaal in het doel gemeten en vertoont deze een toename vanaf het moment van inslag tot aan het einde van de aangelegde spanningspuls, waarna de potentiaal afneemt totdat deze weer nul bereikt. Aangetoond wordt dat de amplitude en duur van de aangelegde spanningspuls de maximale potentiaal bepalen die in het doelwit wordt bereikt. Direct na de inslag is de potentiaal in het doelwit nog steeds laag (bijna geaard), terwijl deze aan het einde van de puls kan toenemen tot de helft van de aangelegde spanning op de elektrode. Daarom is de teruggaande ontlading vergelijkbaar voor het doelwit op zwevende potentiaal en het geaarde doelwit. Resultaten van de simulaties laten zien dat voor een geaard doelwit het elektrische veld en de elektronentemperatuur hoog blijven en de elektronendichtheid toeneemt tijdens de spanningspuls, terwijl dit bij een doelwit op zwevende potentiaal niet het geval is. Voor het doelwit op zwevende potentiaal laten zowel experimenten als simulaties zien dat het elektrische veld, de elektronendichtheid en de temperatuur toenemen na afloop van de spanningspuls. De toename van de elektronendichtheid wordt voor beide doelwitten toegeschreven aan elektronenemissie van de metalen oppervlakken en ladingstransport in het plasma.

Dit proefschrift karakteriseert dus een gepulseerde plasma jet onder atmosferische druk, waarbij verschillende optische (emissie en laser) en elektrische diagnostieken worden gebruikt, evenals resultaten van simulaties om het begrip van de dynamiek in plasma jets te verhogen.

Contents

Contents

1
Introduction

Abstract: This chapter gives a general introduction to plasma, dielectric barrier discharges and plasma jets. The working principle of the atmospheric pressure helium plasma jet that is used in this thesis is explained. Thereafter, the motivation, research goals and structure of this thesis are outlined.

1.1 Plasma

A plasma is a (partially) ionized gas, meaning that apart from the neutral atoms or molecules from the gas, it also contains charged particles: electrons and ions. These charged particles significantly change the behavior of the gas being in the gaseous state and therefore plasma is often considered the fourth state of matter, next to the well-known solid, liquid and gaseous states. Examples of plasma can be found everywhere. Well-known plasmas that can be found in nature are for example the sun and lightning strikes. In your everyday-life, the application of plasma can be seen for example in the chip of your phone and computer, since the manufacturing of these chips relies heavily on the use of plasma.

A plasma is created in the lab by applying a voltage difference over a gas that is placed between electrodes, as shown schematically in figure 1.1(a). The magnitude of the voltage that is needed to created a breakdown in the gas that starts the formation of the plasma depends on the gas type, the pressure of the gas and the distance between the electrodes, according to the Paschen curves [1].

Inside a plasma, we can distinguish different temperatures that belong to different types of species. The most common temperatures are the temperature of the electrons T_e and the temperature of the heavy species, i.e. the atoms, molecules and ions in the plasma. The latter is often referred to as the gas temperature T_{gas}. Based on these two temperatures, a separation can be made between two types of plasmas: thermal plasmas and non-thermal plasmas. Thermal plasmas are in thermal equilibrium, meaning that the gas temperature is equal to the electron temperature ($T_{gas} = T_e$). Non-thermal plasma are not in thermal equilibrium, meaning that the heavy species have not been able to equilibrate to the electron temperature, thus $T_e \gg T_{gas}$. Typically, T_{gas} has values of the order of 10^2 K (10^{-2} eV), while the values for T_e are in the order of 10^4 K (1 eV), which is a difference of two orders of magnitude. Because the gas temperature is low compared to the electron temperature, non-thermal plasmas are also called low temperature plasmas or cold plasmas.

1.1.1 Dielectric barrier discharges

A well established method of achieving a non-thermal plasma is by using a dielectric barrier discharge (DBD). Dielectric material, that acts as a barrier since it is an insulating material, is placed inside the discharge gap on one or both of the electrodes, as is shown schematically in figure 1.1(b). This dielectric barrier prevents the direct flow of current through the plasma from
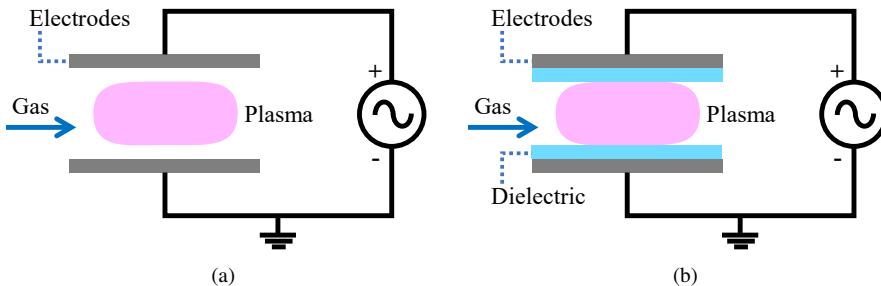
Figure 1.1: Schematic overview of an example of a) a discharge in parallel plate configuration and b) a dielectric barrier discharge.

one electrode to the other electrode, which prevents the formation of a thermal arc. A thermal arc is a plasma channel where the gas temperature is equal to the electron temperature. Preventing the formation of an arc thus prevents the gas to heat to the temperature of the electrons and thus the plasma in a dielectric barrier discharge stays non-thermal. In a regular discharge, as shown in figure 1.1(a), plasma will sustain as long as the amount of gas atoms or neutrals and the applied voltage is sufficient. In a DBD, however, this is not the case, since the charges that are separated by the applied electric field cannot recombine at the electrodes, but instead start to accumulate on the dielectric. This leads to the accumulation of positive charges at the cathode (negative electrode) and negative charges at the anode (positive electrode), which creates an electric field in the opposite direction of the initially applied electric field. In the end, the net electric field is zero and the plasma dies out. To sustain the plasma, the polarity of the applied voltage has to be reversed. Therefore, dielectric barrier discharges operate with an alternating or pulsed voltage.

1.1.2   Plasma jets

DBDs are for example used to purify air or to produce ozone [2, 3], but they are also used in the form of a non-thermal atmospheric pressure plasma jet. Plasma jets in literature can designate all kind of plasma sources, including radio frequency (RF) and microwave (MW) sources and sometimes even a nanosecond discharge embedded in a small volume tube, but here only DBD plasma jets will be considered. These plasma jets exist in all different geometries as shown by Lu *et al.* [4], but the main difference between a plasma jet DBD and a DBD as discussed before is that the plasma is ignited in a tube with a volume that is small enough to spatially force the confinement of the charges, such that the electric field induced by these charges remains high enough for the plasma to develop and propagate. Because of the different geometries, the plasma jets all work slightly different, but the main principle is the same: an alternating voltage (pulsed or sinusoidal) is applied to a constant gas flow inside the jet with dielectric walls, which continues to flow into the ambient gas at atmospheric pressure. The applied gas is generally a noble gas such as helium or argon and the ambient gas is generally air, nitrogen or oxygen.

Figure 1.2 shows the plasma jet that is used in this thesis, based on a coaxial DBD, with a schematic overview on the left and a picture of the jet on the right. Unipolar positive high voltage pulses, with an amplitude of several kV, a µs width and a kHz repetition rate, are applied to the anode at the top of the jet, which is hollow and functions also as the inlet of the gas flow, that is helium in this thesis. The hollow anode extends over a few cm and is surrounded by a dielectric (glass) capillary with an inner diameter of 2.5 mm. Around the capillary sits a copper ring, attached to the ground, that acts as the cathode. The formation of the plasma in the jet can be explained using the example signals of the applied voltage pulse and the current measured at the ground electrode (over a resistor of 1 kΩ) that are shown in figure 1.3. At the rise of the applied voltage (a), an electric field is formed between the anode and the cathode, which causes ionization to take place in this region, leading to an increase in the current. When the voltage is sufficiently high, breakdown takes place between the electrodes (b), but since they are shielded by the dielectric capillary, charge starts to accumulate on the inner walls of the capillary just below the cathode. This charge accumulation is visible as a sharp rise in the current. At the peak of the current (c), an ionization wave is formed due to the accumulation and overflow of space charge beneath the cathode [5]. The ionization wave, also known as plasma bullet or ionization front, then travels towards the end of the capillary, which is visible as a drop in the current at the ground electrode. No change in current is visible until the end of the voltage pulse, since the ionization wave travels further into the ambient air over a few cm and then dies out. When the voltage starts to decrease (d), an electric field is again formed between the electrodes, but now in
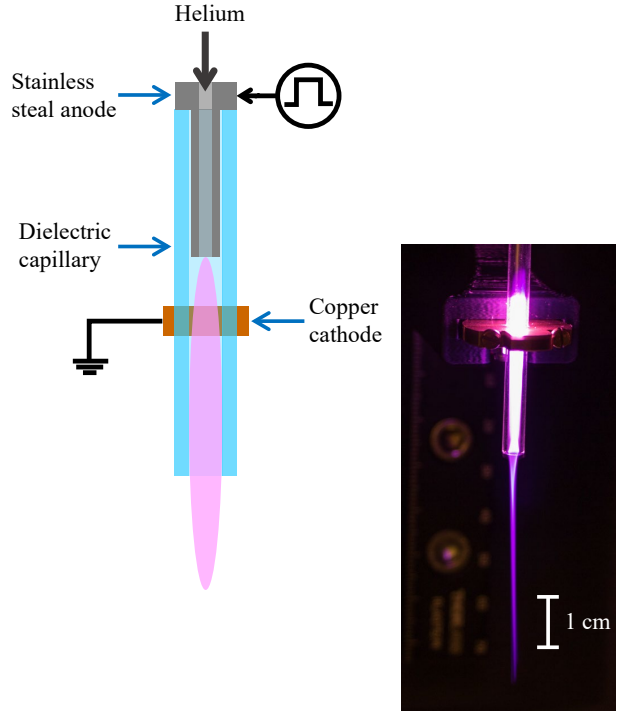
Figure 1.2: Schematic overview of the plasma jet used in this thesis (left, not to scale) and a picture of the same jet (right, to scale as indicated).
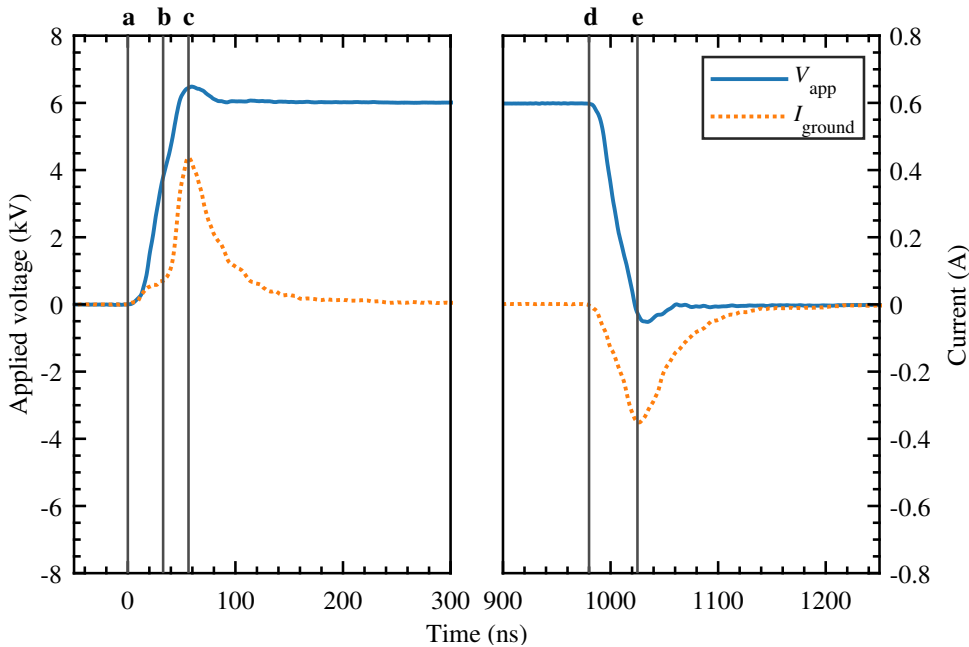
Figure 1.3: Example signals for the applied voltage and the current at the ground electrode of the jet.

the opposite direction. This leads to accumulation of charge on the inner walls of the capillary of opposite polarity compared to the charge accumulation at the rise of the voltage. The current shows therefore an increase again, but with negative polarity. At the peak of the current (e), an ionization wave is formed that travels down the capillary and potentially also into the ambient air, depending on the applied voltage and helium flow rate.

This process of the formation of ionization waves or plasma bullets takes place at every voltage pulse, hence 5000 waves per second are formed when the frequency of the pulses is 5 kHz. It was shown for the first time in [6, 7] that the plasma jet consists of these plasma bullets or ionization waves. In the picture of the jet (figure 1.2) the accumulation of all these individual ionization waves is visible and it shows the plasma as a continuous event, since the exposure time of the camera was significantly larger than the duration of a voltage pulse. This picture represents well how the plasma is visible to the naked eye. The part of the plasma that is present in the ambient air is called the plasma plume or the effluent.

From the region below the cathode where the ionization wave is formed, up until the end of the plasma plume, the ionization wave propagates following the streamer mechanism [8–10]. Using the explanation of [1], for example, the streamer mechanism can be described as follows. Free electrons that are present in the gas are accelerated by the applied electric field, making them collide with the background gas and thus creating ions. The applied electric field then causes a charge separation of the electrons and the positive ions. If the charge density in this charge separation volume is large enough, an electric field of similar strength as the applied electric field is induced. Locally, in front of the charge separation region, this induced electric field can re-enforce the applied electric field, leading to very efficient ionization processes and thus to the spatial propagation of the streamer. Figure 1.4 shows a schematic overview of the streamer propagation mechanism. The propagation it thus driven by the high electric field in the front, which in turn creates a high amount of space charges. This charge is positive for a positive streamer and negative for a negative streamer. A positive streamer (figure 1.4(a)) originates from an initial electric field that pulls electrons to the anode, while for a negative streamer (figure 1.4(b)) this field pushes electrons away from the cathode. Referring again to figure 1.3, in our case a positive streamer occurs at the rise of the applied voltage and a negative streamer at the fall of the applied voltage, since the electric field is reversed in the latter case. In positive streamers, electrons in front of the streamer are accelerated towards the high field
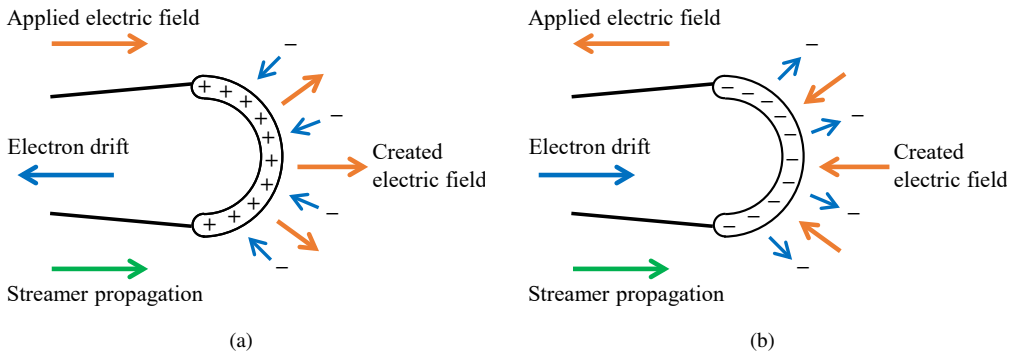
Figure 1.4: Schematic overview the streamer propagation mechanism for a) a positive streamer and b) a negative streamer. Electric field directions are indicated with orange arrows, electron movement with blue arrows and streamer propagation direction with green arrows.

front because of the large amount of space charge there, and they produce ions in collisions underway. These electrons in front of the streamer are important for the streamer propagation and they can be present from the natural electron background due to cosmic rays, leftover from a previous discharge or created by photo-ionization. Photo-ionization is the formation of ions due to collisions of the background gas with energetic photons that are created at the high field front, and Liu *et al.* [11] have shown that this is an important process for the production of electrons in front of a streamer head. Apart from being accelerated towards the front, electrons also drift towards the anode, on the other hand, which is away from the produced ions, and because this happens at much longer times scales than the propagation itself, the electrons thus neutralize the channel behind the high field front. A positive streamer thus propagates in same direction as the initially applied electric field and in the opposite direction of the electron drift. In negative streamers, the propagation principle is the same, but the streamer propagates in the opposite direction of the initially applied field and in the same direction as the electron drift. Photo-ionization as source of electrons in front of the streamer is less important, since ample electrons are available there. Ionization takes place in the front, because there the field is the highest. Both streamer types have a front with a high electric field and a quasi-neutral channel behind this front that has a very low electric field.

While propagation through the ambient air, collisions do not only take place between electrons and helium atoms from the feed gas, but also with the N_2 and O_2 species from the air. Notably, N_2 has a lower ionization potential than He, thus it is easier to ionize N_2 which is present mostly radially around the helium channel. Furthermore, the reaction of helium metastables with N_2 ($He^m + N_2 \rightarrow e^- + He + N_2^+$) is very efficient [9], which increases the production of N_2 ions. The ionization wave propagates therefore mainly over the boundary layer between the helium channel and the ambient air, and can produce a lot of other species on the way. These are reactive oxygen and nitrogen species (RONS) such as NO, NO_2, NO_3 and O_3, but also OH and H_2O_2 from collisions with water molecules from the air.

Plasma jets can thus produce a lot of reactive species, charged species (electrons and ions), high energy photons and high electric fields.

1.1.3   Plasma jet applications

Because the plasma plume can have length of a few cm, plasma jets are able to deliver a number of reactive species (e.g. NO, NO_2, NO_3, O_3, OH, H_2O_2), charged species (ions and electrons), high energy (UV) photons and high electric fields to distant locations, which makes them very promising for all kinds of applications. For over two decades, non-thermal atmospheric pressure plasma jets have been studied for their variety of applications, which range from plasma medicine [12–15] to surface modifications [16–20] and plasma agriculture [21, 22].

The review papers from Fridman *et al.* [13] and Kong *et al.* [14] for example have shown the wide range of applications of non-thermal plasma, among which are the non-thermal plasma jets, in plasma medicine. By testing the amount of bacteria present, Fridman *et al.* have shown that these type of plasma are very effective in sterilization of live tissue, such as wounds and burns, while not damaging the tissue. Additionally, the plasma stimulates blood coagulation and cell renewal, which accelerates the healing process of wounds. Hulsheger *et al.* [23, 24] have shown that the application of electric fields in the order of several kV/cm decreases the survival rate of bacteria by three orders of magnitude. Also, Girard *et al.* [25] have shown that the synergistic effect of H_2O_2 and NO_2, as produced by the plasma jet, contributes to the death of cells when interacting with the plasma jet.

Ito *et al.* [22] have shown the suitability of non-thermal plasma for the decontamination of agricultural products and the enhancement of seed germination and growth of plants.

1.2 Motivation and research goals

For all applications it is important to understand how the plasma jet works and therefore knowledge is needed on the parameters that define the plasma dynamics, among which are the electric field, electron density, electron temperature and gas temperature. Although non-thermal plasma jets have been studied for over two decades, these parameters have never been measured in one and the same jet, to the author's knowledge. There exist some studies on the electric field, electron density and electron temperature in plasma jets, but these studies are not numerous. A possible reason for this is that the plasma jet is in fact a transient discharge, that propagates in space (first inside a dielectric capillary and then into the ambient gas) and mixes the background gas with the ambient gas. The ionization waves are micrometer to millimeter sized and travel at velocities of $10^4 - 10^6$ m/s, making it difficult for the diagnostics to probe. A lot of experiments as well as simulations are performed on jets with different geometries, gas velocities, input power, etc., which makes it difficult to compare the results.

In this thesis, we use a plasma jet with the same geometry as used before in a number of published papers [5, 26–32], an experimental PhD thesis [33] and a numerical PhD thesis [34]. A large part of the experimental results in these publications was performed with a sinusoidal (AC) voltage applied to the jet. As shown in section 1.1.2, the jet in this thesis will be powered by μs long, uni-polar pulses at a kHz frequency, which enables us to compare the experimental results to results from the model presented in [34]. Experimental results of [33] have already been compared to results from this model [35], but this was mainly done for measurements of the deposited charge [36] and the induced electric field [37, 38] and temperature influences [39] in an optically active target when interacting with the plasma jet. The influence of the plasma is thus studied by probing the target. In this thesis, we focus on studying the effluent of the plasma for a freely expanding jet as well as for a jet interacting with a target. Important plasma parameters, such as the electron density and temperature, electric field and gas temperature, are measured in the plasma jet, but since we cannot measure everything, we have also compared these results to the model of [34] and deduced more information from the model, if possible. In order to constraint models and provide a detailed understanding of the dynamics in the plasma jet, it is necessary to measure as many plasma parameters as possible in the same plasma jet source. Several of the parameters that are measured in this thesis have been measured separately in different plasma jet sources in literature, but since all parameters are strongly coupled it is very difficult to draw general conclusions on their influence on the plasma dynamics.

Research questions that will be treated in this thesis are:

- What determines the propagation of the ionization waves in the pulsed plasma jet and how does this relate to the AC jet?

- What is the influence of the plasma on the applied gas flow, i.e. how does it change the gas temperature and the mixing of the flow with the ambient air?

- What is the influence of a conducting target on the plasma and how does the behavior change with a floating or grounded target?

The electric field in the ionization front is key to its propagation and influences different

kinds of processes in the plasma jet. It is therefore the main parameter that is measured throughout the whole thesis.

1.3 Structure of the thesis

This thesis is organized as follows:

- **Chapter 2** explains the different diagnostics and setups that are used to measure different parameters in the plasma jet. These diagnostics include energy measurements; ICCD imaging; Stark polarization spectroscopy; Thomson and rotational Raman scattering; temperature probe measurements; schlieren imaging and target potential measurements. The setups are explained as well as the methods to derive the desired parameters from the measurements.

- Since determining the electric field is the main method in this thesis, **chapter 3** shows the full derivation of the calculation that is necessary to derive electric field values from the measurements. Although the used diagnostic is not new, the full derivation has not been published before and is therefore also included to allow others to adjust the method to their needs.

- By comparing the results from experiments with those from simulations, **chapter 4** studies the propagation of the ionization front in the plasma jet. Based on the comparison of position, velocity, electric field, electron density and electron temperature in the ionization wave for different amplitudes and durations of the applied voltage pulse, criteria are proposed that should hold in the ionization front to sustain propagation.

- In **chapter 5** the flow structure and air entrainment in the plasma jet is studied, with focus on the influence of the plasma on the flow in the jet. Qualitative and quantitative measurements of the air density and the flow profile are performed using different diagnostics.

- **Chapter 6** studies the influence of the plasma on the gas temperature in the plasma jet. Using the results from the previous chapters, the main mechanism is determined that causes the heating of the gas in the jet. Furthermore, it is determined if gas heating or electric wind is the cause for the changes in flow structure as observed in chapter 5.

- The influence of conductive targets on the plasma jet is studied in **chapter 7**, where similar diagnostics are used as in chapter 4 to compare the results from experiments with those from simulations. Additionally, the potential of a floating conductive target is measured and compared. Furthermore, the influence of grounding a target or having it floating is analyzed.

- The thesis is concluded in **chapter 8** with general conclusions based on the results in the different chapters. An outlook with recommendations for future research on the plasma jet is also included.

2

Diagnostics and experimental setups

Abstract: This chapter describes how the different diagnostics are used to characterize the helium plasma jet. The following diagnostics are used and covered in this chapter: energy measurements; ICCD imaging; Stark polarization spectroscopy; Thomson and rotational Raman scattering; temperature probe measurements; schlieren imaging and target potential measurements. The experimental setups are explained as well as the data analysis to obtain quantitative results from the performed measurements.

2.1 General plasma jet setup

The plasma jet that is used in this thesis is shown schematically in the center of figure 2.1, where all dimensions are also indicated. It consists of a capillary tube, made of Pyrex, that acts as the dielectric barrier, which has an inner diameter of 2.5 mm and an outer diameter of 4 mm. Inside, a stainless steel Swagelok tube is placed with a Swagelok connector at the top, that acts both as the powered electrode as well as the inlet for the helium flow. The space at the top between the metal tube and the capillary is air sealed with Teflon tape. On the outside of the capillary, at 5 mm below the metal tube, a copper ring is attached that acts as the ground electrode, since it is connected to the ground via a cable with a 1 kΩ resistor.

In figure 2.1, the plasma jet is shown in the general setup that is needed to operate the jet. Helium, with a purity of $\geq 99,9999$ %, is flowing from the bottle to the inlet of the plasma jet. The flow is controlled by a mass flow controller (Bronkhorst High Tech EL Flow select) and set to a value in the range of 500 to 1500 sccm ($\hat{=} 0.5 - 1.5$ slm). Apart from a small part (≈ 20 cm long) that is connected to the powered electrode, all piping between the helium bottle and the jet inlet are made of stainless steel to limit the amount of impurities in the helium flow. This small part is made of Teflon to prevent the mass flow controller from having a conductive connection to the high voltage. A waveform generator is used to make a square pulse, with a variable width t_f of $0.1 - 10$ μs and repetition rate f of $0.3 - 5$ kHz. This signal and the DC high voltage V_P from the HV power supply, in the range of $4 - 6$ kV, are fed to the HV pulse generator that creates the high voltage unipolar positive square pulses that power the jet. The output of the HV pulse generator and the input of HV probe 1 are connected with the tube from the mass flow controller to the Swagelok connector at the top of the jet. To monitor the plasma when operating, the voltage over the resistor at the grounded side of the jet is measured with HV probe 2, yielding according to Ohm's law the current that flows to the ground. Both voltage signals are monitored on the oscilloscope. Figure 2.2 shows an example of the applied voltage pulse together with the current at the ground electrode, when the parameters of the jet are set to $V_P = 6$ kV, $f = 5$ kHz, $t_f = 1$ us and a flow of 1.5 slm He.

Multiple diagnostics are used to characterize the plasma jet, and therefore it is placed in different experimental setups. In the next sections, the different setups are explained in more detail. The equipment to operate the plasma jet is not the same in every experimental setup. The diagnostics can be divided in two groups, where each group makes use of the same operating equipment. Group A consists of ICCD imaging, energy measurements, Stark polarization spectroscopy, Thomson and rotational Raman scattering, and target potential measurements, while group B consists of temperature probe measurements and schlieren imaging. Table 2.1 gives an overview of the equipment used to operate the jet in the different groups of diagnostics.

Table 2.1: Specifications of the equipment used to operate the jet in the different groups of diagnostics.

	Group A	Group B
Waveform generator	Agilent 33220A	Tektronix AFG 3251
HV power supply	Spellman UHR10P60	FUG HCP 350-6500
HV pulse generator	DEI PVX-4110	DEI PVX-4130
Oscilloscope	LeCroy waveRunner 6100A 1GHz	LeCroy waveAce 230
HV probe 1	LeCroy PHV4-3432	LeCroy PPE 20 kV
HV probe 2	LeCroy 2.5 kV	TESTEC 2.5 kV
Helium bottle	Helium 5.0 from Linde Gas Benelux	Alphagaz helium 2 from Air Liquide
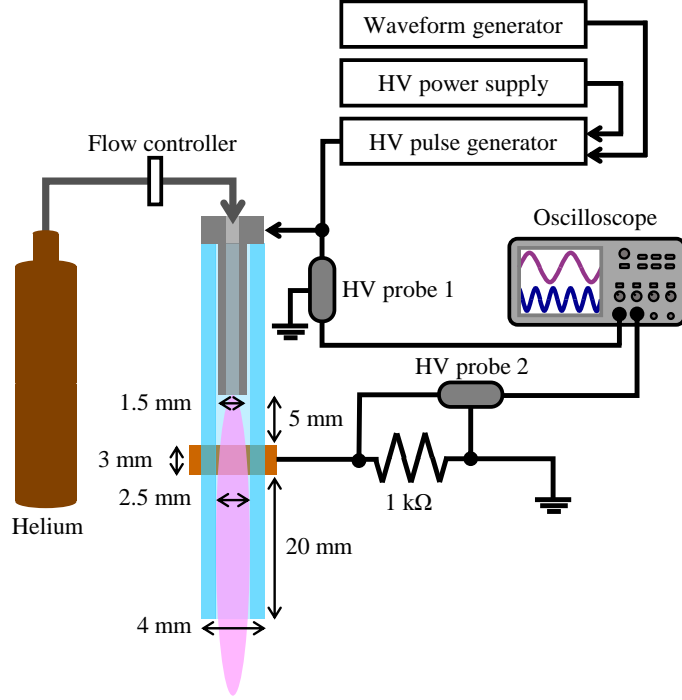
Figure 2.1: Schematic overview of the geometry and the operating setup of the plasma jet.
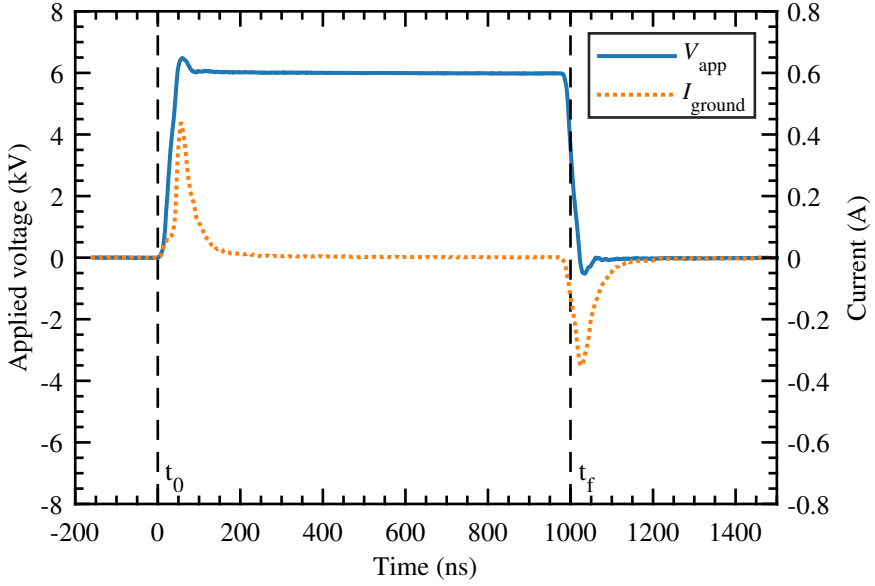
Figure 2.2: Example signals for the applied voltage and the current at the ground electrode of the jet at $V_P = 6$ kV, $f = 5$ kHz, $t_f = 1$ us and 1.5 slm He.

2.2 Energy measurements

The current that flows through the operating circuit of the plasma jet when the plasma is on consists of a capacitive component and a conductive component as given by $I_{tot} = I_{cap} + I_{con}$ [40]. The capacitive current I_{cap}, also known as displacement current, is the current that arises from the circuit of the plasma operating equipment, which acts as a capacitor. The conductive current I_{con} is the current that flows through the plasma, which is a conductor, and therefore we will call this the plasma current from now on. If all settings are kept constant, the capacitive current is the same at plasma On as at plasma Off, when the voltage is still applied but the flow is turned off. Furthermore, it is the only current that flows when the plasma is off. The plasma current, in which we are interested, is thus given by

$$I_{plasma} = I_{tot} - I_{cap} \ . \tag{2.1}$$

Using the setup shown in figure 2.3, the current at the anode of the plasma jet is measured with a Rogowski coil (Pearson Current Monitor 6585) and read out on the oscilloscope (LeCroy waveRunner 6100A 1GHz). I_{tot} is measured as the total current when the plasma is on and I_{cap} as the total current when the plasma is off. Similar as in section 2.1, the voltage that is applied to the anode of the jet is measured with the same high voltage probe (LeCroy PHV4-3432) and read out on the oscilloscope. The voltage in the circuit at plasma On is equal at plasma Off, thus $V_{plasma} = V_{tot} = V_{cap}$ holds. The energy that is dissipated in the plasma can then be calculated as

$$E_{plasma} = \int_0^T P_{plasma} \ \mathrm{d}t = \int_0^T V_{tot} I_{plasma} \ \mathrm{d}t \tag{2.2}$$

where the time integral is taken over one full voltage pulse.

Examples signals of the applied voltage and the different currents are shown in figure 2.4. The plasma energy per pulse is calculated with equation (2.2) and the time integral is performed over the whole time window as shown in this figure.
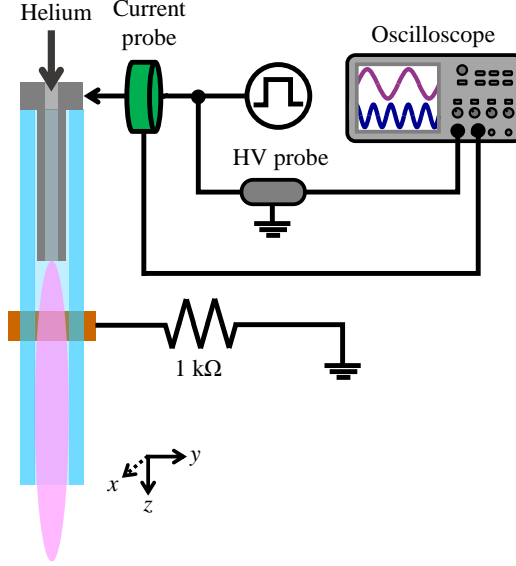
Figure 2.3: Schematic overview of the setup to measure the energy that is applied to the plasma.
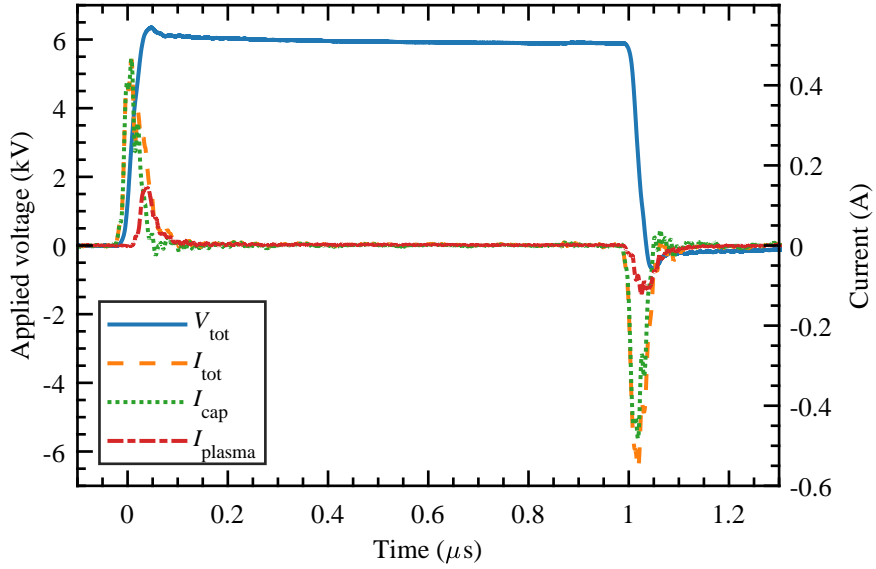
Figure 2.4: Example signals for the applied voltage and the different currents as measured at the anode of the jet to determine the energy that goes into the plasma. The operating conditions are $V_P = 6\,kV, f = 5\,kHz$, $t_f = 1$ us and 1.5 slm He.

2.3 ICCD imaging

2.3.1 Experimental setup

The discharge in the plasma jet is not a continuous event, but rather a series of fast consecutive events, because of the pulsed applied voltage. At every applied voltage pulse, a discharge event takes place, which is called a guided ionization wave, ionization front or plasma bullet. To investigate these ionization waves and determine their velocity, ICCD imaging is used. An ICCD camera consists of a CCD (Charge Coupled Device, the chip) with an intensifier in front that uses a photocathode, a micro-channel plate (MCP) and a phosphor screen to enhance the light of the incoming photons. The gate of the intensifier can be controlled, and both these characteristics make an ICCD camera very suitable for imaging the fast ionization waves that have low light emission.

The setup that is used for the ICCD imaging is shown in figure 2.5. The ICCD camera (Stanford Computer Optics 4Picos S20Q) with objective (TAMRON 70-300 mm, f/4-5.6 DI LD Macro) is placed such that the full trajectory of the ionization wave from below the grounded electrode of the jet until the end of the plasma plume is visible on the chip. The camera is triggered by the output of the waveform generator.

On a computer, the software 4Spec is used to control the camera. In this software, there are different settings to adjust when taking images:

- the delay: the time between which the camera receives the trigger and opens the gate;
- the exposure time: the time that the gate stays open, during which charge can accumulate on the chip;
- the gain: the voltage set on the MCP to accelerate electrons, thus enhancing the incoming light;
- the number of frames: the number of times the gate is opened to accumulate charge on the chip before it is read out.

In general, the delay is set between $160 - 1500$ ns, the exposure time to 2 ns, the gain to 910 V and the number of frames to $10 - 20$, but in particular cases these values may be slightly altered.

Every day a measurement is done and every time a setting is changed, a background image is taken, meaning that the settings are kept the same as for a normal measurement, but something is placed in front of the jet to block the light emission from the jet. This background image is then subtracted from every normal image from that corresponding day and setting. In this way, the signal to noise ratio of the images is increased, since for example stray light is subtracted. A measurement series consists of taking consecutive images with an increasing delay time, to follow the ionization wave in its path from the grounded electrode to the end of the plume.

The images are calibrated by taking an image at a longer exposure time, with the plasma switched off and with a ruler placed next to the jet, such that the ruler and the capillary are visible on the image. The ruler in the image is used to obtain a calibration factor to go from a distance in pixels to a distance in mm. In the same image, the position of the capillary and the grounded electrode are used to set the z-axis, vertically at the center of the jet, where z is negative inside the tube, zero at the nozzle and positive outside the tube.

2.3.2 Data analysis

This section explains how the position and velocity of the plasma bullet is determined from an ICCD imaging measurement series.
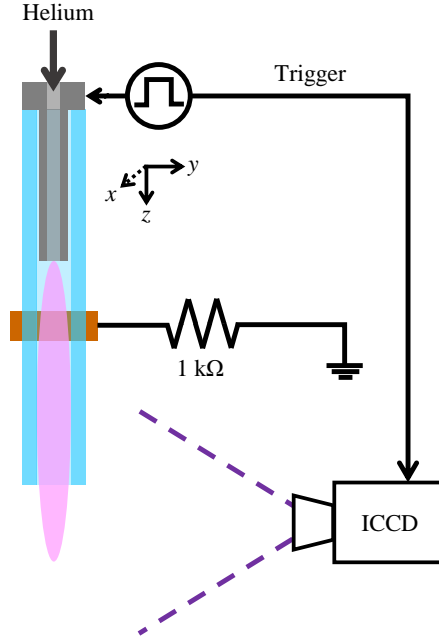
Figure 2.5: Schematic overview of the ICCD imaging setup.

A measurement series at specific settings of the plasma jet consists of a series of images taken at increasing time instants. First, the background image is subtracted from all images. Figure 2.6 shows example images from a measurement series for different time instants. The images are spatially calibrated using the calibration image as explained in section 2.3.1. It is found that 81 pixels correspond to 1 cm, thus the spatial resolution is 0.1235 mm. To determine the position of the plasma bullet, a threshold is set to a value of about 10% of the maximum intensity in the images. Then, at every image, within the columns corresponding to the inner diameter of the capillary (i.e. the region between the white, vertical lines in figure 2.6), every row from the starting position until the end of the image is searched for the maximum intensity if this intensity is higher than the threshold value. The starting position moves along with the images, since the ionization wave is moving, such that no positions can be found too far below the previous position. It starts at the bottom of the cathode and then it is set to 50 pixels (≈ 6.2 mm) below the previously found position of the ionization wave. Only the last found position where the intensity is higher than the threshold value is saved, which then corresponds to the position of the bullet in that image. This is done for every image in the measurement series, yielding the position of the bullet as function of time.

To obtain the velocity of the plasma bullet from the position as function of time, a second order polynomial is fitted trough five consecutive data points at every position. The derivative of this fit to time then yields the velocity of the plasma bullet. The error in the velocity is calculated as

$$S_v = \sqrt{\left(\frac{\partial v}{\partial x}\right)^2 S_t^2 + \left(\frac{\partial v}{\partial t}\right)^2 S_x^2} \tag{2.3}$$

where v is the velocity, x the position and t the time. The error in the position S_x is set to 5 pixels and the error in time to 5 ns.
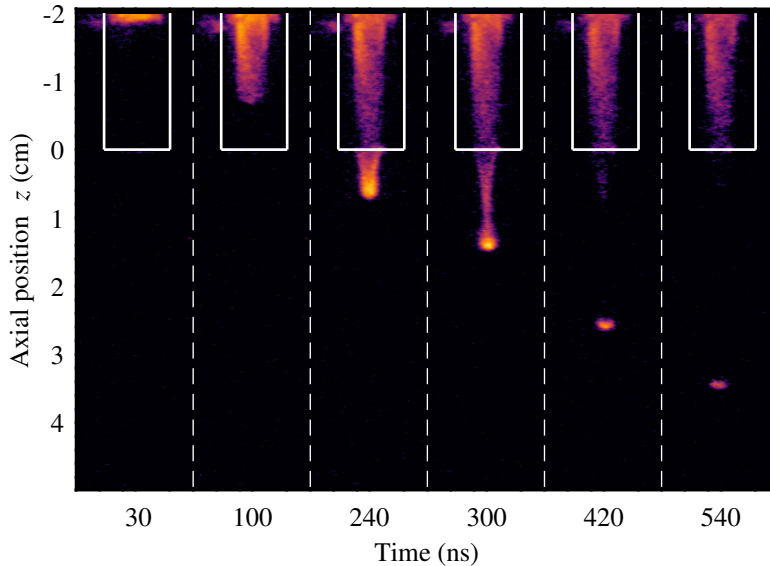
Figure 2.6: Example ICCD images for a jet in upwards configuration at different moments in time, with $V_P = 6$ kV, $f = 5$ kHz, $t_f = 1$ us and 1.5 slm He. The borders of the capillary are indicated in white. The colors represent the intensity of the emitted light and are plotted on a log-scale.

2.4 Stark polarization spectroscopy

2.4.1 Experimental setup

To determine the electric field in the front of the ionization wave, a Stark polarization spectroscopy setup was built, in which the jet is placed. This setup is shown schematically in figure 2.7. As will be shown in section 3.2, the electric field can be determined from the peak-to-peak wavelength difference between the allowed and the forbidden component of a certain helium line. To get this wavelength difference, a high resolution spectrum needs to be obtained of the desired helium line, emitted by the plasma.

The light emission from the plasma is focused with two identical plano-convex lenses (Thorlabs LA1050, $f = 10$ cm) onto the slit of a 1 m spectrometer (Jobin-Yvon HR1000, equipped with a 1200 l/mm grating, blazed at $0.4 - 1.1$ μm). Before entering the spectrometer, the light passes a linear polarizer (Thorlabs) to make sure only linearly polarized light remains, in order to measure the axial electric field, as explained in section 3.5. At the exit of the spectrometer, an ICCD camera (Stanford Computer Optics 4QuickE S20) is mounted to capture the spectral images. The camera is controlled on a computer by the software 4Spec and it is triggered by the output of the waveform generator. The same settings as for the 4Picos ICCD camera in section 2.3 are adjusted when taking images, but now also the integration time is available. The integration time is the time during which exposures (time between the gate opening and closing) are accumulated on the chip within one frame. In general, the delay is set between $180 - 600$ ns, the exposure time to 10 ns, the gain to the maximum value of 1000 V, the number of frames to 20 and the integration time to $2 - 20$ s (depending on the intensity of the light), but in particular cases these values may be slightly altered.

To increase the signal to noise ratio and because the camera has no cooling by itself, the CCD chip is cooled with a Peltier element based cooling, created for [41] and adjusted for this

thesis. This cooling consists of a Peltier element (TEC1-12705) placed on the CCD, with on top of that a copper water cooling system to cool the Peltier element. The temperature is measured with a Pt100 sensor, placed inside a small gap in the CCD. A temperature controller (H-Tronic TSM1000) is connected to the sensor and to a power supply (Delta Elektronica EK 030-10), which in turn is connected to the Peltier element. Setting the On and Off temperatures for the cooling to 3 °C and 4 °C, respectively, and the output of the power supply to 10 V at 4 A, means that the CCD maintained a temperature of $3 - 4.5$ °C. To prevent condensation on the CCD chip, a dry air flow is applied inside the housing of the camera.

The jet is placed on translation stages to move precisely in all (x, y, z) directions, in order to focus the jet well on the slit. In the z-direction, the jet needs to be able to move precisely over a longer distance, since only a small part (< 1 cm) can be imaged at once on the slit. A motorized translation stage (Thorlabs MTS50/M-Z8 DC Servo Actuator) is used, that is controlled on a computer by the Kinesis software from Thorlabs and which has a maximum traveling distance of 5 cm. By adjusting the height of the jet and changing the delay time on the ICCD camera accordingly, the spectrum of the jet can be obtained from inside the tube below the grounded electrode up until outside in the plasma plume at a few cm from the nozzle.
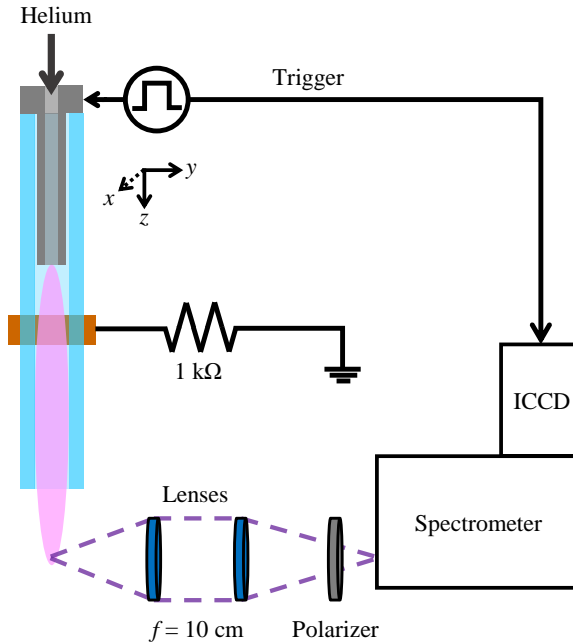
Figure 2.7: Schematic overview of the Stark polarization spectroscopy setup.

2.4.2 Data analysis

This section explains how the electric field values are determined from the spectral images of the ICCD camera.

Images

For all images, first the background image is subtracted. Then, since it is possible that the images still have a background offset that results in noise, the average value of the background in the images is subtracted. To filter out too bright pixels, a third order, 1D median filter is applied over the full image.

Figure 2.8 shows example spectral images as obtained by the ICCD camera, for a position inside the capillary (figure 2.8(a)) and outside the capillary (figure 2.8(b)). The size of the images is 582×782 pixels. The horizontal axis is calibrated by using the position of the N_2 line (at 491.494 nm and at 293 pixels) since it is not shifted due to the Stark effect. Then, the horizontal axis corresponds to the wavelength and 74.15 pixels correspond to 1 nm, thus the spectral resolution is 0.013486 nm. The vertical axis is calibrated by taking a spectral image at the position of the jet where the grounded electrode, which has a known size of 3 mm, is in the center of the image. Then, the vertical axis corresponds to the axial position z, where 67 pixels correspond to 1 mm thus the spatial resolution is 0.0149 mm and the origin of this z-axis is set at the exit of the capillary (2 cm below the grounded electrode).

In figures 2.8(a) and 2.8(b), the bright vertical line in the center corresponds to the emission of the allowed component of the He I 492.2 nm line and the less bright line on the left of this corresponds to the forbidden component. In contrast to figure 2.8(a), figure 2.8(b) also shows a fainter band of emission lines to the left of the forbidden component, which correspond to a molecular band of nitrogen lines.

Spectra

In figure 2.8, the range along the axial position in which the bullet is well visible is determined (meaning that it has a higher intensity). From the start to the end of this range, in steps of 0.5 mm, the intensities of 20 rows above and below the set position are summed. To account for a possible background offset, the mean intensity of the wavelength range $492.9 - 494.3$ nm is subtracted from these spectral intensities, since the intensity should be zero there. Then, the spectrum is normalized on its highest value. Example spectra are shown by the markers in figure 2.9.

Fitting

For the fitting of the peaks in the spectra, a pseudo-Voigt profile is used as approximation for a Voigt profile. A Voigt profile is a combination of Gaussian profile and a Lorentz profile. It was analyzed in [42] that in this case, the contribution of natural broadening ($\propto 10^{-6}$ nm) to the Gaussian profile and the contributions of Doppler ($\propto 10^{-5}$ nm), pressure ($\propto 10^{-4}$ nm), Stark ($\propto 10^{-7}$ nm) and Van der Waals ($\propto 10^{-4}$ nm) broadening to the Lorentz profile are negligible compared to the instrumental broadening in the system ($\propto 10^{-2}$ nm, Gaussian profile) and the resonance broadening ($\propto 10^{-2}$ nm, Lorentz profile).

The pseudo-Voigt profile is a linear combination of a Lorentzian profile with

$$L(x, A, x_0, \Gamma_L) = A \left[1 + 4 \left(\frac{x_0 - x}{\Gamma_L} \right)^2 \right]^{-1} \tag{2.4}$$

and a Gaussian profile with

$$G(x, A, x_0, \Gamma_G) = A \exp \left[-4 \ln(2) \frac{(x - x_0)^2}{\Gamma_G{}^2} \right] \tag{2.5}$$

to yield

$$P_{\text{Voigt}}(x, A, x_0, \Gamma_{\text{L}}, \Gamma_{\text{G}}) = \eta \; L(x, A, x_0, \Gamma_{\text{L}}) + (1 - \eta) \; G(x, A, x_0, \Gamma_{\text{G}}) \, . \tag{2.6}$$

Here, x is the wavelength axis, A the amplitude of the Lorentzian and Gaussian profiles, x_0 is the center position of the profile, Γ_{L} the FWHM of the Lorentz profile, Γ_{G} the FWHM of the Gauss
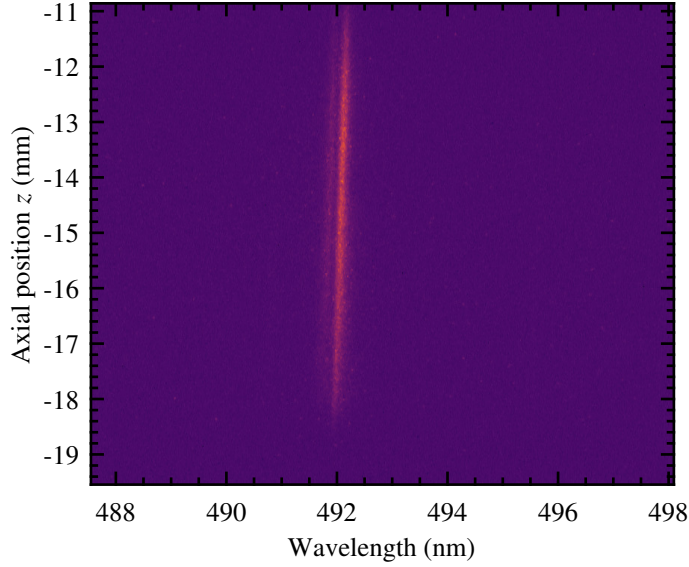
(a)
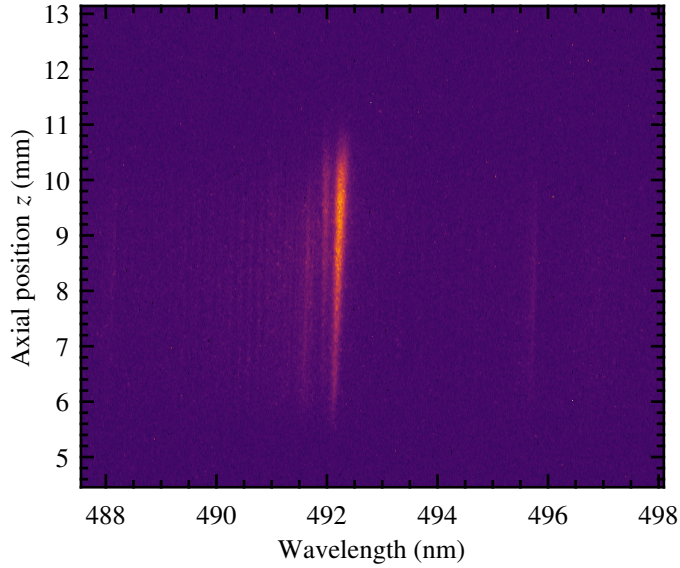
(b)

Figure 2.8: Example spectral image for jet in upwards configuration, with $V_{\text{P}} = 6$ kV, $f = 5$ kHz, $t_{\text{f}} = 1$ us and 1.5 slm He, a) around $z = -14$ mm (i.e. inside the capillary), b) around $z = 9$ mm (i.e. outside the capillary).

profile and η a linear coefficient that is a function of Γ_L, Γ_G and the total FWHM Γ which is given by

$$\Gamma = \left(\Gamma_G{}^5 + 2.69 \, \Gamma_G{}^4 \, \Gamma_L{}^2 + 2.43 \, \Gamma_G{}^3 \, \Gamma_L{}^2 + 4.47 \, \Gamma_G{}^2 \, \Gamma_L{}^3 + 0.078 \, \Gamma_G \, \Gamma_L{}^4 + \Gamma_L{}^5 \right)^{1/5} . \quad (2.7)$$

To an accuracy of 1%, η is then given by

$$\eta = 1.366 \left(\frac{\Gamma_L}{\Gamma} \right) - 0.477 \left(\frac{\Gamma_L}{\Gamma} \right)^2 + 0.111 \left(\frac{\Gamma_L}{\Gamma} \right)^3 . \quad (2.8)$$

Γ_G is determined from the line width of the 435.83 nm emission line from a calibration lamp (AvaLight CAL: HgAr) that was placed inside the setup. For the used slit width of 0.1 µm, Γ_G is equal to 0.082 nm. The total profile that is fitted to the data, as shown in figure 2.9, consists of the sum of two pseudo-Voigt profiles: one for the forbidden peak and one for the allowed peak. The fitting profile then contains the following nine variables: A^F, $x_0{}^F$, $\Gamma_G{}^F$ and $\Gamma_L{}^F$ for the forbidden peak, A^A, $x_0{}^A$, $\Gamma_G{}^A$ and $\Gamma_L{}^A$ for the allowed peak and x. $\Gamma_G{}^F$ and $\Gamma_G{}^A$ are fixed to the instrumental broadening value of 0.082 nm, and x is the wavelength range over which the fitting is performed. This reduces the amount of variables that is fitted to six. The total profile is fitted to the spectral data in figure 2.9 using the non-linear least squares method. Figure 2.9 shows the allowed and forbidden contributions (in blue and red, respectively), as well as the total fit of the spectrum (in black).

Electric field

The most important parameters that result from the fitting procedure are the wavelength position $x_0{}^A$ of the allowed and $x_0{}^F$ of the forbidden component. The electric field is then calculated from the wavelength difference between $x_0{}^A$ and $x_0{}^F$ using equation (3.43) for spectra at the He I 492.2 nm line and equation (3.44) for spectra at the He I 447.1 nm line, which are derived in chapter 3.

The 95% confidence intervals that result from the fitting procedure are used for the error in the results. Following the rules of error propagation and the relations $\Delta\lambda_{AF}(E)$ from equations (3.43) and (3.44), the error in $\Delta\lambda_{AF} = x_0{}^A - x_0{}^F$ is given by

$$S_{\Delta\lambda_{AF}} = \frac{\partial \Delta\lambda_{AF}}{\partial E} S_E , \quad (2.9)$$

thus

$$S_E = \frac{\partial \Delta\lambda_{AF}}{\partial E}^{-1} S_{\Delta\lambda_{AF}} \quad (2.10)$$

is the error in the resulting electric field values, where $\frac{\partial \Delta\lambda_{AF}}{\partial E}$ is the derivative of equation (3.43) or equation (3.44) to E and

$$S_{\Delta\lambda_{AF}} = \sqrt{S_{x_0^A}{}^2 + S_{x_0^F}{}^2} \quad (2.11)$$

with $S_{x_0^A}$ and $S_{x_0^A}$ resulting from the confidence intervals of the fit.
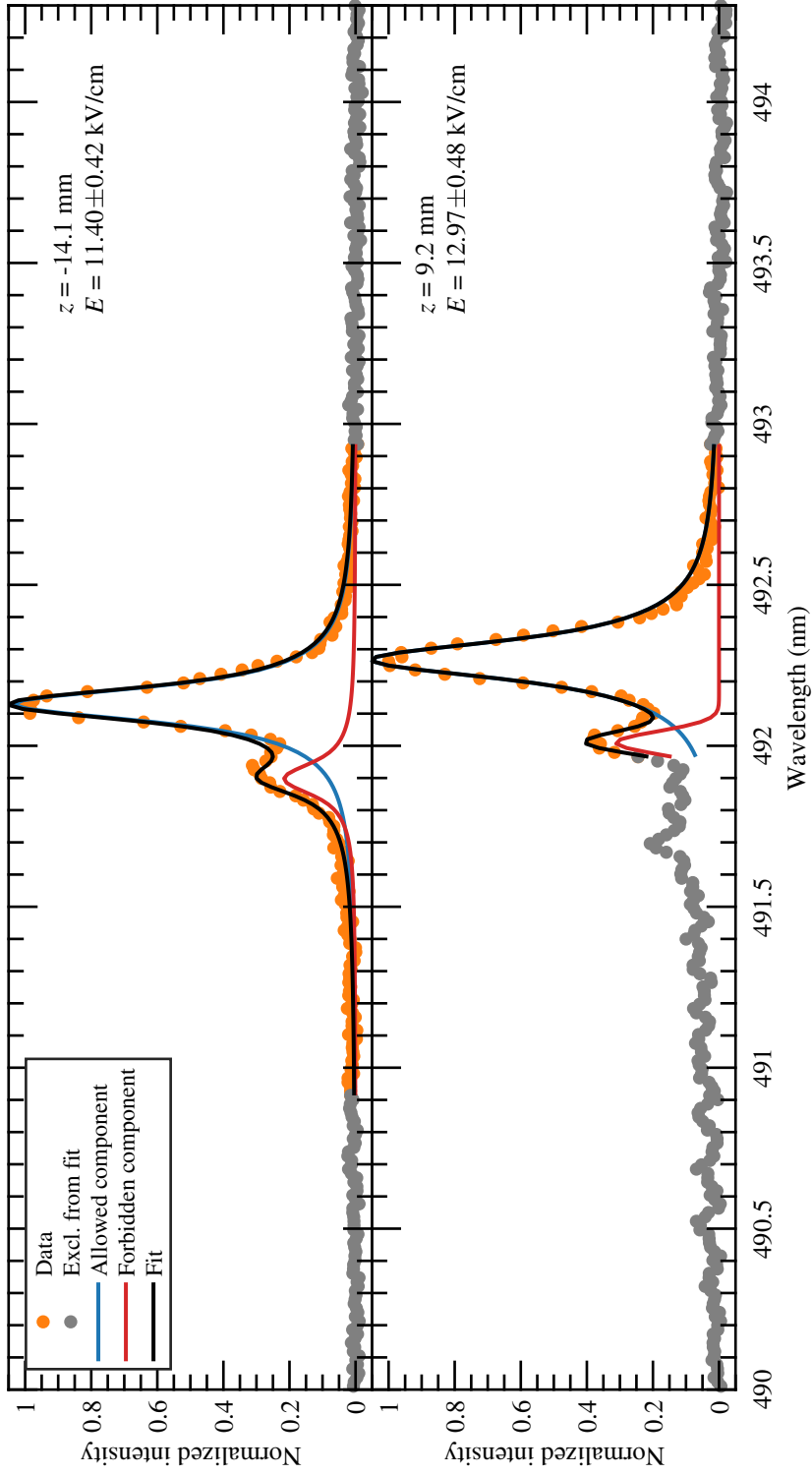
Figure 2.9: Examples of the obtained spectra and their fit for a position inside the capillary (top) and outside (bottom).

2.5 Thomson and rotational Raman scattering setup

2.5.1 Experimental setup

For the measurements on Thomson and rotational Raman scattering, the jet is placed in the laser setup of [30]. The Thomson and rotational Raman scattering setup has been described in detail in [30, 43, 44]. Here, the most important details are summarized.

A schematic overview of the jet in this setup is shown in figure 2.10. A Nd:YAG laser (Spectra Physics, Quanta-Ray, Lab-190-100) is used with a frequency doubled wavelength of 532 nm, operating at 100 Hz with 140 mJ per pulse. Each laser pulse has a width of 100 μm at the focal point and a duration of 10 ns. The laser scattered light is captured at $90°$ to the laser path and the vertical axis of the jet, after which it is focused into a glass fiber. The Rayleigh stray light is removed by a volume Bragg grating (OptiGrate, BragGrate, BNF-532-OD4-12.5M) with a FWHM of 7 cm^{-1} [43] as Notch filter. The remaining Thomson and Raman scattered light is focused onto the 100 μm wide slit of the spectrometer (Jobin-Yvon, HR 640) that has a 1200 l/mm grating (Horiba, 530 24 Holographic Grating, blazed at 500 nm). Then, the spectrum is captured by a self-assembled ICCD camera (Allied vision BigEye G-132B Cool, with KATOD, EPM102G-04-22 F intensifier; ICCD 1 in figure 2.10) integrating every exposure of 70 ns over 2.5 to 50 minutes, depending on the intensity of the signal. This spectrum has a wavenumber range of 510 cm^{-1} and a resolution of 0.398 cm^{-1} [30].

The jet is placed on a mount with translation stages in the x-, y- and z-direction so that it can move precisely in all directions. To align the center of the jet with the focus of the laser beam, an ICCD camera (Andor iStar DH734_18mm; ICCD 2 in figure 2.10) is used from the side of the jet as well as a CCD camera (Hama Webcam HD 00053950; not shown in figure 2.10) next to the top of the jet.

The laser clock is used as trigger signal for the other equipment in the setup: the pulse generator of the jet, ICCD camera 1 and ICCD camera 2.

2.5.2 Data analysis

The obtained spectrum consists of the combination spectrum of the Thomson and Raman signals. Both signals are Gaussian and are convolved with the Voigt instrumental broadening profile [30]. The total scattering power of the Thomson signal is proportional to the electron density n_e and the width is proportional to the square root of the electron temperature T_e [30, 45]. The Raman signal is an addition of the individual rotational transitions of the molecules, in this case O_2 and N_2, from which the total scattering power is proportional to the density of O_2 and N_2, respectively [30, 44, 45]. More information about the calculations and algorithm to determine n_e, T_e, n_{O_2} and n_{N_2} can be found in [30, 44].

An example of a measured spectrum of the free plasma jet is shown in figure 2.11, where the markers show the measured data and the solid curves the fit. Grey markers indicate the data points that are not taken into account for the fit. Two peaks (Rayleigh satellites) are visible ± 0.2 nm around the center wavelength of the laser at 532 nm, which are largely attenuated by the notch filter [30]. These are unwanted and therefore this part of the spectral data is always excluded from the fit. Other parts of the data that are excluded from the fit are emission lines that might arise when the plasma jet interacts with a metallic target. The total fit is shown in black, while the individual components of the fit for the Thomson signal are shown in green and the Raman signals from N_2 and O_2 in blue and red, respectively. The values for the plasma parameters that result from the fit are indicated at the right side of the figure.
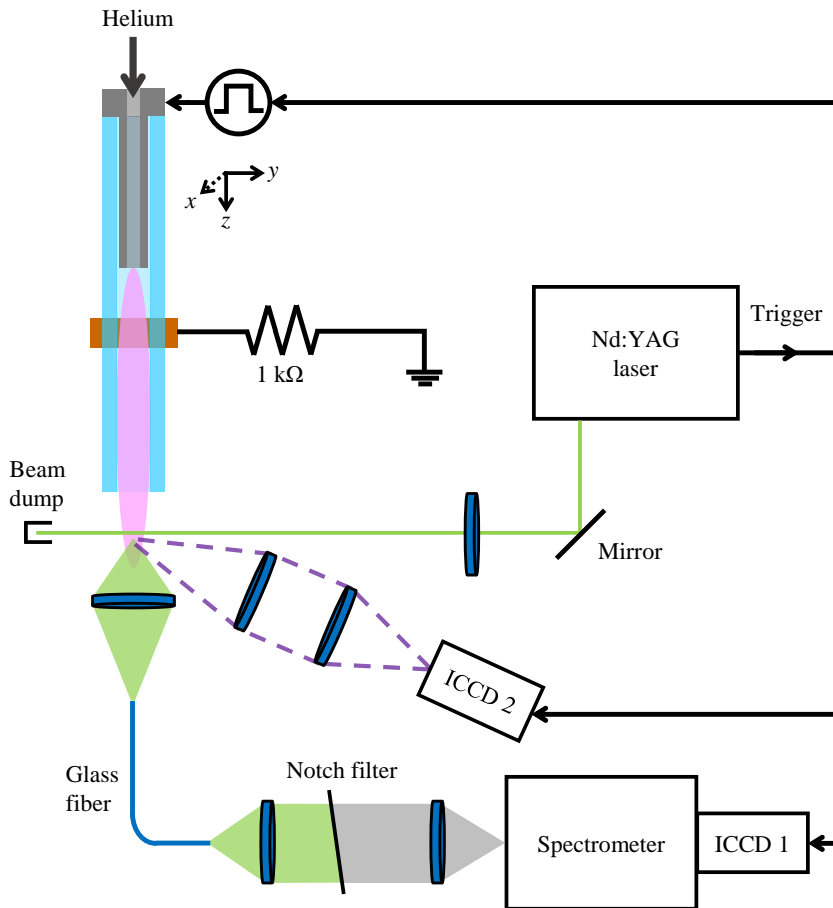
Figure 2.10: Schematic overview of the Thomson and rotational Raman scattering setup.
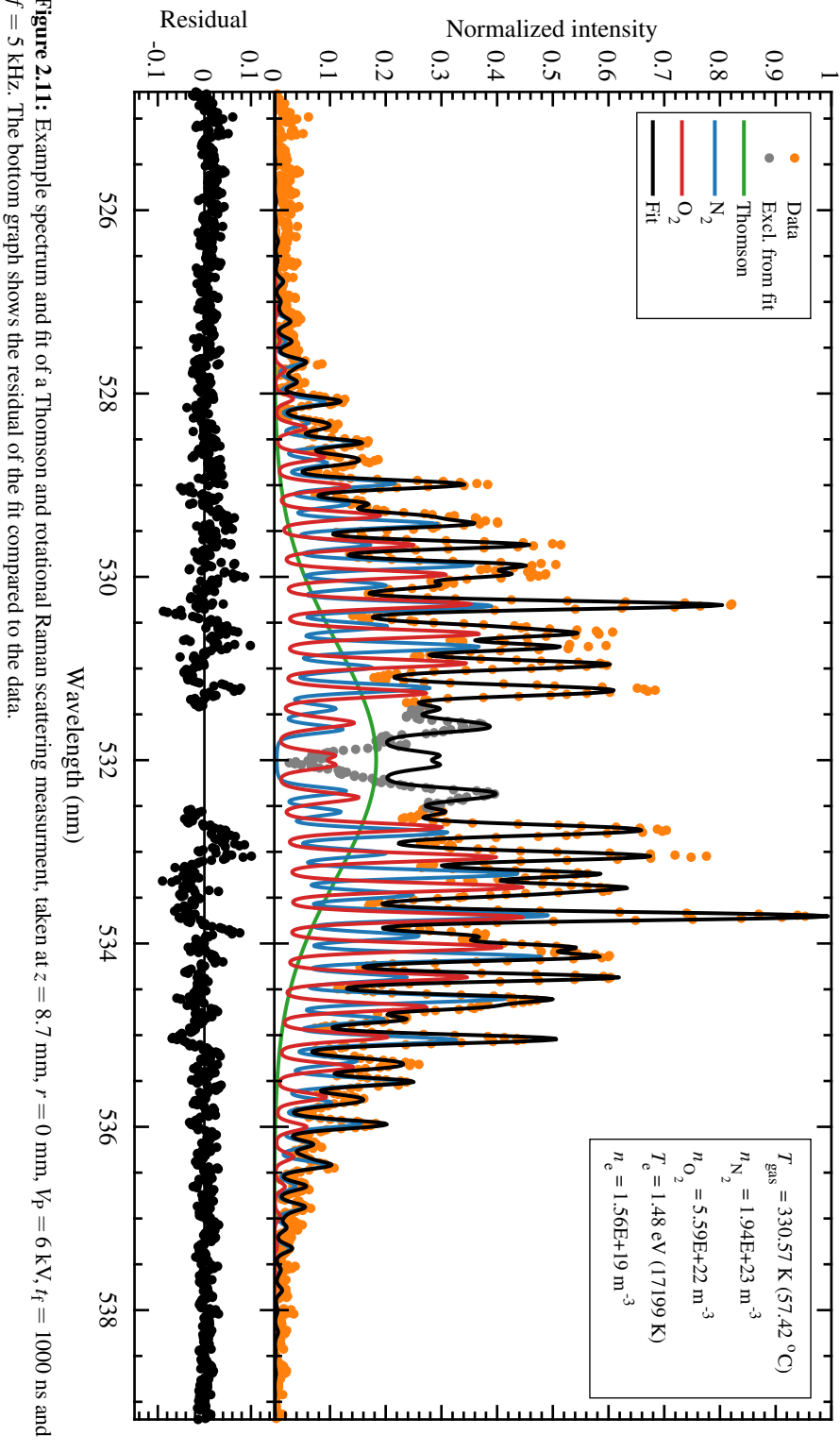
Figure 2.11: Example spectrum and fit of a Thomson and rotational Raman scattering measurment, taken at $z = 8.7$ mm, $r = 0$ mm, $V_P = 6$ kV, $t_f = 1000$ ns and $f = 5$ kHz. The bottom graph shows the residual of the fit compared to the data.

2.6 Temperature probe

2.6.1 Experimental setup

To compare with the gas temperature that is measured by rotational Raman scattering (section 2.5), the gas temperature is also measured independently with a temperature probe (ProSens OTG Fiber Optic Temperature Sensor). Therefore, the jet is placed in the setup as shown in figure 2.12. The temperature probe consists of a small GaAs crystal (diameter 100µm) attached to the controller with an optical fiber. Since the probe is more than 10 times smaller than the plasma jet and made of dielectric material, it is considered to have a negligible influence on the plasma.

The probe is mounted on a motorized x, y, z-stage (Zaber X-XYZ-LSM050A) in order to make a temperature map of the jet. The motorized stage and the oscilloscope are controlled on the computer by a MATLAB script. In this script, the ranges in x-, y- and z-direction are set over which the motion controller loops in steps of the set step size. At every position, the motion controller halts for 1 s, after which the voltage signal of the oscilloscope (LeCroy waveAce 230) is read out that corresponds to the temperature at that position.
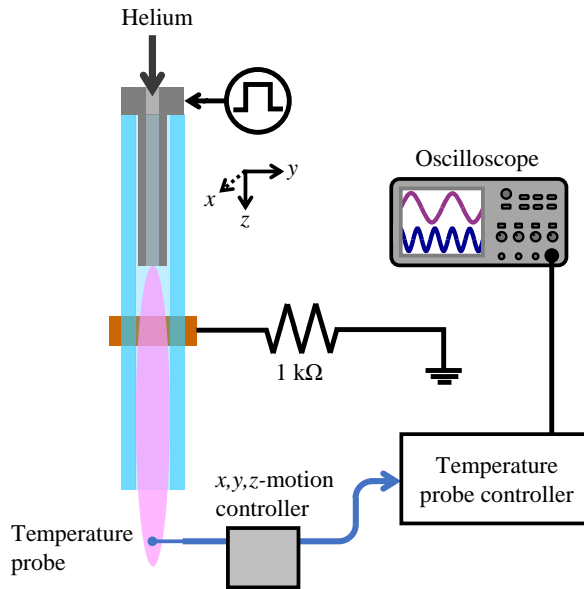
Figure 2.12: Schematic overview of the setup to measure gas temperature in the plasma jet with a temperature probe.

2.6.2 Center of jet determination

To perform temperature measurements along the center of the jet, equally to the rotational Raman measurements, the temperature probe needs to be positioned precisely in the center of the jet. The center of the jet is determined by taking a cross section along the xy-plane of the jet when the plasma is on at $z = 0.9$ mm, which is close to the nozzle, with a range of 8 mm in the x-direction and 6 mm in the y-direction at a step size of 0.2 mm. The result of this measurement

is shown in figure 2.13, where the colors represent the temperature. When the plasma is on, it will heat the gas, which is visible in figure 2.13 as the circle-like shape of higher temperature. Finding the center of this shape then corresponds to finding the center of the jet. In order to do so, cross sections in figure 2.13 are taken around the expected position of the center, thus at y-positions 1.4, 1.6 and 1.8 mm and at x-positions 4.6, 4.8 and 5.0 mm. Then, the mean of the temperature in both the x- and the y-positions is taken and the results are shown as the two curves in figure 2.14. Taking the middle positions of the plateau of both curves then yields the position of the center of the jet at $x = 4.6$ mm and $y = 1.55$ mm.
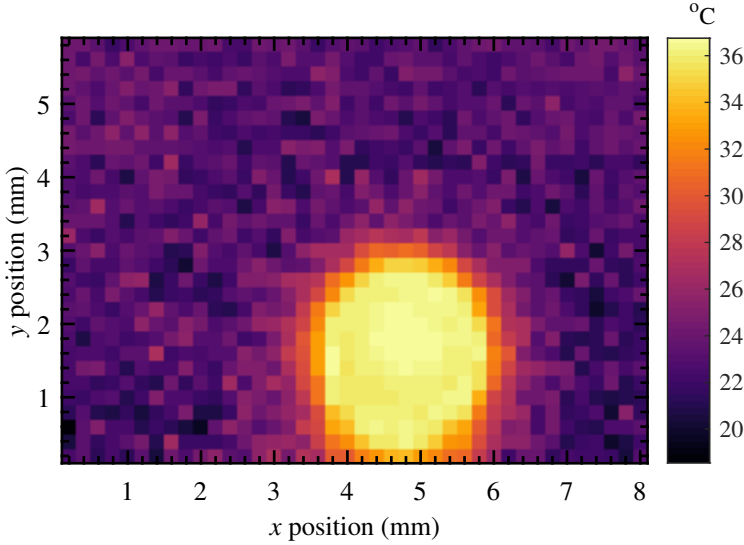
Figure 2.13: Temperature map at $z = 0.9$ mm with the plasma on, to determine the center of the jet.

2.6.3 Measurements

For the regular temperature measurements, the probe is positioned in the center of the jet that is now considered to be at $(x, y, z) = (0, 0, 0)$ mm. A cross section is taken along the xz-plane with x ranging from -8 mm to 8 mm and z from 0 to 45 mm, at a step size of 0.5 mm.

This measurement is performed with the plasma on and with the plasma off, meaning that the voltage is off but the flow still on. Measurements are also performed at different settings for the amplitude, length and frequency of the applied voltage pulse and at different helium flow speeds.

2.6.4 Data analysis

An example temperature map of a measurement with the temperature probe is shown in figure 2.15 at default plasma conditions, for when the plasma is on and when the plasma is off.

To obtain radial profiles from the temperature map, cross sections are taken at $z = 3$ mm and $z = 8.7$ mm. Similarly, the axial profile is obtained by taking a cross section at $x = 0$ mm.
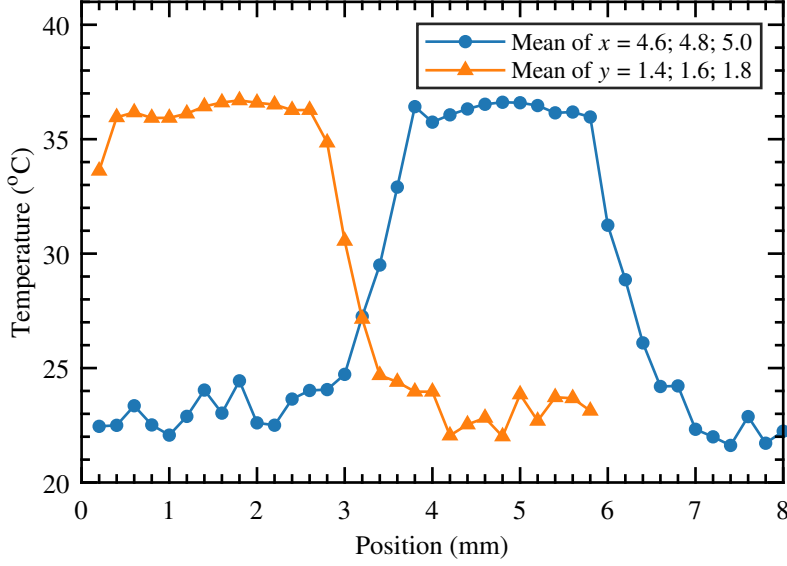
Figure 2.14: Temperature as function of position for the mean of the cross sections at three x-positions and three y-positions. The center of the jet is determined to be at $x = 4.6$ mm and $y = 1.55$ mm.
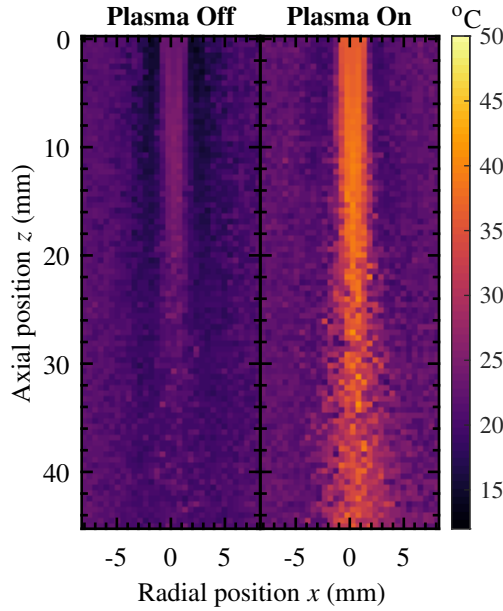
Figure 2.15: Example temperature map of the jet at $V_P = 6$ kV, $t_f = 1000$ ns and $f = 5$ kHz and 1.5 slm He for plasma On and plasma Off.

27

2.7 Schlieren imaging

2.7.1 Experimental setup

For measurements on the visualization of the flow in the plasma jet, a schlieren setup was built of which a schematic overview is shown in figure 2.16. Using a schlieren setup, gradients of the local refractive index of the gas can be made visible [46]. These gradients in the refractive index can be caused by gradients of gas density or temperature. Details of the theory regarding this setup as well as the procedure to make a quantitative analysis of the results will be explained in chapter 5. Here, an overview of the used setup is given.

The setup in figure 2.16 has the arrangement of Toepler's dual-field-lens system [46, 47]. An LED (Thorlabs M625L4-C1, 630 mW, 1000 mA) that emits diffuse light at a wavelength of 625 nm is used as light source. The light is focused by lens L_1 (5 cm diameter, 5 cm focal length) on a pinhole P to make a diverging beam. The pinhole (2 mm opening) is placed in the focal point of lens L_2 (9 cm diameter, 45 cm focal length) and aperture A_1 (8 mm opening) is used to decrease the beam width to a size that is smaller than the size of L_2, to decrease aberrations. The schlieren object, which is the plasma jet, is placed in the parallel beam region that is formed between lenses L_2 and L_3 (9 cm diameter, 45 cm focal length). A knife edge K is placed in the focal point of L_3, after which the light beam is focused on the chip of the CCD camera (Kron Technologies Inc. Chronos 1.4) by lens L_4 (5 cm diameter, 5 cm focal length). Aperture A_2 (2.8 cm opening) is placed in between L_3 and the knife edge with an aperture size equal to the beam diameter to prevent stray light from passing onto the knife edge. A neutral density filter ND (Thorlabs NE05B-A, OD 0.5) is placed in between A_2 and the knife edge to decrease the overall intensity of the beam by 68%, to be able to take images with the CCD camera at longer exposure times without overexposing. The knife edge is a utility blade and it is positioned vertically, with the flat side of the blade along the *xz*-plane and the knife edge side in or next to the beam. It is placed on translation stages to be able to move precisely in the *x*- and *y*-direction.

2.7.2 Measurements

For the measurements, the input current of the LED is set to the maximum value of 1000 mA to have the maximum light intensity. The jet is positioned with the nozzle pointing upwards, such that the plume is visible on the camera. On the camera, the resolution is set to 1280×1024 pixels, the exposure time to 10.42 µs, which corresponds to a frame rate of 1057.36 fps, the gain to zero and the number of frames to 1000.

Measurements to image the flow of the jet (with and without plasma) are performed with the knife edge at the position where it blocks half of the light beam. Therefore, also measurements without flow are performed with changing knife edge position to determine the relation between the knife edge position and the area of the beam that is blocked by the knife edge. Furthermore, a measurement with neither plasma nor knife edge present is performed as well as a measurement with knife edge present and flow absent. These measurements are necessary to calibrate the schlieren setup and to perform quantitative analysis, as will be explained in chapter 5.
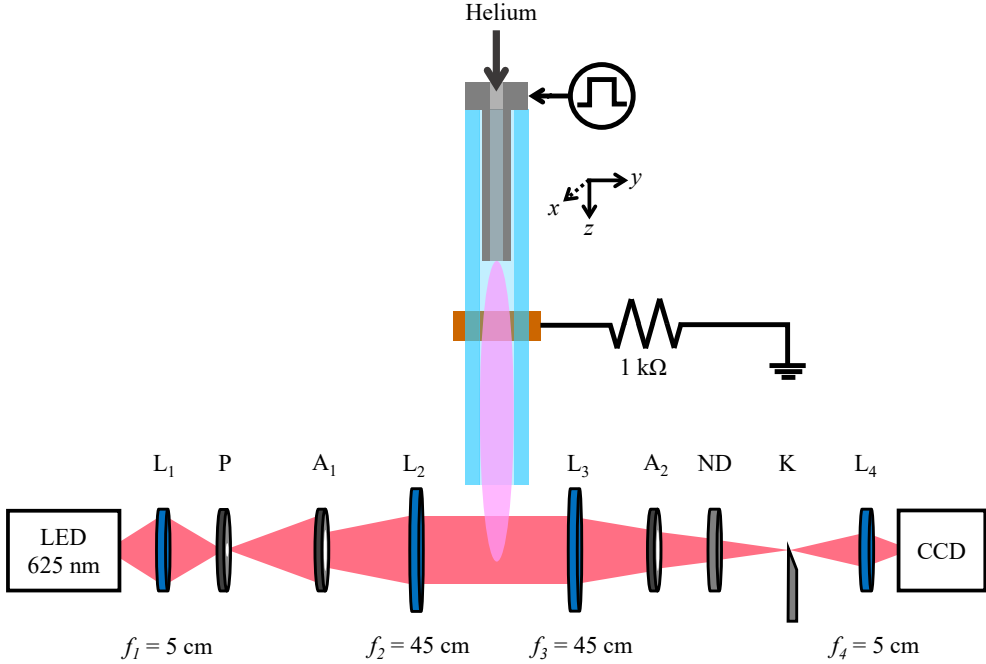
Figure 2.16: Schematic overview of the Schlieren setup, where L = lens, P = pinhole, A = aperture, ND = neutral density filter, K = knife edge.

2.8 Potential of a conductive target

2.8.1 Experimental setup

To get a better understanding of the interaction of the plasma jet with a target, the potential of a floating metallic target is measured when interacting with the plasma jet. A schematic overview of the setup that is used for this, is shown in figure 2.17. As target, a copper plate of $8 \text{ mm} \times 8 \text{ mm}$ with a thickness of 1 mm is used. It is placed on an insulating (plastic) plate that is attached to the holder of the jet itself and the distance d between the target and the nozzle of the jet can be varied. A high voltage probe (Tektronix P6015A 100 MΩ 3.0 pF) is connected to the target and the output is connected to the same oscilloscope (LeCroy waveRunner 6100A 1 GHz [dual 10 GS/s, quad 5 GS/s]) that monitors the applied voltage and the current at the ground of the jet (as seen in figure 2.1). Since the oscilloscope is triggered on the applied voltage signal, this measurement then yields the potential that is induced in the target, as a function of time and with respect to the applied voltage.

2.8.2 Data analysis

Similar to taking a background image in other diagnostics, for every setting of the plasma that a measurement of the potential is taken, there is also a measurement taken with the plasma off, meaning that everything is kept the same, but the flow is turned off. This plasma-off measurement is then subtracted from the normal measurement to yield the potential that is induced in the target by the plasma. An example of these measurements and the resulting potential is shown

in figure 2.18 with respect to the applied voltage V_{applied}, where V_{tot} is the total measured potential on the target, V_{off} the potential when the plasma is off and $V_{\text{target}} = V_{\text{tot}} - V_{\text{off}}$ the resulting potential on the target that will be shown in the results (section 7.3.2).
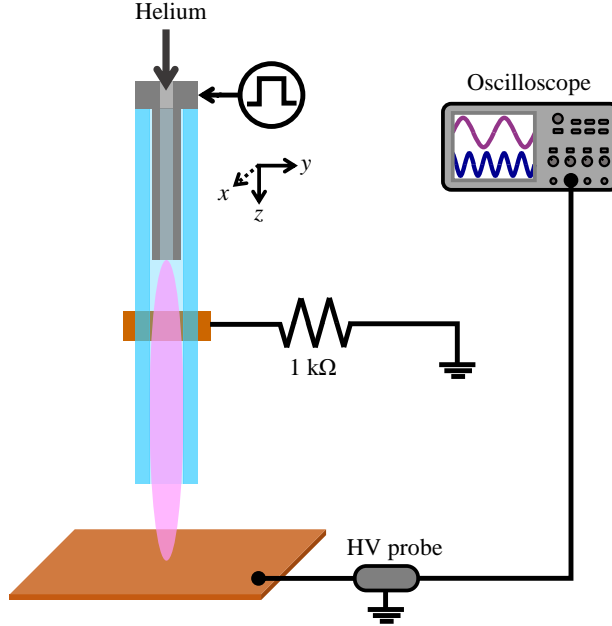
Figure 2.17: Schematic overview of the setup to measure the potential on a floating metallic target while interacting with the plasma jet.
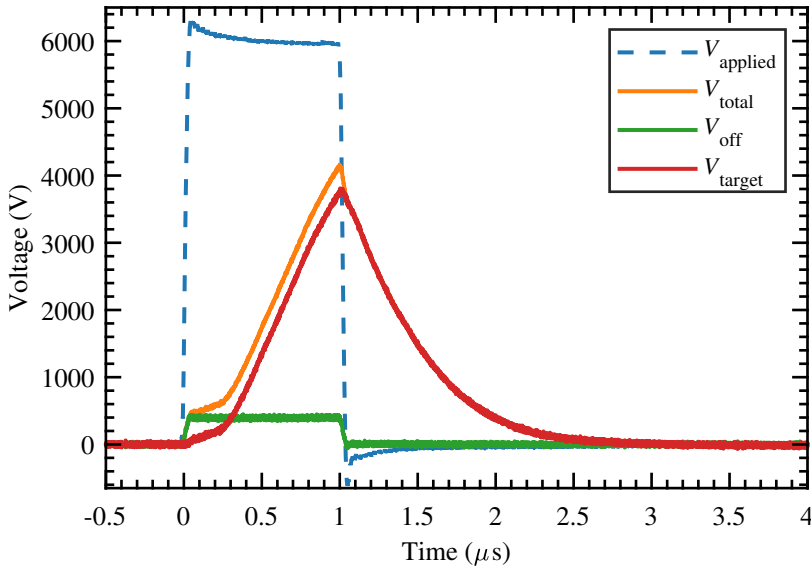
Figure 2.18: An example measurement result of the potential on a floating metallic target when interacting with the plasma jet, at $d = 1$ cm, $V_{\text{P}} = 6$ kV, $t_{\text{f}} = 1000$ ns and $f = 5$ kHz.

2.9 Summary

Since many different diagnostics to characterize the helium plasma jet are used and explained in this chapter, table 7.1 gives an overview of all these diagnostics and the parameters that they yield.

Table 2.2: Overview of the used diagnostics and their resulting parameters.

Diagnostic	Resulting parameter(s)
Electrical measurements	Voltage, current, power and energy applied to the plasma
ICCD imaging	Position and velocity of ionization front
Stark polarization spectroscopy	Axial electric field
Thomson scattering	Electron density and temperature
Rotational Raman scattering	Gas temperature and number density of oxygen and nitrogen
Temperature probe	Gas temperature
Schlieren imaging	Visualization of flow and helium/air fraction
Target potential	Potential in a floating metal target

3

Theoretical calculation of the Stark shifts of the spectral lines of atomic helium

Abstract: The Stark shifts of the energy levels of atomic helium are calculated for an applied electric field in the range of $0 - 40$ kV/cm. Two calculation methods from literature are combined and some assumptions are explained in more detail. For the atomic helium line bands at 447.1 nm and at 492.2 nm, a relation is obtained between the peak-to-peak wavelength difference between the allowed and forbidden transition at each line and the applied electric field. By comparing these relations to different results in literature, a good agreement (i.e. a deviation of about 5%) is obtained in the electric field range where all results are valid.

3.1 Introduction

The Stark effect is named after Johannes Stark who discovered it in 1913 [48], although it was discovered independently by Antonino Lo Surdo [49] around the same time.

The application of the Stark effect on hydrogen [50–54] and hydrogen-like atoms such as helium [54] can be found in literature. In 1996, Milorad Kuraica designed a diagnostic based on the Stark effect and the polarization of states to measure the electric field in the cathode fall of a glow discharge, first in a hydrogen plasma [55] and then in a helium plasma [56]. This diagnostic is called Stark polarization spectroscopy. To obtain the electric field from measurements on the wavelength position of spectral lines, Kuraica performed a theoretical calculation that was based on calculations of the Stark effect in helium by Foster in 1927 [57]. Since then, this diagnostic has been used often by himself and his research group to measure the electric field in a helium plasma, first again in a glow discharge [58, 59], but then also in a DBD [60–62] and a plasma jet [28, 31, 32, 63, 64]. Researchers from other groups have used the diagnostic as well on a plasma jet [65, 66], but for the calibration they all depend on the resulting equations from Kuraica's calculations. The theory behind these calculations is explained in short in the papers published by Kuraica and his research group [56, 59], but neither the full calculations nor an explanation about the made approximations have been published. The calculations and some of the approximations have been elaborated in the PhD thesis from Kuraica [67].

The purpose of this chapter is to fill the gap between the understanding of the Stark effect and the resulting equation as calculated by Kuraica and to better explain the approximations that are made. In this way, the end result and the theory behind the calculations are better understandable, but even more importantly, it allows others to apply the theory to different helium lines or to different atoms, which makes the diagnostic suitable for a larger range of experiments.

First, an introduction to the Stark effect is given (section 3.2). Then, the line shifts of atomic helium are derived as function of the applied electric field and applied to two specific helium lines (section 3.3). The results are compared with existing results in literature (section 3.4). In the end, it is shown that the axial component of the electric field is measured when the line shifts are measured from linearly polarized light (section 3.5).

3.2 Stark effect

In general, the Stark effect is the splitting and shifting of spectral lines under the influence of an externally applied electric field [48, 68, 69]. It is therefore considered [48, 49, 69] as the electric field analogue of the Zeeman effect [70], although the specific influences are different.

The Stark effect is important because the electric field affects the electron charge distribution directly [53]. Because of this perturbation, spectral lines appear that are forbidden in the unperturbed system. These forbidden lines exist because the electric field causes excited states with different orbital quantum numbers l to mix[53]. The dependence of the shifting and splitting on the electric field can be linear (first order contribution to the perturbation) or quadratic (second order contribution) [50, 52, 53, 69, 71].

When placed in an external electric field $\vec{F}$, an atom that does not have a permanent electric dipole moment can be polarized according to [50, 51, 69, 72]

$$\vec{d} = \alpha \vec{F} \tag{3.1}$$

where $\vec{d}$ is the induced dipole moment and α the polarizability. The electric field acts on this induced dipole moment, with interaction energy [50, 51]

$$\Delta E = \int \vec{F} \cdot d\vec{p} = \alpha \int \vec{F} \cdot d\vec{F} = \frac{1}{2}\alpha\vec{F}^2 \tag{3.2}$$

which can be interpreted as a level shift. Since this energy shift depends quadratically on the electric field strength, this effect is called the quadratic Stark effect. It is seen in most atoms [51, 71].

For the hydrogen atom and other hydrogenic atoms, however, the splitting and shifting of levels depends linearly on the electric field strength. This effect is therefore called the linear Stark effect. It can also occur in non-hydrogenic atoms, if the electric field is sufficiently strong that the energy shift is comparable to the splitting of the energy levels in the unperturbed atom (i.e. without electric field), since then saturation of the magnitude of $\vec{p}$ occurs [71]. The linear Stark effect can only be explained in terms of quantum mechanics, in a less intuitive way than the quadratic Stark effect. The degeneracy in l, that is already present in the absence of an electric field, is not present in the presence of the electric field $\vec{F}$, because the Coulomb potential of the nucleus of the atom is perturbed by the electric field $\vec{F}$ [50]. Then, a splitting of the levels occurs that is proportional to the electric field strength [50].

In this thesis helium is used and since helium is hydrogenic (hydrogen-like), the linear Stark effect will be applied. The shifts of the spectral lines of atomic helium as function of the electric field strength are derived in the next section.

3.3 Derivation of the Stark shifts

3.3.1 Solving the Schrödinger equation for hydrogen

To be able to calculate the electric field from the spectra that are measured (with the setup in section 2.4), it is necessary to know the energy levels of helium in an external electric field. Therefore, the time-independent Schrödinger equation needs to be solved:

$$H\psi = E\psi . \tag{3.3}$$

For the hydrogen atom, with Hamiltonian

$$H_{\mathrm{H}} = -\frac{\hbar^2}{2m}\nabla^2 - \frac{e^2}{4\pi\varepsilon_0}\frac{1}{r}, \tag{3.4}$$

exact solutions to the Schrödinger equation can be found by using spherical coordinates and separation of variables:

$$\psi(r,\theta,\phi) = R(r)Y(\theta,\phi) . \tag{3.5}$$

Elaborated calculations can be found in literature [54, 67, 73, 74], here only the results will be given. The radial wave function is given by

$$R_{nl}(r) = \sqrt{\left(\frac{2}{na_0}\right)^3 \frac{(n-l-1)!}{2n[(n+l)!]^3}}\; \mathrm{e}^{-r/na_0}\left(\frac{2r}{na_0}\right)^l \left[L_{n-l-1}^{2l+1}(2r/na_0)\right]$$

where a_0 is the Bohr radius and $L_{q-p}^p(x)$ is an associated Laguerre polynomial, given by

$$L_{q-p}^p(x) = (-1)^p \left(\frac{\mathrm{d}}{\mathrm{d}x}\right)^p L_q(x) \tag{3.6}$$

and L_q is the qth Laguerre polynomial:

$$L_q(x) = e^x \left(\frac{d}{dx} \right)^q (e^{-x} x^q) . \tag{3.7}$$

The angular wave function is given by

$$Y_l^m(\theta, \phi) = \varepsilon \sqrt{\frac{2l+1}{4\pi} \frac{(l-|m|)!}{(l+|m|)!}} P_l^m(\cos\theta) e^{im\phi} \tag{3.8}$$

in which $\varepsilon = (-1)^m$ for $m \geq 0$ and $\varepsilon = 1$ for $m \leq 0$. P_l^m is the associated Legendre function, defined by

$$P_l^m(x) = (1-x^2)^{|m|/2} \left(\frac{d}{dx} \right)^{|m|} P_l(x) \tag{3.9}$$

and $P_l(x)$ is the lth Legendre polynomial, defined by the Rodrigues formula:

$$P_l(x) = \frac{1}{2^l l!} \left(\frac{d}{dx} \right)^l (x^2 - 1)^l . \tag{3.10}$$

The total wave function is then found by substituting equations (3.6) and (3.8) back into equation (3.5).

3.3.2 Approximations for the helium atom

For the helium atom, however, these exact solutions do not exist, but it will be shown that the solutions for the hydrogen atom can also be used for the helium atom. The Hamiltonian of the helium atom is given by

$$H_{He} = -\frac{\hbar^2}{2m} \nabla_1^2 - \frac{e^2}{2\pi\varepsilon_0} \frac{1}{r_1} - \frac{\hbar^2}{2m} \nabla_2^2 - \frac{e^2}{2\pi\varepsilon_0} \frac{1}{r_2} + \frac{e^2}{2\pi\varepsilon_0} \frac{1}{r_{12}} \tag{3.11}$$

where r_1 and r_2 give the distance from the nucleus to electron 1 and 2, and r_{12} gives the mutual distance between the two electrons. The first two terms correspond to one electron of the atom, the second two terms to the other electron and the last term to the interaction between the two electrons. One electron occupies the ground state and the other electron occupies an excited state. When the excited level is a low-lying level, the wave functions of the two electrons overlap and thus they can influence one another. Here, the two electrons are considered to be far enough apart to not influence one another. The validation of this approximation is found by looking at the Coulomb force [72]

$$F_e = \frac{e^2}{4\pi\varepsilon_0} \frac{1}{r_{12}^2} \tag{3.12}$$

where the distance between the two electrons, r_{12}, will be linked to the radius of the electron orbital, given by [69]

$$a_n = \frac{a_0 n^2}{Z} \tag{3.13}$$

in which a_0 is the Bohr radius. For the case when both electrons are in the ground state ($n = 1$), the maximum distance between the two electrons is twice the radius of the first electron orbital:

$$r_{12} = 2a_1 = a_0 .$$

In the case considered here, one electron is in the first electron orbital and one electron in the fourth electron orbital ($n = 4$). The minimum distance between these two electrons is

$$r_{12} = a_4 - a_1 = \frac{15a_0}{2} \ .$$

Thus, the distance between the electrons in this case is at least a factor $15/2$ larger than the distance between two electrons in the ground state. Regarding equation (3.12), this yields a Coulomb force of at least $(15/2)^2$ times smaller, validating the approximation that wave functions of the two electrons in our case are not overlapping.

Therefore, the interaction term in the Hamiltonian (equation (3.11)) can be neglected and what is left is the Hamiltonian of the hydrogen atom (equation (3.4)) with an extra charge.

3.3.3 Applying degenerate perturbation theory for the influence of the electric field

Placing the atom in an externally applied electric field leads to a perturbation of the Hamiltonian, because of the interaction between the electron of the atom and the electric field, given by

$$H^{1'} = eFz \tag{3.14}$$

where the applied field $F = |\vec{F}|$ is directed along the positive z-axis. To account for the extra charge in the nucleus of the helium atom, compared to the hydrogen atom, an extra entry is added to the perturbed Hamiltonian, which corresponds to the difference in energy between the hydrogen and helium terms with the same n, as a function of l:

$$H^{1''} = hc\nu_l \tag{3.15}$$

in which ν_l is the difference (in cm^{-1}) between the helium and the corresponding hydrogen terms. The total perturbation to the Hamiltonian (equation (3.4)) is then

$$H^1 = H^{1'} + H^{1''} = eFz + hc\nu_l. \tag{3.16}$$

To solve the Schrödinger equation with this addition, perturbation theory needs to be applied. Since the solution of the unperturbed Schrödinger equation leads to degenerate energy levels, non-degenerate perturbation theory is not valid and thus degenerate perturbation theory has to be applied.

When the energy E_n^0 is g_n-fold degenerate, there are g_n wave functions with the same energy E_n^0. The unperturbed Schrödinger equation

$$H^0 \psi_n^0 = E_n^0 \psi_n^0 \tag{3.17}$$

then changes into

$$H^0 \psi_{ni}^0 = E_n^0 \psi_{ni}^0 \ , \ \ i = 1, 2, \ldots, g_n \tag{3.18}$$

where H^0 is given by equation (3.4). The degenerate wave functions can be written as a linear combination:

$$\psi_n^0 = \sum_{i=1}^{g_n} c_{ni} \psi_{ni}^0 \tag{3.19}$$

which is also an eigenfunction of the unperturbed Hamiltonian, with the same eigenvalue:

$$H^0 \psi_n^0 = \sum_{i=1}^{g_n} c_{ni} H^0 \psi_{ni}^0 = E_n^0 \sum_{i=1}^{g_n} c_{ni} \psi_{ni}^0 = E_n^0 \psi_n^0 \ .$$

Still, the Schrödinger equation (equation (3.3)) needs to be solved, which changes into

$$\left(H^0 + H^1 \right) \psi_{ni} = E_{ni} \psi_{ni} \ , \quad i = 1, 2, \dots, g_n \ . \tag{3.20}$$

Because H^1 is a small perturbation, the eigenvalues and eigenfunctions can be written as expansion series:

$$E_{ni} = E_n^0 + E_{ni}^1 + E_{ni}^2 + \dots \ , \quad i = 1, 2, \dots, g_n \tag{3.21a}$$

$$\psi_{ni} = \psi_{ni}^0 + \psi_{ni}^1 + \psi_{ni}^2 + \dots \ , \quad i = 1, 2, \dots, g_n \tag{3.21b}$$

where E_n^0 is the same for all values of i. Substituting these expressions into equation (3.20) gives, up to first order,

$$H^0 \psi_{ni}^0 = E_n^0 \psi_{ni}^0 \tag{3.22a}$$

$$H^0 \psi_{ni}^1 + H^1 \psi_{ni}^0 = E_n^0 \psi_{ni}^1 + E_{ni}^1 \psi_{ni}^0 \tag{3.22b}$$

where equation (3.22a) is just the unperturbed Schrödinger equation (equation (3.17)). The first order correction will now be calculated, and analogously higher order corrections can be calculated. Taking the inner product of ψ_{ni}^0 with equation (3.22b) gives

$$\langle \psi_{ni}^0 | H^0 \psi_{ni}^1 \rangle + \langle \psi_{ni}^0 | H^1 \psi_{ni}^0 \rangle = E_n^0 \langle \psi_{ni}^0 | \psi_{ni}^1 \rangle + E_{ni}^1 \langle \psi_{ni}^0 | \psi_{ni}^0 \rangle \ . \tag{3.23}$$

The hermitian property of H^0 makes the first term on the left and right hand side cancel against one another, leaving

$$\langle \psi_{ni}^0 | H^1 \psi_{ni}^0 \rangle = E_{ni}^1 \langle \psi_{ni}^0 | \psi_{ni}^0 \rangle \ . \tag{3.24}$$

Substituting equation (3.19) and using the orthonormality $\langle \psi_{ki}^0 | \psi_{ni}^0 \rangle = \delta_{kn}$ yields

$$\sum_{j=1}^{g_n} c_{nj} \langle \psi_{ni}^0 | H^1 | \psi_{nj}^0 \rangle = E_{ni}^1 \sum_{j=1}^{g_n} c_{nj} \langle \psi_{ni}^0 | \psi_{nj}^0 \rangle = E_{ni}^1 c_{ni} \tag{3.25}$$

or

$$\sum_{j=1}^{g_n} c_{nj} \left(H_{ni,nj}^1 - E_{ni}^1 \delta_{ij} \right) = 0 \tag{3.26}$$

where $H_{ni,nj}^1 = \langle \psi_{ni}^0 | H^1 | \psi_{nj}^0 \rangle$. For equation (3.26) a trivial solution is $c_{nj} = 0$ for all j. A nontrivial solution only exists if the determinant with elements $(H_{ni,nj}^1 - E_{ni}^1 \delta_{ij})$ vanishes, which yields the secular equation:

$$|H_{ni,nj}^1 - E_{ni}^1 \delta_{ij}| = 0 \ . \tag{3.27}$$

Satisfied, it will give g_n roots: $E_{n1}^1, E_{n2}^1, \dots, E_{ng_n}^1$, yielding the first-order corrections to the degenerate eigenvalues:

$$E_{ni} = E_n^0 + E_{ni}^1 \ , \quad i = 1, 2, \dots, g_n \ . \tag{3.28}$$

Because of the perturbation, the degeneracy is removed as it vanishes. Instead, the degenerate level E_n is split into sub levels with energies given in equation (3.28) and the appropriate wave functions ψ_{ni}.

Returning to the case of the helium atom in an external electric field, the energy levels E_n (principal quantum number n) split into m (magnetic quantum number) sub levels, in which the individual terms are arranged to index l (angular momentum quantum number). Since only linearly polarized light is taken into account, $\Delta m = 0$ and thus $m = m'$. The secular equation (equation (3.27)), which needs to be solved, becomes then

$$\left| H^1_{nlm,nl'm} - E^1 \delta_{ll'} \right| = 0, \; |m| \leq l \leq (n-1) \tag{3.29}$$

where the matrix elements $H^1_{nlm,nl'm}$ are given by the inner product of equation (3.16) with the unperturbed eigenfunctions $\psi_{nlm}(r, \theta, \phi)$. Equation (3.29) gives then

$$\begin{vmatrix} H_{ll} - E^1 & H_{l,l+1} & \dots & H_{l,n-1} \\ H_{l+1,l} & H_{l+1,l+1} - E^1 & \dots & H_{l+1,n-1} \\ \dots & \dots & \dots & \dots \\ H_{n-1,l} & H_{n-1,l+1} & \dots & H_{n-1,n-1} - E^1 \end{vmatrix} = 0 . \tag{3.30}$$

The quantum numbers n and m are still inside equation (3.30), but since they are constant for every element in the matrix, they are not written for simplicity. The matrix elements $H_{ll'}$ are given by

$$H_{ll'} = eF \int \psi_{nlm}(\vec{r}) z \psi^*_{nl'm}(\vec{r}) \, d\vec{r} + hc v_l \int \psi_{nlm}(\vec{r}) \psi^*_{nl'm}(\vec{r}) \, d\vec{r} . \tag{3.31}$$

The second integral yields $hc v_l \delta_{ll'}$, while using spherical coordinates ($z = r \cos \theta$) and equation (3.5), the first integral becomes

$$eF \int_0^\infty R_{nl} r R_{nl'} r^2 \, dr \int_0^{4\pi} Y_{lm} \cos \theta Y^*_{l'm} \, d\Omega .$$

The radial wave function is given by equation (3.6), yielding [54, 67]

$$\int_0^\infty R_{nl-1} r R_{nl} \, r^2 \, dr = \int_0^\infty R_{nl} r R_{nl-1} r^2 \, dr = \frac{3}{2} a_0 n \sqrt{n^2 - l^2} \tag{3.32}$$

and the angular wave function is given by equation (3.8), yielding [54, 67]

$$\int_0^{4\pi} Y_{l-1m} \cos \theta Y^*_{lm} \, d\Omega = \int_0^{4\pi} Y_{lm} \cos \theta Y^*_{l-1m} \, d\Omega = \sqrt{\frac{l^2 - m^2}{(2l+1)(2l-1)}} . \tag{3.33}$$

Thus, the first term of equation (3.31) is given by

$$H_{l-1,l} = H_{l,l-1} = \frac{3}{2} eF a_0 n \sqrt{n^2 - l^2} \sqrt{\frac{l^2 - m^2}{(4l^2 - 1)}} \tag{3.34}$$

which are off-diagonal elements, while the second term is given by

$$H_{ll'} = hc v_l \delta_{ll'} \tag{3.35}$$

which are diagonal elements. Dividing all elements by -1 and setting

$$f(n, m, l) = \frac{(n^2 - l^2)(l^2 - m^2)}{(4l^2 - 1)} \tag{3.36}$$

and

$$\kappa = \frac{3ea_0}{2hc} \approx 6.40 \cdot 10^{-5} \text{cm}^{-1},\tag{3.37}$$

gives the secular equation for the helium atom:

$$\begin{vmatrix} v_l + E^1 & -n\kappa F\sqrt{f(n,m,l+1)} & 0 & \dots \\ -n\kappa F\sqrt{f(n,m,l+1)} & v_{l+1} + E^1 & -n\kappa F\sqrt{f(n,m,l+2)} & \dots \\ 0 & -n\kappa F\sqrt{f(n,m,l+2)} & v_{l+2} + E^1 & \dots \\ \dots & \dots & \dots & \dots \end{vmatrix} = 0.\tag{3.38}$$

The displacements of the energy levels are measured from the diffuse (D) line, therefore $x = E^1 + v_l$, which is the displacement of the helium line in cm^{-1}, measured from the D-line and $\lambda_l = v_2 - v_l$ are substituted into equation (3.38) to yield the final secular equation:

$$\begin{vmatrix} x + \lambda_l & -n\kappa F\sqrt{f(n,m,l+1)} & 0 & \dots \\ -n\kappa F\sqrt{f(n,m,l+1)} & x + \lambda_{l+1} & -n\kappa F\sqrt{f(n,m,l+2)} & \dots \\ 0 & -n\kappa F\sqrt{f(n,m,l+2)} & x + \lambda_{l+2} & \dots \\ \dots & \dots & \dots & \dots \end{vmatrix} = 0.\tag{3.39}$$

3.3.4 Application to specific helium lines

For this thesis, two helium lines are considered. The secular equation (equation (3.39)) will be solved for both lines, yielding expressions for the wavelength shift as a function of the electric field.

He I 492.2 nm

The allowed transition at the 492.2 nm helium line is $1s4d\ ^1\text{D} \rightarrow 1s2p\ ^1\text{P}^\text{o}$ and the forbidden transition is $1s4f\ ^1\text{F}^\text{o} \rightarrow 1s2p\ ^1\text{P}^\text{o}$. Therefore, we have the line groups $4(S,P,D,F) \rightarrow 2P$, or $n = 4(l = 0,1,2,3) \rightarrow n = 2(l = 1)$, at $S = 0$.

- The level $n = 4$, $S = 0$, $m = 1$:
  For $m = 1$, $|m| \leq l \leq (n-1) \leftrightarrow 1 \leq l \leq 3$ and the matrix in equation (3.39) is a 3×3 matrix, thus the equation we need to solve is

$$\begin{vmatrix} x + \lambda_1 & -4\kappa F\sqrt{f(4,1,2)} & 0 \\ -4\kappa F\sqrt{f(4,1,2)} & x & -4\kappa F\sqrt{f(4,1,3)} \\ 0 & -4\kappa F\sqrt{f(4,1,3)} & x + \lambda_3 \end{vmatrix} = 0.$$

From the data in table 3.1 and table 3.2, λ_1 and λ_3 have been calculated to give $\lambda_1 = 46.3$ cm^{-1} and $\lambda_3 = 5.43$ cm^{-1}. Furthermore, we have

$$f(4,1,2) = \frac{12}{5}, \quad f(4,1,3) = \frac{8}{5}$$

to get

$$\begin{vmatrix} x + \lambda_1 & -4\kappa F\sqrt{\frac{12}{5}} & 0 \\ -4\kappa F\sqrt{\frac{12}{5}} & x & -n\kappa F\sqrt{\frac{8}{5}} \\ 0 & -n\kappa F\sqrt{\frac{8}{5}} & x + \lambda_3 \end{vmatrix} = 0.$$

Expanded, this gives the characteristic polynomial equation

$$x^3 + x^2(\lambda_1 + \lambda_3) + x\left[\lambda_1\lambda_3 - 4(4\kappa F)^2\right] - (4\kappa F)^2\left(\frac{8}{5}\lambda_1 + \frac{12}{5}\lambda_3\right) = 0 \qquad (3.40)$$

which has three solutions, for the energy levels $l = 1,2,3 \leftrightarrow P,D,F$.

- The level $n = 4$, $S = 0$, $m = 0$:
  For $m = 0$, $|m| \leq l \leq (n-1) \leftrightarrow 0 \leq l \leq 3$ and the matrix in equation (3.39) is a 4×4 matrix, thus the secular equation becomes

$$\begin{vmatrix} x + \lambda_0 & -4\kappa F\sqrt{5} & 0 & 0 \\ -4\kappa F\sqrt{5} & x + \lambda_1 & -4\kappa F\sqrt{\frac{16}{5}} & 0 \\ 0 & -4\kappa F\sqrt{\frac{16}{5}} & x & -4\kappa F\sqrt{\frac{9}{5}} \\ 0 & 0 & -4\kappa F\sqrt{\frac{9}{5}} & x + \lambda_3 \end{vmatrix} = 0$$

  where

$$f(4,0,1) = 5 \ , \ f(4,0,2) = \frac{16}{5} \ , \ f(4,0,3) = \frac{9}{5}$$

  have already been substituted and $\lambda_0 = -506.2$ cm^{-1}. The characteristic polynomial equation is

$$\begin{aligned} x^4 &+ x^3\left(\lambda_0 + \lambda_1 + \lambda_3\right) + x^2\left[\lambda_0\lambda_1 + \lambda_1\lambda_3 + \lambda_0\lambda_3 - 10\left(4\kappa F\right)^2\right] \\ &+ x\left[\lambda_0\lambda_1\lambda_3 - (4\kappa F)^2\left(5\lambda_0 + \frac{9}{5}\lambda_1 + \frac{41}{5}\lambda_3\right)\right] - (4\kappa F)^2\lambda_0\left(\frac{9}{5}\lambda_1 + \frac{16}{5}\lambda_3\right) \\ &+ 9\left(4\kappa F\right)^4 = 0 \ . \end{aligned}$$

$$(3.41)$$

- The level $n = 4$, $S = 0$, $m = 2$:
  For the $m = 2$, $|m| \leq l \leq (n-1) \leftrightarrow 2 \leq l \leq 3$ and the matrix in equation (3.39) is a 2×2 matrix, thus the secular equation becomes

$$\begin{vmatrix} x & -4\kappa F \\ -4\kappa F & x + \lambda_3 \end{vmatrix} = 0$$

  where

$$f(4,2,1) = 1$$

  has already been substituted and the characteristic polynomial is

$$x^2 + \lambda_3 x - (4\kappa F)^2 = 0 \ . \qquad (3.42)$$

He I 447.1 nm

The allowed transition at the 447.1 nm helium line is $1s4d$ ^{3}D $\rightarrow 1s2p$ ^{3}P$^{\text{o}}$ and the forbidden transition is $1s4f$ ^{3}F$^{\text{o}} \rightarrow 1s2p$ ^{3}P$^{\text{o}}$. Therefore, we have the line groups $4(S,P,D,F) \rightarrow 2P$, or $n = 4(l = 0,1,2,3) \rightarrow n = 2(l = 1)$, at $S = 1$. Compared to the transitions at the helium 492.2 nm line, the only quantum number that changes is the total spin S. Because this only influences the energy levels and thus the values of the λ_i, the calculation and thus the characteristic polynomial equations are equal for the 447.1 nm line and only the λ_i need to be adapted. λ_0, λ_1 and λ_3 are again calculated from the data in table 3.1 and table 3.2 to give $\lambda_0 = -1146.3$ cm^{-1}, $\lambda_1 = -227.42$ cm^{-1} and $\lambda_3 = 7.39$ cm^{-1}.

Table 3.1: Energy levels of helium I [75].

S	n	L	J	Configuration	Term symbol	Energy level (cm^{-1})
0	4	0	0	1s4s	^{1}S	190940.226355
0	4	1	1	1s4p	^{1}P^0	191492.711909
0	4	2	2	1s4d	^{1}D	191446.4557405
0	4	3	3	1s4f	^{1}F^0	191451.89746084
1	4	0	1	1s4s	^{3}S	190298.113260
1	4	1	2	1s4p	^{3}P^0	191217.040967
1	4	2	3	1s4d	^{3}D	191444.4809292
1	4	3	4	1s4f	^{3}F^0	191451.88108855

Table 3.2: Energy levels of hydrogen I [76].

S	n	L	J	Configuration	Term symbol	Energy level (cm^{-1})
-1/2	4	0	1/2	4s	^{2}S	102823.8530211
-1/2	4	1	1/2	4p	^{2}P^0	102823.8485825
-1/2	4	2	3/2	4d	^{2}D	102823.894250
-1/2	4	3	5/2	4f	^{2}F^0	102823.909490
1/2	4	0	1/2	4s	^{2}S	102823.8530211
1/2	4	1	3/2	4p	^{2}P^0	102823.8943175
1/2	4	2	5/2	4d	^{2}D	102823.9094871
1/2	4	3	7/2	4f	^{2}F^0	102823.917091

Results

The results for the displacement as a function of the electric field for both the allowed transition ($L = 2$) and the forbidden transition ($L = 3$) for different values of $m(0, 1, 2)$ are shown as the symbols in figures 3.1(a) and 3.2(a). Third order polynomials have been fitted to the curves. These fitted curves are also shown in figures 3.1(a) and 3.2(a) as the lines through the data points. As explained in section 3.5 and by using a linear polarizer, since the axial field is measured, only the π-components ($\Delta m = 0$) are detected. Therefore, the polynoms of only the $m_i = 0 \rightarrow m_k = 0$ and $m_i = 1 \rightarrow m_k = 1$ components are used to calculate the difference between the allowed and the forbidden band, and not the transitions with $\Delta m = \pm 1$. These curves are shown in figures 3.1(b) and 3.2(b), together with the average of these two components. The curves in figures 3.1(a) and 3.2(a) for the forbidden and the allowed components are so close together that the different m components cannot be resolved with the used setup, where we have a resolution of 0.013486 nm (section 2.4). Instead, only one allowed and forbidden band can be detected. Therefore, the curves of the $m = 0$ and $m = 1$ components are averaged to obtain a single relation between the difference of the allowed and forbidden band, and the electric field. This average curve will be used to calculate the electric field from the difference between the allowed and the forbidden peak of the lines that will be measured in the experiments. For He I 492.2 nm it is

given by

$$\Delta\lambda_{AF} = -5.2140 \cdot 10^{-6}E^3 + 3.9844 \cdot 10^{-4}E^2 + 0.0058E + 0.1226 \qquad (3.43)$$

with $\Delta\lambda_{AF}$ in nm and E in kV/cm, and for He I 447.1 nm it is

$$\Delta\lambda_{AF} = -3.9620 \cdot 10^{-6}E^3 + 3.4558 \cdot 10^{-4}E^2 + 0.0025E + 0.1433 . \qquad (3.44)$$

The electric field in the experiment is obtained by numerically solving the above equations for E with the measured wavelength difference substituted for $\Delta\lambda_{AF}$.
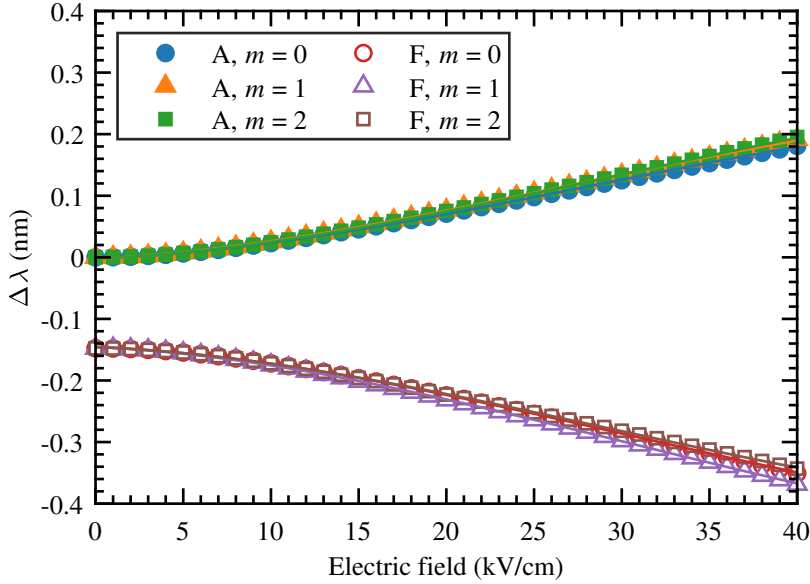
(a)
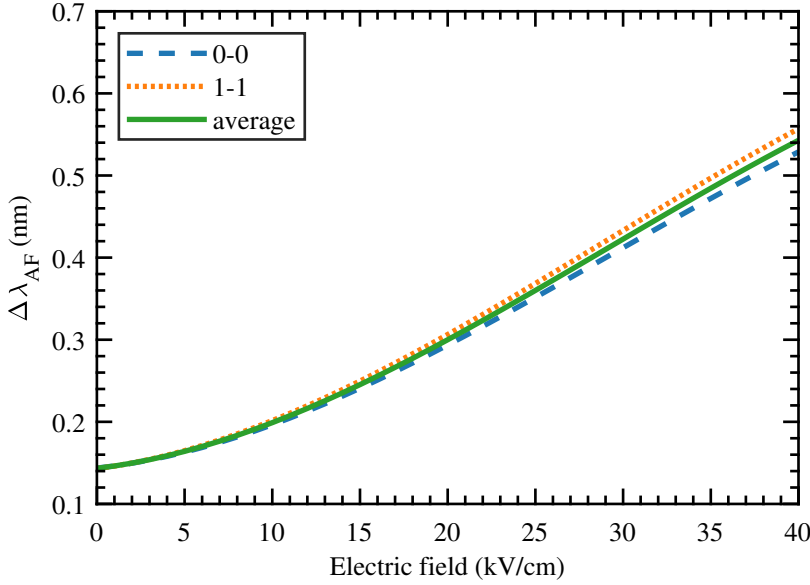
(b)

Figure 3.1: Results of the theoretical calculation for the He I 447.1 nm line: (a) the shift in wavelength of the forbidden (F) and the allowed (A) line as a function of the electric field and (b) the difference between the shifted allowed and forbidden line as a function of the electric field, for the $m_i = 0 \rightarrow m_k = 0$ and $m_i = 1 \rightarrow m_k = 1$ transitions and the average of these two.
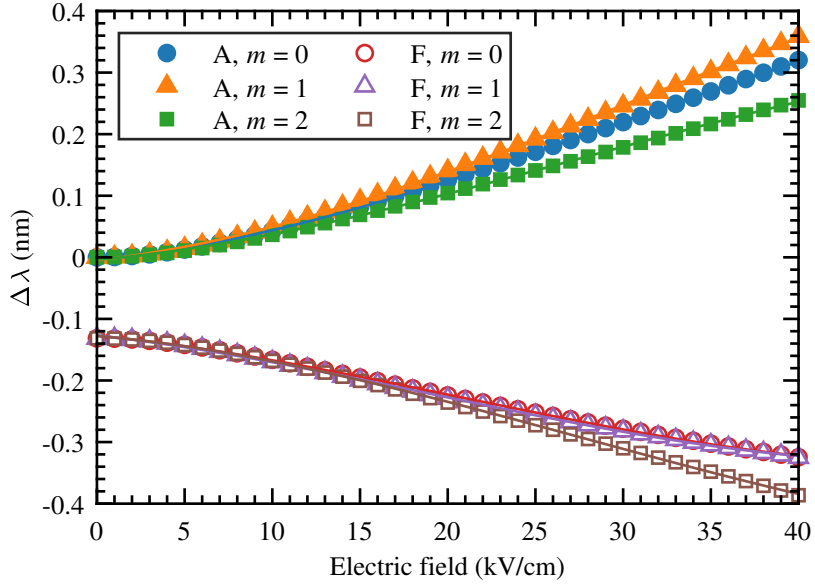
(a)
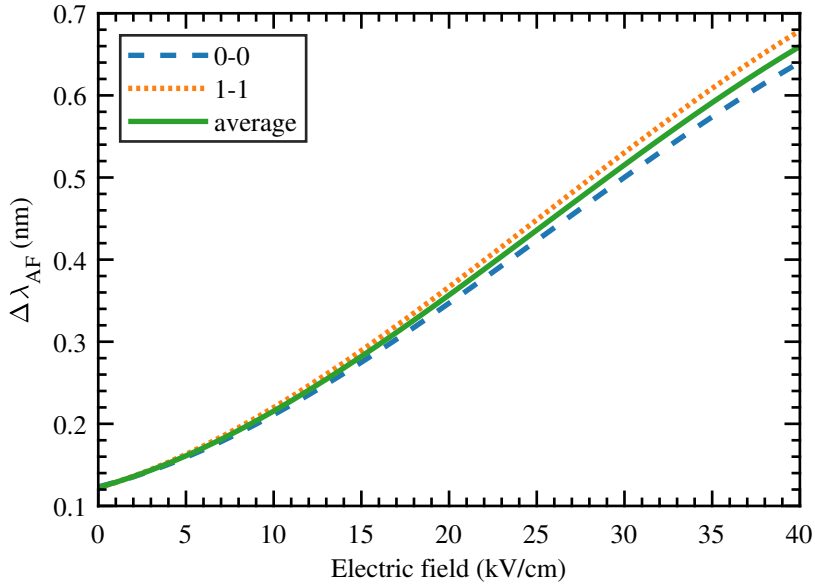
(b)

Figure 3.2: Results of the theoretical calculation for the He I 492.2 nm line: (a) the shift in wavelength of the forbidden (F) and the allowed (A) line as a function of the electric field and (b) the difference between the shifted allowed and forbidden line as a function of the electric field, for the $m_i = 0 \rightarrow m_k = 0$ and $m_i = 1 \rightarrow m_k = 1$ transitions and the average of these two.

3.4   Comparison to previous work

In this section the resulting relation between $\Delta\lambda_{\text{AF}}$ and the electric field is compared to the relation obtained from Cvetanovic *et al.* [59], Foster [57] and Kuraica [67].

The supplementary material of Cvetanovic *et al.* gives the wavelength shift of the different $n = 4$ levels for the He I 447.1 nm line and the He I 492.2 nm line, as a function of the electric field (ranging from 0 kV/cm to 101 kV/cm, in steps of 1 kV/cm). From these shifts, the distance between the shifted allowed and forbidden components is calculated as a function of the electric field. Similar to figures 3.1(b) and 3.2(b) the average is taken over the $\Delta m = 0$ components with $m = m' = 0, 1$, to obtain the relation $\Delta\lambda_{\text{AF}}(E)$ for the two helium lines.

Foster gives the energy shift of the different $n = 4$ levels for the He I 447.1 nm line and the He I 492.2 nm line for electric fields from 0 kV/cm to 100 kV/cm, in steps of 10 kV/cm. These energy shifts are first converted to wavelength shifts and then the same procedure is followed as with the results from Cvetanovic *et al.*.

From Kuraica, the relations $\Delta\lambda_{\text{AF}}(E)$ are directly taken for the He I 447.1 nm line and the He I 492.2 nm line. It is important to note that this relation is only valid from 0 kV/cm to 20 kV/cm [67].

The results from these calculations together with the results from this thesis are shown in figure 3.3 for the two helium lines. In the bottom graphs, the deviation of the different results to this thesis is shown.

For the results of Foster, the data is only given in steps of 10 kV/cm, and since only partial data was given at 0 kV/cm, no data point is possible there. At electric fields below 20 kV/cm the deviation in the results is with up to 10-15% relatively large, while at higher electric fields the deviation is less than 5%. The deviation may be explained by the difference in accuracy of the energy levels, from which $\lambda_{0,1,2,3}$ are calculated, since the energy levels in Foster's paper originate from before 1927 [77] and the used energy levels in this paper are from 2006[75] and 2010[76]. The results from Kuraica are only valid between 0 kV/cm and 20 kV/cm. In this region, the deviation is less than 5%, while outside this region the deviation is large (up to 35%). The deviation of the results from Cvetanovic is up to 5% in the full range of the electric field, thus these results are in good agreement.

In general, the results from this thesis are in good agreement with previous work, in the electric field range where the results are valid.

(a)

(b)
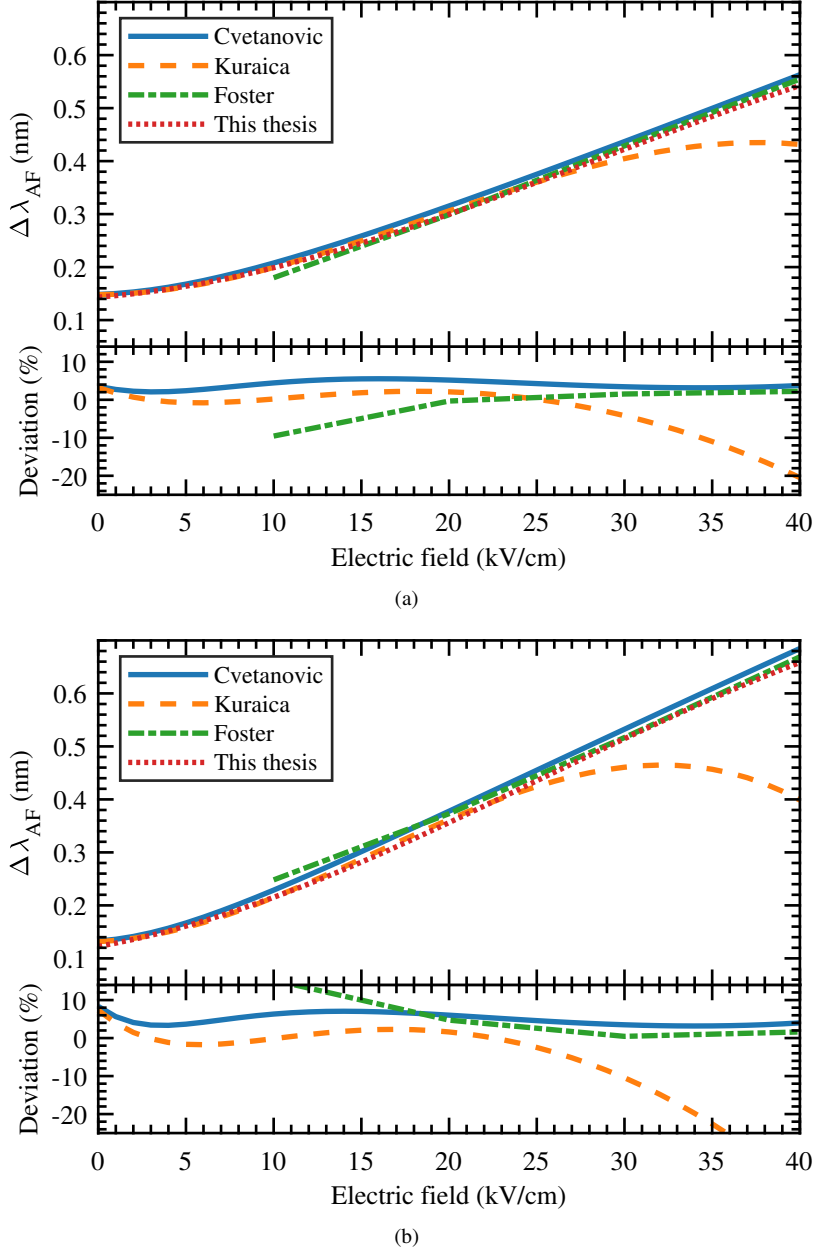
Figure 3.3: Comparison of the results from this paper and the results from Cvetanovic *et al.* [59], Kuraica [67] and Foster [57] for the difference between the shifted allowed and forbidden line as a function of the electric field: (a) for the He I 447.1 nm line, and (b) for the He I 492.2 nm line. The bottom graph shows the deviation (in percentage) of the difference between the different results and the results from this paper.

3.5 Selecting the axial component of the electric field

By choosing to measure only the light emitted with the polarization direction in the z-direction (which is parallel to the propagation direction of the ionization wave), we select only the π-component (component with $\Delta m = 0$). This will be shown in this section.

In this thesis, a helium plasma is studied. The helium atom has a dipole and when the atom is placed in an electric field, it will align its dipole axis with the axis of the electric field [68]. The (positive) nucleus is pushed in the direction along the electric field and the (negative) electrons in the opposite direction. On the other hand, there is the attractive force between the nucleus and the electrons, and thus an equilibrium establishes between these two forces [68]. Repeating equation (3.1) here, the dipole moment $\vec{d}$ is given by

$$\vec{d} = \alpha \vec{E} \tag{3.45}$$

in which α is the polarizability and $\vec{E}$ the electric field. The polarizability is a tensor for molecules, but a constant for atoms, since they are spherically symmetric [78]. For the helium atom the value is $0.204956 \cdot 10^{-24}$ cm^3 [79]. Therefore, the dipole moment of the helium atom lies parallel to the electric field.

The probability W that an atom will undergo a transition from state n to n', while emitting light of polarization direction $\vec{e}_j$ into solid angle $d\Omega$ is [54, 67]

$$W(\Omega, j)\mathrm{d}\Omega = \frac{e^2 \omega_{nn'}^3}{2\pi\hbar c^3} \left(\vec{e}_j \cdot \vec{d}_{n'n} \right)^2 \mathrm{d}\Omega \tag{3.46}$$

in which e is the elementary charge, c the speed of light, $\omega_{nn'} = (E_n - E_{n'})/\hbar$ the oscillation frequency of the dipole and $\vec{d}_{n'n}$ the dipole matrix element:

$$\vec{d}_{n'n} = \int \psi^* \vec{d} \psi \, \mathrm{d}\tau. \tag{3.47}$$

The intensity J_j of this light is obtained by multiplying equation (3.46) with the energy of a light quantum $\hbar\omega$ [54, 67], yielding

$$J_j \mathrm{d}\Omega = \frac{e^2 \omega_{nn'}^4}{2\pi c^3} \left(\vec{e}_j \cdot \vec{d}_{n'n} \right)^2 \mathrm{d}\Omega, \tag{3.48}$$

meaning that the intensity of the emitted light depends on the polarization direction.

A transition from state n to n' is only possible if $W(\Omega, j) \neq 0$, thus only if $\vec{d}_{n'n} \neq 0$. Calculating the different components of the matrix element gives the following. Using equation (3.45), equation (3.47) and $E_z = E_0 \cos\theta$, the z-component of $\vec{d}_{n'n}$ is

$$\begin{aligned} d_{n'n}^z &= \int \psi_{n'l'm'}^* \alpha E_z \psi_{nlm} \, \mathrm{d}\vec{r} \\ &= \alpha E_0 \int_0^\infty R_{n'l'}(r) R_{nl} r^2 \, \mathrm{d}r \int_0^{2\pi} \frac{1}{2\pi} e^{i(m-m')\phi} \, \mathrm{d}\phi \int_0^\pi P_{l'm'}(\theta) \cos\theta P_{lm}(\theta) \sin\theta \, \mathrm{d}\theta \end{aligned} \tag{3.49}$$

with

$$\psi_{nlm} = R_{nl}(r) P_{lm}(\theta) \, e^{im\phi} \frac{1}{\sqrt{2\pi}} \,. \tag{3.50}$$

The integral over ϕ vanishes if $m \neq m'$, thus $m = m'$ should hold and the selection rule for m is obtained:

$$\Delta m = m' - m = 0 \,. \tag{3.51}$$

For the integral over θ, the substitution of

$$P_{lm}\cos\theta = \sqrt{\frac{(l+1)^2 - m^2}{(2l+3)(2l+1)}}P_{l+1m} + \sqrt{\frac{l^2 - m^2}{(2l+1)(2l-1)}}P_{l-1m} \tag{3.52}$$

in the integral and the use of

$$\int_0^\infty P_{l'm'}P_{lm}\sin\theta \ \mathrm{d}\theta = \delta_{ll'} \tag{3.53}$$

yield that the integral vanishes unless

$$\Delta l = l' - l = \pm 1 \tag{3.54}$$

holds. Therefore, equation (3.54) is the selection rule for l. The final expressions for the matrix elements $d_{n'n}^z$ (equation (3.49)) then become

$$(d_z)_{nlm}^{n'l+1m} = \alpha E_0 \sqrt{\frac{(l+1)^2 - m^2}{(2l+3)(2l+1)}}R_{nl}^{n'l+1} \tag{3.55a}$$

$$(d_z)_{nlm}^{n'l-1m} = \alpha E_0 \sqrt{\frac{l^2 - m^2}{(2l+1)(2l-1)}}R_{nl}^{n'l-1} \tag{3.55b}$$

with

$$R_{nl}^{n'l'} = \int R_{n'l'}(r)R_{nl}(r)r^2\mathrm{d}r. \tag{3.56}$$

Thus, an electric field in the direction parallel to the axis of the jet, in this case the z-direction, will only induce transitions in the helium atom that emit linearly polarized light, i.e. transitions with $\Delta m = 0$ (the π-component).

The x and y components of $\vec{d}_{n'n}$ originate from an electric field with x and y-components. To simplify the calculation, a linear combination of $d_{n'n}^x$ and $d_{n'n}^y$ is made:

$$E_x + iE_y = E_0\sin\theta \ \mathrm{e}^{i\phi}, \ E_x - iE_y = E_0\sin\theta \ \mathrm{e}^{-i\phi}.$$

The corresponding matrix elements then become

$$
\begin{aligned}
d_{n'n}^x \pm i d_{n'n}^y = \\
\frac{\alpha E_0}{2\pi}\int_0^\infty P_{l'm'}(\theta)P_{lm}(\theta)\sin^2\theta \ \mathrm{d}\theta \int_0^\infty R_{n'l'}(r)R_{nl}(r)r^2 \ \mathrm{d}r \int_0^\infty \mathrm{e}^{\pm i\phi} \ \mathrm{e}^{-i(m-m')\phi} \ \mathrm{d}\phi.
\end{aligned}
\tag{3.57}
$$

The integral over ϕ again vanishes unless $m' - m \pm 1 = 0$, which yields the selection rule for m:

$$\Delta m = m' - m = \pm 1. \tag{3.58}$$

For the θ part, substituting

$$P_{lm}\sin\theta = \pm\sqrt{\frac{(l\pm m+1)(l\pm m+2)}{(2l+1)(2l+3)}}P_{l+1m\pm1} \mp \sqrt{\frac{(l\mp m)(l\mp m-1)}{(2l+1)(2l-1)}}P_{l-1m\pm1} \tag{3.59}$$

and using equation (3.53) again yields the selection rule for l:

$$\Delta l = l' - l = \pm 1. \tag{3.60}$$

The final matrix elements $d_{n'n}^x \pm i d_{n'n}^y$ then are

$$(d_x \pm i d_y)_{nlm}^{n'l+1m\pm1} = \pm \alpha E_0 \sqrt{\frac{(l \pm m + 1)(l \pm m + 2)}{(2l+1)(2l+3)}} R_{nl}^{n'l+1} \qquad (3.61a)$$

$$(d_x \pm i d_y)_{nlm}^{n'l-1m\pm1} = \mp \alpha E_0 \sqrt{\frac{(l \mp m)(l \mp m - 1)}{(2l+1)(2l-1)}} R_{nl}^{n'l-1} \qquad (3.61b)$$

with $R_{nl}^{n'l'}$ as in equation (3.56). Thus, an electric field in the direction perpendicular to the axis of the jet, thus in the xy-plane, will only induce transitions in the helium atom that emit circularly polarized light, i.e. transitions with $\Delta m = \pm 1$ (the σ-component).

3.6 Summary

In this chapter, the relation between the peak-to-peak wavelength difference between the allowed and the forbidden component of a helium transition and the electric field has been obtained for two different helium lines. The resulting equations are

$$\Delta \lambda_{AF} = -5.2140 \cdot 10^{-6} E^3 + 3.9844 \cdot 10^{-4} E^2 + 0.0058E + 0.1226$$

for He I 492.2 nm and

$$\Delta \lambda_{AF} = -3.9620 \cdot 10^{-6} E^3 + 3.4558 \cdot 10^{-4} E^2 + 0.0025E + 0.1433 \ .$$

for He I 447.1 nm, with $\Delta \lambda_{AF}$ in nm and E in kV/cm in both cases. These equations have been shown to compare well with results from literature, since a deviation between the results of about 5 % was found in the electric field range where all results are valid.

The above equations are applied when using Stark polarization spectroscopy, in the setup that is explained in section 2.4. It has also been shown that they yield the axial component of the electric field in the plasma if the linearly polarized components of the spectral lines of helium are measured.

4

Comparison of discharge propagation parameters in experiments and simulations of a helium jet without target

Abstract: This chapter quantitatively characterizes a kHz atmospheric pressure He plasma jet without target powered by a pulse of positive applied voltage. It focuses on a quantitative comparison between experimental measurements and numerical results of a two-dimensional fluid model using the same configuration, for different values of magnitude and width of pulsed applied voltage. Excellent agreement is obtained between experiments and simulations on the gas mixture distribution, the length and velocity of discharge propagation and the electric field in the discharge front. For the first time in the same jet, the experimentally measured increase of the electric field in the plume is confirmed by the simulations. The electron density and temperature, measured behind the high field front, are found to agree qualitatively. Moreover, the comparison with simulations shows that discharge propagation stops when the potential in the discharge head is lower than a critical value. Hence, pulse width and magnitude allow to control propagation length. For long pulses (≥ 1000 ns), the potential in the discharge front reaches this critical value during the pulse. For shorter pulses, propagation is determined by the pulse shape, as the critical value is reached around $90 - 130$ ns after the fall of the pulse. The results suggest that the magnitude of this critical value is defined by the gas mixture at the position of the front.

4.1 Introduction

As shown in chapter 1, plasma jets are widely studied because of their broad range of applications such as medicine (e.g. wound healing and infection control [80]), agriculture [22] and surface modifications (e.g. on polymer fibres [19]). Although a plasma jet may look simple, it is in fact a transient discharge that is produced in a dielectric tube, through which it propagates in a flow of a rare gas (usually helium) that mixes with air at the end of the tube before it touches the target for the applications. For all these applications, as well as for the optimization of the plasma jet, it is important to understand the discharge dynamics of propagation in plasma jets. The electric field, electron density and electron temperature are important parameters to characterize the plasma jet propagation. This chapter shows the results of measurements of these plasma parameters, using different diagnostics, and focuses on the comparison with results from a two-dimensional fluid model. Combining experiments and simulations, we are able to supply conditions that need to be fulfilled in order to sustain the propagation of ionization waves in the plasma jet.

Although there have been some studies on the electric field [63], electron density [81, 82] and electron temperature [83] in jets, to our knowledge these parameters have never been experimentally assessed in one and the same free jet. To couple the results, it is important to measure them in the same jet. Moreover, comparison of experimental results with numerical simulations allows to validate diagnostics and models and to provide complementary information on each other. Also, there is an effort to increase the understanding of discharge dynamics through comparisons between simulations and experiments. So far, these comparisons focus mostly on evaluating tendencies and macroscopic parameters like discharge structure and light emission [84–89]. More recently, quantitative comparisons are performed on jets, focusing on ionization front propagation velocity [90, 91], breakdown voltage [92] and electric field inside a dielectric target [35, 36].

Concerning discharge dynamics of propagation in jets, the influence of different parameters has been addressed in several studies at atmospheric pressure. Firstly, studies have been performed on streamer discharges, which are relevant for the discharge propagation in jets, since it has been shown [8–10, 93–95] that plasma jets are ionization waves that propagate with the same mechanisms as streamer discharges in tubes and then in a plasma plume. In [96], two-dimensional positive streamer simulations in air have assessed these parameters. On the one hand, they have shown that the magnitude of the applied voltage determines the streamer dimensions, velocity and current. On the other hand, it has been reported that the electric field in the streamer head and in the plasma channel and the electron density in the channel do not change appreciably with the value of applied voltage. Moreover, in [97] it has been shown that the streamer velocity in air is proportional to the radius of the space charge layer in the discharge front.

Furthermore, in positive pulsed helium jets, [98] has revealed by fast photography that the time of ignition and velocity of propagation of the discharge are strongly dependent on the magnitude of the applied voltage and that the time at which the discharge stops propagating is set by the fall of the voltage pulse. Numerically, it has been reported in [99] that the velocity and length of propagation of helium plasma jets emerging in ambient air depend on the helium flow rate, thus on the helium-air mixing, and on the magnitude of the applied voltage. Furthermore, it has been shown experimentally in [100] that the discharge front leaves behind a quasi-neutral plasma channel, with a low electric field, that connects the potential in the powered electrode to that in the discharge front. In addition, through numerical simulations in [8] with a pure helium jet without air impurities and without helium-air mixing, the length of the discharge propagation

has been related to the electric potential on the discharge head. In that work it has been estimated that the potential at the discharge front needs to be 2.75 kV for propagation to be maintained. Thus, it has been argued that the length of propagation is determined by the conductivity in the plasma channel, the value of applied voltage and the shape of the applied voltage.

In this chapter, some of the important plasma parameters (electric field, electron density and electron temperature) of the discharge propagation in a positive pulsed helium jet without target are measured and quantitative comparisons are performed with results from a two-dimensional fluid model. Furthermore, the criteria for discharge propagation and the end of discharge propagation are investigated.

In the coming sections, the experimental and numerical setups are discussed. In section 7.2.1, the experimental setup is described, together with the diagnostics used to determine the different plasma parameters. Section 4.2.2 exposes the numerical model, using the same configuration as in the experiments. Measurements of air density confirm that the flow considered in the model is in agreement with the experiments. In section 7.3 the dynamics of discharge propagation are characterized through both experiments and simulations. The position of the discharge front, velocity of propagation, electric field in the discharge front and electron density behind the front are evaluated and directly compared. Finally, in section 4.3.3, experimental and numerical results of discharge propagation and electric field with different applied voltages and pulse widths are used to evaluate the criteria for discharge propagation. In particular, the electric potential on the discharge front required for propagation and the timescales on which it evolves with respect to the fall of applied voltage are assessed through the simulations.

4.2   Setup

4.2.1   Experimental setup

The atmospheric pressure plasma jet that is used in this chapter, was described in detail in section 2.1. It is operated vertically, downwards, and placed in the general setup of figure 2.1. The helium flow has a constant value of 1500 sccm. The jet is powered by uni polar positive voltage pulses, as shown in figure 4.1, for which the default settings are an amplitude V_P of 6 kV, a pulse length t_f of 1 µs and a repetition rate f of 5 kHz. In this figure the total current is also shown, which was measured at the anode with a Rogowski coil (Pearson Current Monitor 6585).

Different diagnostics have been used to determine electrical, gas and optical properties of the plasma jet. In the next paragraphs, these used diagnostics are summarized.

ICCD imaging

The position and velocity of the ionization front in the plasma jet are determined by ICCD imaging, for which the setup of figure 2.5 in section 2.3 is used. The delay time on the camera is increased in steps of 20 ns, to follow the vertical movement of the front. Images are taken at an exposure time of 2 ns with an integration on chip of 10 to 20 exposures. The camera is triggered by the 5 kHz pulses that also drive the high voltage of the jet. In every consecutive image, the position and velocity of the ionization front are determined, according to the method in section 2.3.2.
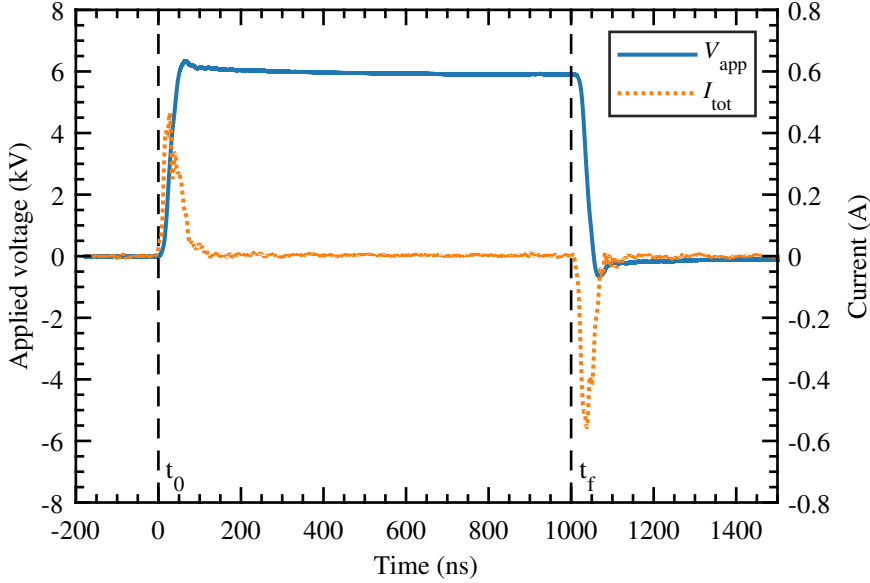
Figure 4.1: Applied voltage and current signals measured at the anode as a function of time, with $V_P = 6$ kV, $t_f = 1$ μs, $f = 5$ kHz, and 1500 sccm He.

Stark polarization spectroscopy

For the electric field measurements, the Stark polarization spectroscopy setup is used that is described in detail in section 2.4. Spectroscopy is performed on the helium 492.2 nm line, where the wavelength distance between the allowed and the forbidden component of the line determines the magnitude of the axial electric field in the ionization front, according to the calibration in chapter 3. The electric field is determined at the center of the jet along the (vertical) z axis according to figure 2.1, from inside the capillary just below the cathode up until about 2 cm in the effluent of the jet.

The images consist each of an on-chip accumulation of 20 frames that each integrate during 2 to 15 s every 10 ns long exposure that is triggered by the pulse of the jet. The integration time depends on the intensity of the signal. The slit width of the spectrometer was 100 μm.

Thomson and rotational Raman scattering

The Thomson and rotational Raman scattering setup and analysis algorithms that are used in this work are described in more detail in [30, 43, 44]. For the measurements, the plasma jet is placed in the laser setup of figure 2.10 that was explained in section 2.5. In short, the light of the 532 nm Nd:YAG laser is scattered on the plasma jet. Spectral images are taken of this Thomson and Raman scattered light, after the Rayleigh stray light is removed by a volume Bragg grating. From the fitting of the Thomson signal, the electron density n_e and electron temperature T_e can be determined, while the densities of the molecules N_2 and O_2 can be determined from the fitting of the rotational Raman signal. Instead of taking the fitting error as the error in n_e, the error is determined from statistics, since this error is found to be the largest. Measurements at $z = 8.7$ mm are performed on different days and the resulting spread in the values for n_e of about 20% is taken as the error bar for all n_e measurements.

4.2.2 Numerical setup

The numerical setup is shown in figure 4.2. The geometry taken is the same as in the experiments. A dielectric pyrex tube with a relative permittivity of $\varepsilon_r = 4$, length 3.3 cm (between $z = 0.0$ cm and $z = -3.3$ cm), internal radius $r_{in} = 1.25$ mm and outer radius $r_{out} = 2.0$ mm is used. Helium flows through the tube with a 1500 sccm flux as in the experimental conditions. A free jet is studied, and thus no target is present, but a grounded plane is set far from the tube at $z = 20$ cm. A powered ring electrode of inner radius 0.4 mm and outer radius 1.25 mm is set inside the tube between $z = -2.8$ cm and $z = -3.3$ cm and a grounded ring is wrapped around the glass tube between $z = -2.0$ cm and $z = -2.3$ cm, at a distance of 0.5 cm from the inner ring. As in the experiments, the inner ring is powered by a positive applied voltage that rises from $t_0 = 0$ ns during 50 ns until reaching a plateau voltage V_P (as is shown in figure 4.1). Then, the applied voltage is constant until $t = t_f$ and decreases from there until $t_f + 50$ ns, when it reaches zero. Taking into account the high repetition rate in experiments ($f = 5$ kHz), we consider as in our previous works [35, 36, 101] that relatively high densities of electrons and positive ions remain in the discharge domain between pulses, as is also argued in [94]. Given the uncertainty on what the exact initial conditions should be to reproduce the repetitive discharges, we take into account a standard uniform initial preionization density $n_{init} = 10^9$ cm^{-3} of electrons and O_2^+. However, no initial surface charges are considered on the dielectric tube surface.

Figure 4.2 also shows that the discharge setup is placed inside a grounded cylinder with a radius of 10 cm. Between the dielectric tube and the grounded cylinder, the space is considered as a dielectric of air with permittivity $\varepsilon_r = 1$. On the last boundary of the domain (i.e. at $z = -3.3$ cm), the axial gradient of the electric potential is set to zero. The simulations have been carried out in a cylindrically symmetrical computational domain at atmospheric pressure and at $T = 300$ K. A 2D axisymmetric fluid model is used to simulate discharge dynamics as in [36, 101]. It is based on drift-diffusion-reaction equations for electrons, positive ions and negative ions and mean electron energy, and reaction equations for neutral species, coupled with Poisson's equation in cylindrical coordinates (z, r):

$$\frac{\partial n_i}{\partial t} + \vec{\nabla} \cdot \vec{j}_i = S_i \tag{4.1a}$$

$$\vec{j}_i = (q_i/|e|)n_i\mu_i\vec{E} - D_i\vec{\nabla}n_i \tag{4.1b}$$

$$\frac{\partial}{\partial t}(n_e\varepsilon_m) + \nabla \cdot \vec{j}_\varepsilon = -|q_e|\vec{E} \cdot \vec{j}_e - \Theta_e \tag{4.1c}$$

$$\vec{j}_\varepsilon = -n_e\varepsilon_m\mu_\varepsilon\vec{E} - D_\varepsilon\nabla(n_e\varepsilon_m) \tag{4.1d}$$

$$\varepsilon_0\nabla \cdot (\varepsilon_r\nabla V) = -\rho - \sigma\delta_s \tag{4.1e}$$

$$\vec{E} = -\vec{\nabla}V \; ; \; \rho = \sum q_i n_i \tag{4.1f}$$

where $n_\varepsilon = n_e\varepsilon_m$ is the electron energy density, defined as the product of the electron density with the mean electron energy, Θ_e represents the power lost by electrons in collisions ($\Theta_e = P_{loss}/N_g(\varepsilon) \times N_g \times n_e$) and j_ε is the flux of n_ε by drift and diffusion. The subscript i refers to each species and n_i, q_i, j_i, μ_i and D_i are the number density, the charge, the flux, the mobility and the diffusion coefficient of each species i, respectively. S_i is the total rate of production and destruction of species i by kinetic processes and by photoionization. V is the electric potential, $\vec{E}$ the electric field, e the electron charge, ε_0 the vacuum permittivity, ε_r the relative permittivity and δ_s the Kronecker delta (equal to 1 on the dielectric/gas interfaces). The electron temperature is $T_e = 2/3\varepsilon_m$.
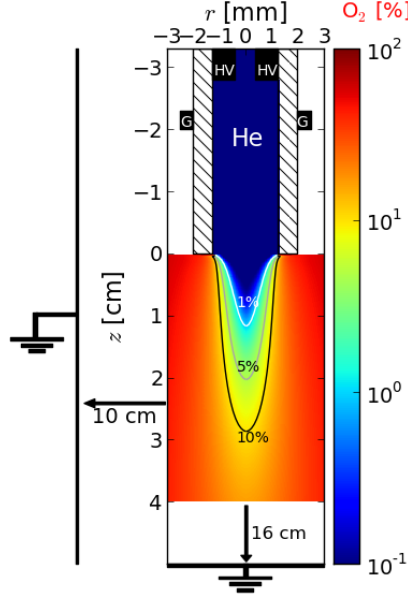
Figure 4.2: Side view schematics of the discharge setup used in the simulations. The colour plot and the contour curves show the O_2 spatial distribution in the He-O_2 mixture (percentage over a total of 2.45×10^{19} cm^{-3} gas density).

It is important to point out that at the surface of the tube, secondary emission of electrons by ion bombardment ($\gamma = 0.1$ for all ions) is taken into account. The surface charge density σ on the surface of the dielectric is obtained by time-integrating charged particle fluxes through electric drift to the surface. We consider that these charges then remain immobile on the surface of the dielectric. As in our previous works, the plasma model has been coupled with static flow COMSOL calculations [34, 102]. In this chapter, we use the same flow calculation as has been used in [28] with 1.5 slm of helium with 1000 ppm of air impurities flowing through the tube. In this work, we consider that helium contains O_2 impurities and flows downstream into an O_2 environment, as an approximation to air. Both experiments and simulations [103, 104] have shown that the use of O_2 or air as surrounding gas for a He jet present similarities with respect to discharge dynamics in the plasma plume. In [94, 104] the important role of the electronegativity of the surrounding gas, either O_2 or air, has been highlighted. Finally, in [34, section III.6 and appendix F], attachment in oxygen has been shown to be relevant for the radial confinement of the discharge in the plume. The spatial distribution of O_2 in the He-O_2 mixture obtained from the flow calculation is presented in figure 4.2. The O_2 density in the model has been compared with radially-resolved Raman scattering measurements of the air density ($N_2 + O_2$). The comparison for two locations close to the tube exit, $z = 3$ mm and $z = 8.7$ mm, can be observed in figure 4.3 and shows that the flow calculations accurately reproduce the He-air mixture in the experiments for the region of interest: radial positions below 2 mm, which is the tube outer radius. Furthermore, it can be observed from the measurements that in that region the plasma has no effect on the composition of the flow.

The reaction scheme proposed in [101] has been used to describe the kinetics in the He-O_2 plasma. The scheme includes a total of 55 reactions with 10 species: e, O_2^-, He$^+$, He$_2^+$, O_2^+, He,
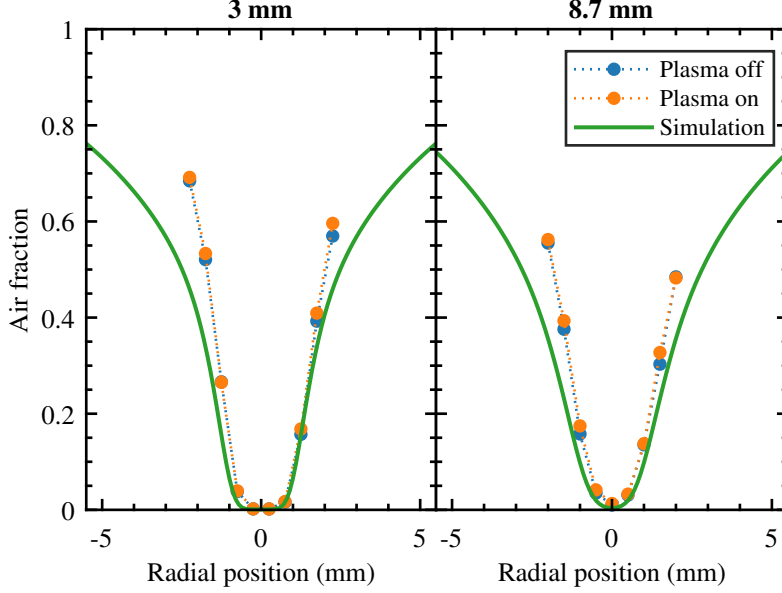
Figure 4.3: Comparison of the air fraction in the flow from the COMSOL flow calculation with experimentally measured air fractions with and without plasma, as function of the radial position for $z = 3$ mm and $z = 8.7$ mm.

He(2^3S,2^1S), O, O$_2$, O$_2(a_1\Delta_g)$. The electron and electron energy transport parameters, power loss terms and rate coefficients of electron-impact reactions are calculated with the electron Boltzmann equation solver BOLSIG+ [105], using the IST-Lisbon database of cross sections in LXCat [106, 107], and tabulated as functions of both the local gas mixture and the local mean electron energy ε_m. In each cell and at each timestep, each coefficient k is calculated for the local values of the mixture and ε_m by linear interpolation between the local upper and lower tabulated values and we obtain k as a function of ε_m and the mixture, as in [34]. For the photoionization model, we use the approach described in [36, 90]. The ionizing radiation is assumed to be proportional to the excitation rate of helium atoms by impact of electrons. The photoionization source term A_{ph} is proportional to the amount of O$_2$ admixture (X_{O_2}) and we use $A_{\text{ph}} = \xi \times X_{O_2}$. In [34], we have varied ξ in the range of $10 - 1000$ for different plasma jet configurations. A small influence on the discharge structure and dynamics has been observed. In this work, $\xi = 100$ is used.

A finite volume approach and a Cartesian mesh are used. The mesh size is 10 µm, axially between $z = 5.0$ cm and $z = -3.3$ cm and radially between $r = 0$ and $r = 3.0$ mm. Then, both for $z > 5.0$ cm and for $r > 4.0$ mm, the mesh size is expanded using a geometric progression. The refinement taken requires a mesh of $n_z \times n_r = 8350 \times 370 = 3.090$ million points. The average computational time required for a 2 µs simulation run to obtain the results presented in this paper was of five days with 64 MPI processes on a multicore cluster "Hopper" (32 nodes DELL C6200 bi-pro with two 8-core processors, 64 GB of memory and 2.6 GHz frequency per node). Further details on the numerical schemes and other characteristics of the simulations are given in [34].

4.3 Results and discussion

4.3.1 Characterization of discharge propagation and peak electric field

In this section and in the next section (section 4.3.2), the plasma jet operates at the default conditions: $V_P = 6$ kV, $t_f = 1$ µs, $f = 5$ kHz, and 1500 sccm He.

The propagation of the ionization wave as measured with ICCD imaging is shown in figure 4.4 for $t = 17 - 717$ ns with respect to the start of the pulse at $t_0 = 0$ ns as in figure 4.1. It can be seen that inside the tube, the ionization wave is wide and propagates along the walls towards the nozzle. When the ionization wave enters the ambient air, it is confined due to the mixing with the oxygen and nitrogen species in air. The discharge starts propagating from $z = -2.0$ cm around $t = 25$ ns, reaches the end of the tube around $t = 177$ ns and reaches the end of propagation at around $z = 4.0$ cm and $t = 617$ ns. Figure 4.5 shows the spatial distribution of the electric field magnitude from the simulations at different times. The peak of the electric field is located at the discharge front. Behind the front, there remains a quasi-neutral plasma channel with electron density in the order of $10^{12} - 10^{13}$ cm^{-3}. It is shown that the discharge crosses $z = -2.0$ cm around $t = 60$ ns in the simulations, while in the experiments this position is reached around $t = 25$ ns. The discharge fills the tube during propagation and reaches the end of the tube at around $t = 200$ ns. Thereafter, as in the experiments, the discharge is progressively radially confined as it propagates in the plasma plume, mostly due to higher electron-impact ionization source term in the region with more helium and less molecular gases. A more detailed study of the mechanisms leading to the radial confinement in the plume has been carried through in [34] (section III.6). Finally, the end of discharge propagation is reached at around $t = 700$ ns and $z = 3.5$ cm, where the gas-mixture at $r = 0$ mm is close to 86% He + 14% O_2.
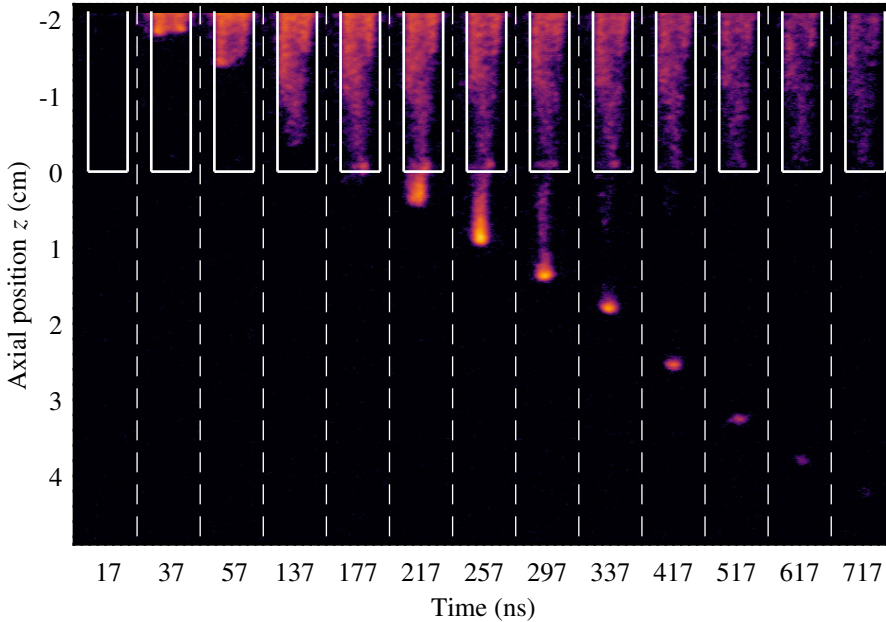
Figure 4.4: Images of the propagation of the ionization wave in space and time, with the colors, that represent the intensity of the light emission, plotted on a log scale. In these images, the jet operates at default conditions.
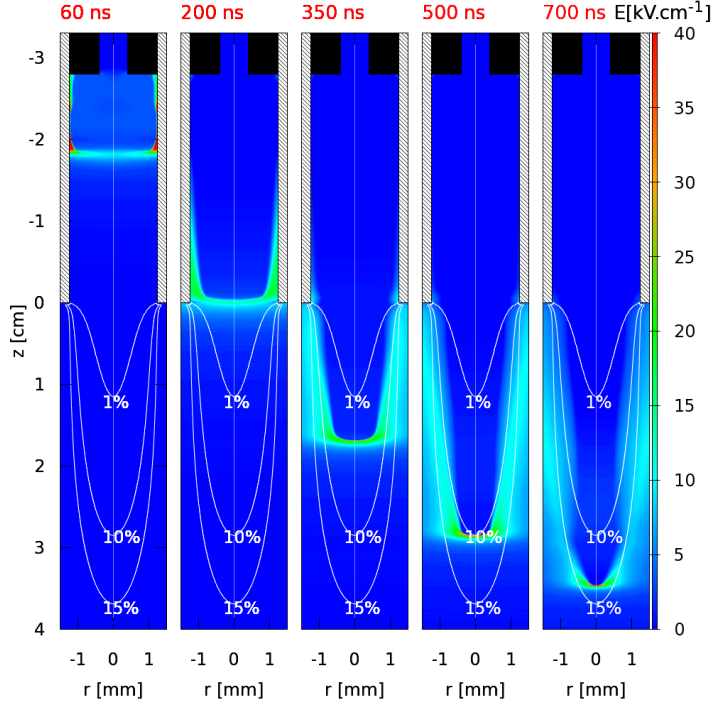
Figure 4.5: Cross sections of the spatial distribution of the electric field magnitude E_t from the simulations at different times. The contour curves show the O_2 spatial distribution in the He-O_2 mixture (percentage over a total of 2.45×10^{19} cm^{-3} gas density N_g).

To study and quantify the propagation of the discharge better, the axial position of the ionization wave as a function of time and the velocity as function of position are shown in figure 4.6(a) and figure 4.6(b), respectively, where an average agreement between measurements and simulations within 5 mm at the position and of about 80% in the velocity is shown. The position and velocity of the ionization front in the simulations is obtained by following the maximum of the magnitude of the axial electric field E_z every 10 ns. There is a small difference in ignition time between the experiments and the simulations: in the experiments the discharge starts propagating from $z = -2.0$ cm at around 25 ns, while in the simulations this takes place around $t = 60$ ns. In the experiments, the discharge has a repetition rate of 5 kHz, while the simulations contain only one pulse. The difference between experiments and simulations is attributed to the uncertainty in memory effects, such as the possibility of leftover surface charges between pulses on the inner surface of the dielectric tube, that are not taken into account in the model.

In figure 4.6(a) it can be seen that the difference between the experimental and numerical axial position of the ionization front stays approximately constant during the propagation. Thus, the discharge takes the same amount of time in the experiments and simulations to propagate from the grounded electrode to the nozzle and from the nozzle to its maximum propagating distance of 3.5 cm at about 600 ns. Since the length t_f of the applied voltage pulse is 1000 ns, it can be noticed that the discharge stops propagating before the voltage pulse has ended. After $t = 600$ ns, the discharge in the experiments is too faint for light to be captured with the camera. We can conclude that the propagation length agrees well within 5 mm.

About the velocity results in figure 4.6(b), the first data point corresponds to a time of 37 ns

in the experiments, while in the case of the simulations it has been obtained from the difference between the positions at 60 and 70 ns. The experiments and the simulations show the same behaviour. The velocity starts at a high value of about 1.8×10^5 m/s and decreases until the end of the tube. This can be attributed to the increasing distance between the front and the powered

(a)

(b)
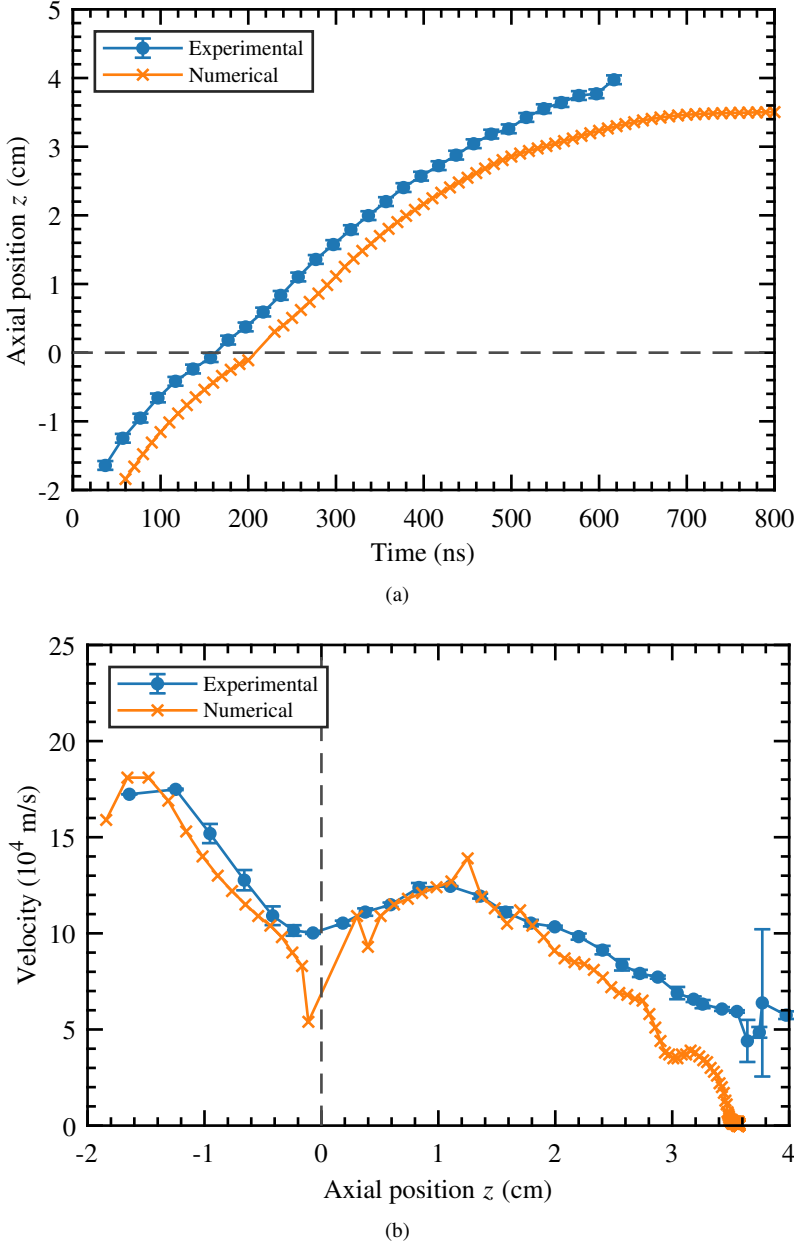
Figure 4.6: Results from the experiments and simulations on a) the position of the discharge as a function of time, and b) the velocity of the discharge during axial propagation in the tube and the plume.

electrode [34, section III.2] or to the charge losses to the tube walls [108, 109]. When the ionization wave enters the ambient air, the velocity first increases and then decreases again until the discharge reaches its maximum propagating distance, where the velocity drops to zero in the simulations and becomes immeasurable in the experiments. This behaviour was also observed in other experiments [86, 110–112] and simulations [8, 113, 114]. There are two effects that can play a role to explain this behaviour. First, as explained in [110], when entering the ambient air, the discharge ionizes and excites the N_2 and O_2 species in the air. Close to the nozzle there is enhanced plasma chemistry, due to the influence of the applied voltage and He metastables that induce Penning ionization of N_2 that has a lower ionization energy than He. Therefore, the velocity of the discharge increases in the first cm of the plume. Further away, the influence of the applied voltage decreases and thus the velocity too [110]. The radial confinement itself of the discharge can also contribute to the decrease of the velocity, since it was shown in [97] that the radius of the discharge front is proportional to the streamer velocity in air. Second, as shown in [114] with simulations of pure helium in tubes with varying permittivity, a change in permittivity from $\varepsilon_r = 4$ (the tube) to $\varepsilon_r = 1$ (the ambient air) causes the velocity to rise. No He/air mixing or Penning ionization were taken into account in these simulations, making the difference in permittivity the main cause for the increasing velocity that has been observed.

The discharge propagates because of charge separation at the high electric field front. In figure 4.7, the maximum of the axial component of the electric field E_{zMAX} as function of axial position is shown from both the experiments and the simulations. In both cases, E_{zMAX} is the peak electric field in the center of the front [109], with a radial uncertainty of the size of the slit width of 100 μm. In the simulations, E_{zMAX} is obtained with a 1 ns resolution. As explained in [109], E_{zMAX} in the experiments comes from the distance between the allowed and forbidden line of the studied helium band, where the position of the forbidden line changes the most due to the high electric field. The uncertainty of the fit in determining the wavelength position of both lines is used as the error, yielding an error in the electric field values of around ± 1 kV/cm, as can be seen in figure 4.7. This means that the E_{zMAX} we measure might not be the highest at the measured position, but actually an average value and the real value lies within a range of ± 1 kV/cm. In the simulations, a range of ± 1 kV/cm around the maximum E_z corresponds to a distance of around $z \pm 0.1$ mm around the position of this E_z. Therefore, we take the average E_z within a distance of ± 0.1 mm around z, and this is the green curve that is shown in figure 4.7. This average corresponds better to the experimentally obtained values than the absolute E_{zMAX} from the simulations.

There is no experimental data of E_{zMAX} for $z > 2.0$ cm present in figure 4.7, because the intensity of the discharge is too low to obtain a fittable spectrum here. For the other positions, the agreement in E_{zMAX} obtained from the experiments and from the simulations shows a discrepancy up to a maximum of 11%, with E_{zMAX} around 10 kV/cm inside the tube and rising up to 20 kV/cm in the plume. A larger difference can only be seen just outside the tube, where E_{zMAX} shows a decrease in the experiments, but an increase in the simulations. This increase may be due to the change of permittivity between the tube with $\varepsilon_r = 4$ and the ambient air with $\varepsilon_r = 1$ [114]. The fact that the tube edges are sharp in the model, while they are rounded in the experiments, might account for the difference. From imaging (figure 4.4) it can also be seen that the discharge is slightly wider close to the nozzle than further away. The highest value of the electric field at z positions close to the nozzle might then radially be just off-center. Since in the experiments E_{zMAX} is measured at $r = 0$ mm, this measured value might be lower than the highest electric field value at these z positions, thus contributing to the difference in E_{zMAX} between the experiments and the simulations at positions close to the nozzle.

The experimental results of E_{zMAX} are similar to previously published experimental results
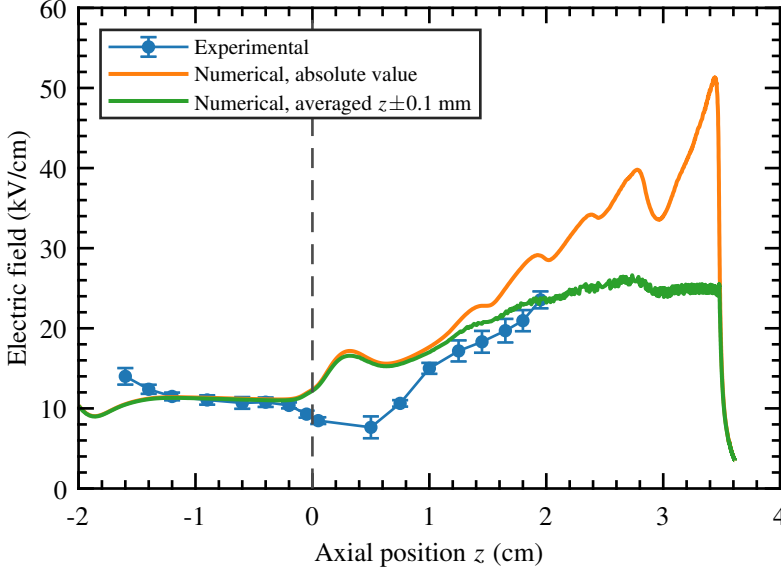
Figure 4.7: Maximum axial component of electric field E_z for $r < 0.1$ mm at the discharge front during propagation in the tube and the plume, in experiments and simulations.

without target [109], and also for a plasma jet with a different geometry [65, 115] or a different shape of the applied voltage [28, 31]. E_{zMAX} increases when the discharge propagates through the ambient air, in both the experiments and the simulations. Thus, this trend of the electric field from experiments is confirmed and quantitatively compared with simulations on the same jet configuration. The simulations also allow an explanation for this behaviour. With the admixture of molecular gases along the plume, the electron-impact ionization coefficient decreases [93] and the losses of electrons through recombination and attachment increase (see [34, section III.6]). Thus, the peak electric field required to produce free electrons ahead of the discharge front effectively enough to sustain discharge propagation increases along the plume. The volume where this production is effective is dependent on the gas-mixture and decreases along the propagation in the plume, leading to the radial confinement observed in figure 4.4 and figure 4.5.

4.3.2 Characterization of electron density and temperature

The axial profiles of the electron density n_e and electron temperature T_e along the propagation are shown in figure 4.8(a). In the experiments, these are determined with a 10 ns laser pulse around the center of the ionization wave that propagates at a velocity of about 1.0×10^5 m/s (see figure 4.6(b)), meaning that the ionization wave propagates over about 1 mm during the laser pulse. Therefore, n_e is found in the simulations by looking every 10 ns for the maximum of E_z and then searching the maximum n_e within a 1 mm distance from this position. T_e is found in the simulations at $r = 0$ mm and axially 0.5 mm behind the position of the maximum of E_z. This is a way to make sure that T_e lies in the quasi-neutral plasma channel, and not in the region of charge separation where gradients are very strong. The results show a qualitative agreement, as n_e increases and T_e decreases in the plume in both experiments and simulations.

Yet, discrepancies are visible, reaching up to a factor 4. The increase of n_e in the plume is expected and is in correspondence with the behaviour of the electric field in figure 4.7. Several simulations [94, 99, 116, 117] and experiments [30, 81, 82] have observed this increase too. Moreover, the obtained values of T_e are similar to other simulations [118] and experiments [81, 83].

Several jet simulation results in the past have reported electron density values lower than those experimentally observed here. In [94], simulations have been done on a jet that is powered at 7 kV and where 7 slm He flows through a 3 mm wide tube into air. The obtained values for n_e are 0.75×10^{12} cm^{-3} just outside the tube and 1.6×10^{12} cm^{-3} at $z = 4$ cm. These values are lower than the simulation values in our case. For a similar jet, powered at 4 kV, n_e values of 0.2×10^{12} cm^{-3} have been obtained just outside the tube and 6.7×10^{12} cm^{-3} at 1.3 cm from the nozzle in the simulations in [99]. This first value is lower than our simulation values and the second value compares better to $z = 1.8$ cm in our case. The n_e that have been obtained in [8], for a 4 kV powered jet where He flows through a tube with 2 mm inner diameter into N_2 with no He/N_2 mixing taken into account, are 0.2×10^{12} cm^{-3} at $z = 0.5$ cm and 0.7×10^{12} cm^{-3} at $z = 3$ cm. Both these values are lower than n_e obtained in our simulations. A jet where 2 slm He is flowing through an ≈ 0.8 mm wide tube into air and that is powered with 130 ns long -10 kV pulses is used in [87]. There, the highest value of 5×10^{12} cm^{-3} was found in the plume, which corresponds to our value in the simulations at $z = 1.5$ cm. Recently, simulations were done on a jet interacting with different targets [116]. Powered by 200 ns long 8 kV pulses, 3 slm He was flowing into a humid air atmosphere and the targets were placed at $z = 17$ mm. With a non conductive, dielectric target, n_e values were found of 1.2×10^{12} cm^{-3} just outside the tube and 2.4×10^{12} cm^{-3} in the vicinity of the target. With a grounded metal target, n_e increases to 7.5×10^{12} cm^{-3} just outside the tube and 9×10^{12} cm^{-3} in the vicinity of the target. The n_e obtained from our simulations without a target fit in between the results for these targets, since our values are larger than the results for the dielectric target, but smaller than the grounded metal results.

The experimental values for n_e in this work agree with already published results [30], where the same jet was used. At $z = 0.3 - 0.5$ cm, the experimental n_e of around 0.4×10^{13} cm^{-3} is similar to n_e at $z = 0.2$ cm in [81], where an AC-powered jet is used with a slightly different geometry. Therefore, not the full axial profile is similar and their measured value of 0.8×10^{13} cm^{-3} at $z = 1.1$ cm corresponds more to $z = 0.7$ cm in our case. A different jet was used in [82], with a smaller nozzle diameter of 1 mm, a lower flow of 1 slm He and powered by 150 ns long 9 kV pulses. The experimentally obtained values for n_e in [82] are 1.5×10^{13} cm^3 at $z = 1$ mm and 2.0×10^{13} cm^{-3} at $z = 5$ mm, that correspond to our experimental n_e at $z = 8.7$ mm and $z = 11$ mm, respectively. Thus, in general the obtained n_e are similar to results from literature, but the experimentally obtained values are higher than the values obtained from the simulations.

To be certain of the validity of the experimental results for n_e and T_e, a number of things has been checked. During the experiments, the laser intensity is constantly monitored, but no irregularities could be found in these results: the laser intensity was approximately constant during all measurements. Also, measurements have been done at the same conditions, but at different times and days. The obtained results are constant within the error bars, thus the measurements are reproducible. In the spectra and fits of all measurements, no irregularities are visible. At least once per day, a calibration of the laser setup is performed: switching the plasma and the helium flow off, a measurement is taken of the ambient air at the position of the jet. Knowing the ratio of N_2 and O_2 in air, this gives us the relation between the intensities of N_2 and O_2 in the total spectrum and their densities. From the measured spectra of that day, the densities of N_2

and O_2 can then be calculated.

An important difference between the simulations and the experiments is the presence of the laser pulse. We have not observed distortion of the plasma by the laser: using (ICCD) imaging


(a)

(b)
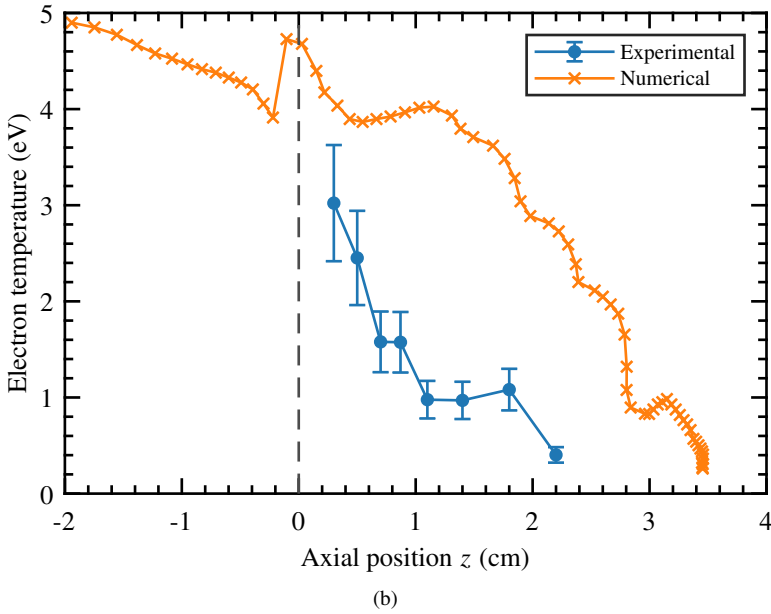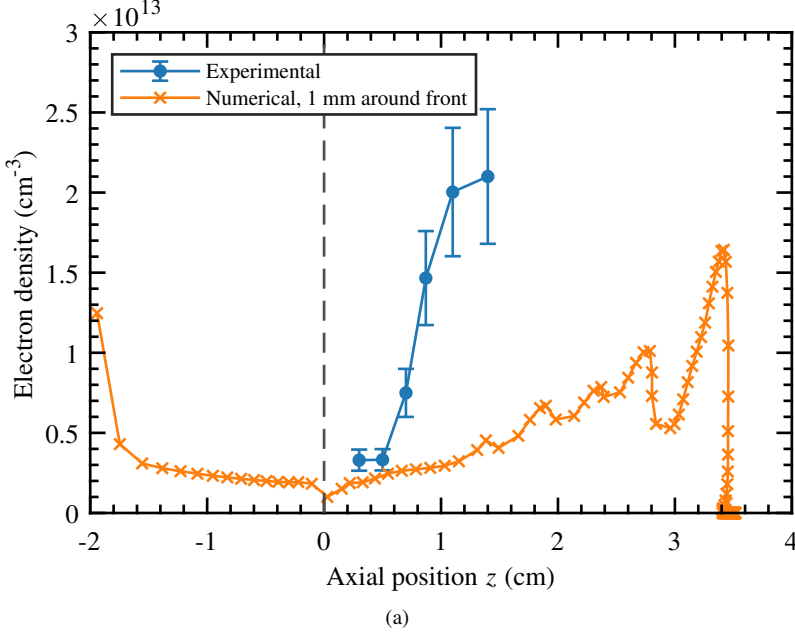
Figure 4.8: a) Electron density, and b) electron temperature, behind the discharge front during propagation in the tube and the plume, in experiments and simulations.

and current-voltage characterization, the plasma looked the same with the laser on as with the laser off. However, according to [119] the high intensity of the laser might ionize Rydberg states, leading to a higher measured n_e in the experiments. To account for the discrepancy of almost one order of magnitude, it would mean that the density of these Rydberg states has to be in the order of 10^{13} cm^{-3}. According to the simulations, the density of helium metastables He* in the jet is in the order of 10^{12} cm^{-3} [35, 101]. Since the Rydberg states have a higher energy level than He*, it is reasonable to assume that their population density would be even lower in the absence of a preferred population channel for the Rydberg states. Therefore, the ionization of Rydberg states cannot account for the one order of magnitude discrepancy. It could also be possible that the laser is photodetaching electrons from O$_2^-$, leading to a higher electron density. However, the density of O$_2^-$ is never exceeding 10^{12} cm^{-3} [101], which is too low to account for the discrepancy.

Another difference is that in the simulations only oxygen species are taken into account and no nitrogen species. N$_2$ is together with He* via Penning ionization an efficient source of electrons. Although O$_2$ takes part in Penning ionization too, it is also efficient in electron attachment. Therefore, the simulations may overestimate the attachment. To account for that difference, simulations have been performed with Penning ionization enhanced by a factor 10 and with attachment decreased by a factor 5. Although the enhanced Penning ionization can increase n_e by a factor 2, these changes cannot reproduce the experimental values of n_e. As argued before, there is also an uncertainty in the memory effect of the discharge.

Further insight into the spatial gradients of n_e and T_e during discharge propagation is ob-
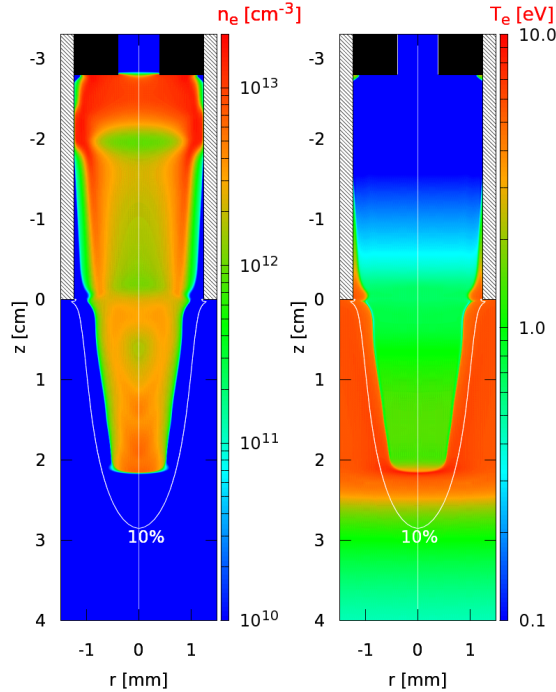
Figure 4.9: Cross sections of the spatial distribution of the electron density n_e and electron temperature T_e from the simulations at $t = 400$ ns.

tained through the 2D spatial distribution of these quantities from simulation results at $t = 400$ ns, represented in figure 4.9. It shows that at each moment, these quantities are highly dependent on the position, both radially (with respect to the center) and axially (with respect to the front). figure 4.10 shows simulation results of the axial profile of E_z, n_e and T_e in the discharge front region at $r = 0$ mm and $t = 500$ ns. It is shown clearly that E_z and T_e are high at the discharge front, but are significantly lower behind the front, in the region where n_e is the highest. Indeed, the maxima of E_z and T_e are both located around $z = 2.85$ cm, while the maximum of n_e is around 0.5 mm behind this position (around $z = 2.80$ cm). These simulation results suggest that the Thomson measurements assess the region behind the front, where n_e is high and T_e is low, and that the measurements in this region are not proportional to the peak of T_e. Behind the front, quasi-neutrality leads to a low electric field and therefore to a low acceleration of the electrons (according to the $-|q_e|\vec{E} \cdot \vec{j_e}$ term in equation (4.1c)). Simultaneously, the higher density of electrons and of molecular gases leads to higher losses of electron energy through collisions (the $-\Theta_e$ term in equation (4.1c)). These factors justify why T_e is higher ahead of the front than behind the front. Moreover, they explain the decrease of T_e behind the front as the discharge propagates along the plume, that is registered in both experiments and simulations in figure 4.8. As $E_{z\mathrm{MAX}}$ increases along the plume (figure 4.7), the electron production increases too and the increase of n_e leads to a decrease of T_e behind the front. The results of figure 4.10 also indicate that the criteria used to choose the locations of the numerical n_e and T_e to compare with experiments in figure 4.8 are appropriate.
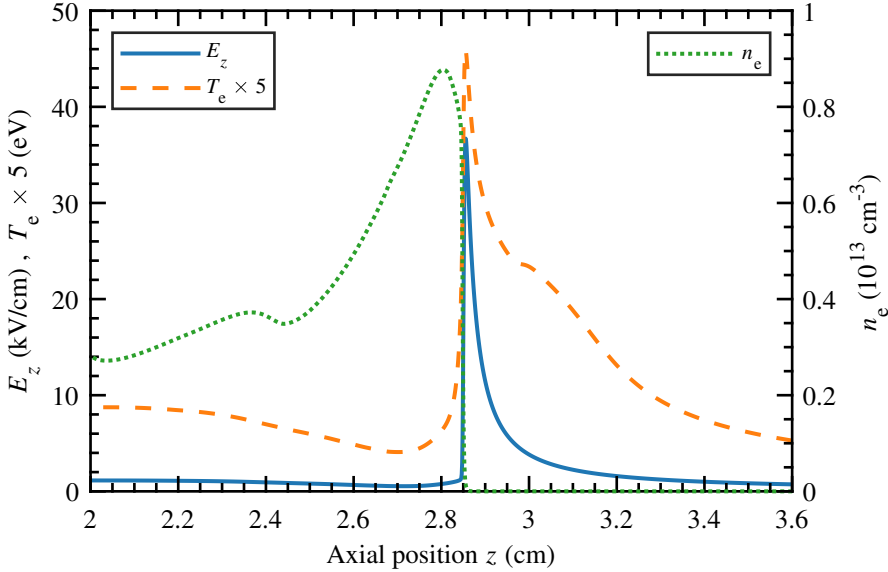
Figure 4.10: Axial profiles of E_z, T_e and n_e at $r = 0$ mm, from the simulations at $t = 500$ ns.
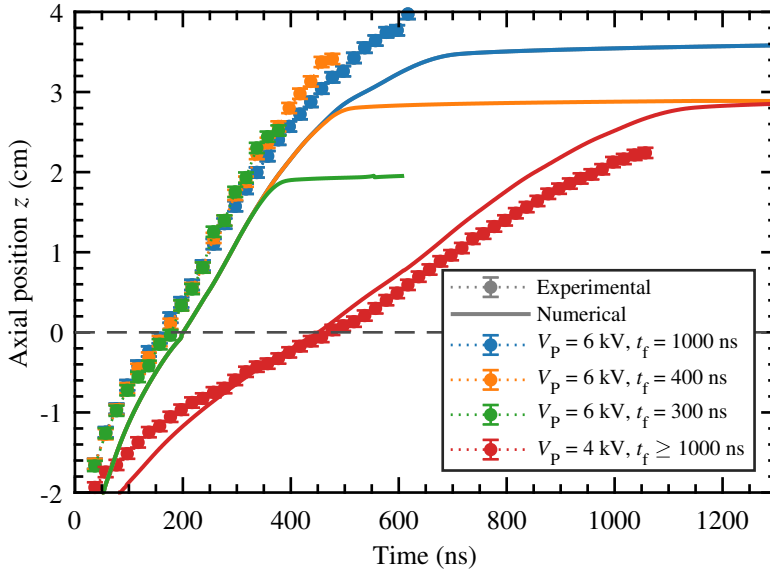
4.3.3 End of discharge propagation

The previous sections have shown that the discharge propagates up to 4 cm after the end of the tube and stops propagating before the end of the applied voltage pulse, both in the experiments and in the simulations. In this section, we change the magnitude of the applied voltage V_P and the

pulse width t_f, and study their effect on the discharge propagation. In [36] these two parameters have been shown to determine the charging time of a jet impacting on a dielectric surface and thus the electric field experienced by the surface. Figure 4.11 presents the temporal evolution of the axial position of the discharge front during its propagation, in experiments and simulations, for $V_P = 6$ kV and pulse width $t_f = 300$, 400 and 1000 ns. Moreover, the case with $V_P = 4$ kV and pulse longer than the time of propagation is also shown. In the simulations, the propagation at $V_P = 4$ kV takes slightly longer than 1000 ns. In the experiments, the propagation ends sooner in this case and is not affected by the fall of the pulse. Thus, to be sure that the fall of the pulse in this case does not interfere with the end of propagation, we have taken $t_f = 2000$ ns instead of 1000 ns in the simulations. In the experiments, the position is obtained by imaging and in the simulations by following the maximum of $|E_z|$ every 1 ns.

In agreement with [36, 96–99], figure 4.11 shows that the discharge with a lower applied voltage propagates slower. Moreover, it confirms through both experiments and simulations the later time of ignition with lower applied voltage reported in [98]. As in the previous section, ignition (time when the discharge has been formed and begins propagating beyond the grounded ring) takes place earlier in experiments than in simulations. It is visible in figure 4.11 that for most cases the difference in experimental and numerical position of the discharge front stays approximately constant, which shows that the velocity of propagation is very similar in experiments and simulations. The length of propagation in experiments and simulations also presents an agreement within 5 mm. With $V_P = 6$ kV, the discharge propagates in every case about 0.5 cm longer in the experiments than in the simulations, while with $V_P = 4$ kV the length of the plume is about 0.5 cm shorter.

Figure 4.11 also shows that the discharge with $V_P = 6$ kV and $t_f = 1000$ ns stops propagating at around $t = 600$ ns in experiments and $t = 700$ ns in simulations. In both cases, the end of discharge propagation takes place during the pulse, when the applied voltage is still 6 kV.

Figure 4.11: Temporal profile of axial position of discharge front during propagation in the tube and in the plume, in experiments and simulations, for several cases of V_P and t_f.

When the pulse is shortened, we observe that the time and position of the end of propagation are also shortened, in both experiments and simulations. In fact, the discharge propagation is the same for every case with $V_P = 6$ kV, until later than $t = t_f$. When t_f is lower than the natural time of discharge propagation, the fall of the pulse of applied voltage forces the discharge to stop propagating, as reported in [98]. Furthermore, decreasing V_P from 6 to 4 kV also leads to a shorter discharge propagation. As happened in [36] with a discharge-target interaction, also the discharge propagation can be controlled through pulse width and magnitude of applied voltage. In figure 4.12 we study the evolution of the electric field on the discharge front for three different cases of V_P and t_f to evaluate its relationship with the end of discharge propagation. The maximum electric field from the simulations is obtained every 5 ns in the region with $r < 0.1$ mm and is averaged over 0.2 mm axially.

Firstly, figure 4.12 shows that in experiments the electric field on the ionization front is approximately the same for different V_P and t_f, all along the propagation, in agreement with [96]. The simulation results show values very close to the experimental ones, except for the 1 cm region after the end of the tube, and also reveal very close electric field values for different V_P and t_f, until the end of discharge propagation. It is shown in figure 4.12 that when the discharge stops propagating, whether during the pulse or after the fall of the pulse, the maximum electric field decreases very rapidly. In fact, the electric field increases during propagation in the plume and then, once the discharge stops propagating, the maximum electric field decreases from about 25 kV/cm to 10 kV/cm in around 100 ns. Hence, the end of discharge propagation is not determined by a slow decrease of electric field in the ionization front. As in [8], we relate the discharge propagation with the electric potential in the discharge front. Figure 4.13 presents the temporal evolutions of the applied voltage (V_{app}) and the electric potential in the discharge front (V_{head}) from the simulations for every case of V_P and t_f. V_{head} is identified by taking the electric potential at $r = 0$ mm and axially 0.5 mm behind the position of the maximum of $|E_z|$.
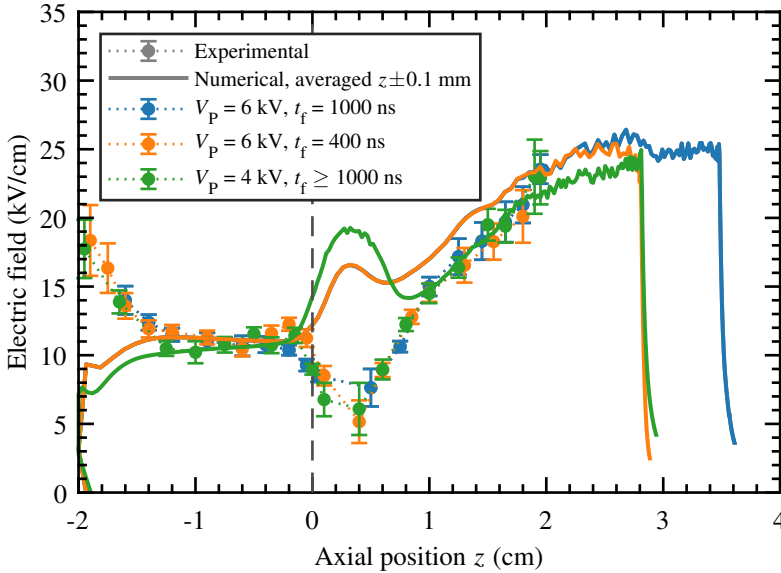

Figure 4.12: Maximum axial component of electric field E_z for $r < 0.1$ mm at the discharge front during propagation in the tube and the plume, in experiments and simulations, for several cases of V_P and t_f.

Thus, V_{head} is at a position in the quasi-neutral plasma channel, and not in the region of charge separation where the gradient of electric potential is very strong.

During propagation, the discharge front leaves a quasi-neutral plasma channel behind, with a low electric field, that connects the potential in the powered electrode to that in the discharge front. Figure 4.13 shows that with $V_P = 6$ kV, the electric potential in the discharge front slowly decreases during the propagation and with $V_P = 4$ kV it stays almost constant until around 1200 ns, which is after the end of propagation. With $V_P = 6$ kV and $t_f = 1000$ ns, the slow decrease continues even after the discharge has stopped propagating at around $t = 700$ ns. Then, in every case, it is visible that the potential in the discharge head is forced to decrease at the end of the pulse. However, figure 4.13 shows that the decrease takes place with some delay, and so does the end of propagation. That delay is variable, as it is shown that the fall of V_{head} after the end of the pulse is slower when V_{head} at $t = t_f$ is lower and thus more losses are present along the channel.

Table 4.1 reports on the parameters of propagation from simulations for several cases of V_P and t_f. For every case of V_P and t_f, the time of end of discharge propagation t_{stop} has been found by identifying the axial velocity of propagation as being $\leq 0.1 \times 10^5$ m/s, with a 10 ns resolution. The axial position of the maximum of $|E_z|$ at $t = t_{stop}$ is called z_{stop}. The electric potential 0.5 mm behind z_{stop}, V_{head}, and the relative density of O_2 in the He-O_2 mixture at $z = z_{stop}$ and $r = 0$ mm have also been found and tabulated. V_{head} in this table provides an estimation of the electric potential in the discharge front required to propagate.

Table 4.1 shows that with short pulses ($t_f < 1000$ ns) the discharge propagation stops always between 90 and 130 ns after the beginning of the fall of the pulse (t_f). With long pulses ($t_f \geq 1000$ ns) the propagation ends during the pulse. It also shows that in the cases with $t_f < 1000$ ns the potential in the discharge front V_{head} at t_{stop} is lower than V_{head} at t_f (figure 4.13), which clearly shows the influence of the fall of applied voltage. In [8] it has been suggested that
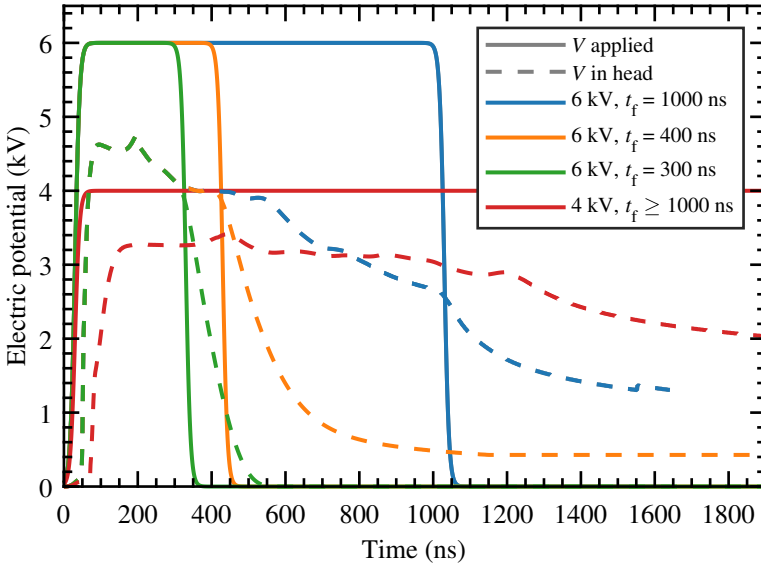
Figure 4.13: Temporal profile of applied voltage and electric potential in discharge front, in simulations, for several cases of V_P and t_f.

Table 4.1: Time, position, electric potential and oxygen relative density in discharge front at $r = 0$ mm at moment of end of propagation, for several V_P and t_f.

V_P (kV)	t_f (ns)	t_{stop} (ns)	z_{stop} (cm)	$[O_2]/N_g$ (%)	V_{head} (kV)
6	300	400	1.90	4.34	1.92
6	400	520	2.80	9.68	2.31
6	600	690	3.44	13.53	2.67
6	1000	700	3.47	13.71	3.23
5	600	730	2.82	9.80	2.34
5	1000	840	3.12	11.62	3.11
4	600	720	1.17	1.04	1.71
4	2000	1130	2.79	9.62	2.87

V_{head} required to propagate is close to 2.75 kV. Here, it is shown that this value is variable and proportional to the relative density of O_2 at $z = z_{stop}$ and $r = 0$ mm. The obtained values are in the same range as the value proposed by [8]. V_{head} required for the discharge to propagate is represented in figure 4.14 as function of the relative density of O_2 at $z = z_{stop}$ and $r = 0$ mm, from all the cases in table 4.1. In fact, with the admixture of O_2, the electron-impact ionization coefficient decreases [93] and the losses of electrons through recombination and attachment increase [34, section III.6]. The peak electric field required to produce free electrons ahead of the discharge front effectively enough to sustain discharge propagation increases along the plume. On the one hand, that electric field is dependent on the electric potential in the plasma. On the other hand, it is generated by charge separation, which is directly affected by the chemistry in the local gas-mixture. Hence, the combination of the two factors determines if a high enough electric field can take place and in which volume it effectively produces free electrons to sustain discharge propagation. The higher the mixing of O_2 in helium, the more difficult it is to obtain the charge separation necessary to produce the required electric field to sustain propagation and thus V_{head} required for the discharge to propagate is higher. Figure 4.14 shows that the relationship between V_{head} required for the discharge to propagate and $[O_2]/N_g$ is approximately linear for the cases where the discharge is forced to stop propagating by the fall of the applied voltage ($t_f < 1000$ ns) and can be formulated as

$$V_{head} = 0.076 \times [O_2]/N_g + 1.606 \tag{4.2}$$

with $[O_2]/N_g$ in % and V_{head} in kV. For long pulses ($t_f \geq 1000$ ns), as the applied voltage still has an influence on the potential in the plasma at the moment when the discharge stops, V_{head} is higher than in equation equation (4.2) but can also be approximately expressed by a linear relationship with $[O_2]/N_g$ in the front:

$$V_{head} = 0.084 \times [O_2]/N_g + 2.087 \tag{4.3}$$

where $[O_2]/N_g$ is again in % and V_{head} in kV. According to equations (4.2) and (4.3), V_{head} thus depends on two parameters: the first is the slope parameter that is controlled by the gas composition and the second is the offset parameter that is related to the potential that is applied to the powered electrode of the jet during the propagation of the ionization wave.
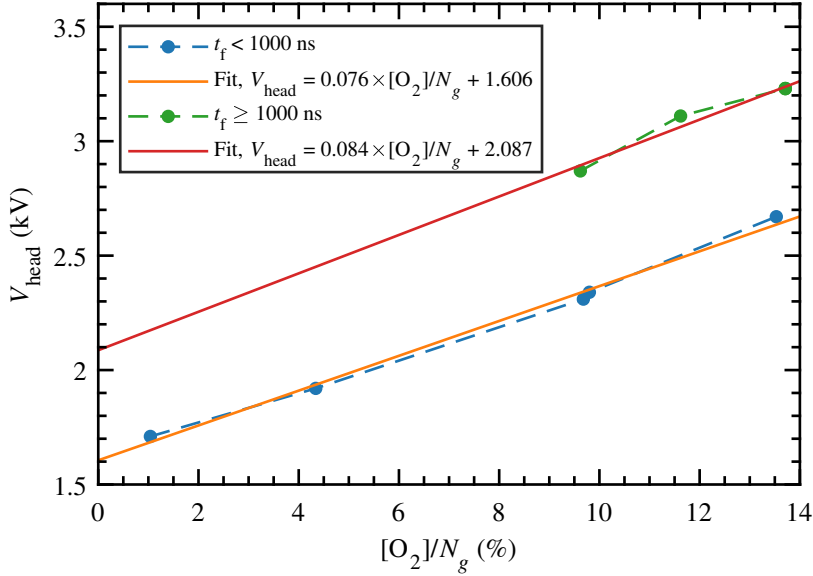
Figure 4.14: V_{head} at $r = 0$ mm and 0.5 mm behind the position of the maximum of $|E_z|$ when the discharge stops, as function of the relative O_2 density at that position, from simulation results. Linear fits of data with $t_f < 1000$ ns and data with $t_f \geq 1000$ ns are also shown, where V_{head} is in kV and $[O_2]/N_g$ in %.

4.4 Conclusions

This chapter quantitatively characterizes a kHz atmospheric pressure He plasma jet without target powered by a pulse of positive applied voltage. It focuses on a quantitative comparison between experimental measurements and numerical results of a two-dimensional fluid model.

Experiments have assessed the distribution of number density of N_2 and O_2 in the plasma plume through rotational Raman scattering and have followed the position and velocity of discharge propagation through ICCD imaging. Moreover, the peak electric field in the discharge front has been measured through Stark polarization spectroscopy and the electron density and temperature behind the front have been measured through Thomson scattering. These results have been compared with those of the two-dimensional model using the same configuration. It has been shown that the gas mixture distribution obtained through flow simulations and used in the plasma model agrees with the one measured. Moreover, an agreement of about 80 % has been obtained on discharge velocity and within 5 mm for the length of propagation for different values of magnitude of applied voltage (4 kV and 6 kV) and pulse width (between 300 and 1000 ns). An agreement with a maximum discrepancy of 11 % has been achieved between simulations and experiments on the axial component of electric field in the discharge front propagating inside the tube, of around 10 kV/cm, and in the plasma plume up to 2 cm out of the tube, where it rises up to 20 kV/cm. The comparison with the simulations suggests that the measured electric field does not correspond to the absolute peak of electric field in the front, but to an average of the axial component of electric field within a distance of 0.1 mm around the axial position of the peak. Moreover, it is the first time that the rise of the electric field in the plume as measured by experiments has been compared quantitatively and agree with results from simulations in the same jet. The comparison of electron density around the discharge

front in the plasma plume has provided the same trends in experiments and simulations, with an increase in the plume, but no quantitative agreement. The measurements show an increase of electron density from 0.4×10^{13} cm^{-3} near the tube nozzle up to 2×10^{13} cm^{-3} at a 1 cm distance, while in the simulations the electron density remains between 0.2 and 0.5×10^{13} cm^{-3} in that region. The electron temperature agrees also qualitatively, with a decrease in the plume. Values of electron temperature of up to around 3 eV near the nozzle down to around 0.5 eV at a distance of around 2 cm have been obtained from the experiments, while the simulations provide values of around 4 eV near the nozzle down to around 0.5 eV at around 3.5 cm from the nozzle. The divergence is attributed to the uncertainty in memory effects between pulses and in plasma chemistry coefficients.

We have shown that the values of electron density and temperature depend highly on the position in the jet where they are measured, since both show large gradients in radial and axial direction. The simulations results suggest that the location where Thomson scattering measures the electron density and temperature is in the quasi-neutral channel behind the front and not inside the high field front. Therefore, the electron density is higher than in the front and increases along the plume, while the electron temperature is lower and decreases along the plume.

Both experiments and simulations have shown that discharge propagation stops during the pulse in the case of long pulses (≥ 1000 ns width) and by the action of the fall of the pulse in the case of shorter pulses (< 1000 ns width). In fact, the length of discharge propagation has been shortened by decreasing the magnitude of applied voltage and by decreasing pulse width. Measurements and simulations have shown that the electric field in the discharge front is invariable with these parameters. Then, the numerical simulations have assessed the temporal evolution of the electric potential in the discharge head for the different cases. This potential slowly decreases during discharge propagation and is forced to decrease faster at the end of the pulse. Propagation stops when the potential in the discharge head is lower than a certain threshold.

The results suggest that this threshold is defined by the gas mixture at the position of the front. In fact, the peak electric field required to produce free electrons ahead of the discharge front high enough to sustain discharge propagation increases with the air admixture along the plume. On the one hand, that electric field is dependent on the electric potential in the plasma. On the other hand, it is generated by charge separation, which is directly affected by the chemistry in the local gas-mixture. Hence, the combination of the two factors determines if a high enough electric field can take place to sustain discharge propagation. The relationship between threshold potential in the discharge head required to sustain propagation and local relative oxygen density has been derived for the cases of short and long pulses.

5

Flow profile and air entrainment in a free helium jet

Abstract: The air entrainment in a free helium plasma jet is assessed using different diagnostics. Flow profiles are visualized by schlieren imaging at different flow rates and turbulence is observed at a large flow rate of 1500 sccm helium. The addition of plasma to helium flow shows the onset of turbulence also at lower flow rates. Number densities of N_2 and O_2 are measured at different radial and axial positions in the jet and no difference in densities is found whether the plasma is applied or not. Likewise, the densities are also found to be independent on the applied voltage pulse when the amplitude was varied between 4 and 6 kV, the duration between 0.16 and 5 μs or the frequency between 0.1 and 5 kHz. Quantitative schlieren imaging is also applied to determine the air density inside the helium jet, but it is found to be insufficiently accurate to yield exact values, although the order of magnitude is correct. Still, the same similarity of the air density on the plasma being On or Off is observed as with the Raman scattering.

5.1 Introduction

It was shown in chapter 4 that the maximum distance the ionization wave in the plasma jet can travel is strongly linked to the local gas composition, since the potential in the ionization front that is needed to sustain propagation depends linearly on the local O_2 concentration. O_2 is present in the helium plasma jet due to the mixing of the helium flow with the ambient air, in which the ionization wave propagates. This chapter focuses on the role of the plasma on the flow profile and the air entrainment in the free helium jet.

The plasma jet is used for many different applications [19, 22, 80] and in most applications, the jet operates in an air atmosphere, which causes mixing of the species from the air (mainly N_2 and O_2) with the gas from the plasma (often a noble gas such as helium or argon). This mixing causes a rich chemistry and the production of reactive oxygen and nitrogen species [120, 121]. The plasma jet transports these reactive species to the target that is used in the applications, where they can react again, depending on the nature of the target. Zhang *et al.* [122] have shown that the air density in the plasma jet influences the production of reactive species such as ozone and atomic oxygen.

It has been shown by Xiong *et al.* [123] that turbulent structures, such as vortices, in the jet can influence the gas mixing of the surrounding air with the supplied noble gas flow. Apart from simulations [123–125] and particle image velocimetry [126, 127], schlieren imaging has been widely used to study the flow and possible turbulence in various plasma jets [28, 32, 125, 128–131] since it visualizes the flow structure. The presence of turbulence has been mainly found in jets with a high Reynolds number and increased turbulence was found when the plasma was turned on with respect to when only the gas flow was applied [123, 125, 128, 130]. On the other hand, also an extension of the laminar flow, thus decreased turbulence, has been found with the application of the plasma [130].

Schlieren imaging has also been used to quantify the air entrainment or the gas temperature in a plasma jet actuator [132], nanosecond discharges [133] and plasma jets [104, 134]. This technique is less widely used, since it needs a precise calibration for which generally simulations have been used. Rayleigh scattering [135] and molecular beam mass spectrometry [136] are other diagnostics that have been used to determine the air entrainment in a plasma jet by measuring, respectively, the air fraction and the density of N_2 and O_2 .

In this chapter, we first asses the flow profile of the helium jet and the presence of turbulence by schlieren imaging. The influence of the plasma as well as the influence of the rate of the applied flow is also studied. Then, the amount of air entrainment in the helium jet and the influence of the plasma on this is determined by rotational Raman scattering by measuring the densities of N_2 and O_2 at different locations in the jet. The schlieren images are used to perform a quantitative analysis, following the method in [104], in order to determine the air fraction in the plasma jet, where the results from rotational Raman scattering are used as calibration method. Furthermore, based on the results of this chapter and chapter 4, the difference in propagation length is studied between the pulsed jet used in this thesis and the same jet powered by AC voltage, using the results from [28]. Finally, the obtained results are placed in perspective by comparing them to results from literature for other plasma jets with different geometries, flow rates and applied voltages.

5.2 Experimental setup

The plasma jet is operated vertically and powered by unipolar positive pulses at a kHz frequency, using the setup of figure 2.1 that was explained in more detail in section 2.1. The applied voltage pulses have an amplitude V_P of $4 - 6$ kV, a duration t_f of $0.16 - 5$ µs and a frequency f of $0.1 - 5$ kHz. The jet is fed by helium flows Q_{He} of 500, 1000 and 1500 sccm.

5.2.1 Rotational Raman scattering

To determine the amount of air inside the helium jet, the number densities of N_2 and O_2 are measured with the Thomson and rotational Raman scattering setup of figure 2.10 that was explained in more detail in section 2.5. In this case, the jet is pointing downwards. The results from the fitting of the Thomson signal are not used in this chapter. Fitting of the rotational Raman signal yields the number densities of N_2 and O_2 . Instead of taking the error from the fit, we take the statistical error in the spread of the values. By taking measurements at different dates at the same position and settings, a spread of 10% is found in the values for the number densities, which is larger than the error from the fit.

Measurements are done with $Q_{He} = 1500$ sccm at the center of the jet along the jet axis and at two axial positions while varying the radial position. Also measurements are done at $z = 8.7$ mm and $r = 0$ mm, while varying V_P, t_f and f.

5.2.2 Stark polarization spectroscopy

To compare the results of different jets, the electric field in the ionization front is also compared. This electric field is measured using the Stark polarization spectroscopy setup of figure 2.7. This setup was also used in chapter 4 and explained in more detail in section 2.4. The only difference is that for the results in this chapter the plasma jet is placed vertically upwards in the setup, while in chapter 4 it was positioned vertically downwards.

5.2.3 Schlieren imaging

Setup

For the schlieren imaging, the setup is used that was shown in figure 2.16 and explained in more detail in section 2.7. Measurements are done at helium flows of 500, 1000 and 1500 sccm and with the jet pointing upwards. Every measurement consists of 1000 frames at 10.34 µs exposure time and is repeated 3 times, whereas the final image is the average of these 3 repeats.

Theory

To quantify the schlieren images, the intensity of the images needs to be correlated to the refractive index. This is done following the analysis described in [104]. We start with the intensity at the knife edge without any schlieren object present I_k, that is related to the background intensity I_0 without schlieren object and knife edge present as

$$I_k(h) = I_0 A(h) \tag{5.1}$$

in which h is the height of the undisturbed beam that is not blocked by the knife edge, normalized by the diameter d of the undisturbed beam, and $A(h)$ the normalized area of the undisturbed

beam that is not blocked by the knife edge. $h = 0$ when the undisturbed beam is fully blocked and $h = 1$ when the undisturbed beam is fully unblocked. Applying trigonometry, $A(h)$ is then given by

$$A(h) = \frac{1}{\pi}\left[\arccos(1-2h) - 2\sqrt{h(1-h)}(1-2h)\right].$$ (5.2)

With the knife edge in place and the schlieren object present, the intensity changes to I, and the beam gets deflected under angle α in the x-direction. At the knife edge, the beam is displaced by

$$\Delta h = \pm \alpha f_3 / D \quad \text{for} \quad \alpha \ll 1$$ (5.3)

where the sign depends on the orientation of knife edge. f_3 is the focal length of lens L_3 in figure 2.16 and D is the diameter of the beam at the knife edge. The height of deflected beam at knife edge is $h + \Delta h$, as schematically shown in figure 5.1. Using equations (5.2) and (5.3), the intensity I of the deflected beam after passing the knife edge, which is the intensity of the image that is captured by the CCD, is then

$$I = I_k(h + \Delta h) = I_k(A(h + \Delta h)) \approx I_k(A(h) + \Delta h\, A'(h))$$ (5.4)

where the approximation comes from a Taylor series of $A(h + \Delta h)$ at h. The contrast C is defined as

$$C \equiv \frac{I - I_k}{I_k}$$ (5.5)

and can be evaluated as

$$C = \frac{I_k(A(h) + \Delta h\, A'(h)) - I_k(A(h))}{I_k(A(h))} = \frac{\Delta h\, A'(h)}{A(h)} = \pm\frac{f_3\, A'(h)}{D\, A(h)}\alpha \equiv S\alpha$$ (5.6)

where equations (5.3) and (5.4) are substituted. S is defined as the sensitivity of the schlieren system. Using equation (5.6) and the expression for the deviation angle [137]:

$$\alpha = \int \frac{\partial n}{\partial x}\mathrm{d}y,$$ (5.7)

in which n is the refractive index, yields

$$C = S\int_{-\infty}^{\infty}\frac{\partial n}{\partial x}\mathrm{d}y = S\frac{\partial}{\partial x}\left(2\int \frac{n(r)r}{\sqrt{x^2 - r^2}}\mathrm{d}r\right)$$ (5.8)

where r is the position along the x-axis that follows the radius of the plasma jet. Equation (5.8) is the x-derivative of the Abel transform of $n(r)S$. Applying Abels inversion formula to equation (5.8) gives

$$n(r) - n_\infty = \frac{1}{S}\int_r^{r_\infty}\frac{C(x)\mathrm{d}x}{\pi\sqrt{x^2 - r^2}}$$ (5.9)

where n_∞ is the refractive index of the surrounding air and r_∞ is the position where $n = n_\infty$. Thus, $n(r)$ can be calculated for $r = 0$ to $r = r_\infty$.
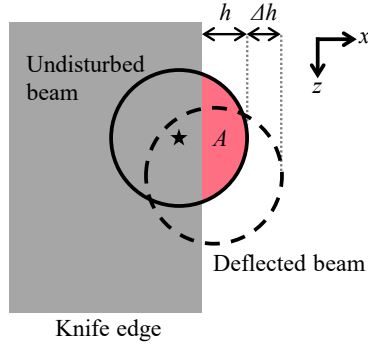
Figure 5.1: Schematic overview of the undisturbed beam and the deflected beam at the knife edge. The star indicates the focal point of the undisturbed beam. h is scaled to the diameter of the undisturbed beam and A is scaled to the total area of the undisturbed beam.

Calibration of the system

The x-position of the knife edge in the schlieren setup needs to be calibrated to calculate h, $A(h)$ and S that are necessary for the analysis of the schlieren images. Therefore, schlieren measurements are performed at various positions of the knife edge in steps of 0.1 mm along the x-axis, to yield the schlieren images I_k. The origin of the axis over which the knife edge is translated, is chosen arbitrarily and all positions are thus with respect to this origin, which is fine since these positions are calibrated to h. The resulting images for I_k are shown in figure 5.2. We now need to determine the position where the beam is fully blocked, which corresponds to $h = 0$, and the position where the beam is fully unblocked, which corresponds to $h = 1$. Since this is not unambiguously visible from figure 5.2, we take the average of the area indicated with the white rectangle at the images in the center column that corresponds to pixels 400 to 500 of the z-direction and pixels 100 to 1250 in the x-direction. This region of interest (ROI) is chosen as to have no influence of the aberrations that are visible at the edges of the images in figure 5.2. In figure 5.3 the average intensity of the area in the images as function of position of the knife edge is shown. From this figure, $h = 0$ is determined to correspond to a knife edge position of 2.50 mm and $h = 1$ to a position of 4.05 mm, meaning the the diameter of the beam D at the knife edge is $D = 1.55$ mm.

The next thing to calculate is $A(h)$, which is done using the trigonometric expression of equation (5.2) as well as by using equation (5.1) where the average intensity over the ROI in image I_k and image I_0 is taken. From $A(h)$, the sensitivity S can be calculated according to equation (5.6) with $D = 1.55$ mm and $f_3 = 45$ mm and the results are shown in figure 5.4 for the two methods of calculating $A(h)$. The discrepancy close to $h = 0$ indicates a discrepancy in $A(h)$ calculated from the average I_k and I_0, since from equation (5.6), S is expected to sharply increase as h approaches zero because $A(h)$ in the denominator also approaches zero then. It can be seen that the two methods do not yield equal sensitivity values and although the difference may seem small, they are actually $20 - 40$ % (except close to $h = 0$) when calculated, which will yield the same variation in the refractive index n as $n \propto 1/S$. Since there are more uncertainties in the calculation of S from the average values of I_k and I_0, we deem the sensitivity as calculated from the trigonometric expression (equation (5.2)) more reliable and therefore we use these values of S in the further calculations.

We are aware that the knife edge is not perfectly placed in the focal point of L$_3$, because the

intensity of the images in figure 5.2 does not decrease uniformly when the knife edge cuts the beam. Instead of searching for the knife edge position where the image has half the intensity of the image when the knife edge does not cut the light beam, we search for the most symmetric image. By taking horizontal cross sections of the schlieren images of figure 5.2, we find that the most symmetric image is obtained at 3.35 mm which corresponds to $h = 0.55$. The measurements of the flow and plasma of the jet are therefore performed with the knife edge at this position and the corresponding sensitivity value is 657.5 .
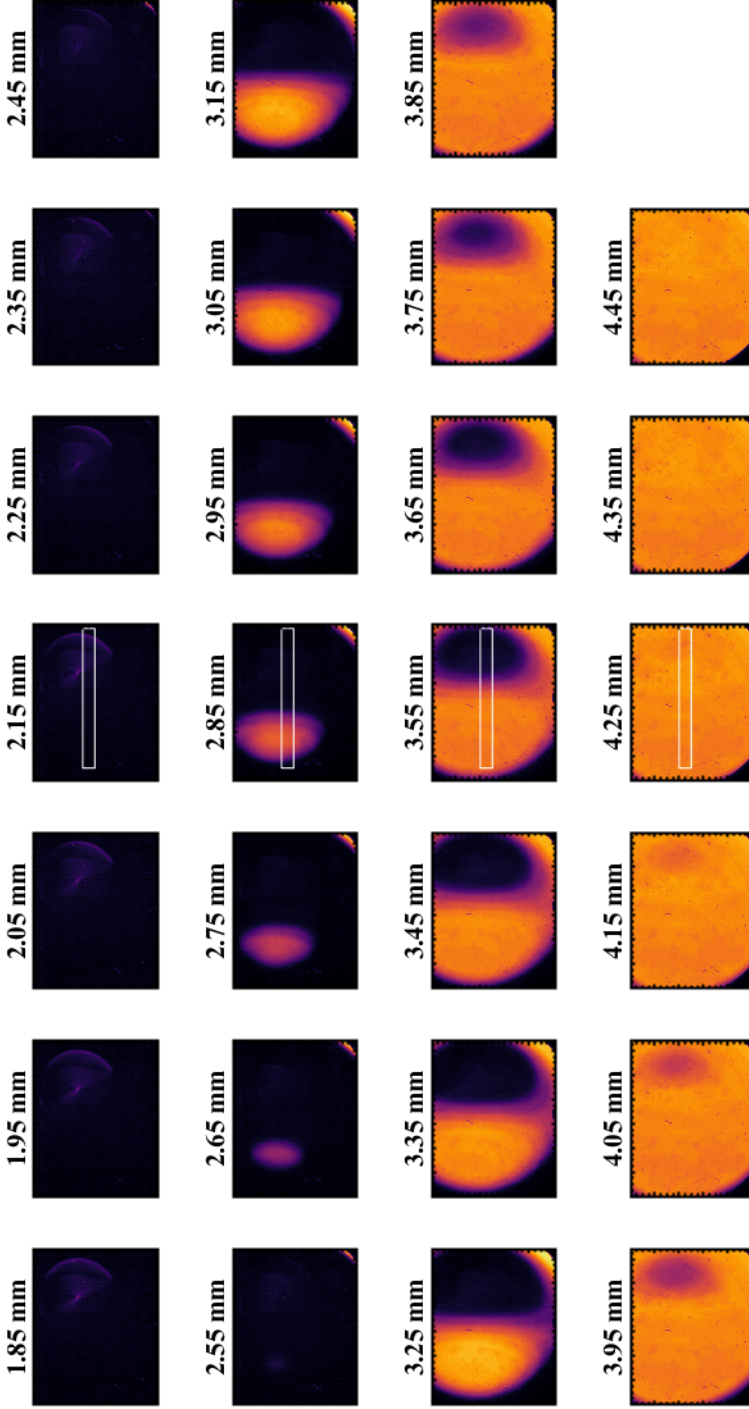
Figure 5.2: Schlieren images I_k at various positions of the knife edge. The vertical axis in the images corresponds to the z-axis and the horizontal axis to the x-axis. The white rectangle at the images in the center column indicates the chosen ROI.
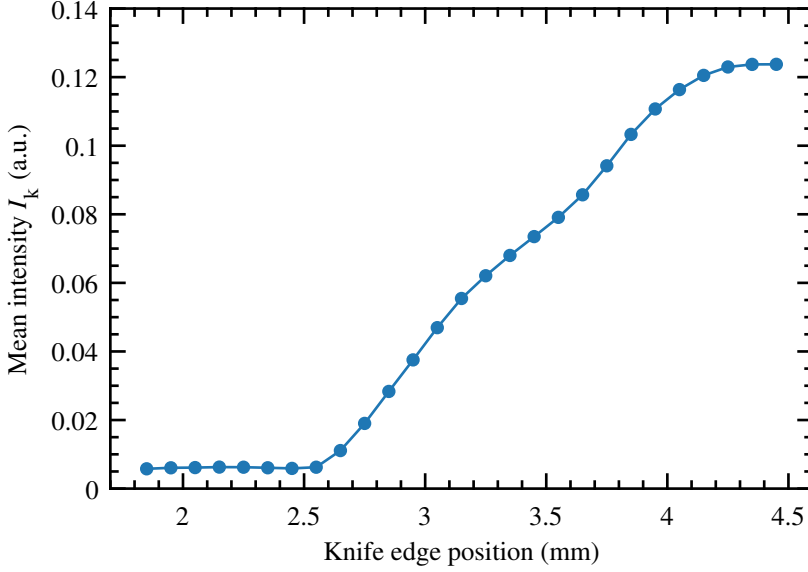
Figure 5.3: Mean intensity I_k as calculated from the images in figure 5.2 for different positions of the knife edge.
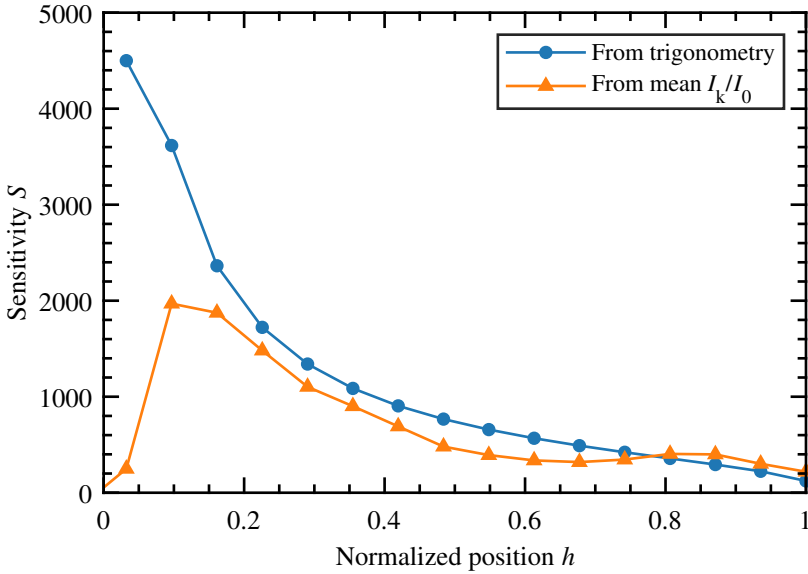
Figure 5.4: Sensitivity of the system as function of the normalized position with $A(h)$ calculated from the trigonometry expression (equation (5.2)) and from the mean intensity of I_k and I_0 (equation (5.1)).

Data analysis

As shown in the previous section, the refractive index can be calculated as

$$n(r) = \frac{1}{S} \int_r^{r_\infty} \frac{C(x)\mathrm{d}x}{\pi\sqrt{x^2 - r^2}} + n_\infty \; . \tag{5.10}$$

From the calibration in the previous section, the sensitivity value of 657.5 was obtained at the position of the knife edge of $h = 0.55$ where the measurements are performed. The contrast C is calculated according to equation (5.5), where I is the image at the desired measurement condition (helium flow without or with plasma present) and I_k the image with the knife edge at the same position but without any flow or plasma present. Image I consists of an average of three measurements at the same condition, that each contain the average of 691 frames. Initially, measurements of 1000 frames were performed, but at plasma On some frames were not saved correctly and thus we take for all measurements the average over the lowest amount of frames that was correct for a certain measurement. Consequently, image I_k is also averaged over 691 frames.

Example images for I, I_k and C are shown in figure 5.5. On the right hand side of the contrast image some artifacts are visible, that are better visible in figure 5.6 where radial cross sections at different axial positions of the contrast are shown. These artifacts are probably caused by the slight misalignment of the knife edge in y-direction or by aberrations from other optical components in the schlieren setup. The integral in equation (5.10) to calculate the refractive index from the contrast image is only taken over half of the profile, since axial symmetry is considered, and therefore we take the left half of the contrast to integrate over, as that part contains no artifacts. r_∞ is then set at 5 mm, since at this position the influence of the flow on the contrast in figure 5.6 seems zero. The corresponding refractive index n_∞ is calculated as function of axial position z from the corresponding air fractions, using the relation equation (5.16) that is derived in the next section. These air fractions come from the results of a COMSOL flow model that will be explained some more in section 5.3.1 where also more results from this model are shown. The integral in equation (5.10) is then solved iteratively for every axial position z (every row in figure 5.5), i.e. we calculate $n(z,r)$, in MATLAB using the *trapz*-function with $\mathrm{d}x = 0.0533$ mm, which is the resolution of the images, and with $0 \leq x \leq r$ and $0 \leq r \leq r_\infty$. The result is a 2D map of the refractive index in the image, which is then transformed into an air fraction map according to the calculation in the next section.
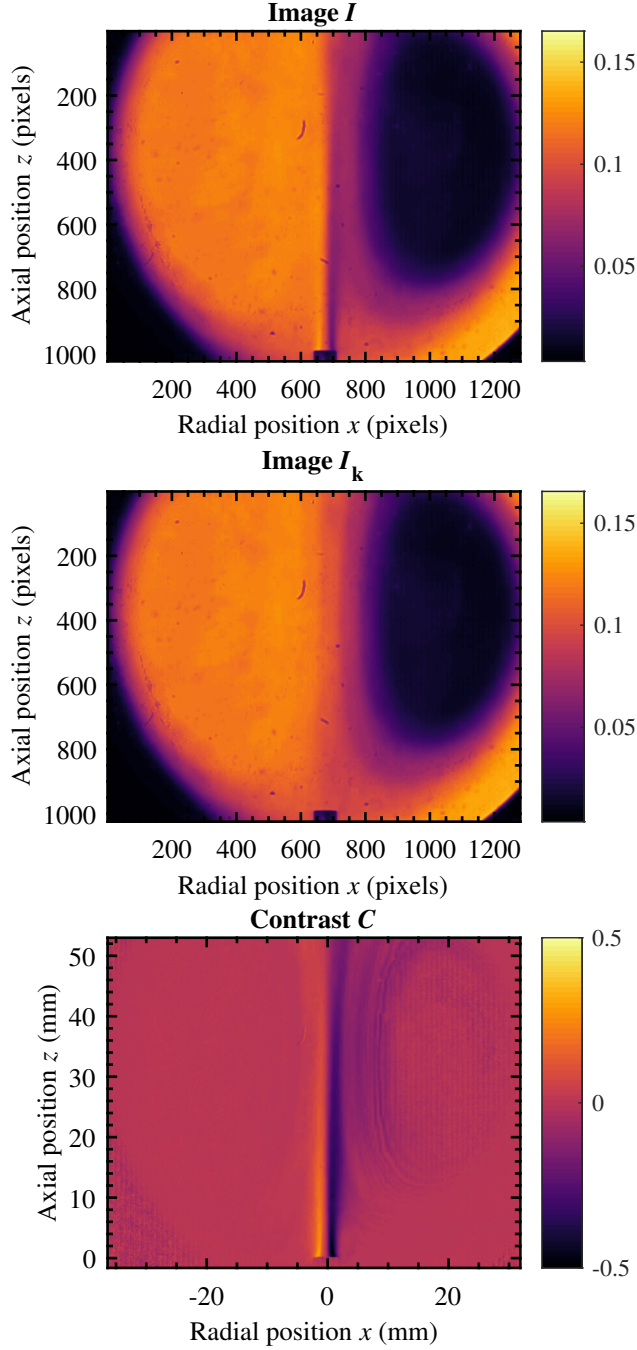
Figure 5.5: Example images I, I_k and the resulting contrast C for plasma Off at $Q_{He} = 1500$ sccm. The exit of the capillary is at $z = 0$ and the flow goes upwards.
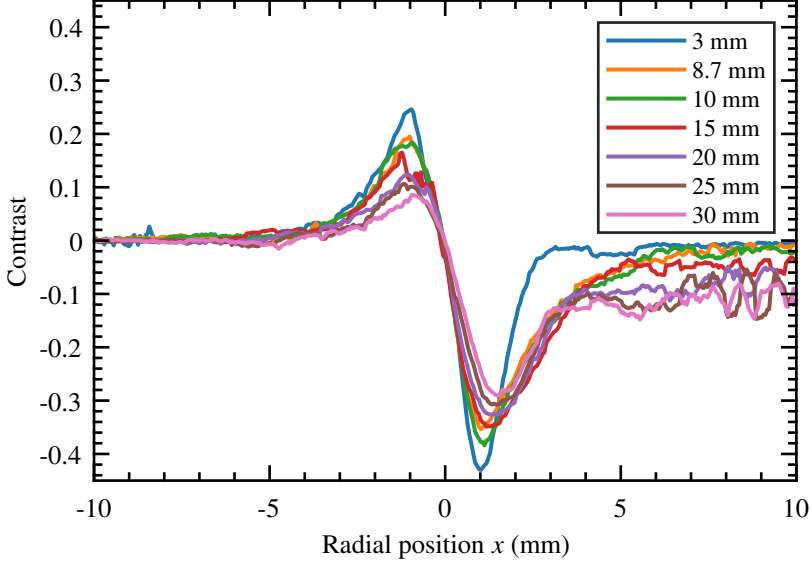
Figure 5.6: Radial profiles of the contrast at different axial positions for plasma Off at $Q_{\text{He}} = 1500$ sccm.

How to calculate the air fraction from the refractive index

The refractive index n of a medium depends on the mean polarizability and number density of the molar species via the Lorentz-Lorentz equation [104]

$$\frac{n^2-1}{n^2+2} = \frac{4\pi}{3}N_{\text{tot}}\sum_i x_i \alpha_i \tag{5.11}$$

in which N_{tot} is the total number density of the gas, x_i the molar fraction and α_i the mean polarizability of species i. The species considered here are helium (He), nitrogen (N_2) and oxygen (O_2). Being an atom, helium has a constant polarizability of $0.205 \cdot 10^{-30}$ [72, 79]. Since nitrogen and oxygen are molecules, their polarizabilities are tensors [72], but since the calculation then becomes too complex, we will approximate them by constants. Rewriting equation (5.11) for the polarizability gives

$$\alpha_i = \frac{3}{4\pi N_{\text{tot}}}\frac{n_i^2-1}{n_i^2+2} \tag{5.12}$$

where n_i is the refractive index for each species i. Using the ideal gas law to calculate the total number density as

$$N_{\text{tot}} = \frac{p}{k_B T_{\text{gas}}} \tag{5.13}$$

at room temperature ($T_{\text{gas}} = 20^{\circ}$C) and atmospheric pressure ($p = 101,325$ Pa) and substituting the corresponding refractive index from table 5.1 for both a pure N_2 gas and a pure O_2 gas in equation (5.11), their corresponding effective polarizabilities are calculated. The resulting polarizabilities are also shown in table 5.1. The feasibility of this procedure has been tested by taking a pure helium gas at atmospheric pressure and room temperature with the refractive index as in table 5.1. The calculated polarizability is $0.2061 \cdot 10^{30}$ m^3, which is 0.6% larger than the value from literature and this is small enough to deem the described method feasible.

The value for the refractive index that corresponds to number densities for N_2 and O_2 as measured with Raman scattering can then be calculated as follows, rewriting equation (5.11) for n:

$$n = \sqrt{\frac{2 \times \frac{4\pi}{3}\left(N_{He}\alpha_{He} + N_{N2}\alpha_{N2} + N_{O2}\alpha_{O2}\right) + 1}{\left|1 - \frac{4\pi}{3}\left(N_{He}\alpha_{He} + N_{N2}\alpha_{N2} + N_{O2}\alpha_{O2}\right)\right|}} \tag{5.14}$$

with $N_i = x_i N_{tot}$ from the Raman results and α_i as in table 5.1.

If we now calculate the fraction of air x_{air} from the same densities as

$$x_{air} = \frac{N_{air}}{N_{tot}} = \frac{N_{N2} + N_{O2}}{N_{tot}}, \tag{5.15}$$

we can obtain a relation between the refractive index n and the fraction of air x_{air}. Figure 5.7 shows the air fraction as function of the refractive index, where Raman results at different plasma conditions are used. A linear fit yields the equation

$$x_{air} = 4141.44970\,n - 4141.58113 \tag{5.16}$$

for the air fraction as function of refractive index that is also shown in figure 5.7 and which will be used as calibration equation to deduce values for the air fraction from schlieren imaging.
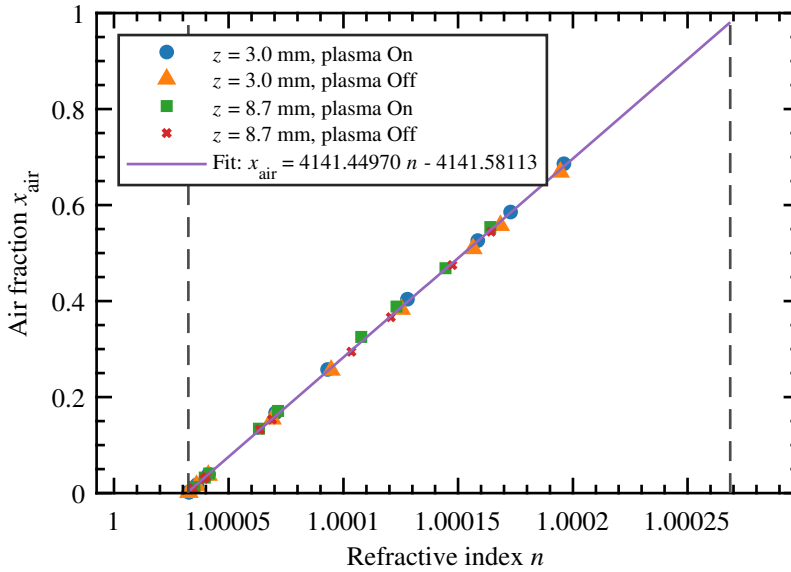
Figure 5.7: Air fraction as function of refractive index for different conditions and a linear fit that is performed on the data points. The left dashed line indicates the refractive index of pure helium, which corresponds to an air fraction of 0, and the right dashed line indicates the refractive index of air, which corresponds to an air fraction of 1.

Table 5.1: Refractive indices of He, N_2, O_2 and air, and the corresponding polarizabilities (either calculated or from literature) at a pressure of $101,325$ Pa, temperature of 20°C and wavelength of 633 nm.

Species	Refractive index	Polarizability (m^3)
He	1.00003246 [138]	$0.2050 \cdot 10^{-30}$ [79]
N_2	1.00027738 [139]	$1.7633 \cdot 10^{-30}$
O_2	1.00025140 [139]	$1.5982 \cdot 10^{-30}$
Air	1.00026855 [140]	$1.7072 \cdot 10^{-30}$

5.3 Results

5.3.1 Helium flow expanding in air

Before studying the influence of the plasma on the flow structure in the jet, let us first take a look at the structure of the helium flow when no voltage is applied. Figure 5.8(a) shows the obtained contrast images for different helium flow rates (500, 1000 and 1500 sccm), where it is visible how the helium flow expands out of the capillary (the black rectangle at the bottom of the image, thus the flow goes upwards) into the ambient air. Since with schlieren imaging refractive index gradients are imaged, in this case caused by the mixing of the applied helium gas with the ambient air, the colors in the images indicate the amount of gas mixing. Next to the capillary there is no color change, since here no flow is applied and only the ambient air is present. In the center of the applied flow at $r = 0$, starting at the exit of the capillary at $z = 0$, mostly helium is present and also no color change is visible. Moving outwards in radial direction, there is a boundary layer where the helium flow mixes with the ambient air, which is visible as a color change in both positive and negative radial direction. As a function of flow rate, it can be seen that the color change in radial direction is more abrupt at larger flow rates and more gradual for smaller flow rates. Already at the exit of the capillary the divergence of the flow is slightly larger at a flow rate of 500 sccm compared to the larger flows, while for larger flow rates the flow is confined over a longer distance in axial direction. This better confinement at higher flow rates is caused by the difference in flow velocity which allows the helium to propagate further along in axial direction without dispersing radially into the ambient air.

The images show an axial range of 5 cm, which is longer than the visible jet length when the plasma is turned On (visible in figure 5.8(b)), but shorter than the full distance over which the helium travels before being fully diluted in the ambient air. The reason for focusing on this part of the helium expansion is to maintain a sufficiently high resolution in the region where the plasma jet is present.

The Reynolds number can be used as a measure for the amount of turbulences in a gas or liquid flow, as it represents the ratio of inertial forces to viscous forces [141]. Since it is dimensionless, it allows for a comparison between our results and results from literature, regardless of the geometry and other properties of the systems being investigated. The Reynolds number is defined as [141]

$$Re = \frac{Lv\rho}{\mu} \tag{5.17}$$

where L is a reference length, v the velocity of the gas, ρ the density and μ the dynamic viscosity of the gas. In the case of our jet, L is equal to the inner diameter of the capillary and v is calculated from the mass flow rate of the helium flow through the capillary. For helium at atmospheric pressure and 300 K (≈ 26 °C), $\rho = 0.16039$ kg m^{-3} and $\mu = 1.9912 \times 10^{-5}$ kg m^{-1} s^{-1}

[142]. The used helium flow rates of 500 sccm, 1000 sccm and 1500 sccm correspond to flow velocities of, respectively, $v = 1.6977$ m/s, $v = 3.3953$ m/s and $v = 5.093$ m/s. Using these values, as well as $L = 2.5$ mm, yields $Re = 34.1862$ for the jet with a helium flow of 500 sccm, $Re = 68.3725$ for 1000 sccm and $Re = 102.5587$ for 1500 sccm.

The absence of turbulence within our setup at the flow rates of 500 sccm and 1000 sccm, as visible from figure 5.8(a), is in agreement with flow simulations carried out by Satti *et al.* [124] that show the first signs of turbulence around a Reynolds number of 90. According to the simulations, vortices may appear outside the capillary at time scales of 100 ms after the initiation of the flow for higher flow rates and thus higher Reynolds numbers [124]. In the presented images at 1500 sccm of figure 5.8(a) no turbulence is visible because the image is averaged over 1000 frames of 10 μm exposure time. However, looking at the individual images, turbulent structures appear at a distance of around 40 mm from the capillary exit, as can be seen in figure 5.9 at the flow of 1500 sccm for plasma Off. These turbulent structures are not present continuously: in some frames they appear, while they are absent in other frames, such as also shown in figure 5.9. In the individual frame images of the lower flows of 500 sccm and 1000 sccm, no turbulence is observed.

A different way to assess the mixing of ambient air with the supplied helium is to look at the air fraction at different positions in the flow. In order to calculate the air fraction, the radial profiles of the N_2 and O_2 densities were measured at two different axial positions ($z = 3$ and 8.7 mm) with rotational Raman scattering at a helium flow of 1500 sccm as shown in figure 5.10(a). There is difference of more than one to two orders of magnitude between the N_2 and O_2 densities around the center at $r = 0$ mm and the densities at $r = 1$ mm (for example at $z = 3$ mm: 1.1×10^{22} m^{-3} O_2 and 3.6×10^{22} m^{-3} N_2 vs. 8.4×10^{23} m^{-3} O_2 and 3.2×10^{24} m^{-3} N_2). In the center of the jet, the densities of N_2 and O_2 are relatively low because there most helium from the gas flow is present, while further away from the center the helium mixes with the surrounding air and thus the densities of N_2 and O_2 increase. This is also illustrated by figure 5.10(b), which shows the air fraction in the flow structure as calculated from the N_2 and O_2 number densities. As we have seen in chapter 4, the amount of air species in the jet is directly related to the potential in the ionization front that is needed to sustain propagation. From $r = 0$ mm to $r = 1$ mm, the air fraction increases to almost 20 %, which according to equation (4.3) means that a potential increase of around 1.7 kV is needed to sustain the plasma in radial direction over more than a millimeter.

The radial profiles of the air fraction at $z = 3$ mm and $z = 8.7$ mm with a helium flow rate of 1500 sccm have been compared in section 4.2.2 (figure 4.3) to results from the static flow COMSOL model of [28], in which the jet pointed downwards. It was shown that the profiles compare accurately, which gives confidence on the validity of the density measurements. In short, the model calculates the air fraction when helium with 1000 ppm air impurities flows from a capillary (with the same dimensions as used in this thesis) into ambient air. More details on the COMSOL model can be found in [28], where the model was introduced. Here, only the resulting 2D air fraction maps (the same as shown in [28]) are used to compare with results from the measurements.
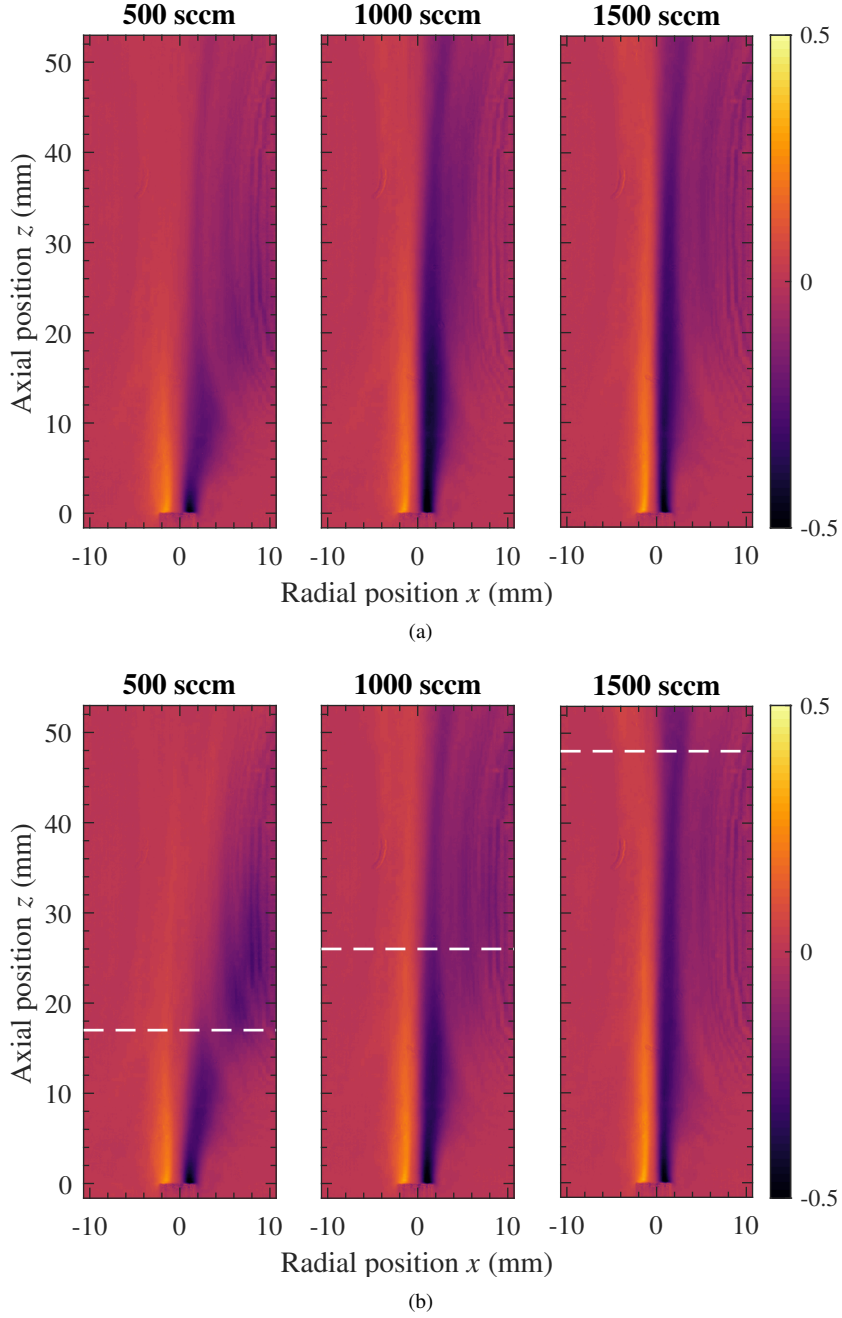
Figure 5.8: Contrast images for different flow rates of He with a) plasma Off and b) plasma On. The white dashed line in b) indicates the visible end of the plasma plume, as determined from ICCD imaging.
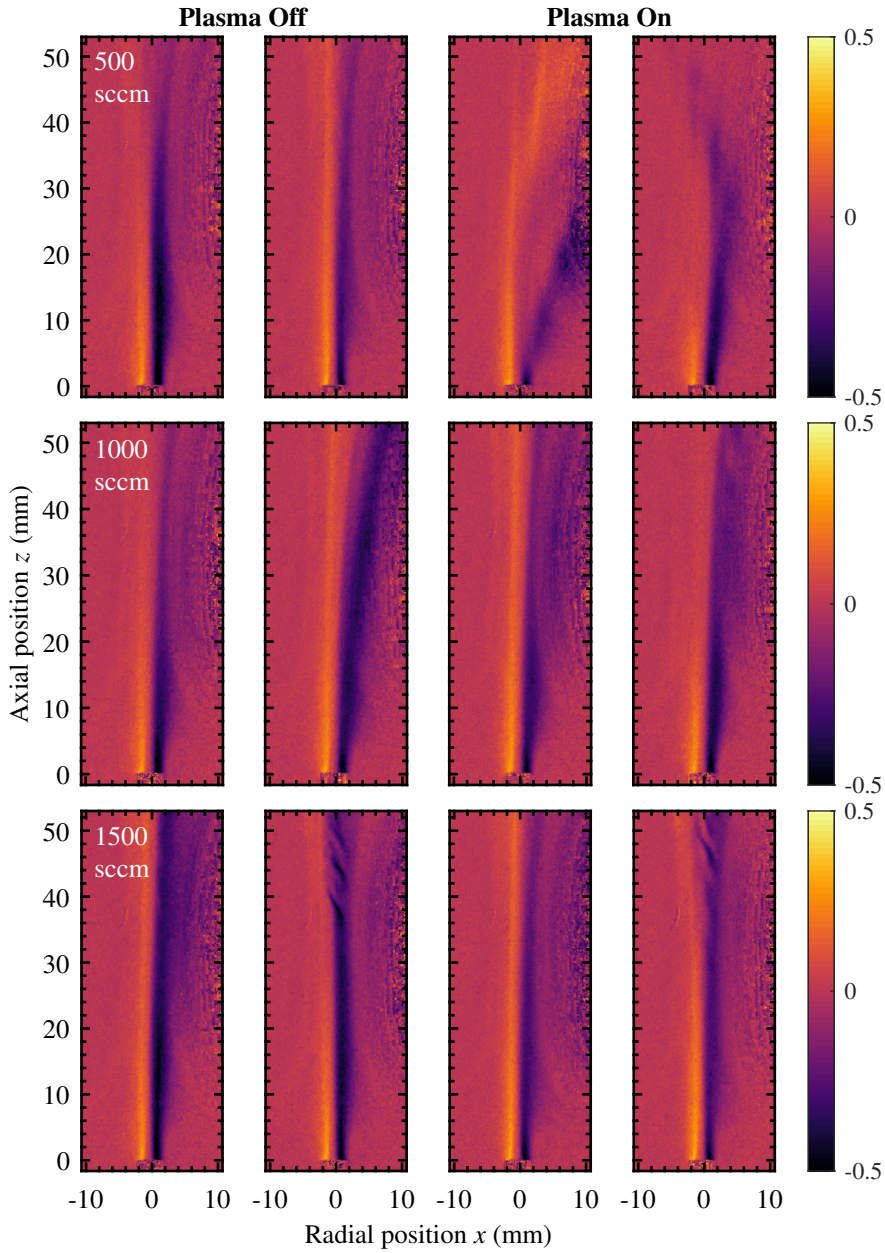
Figure 5.9: Single frame contrast images, taken at random time instants, for plasma Off (left two columns) and plasma On (right two columns) and for helium flow rates of 500 sccm (first row), 1000 sccm (second row) and 1500 sccm (third row).

### 5.3.2 Influence of plasma on the flow structure

In figure 5.8(b), the contrast images are shown for the helium flow when the plasma is turned on. The visible length of the plasma plume, as determined by ICCD imaging like in chapter 4, is indicated by the white dashed line. Comparing the images with figure 5.8(a), the impact of the plasma on the helium flow structure seems negligible. However, when looking at the individual images in figure 5.9 for plasma On, the onset of turbulence is visible at a lower flow rate, for example in the images at 500 sccm. As is the case for the turbulence at plasma Off for 1500 sccm, the turbulence is not visible in all individual images and especially at lower flows, the turbulence is better visible when the individual images are played as a movie then when looking at the individual frames themselves. Nevertheless, the onset of turbulence in the presence of a plasma is in line with earlier observations as shown in [28, 123, 125, 128, 130, 131, 143]. From these images it can also be seen that the length of the plasma plume is not uniquely determined by the distance at which the turbulence starts, since less turbulence is visible at low flow rates, while the plasma plume is shorter, and turbulence is present at a high flow rate of 1500 sccm almost 1 cm before the plasma plume ends.

In the same way as in the previous section, the radial N_2 and O_2 density profiles have been measured when the plasma was turned on, the results of which can be seen in figure 5.10(a). The difference in densities between plasma On and plasma Off is marginal: the density profile at plasma Off is only slightly wider than at plasma On, meaning that slightly less air is admixed in the helium plume when the plasma is Off. The corresponding air fractions are shown in figure 5.10(b) and indicate that within the measured range there is no substantial difference in air entrainment regardless of whether the plasma is turned on or off.

In axial direction the N_2 and O_2 densities have also been measured using rotational Raman scattering for a flow rate of 1500 sccm, the results of which can be seen in figure 5.11(a), but only for the plasma On case. However, since we have seen from the radial profiles that the difference between both cases is negligible for positions close to the capillary exit, we assume that the shown axial profile of the number densities is also applicable to the plasma Off case, at least until $z = 8.7$ mm. It can be seen that the number densities of respectively N_2 and O_2 increase from 4.0×10^{22} m^{-3} and 1.2×10^{22} m^{-3} at $z = 3$ mm to 3.8×10^{24} m^{-3} and 1.0×10^{24} m^{-3} at $z = 22$ mm. This two order of magnitude increase in number density along the axial distance leads to an increase of approximately 20% in the air fraction as shown in figure 5.11(b), which is the result of the dilution of helium by the surrounding air. Meanwhile, the measured ratio between N_2 and O_2 stays approximately constant, as indicated by figure 5.11(a) although always slightly below the ratio in air, indicating that both air species are mixed with the helium in equal measures. The slightly lower fraction of N_2 with respect to air could be a consequence of the difference in diffusion coefficient of N_2 and O_2 in helium, as the diffusion coefficient of N_2 (6.78×10^{-5} m^2/s [144]) is then almost 10 % lower than that of O_2 (7.36×10^{-5} m^2/s [144]). This behavior of the air fraction has also been seen by Klarenaar *et al.* [30].

In figure 5.11(b) axial air fraction profiles are shown for different flow rates, as simulated by the COMSOL static flow model mentioned in section 5.3.1. It can be seen that the air fraction as measured by rotational Raman scattering for the 1500 sccm case does not correspond as well as the radial profiles shown in figure 4.3. Especially for increasing axial positions, the measured air fraction is higher than simulated and corresponds better to the simulated profiles matching lower flow rates. In both the simulations and the Raman measurements, the jet was positioned downwards, which increases the amount of turbulence with respect to the upwards position of the jet. The reason for this is that helium has a significantly lower mass than the surrounding air, causing the helium to drift upwards, making the flow more unstable and more susceptible

to turbulence when the jet is operated in downward position. Turbulence enhances the mixing of air with helium, especially further away from the capillary exit [123], causing the air fraction to increase faster along the axis. However, schlieren measurements of the same jet at plasma

(a)

(b)
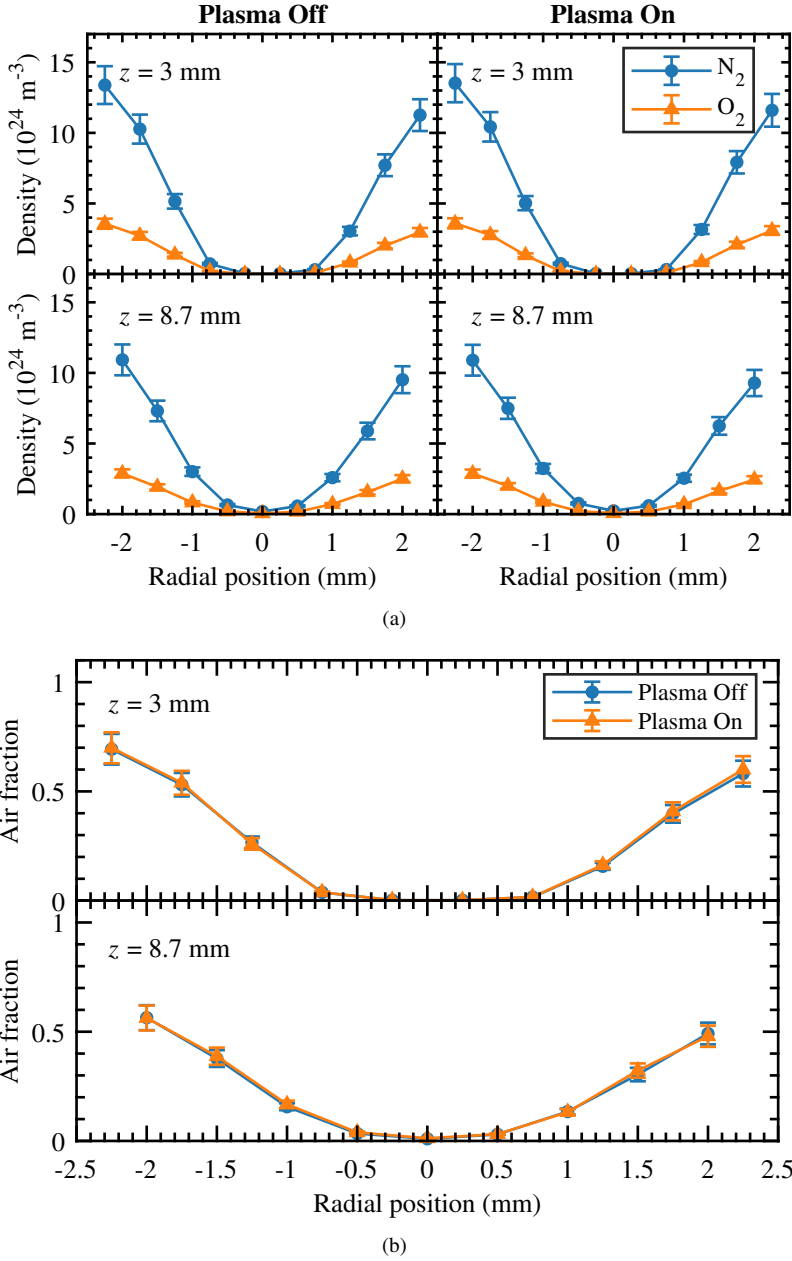
Figure 5.10: Radial profiles at $z = 3$ mm and $z = 8.7$ mm of a) the number densities of N_2 and O_2 as measured by Raman scattering and b) the corresponding air fraction. Both figures show plasma Off and plasma On results and are measured at $Q_{He} = 1.5$ slm.

Off with the jet pointing downwards [32], have shown no turbulence for helium flows up to 1500 sccm in the region $z = 0 - 20$ mm. Turbulence can thus play a role in the air admixing at distances further away from the capillary exit, but not in the region of the Raman measurements ($z = 8.7 - 22$ mm). In the COMSOL model, a large amount of air impurities (1000 ppm [28]) in the helium flow was taken into account, but since the amount of impurities in the plasma jet have not been measured, the actual amount can be lower. This could then be attributed to a larger air fraction in the simulations than measured in the experiments. The Raman results could also have a larger uncertainty than displayed in the figure, due to the fitting procedure. The displayed error bars are calculated from the 10 % error in the N_2 and O_2 densities, resulting from the statistical spread as explained in section 5.2.1, that is larger than the original error from the fit. Nevertheless, the actual error could be even larger due to uncertainties in settings on the Gaussian and Lorentzian part of the individual peaks in the spectrum, for example, that influence the area between the peaks (an example spectrum was shown in figure 2.11), from which eventually the N_2 and O_2 densities are determined [30]. Lastly, the plasma itself could have an influence on the air admixture in the region $z = 8.7 - 22$ mm, although it has no influence in the region closer to the jet exit, which would lead to an increase in the air fraction measured with Raman (at plasma On) with respect to the air fraction from the simulations (at plasma Off).

(a)

(b)
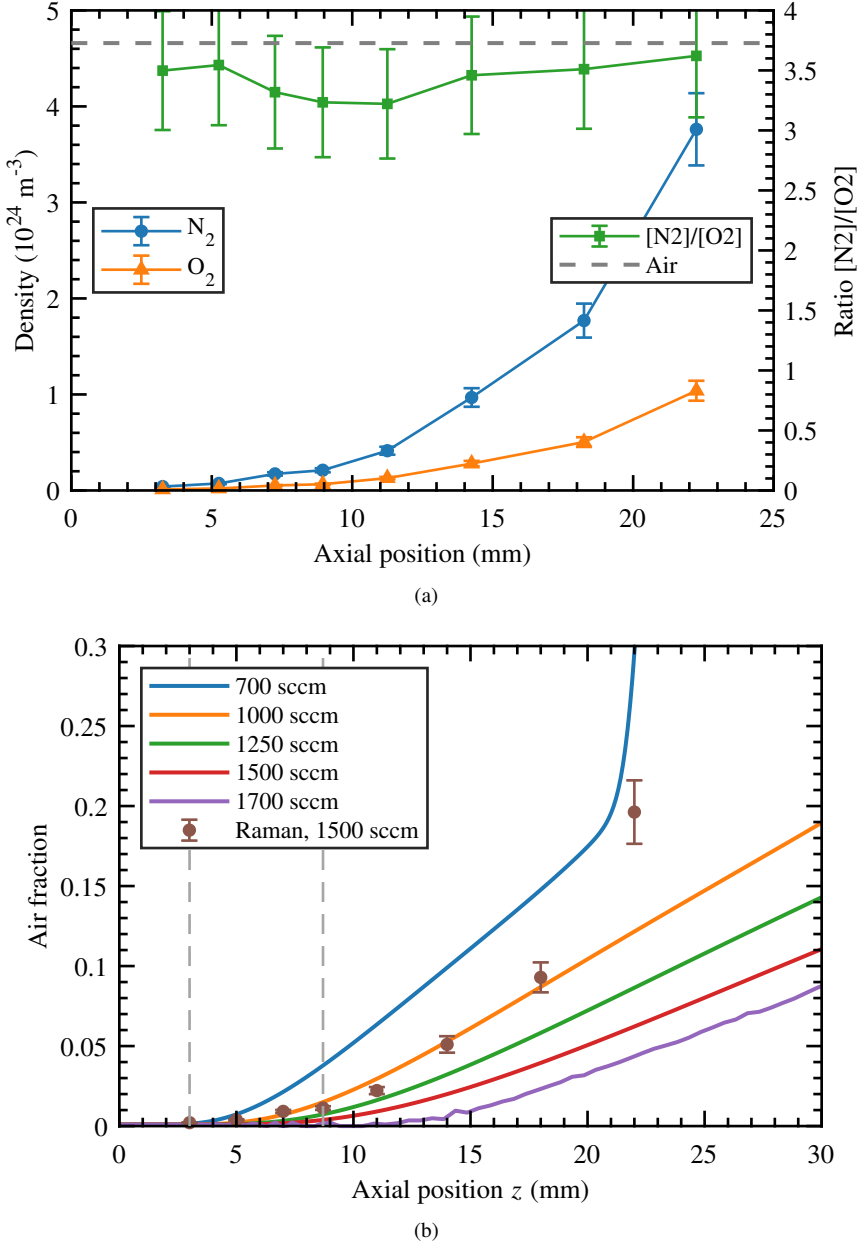
Figure 5.11: Axial profiles of a) the number densities of N_2 and O_2 as measured by Raman scattering, together with the ratio of the N_2 and O_2 densities and b) the corresponding air fraction together with the air fraction for different flows as calculated from flow simulations. In b) the dashed lines indicate the positions at which radial Raman measurements have been performed. The Raman data in both figures is obtained for plasma On with $Q_{He} = 1.5$ slm and at $r = 0$ mm.

5.3.3   Quantitative schlieren results

Figures 5.12 to 5.14 show the radial profiles of the air fraction in the jet at different axial positions as obtained from quantitative schlieren measurements, as well as the corresponding results from the COMSOL simulations, for helium flow rates of 500, 1000 and 1500 sccm, respectively. For all flows, it can be seen that the profiles at the center of the jet are not in agreement with the simulations, while the slope is similar for $r = 1 - 3$ mm. Around the center ($r = 0$) the denominator in equation (5.10) is close to zero, which causes this integral to become extremely large. The increase in air fraction around $r = 0$ mm is therefore due to the fact that the contrast is basically zero there. If the contrast would be better in this region of small refractive index gradients, the eventual values of the air fraction would also be more reasonable. At the flow of 1500 sccm (see figure 5.14) the slopes of the profiles are also similar to the results obtained using Raman scattering. Furthermore, there is almost no difference to be seen between the plasma On and plasma Off cases, as is in agreement with the results from Raman as shown in figure 5.10. As expected, the air fractions at lower flows are higher, because the helium flow has a lower velocity and thus more air admixing takes place.

However, the exact values of the air fraction as obtained from the quantitative schlieren measurements do not compare well to the simulation results and the Raman results within a reasonable error bar of $10 - 20$ %. It can therefore be concluded that the quantitative schlieren method in its current shape is not accurate enough to yield air fraction values that are more precise than being of the correct order of magnitude.
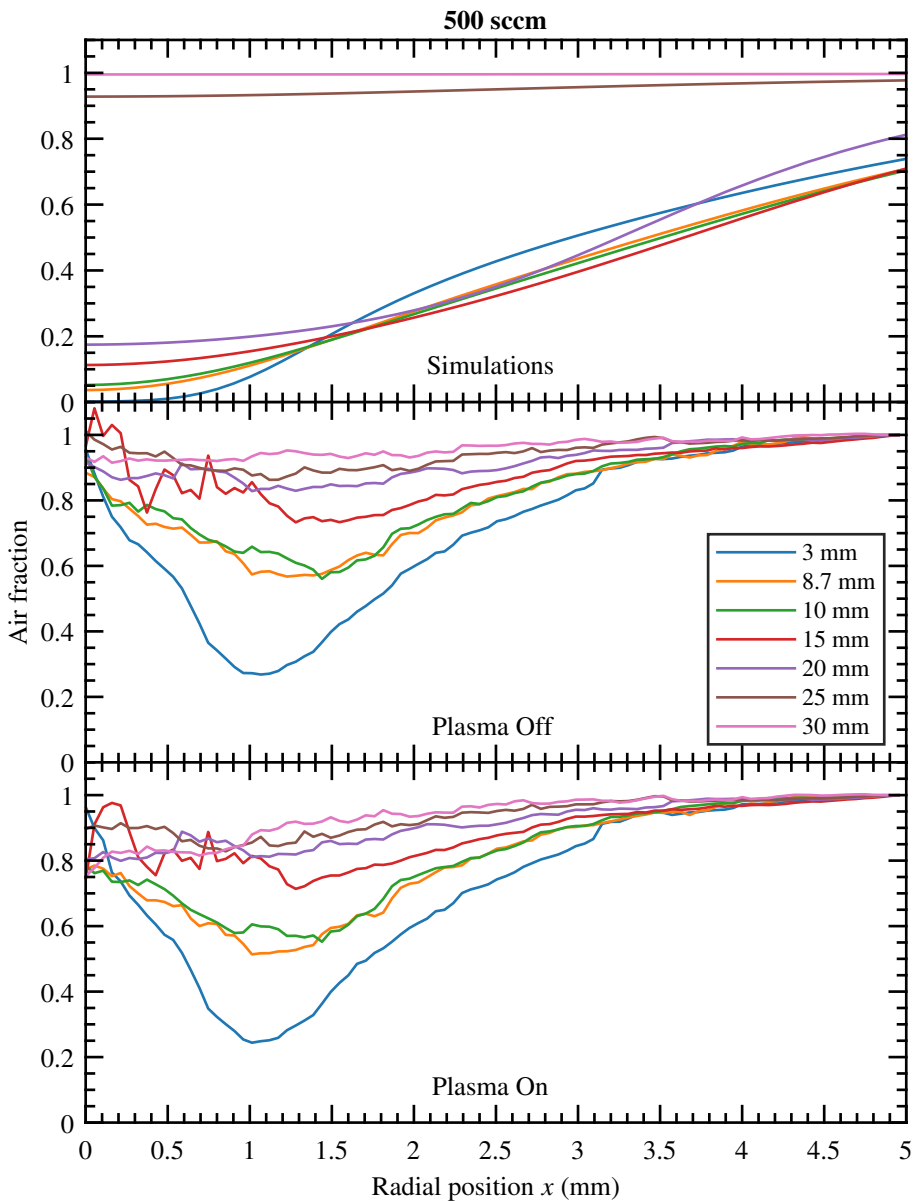
Figure 5.12: Radial profiles of the air fraction in the jet for a helium flow of 500 sccm as obtained from the model (top figure), for plasma Off from schlieren (middle figure) and for plasma On from schlieren (bottom figure).
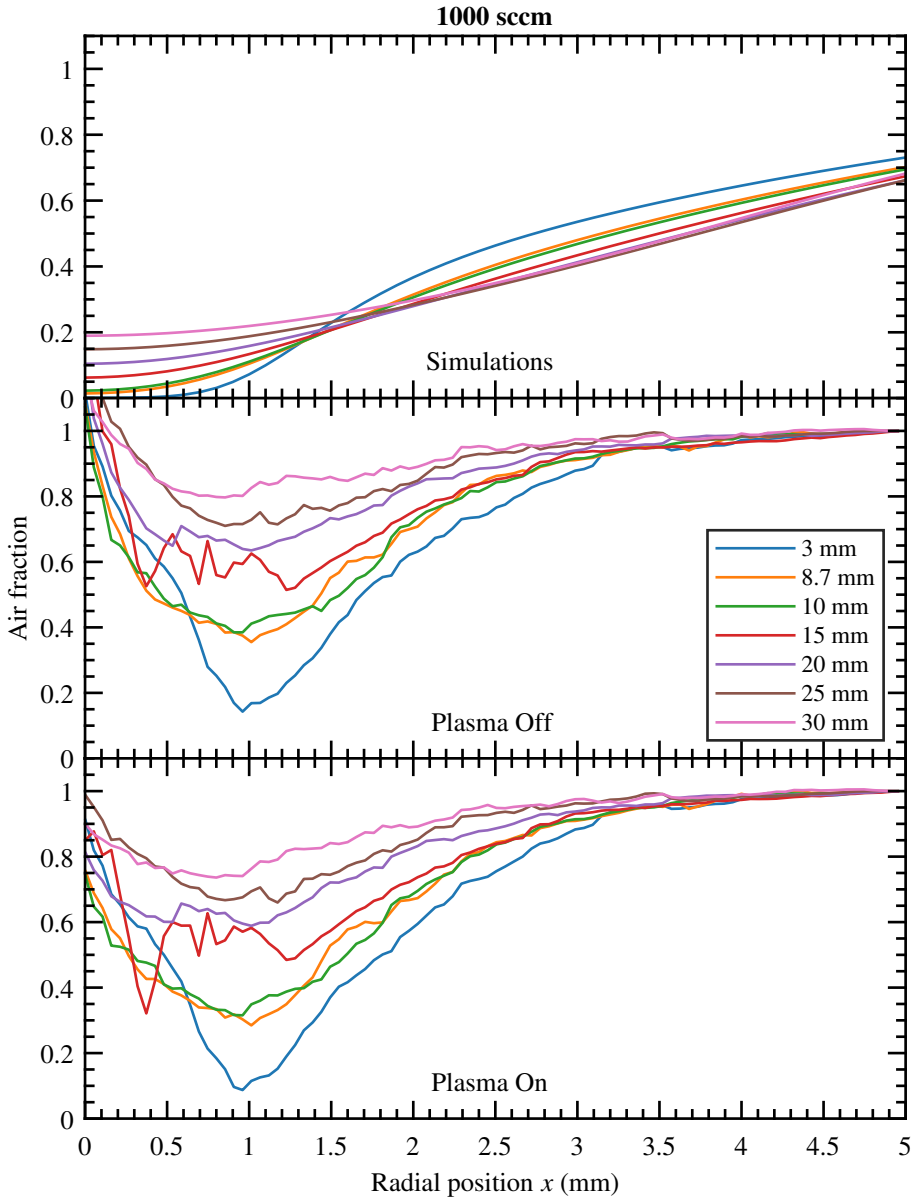
Figure 5.13: Radial profiles of the air fraction in the jet for a helium flow of 1000 sccm as obtained from the model (top figure), for plasma Off from schlieren (middle figure) and for plasma On from schlieren (bottom figure).
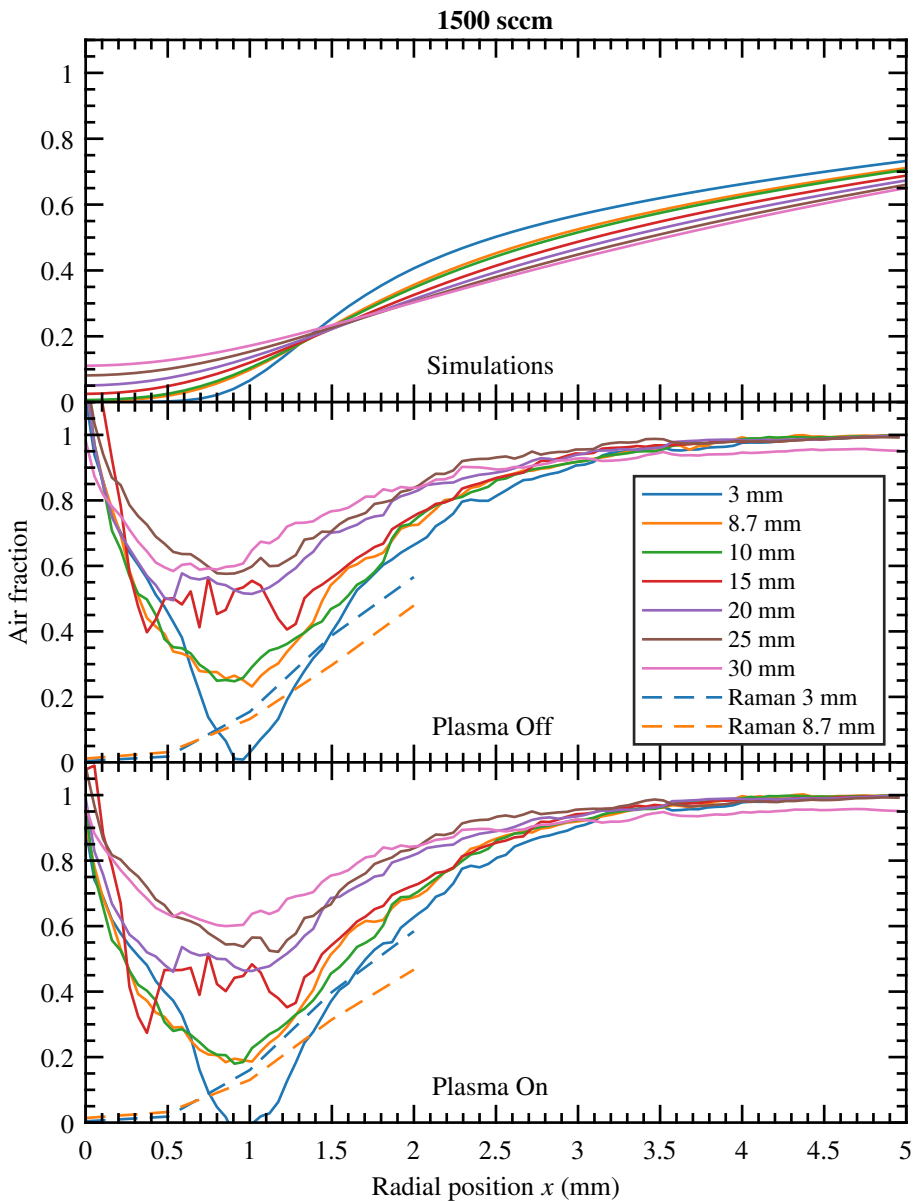
Figure 5.14: Radial profiles of the air fraction in the jet for a helium flow of 1500 sccm as obtained from the model (top figure), for plasma Off from schlieren (middle figure) and for plasma On from schlieren (bottom figure).

5.3.4 Influence of applied voltage pulse

Figure 5.15 shows the dependency of the density of N_2 and O_2 and the air fraction on the a) amplitude, b) frequency and c) pulse length of the applied voltage as measured by Raman scattering at $z = 8.7$ mm and $r = 0$ mm with $Q_{He} = 1500$ sccm. From these figures it can be seen that the densities of N_2 and O_2 have constant values of about 2×10^{23} m^{-3} and 0.8×10^{23} m^{-3},
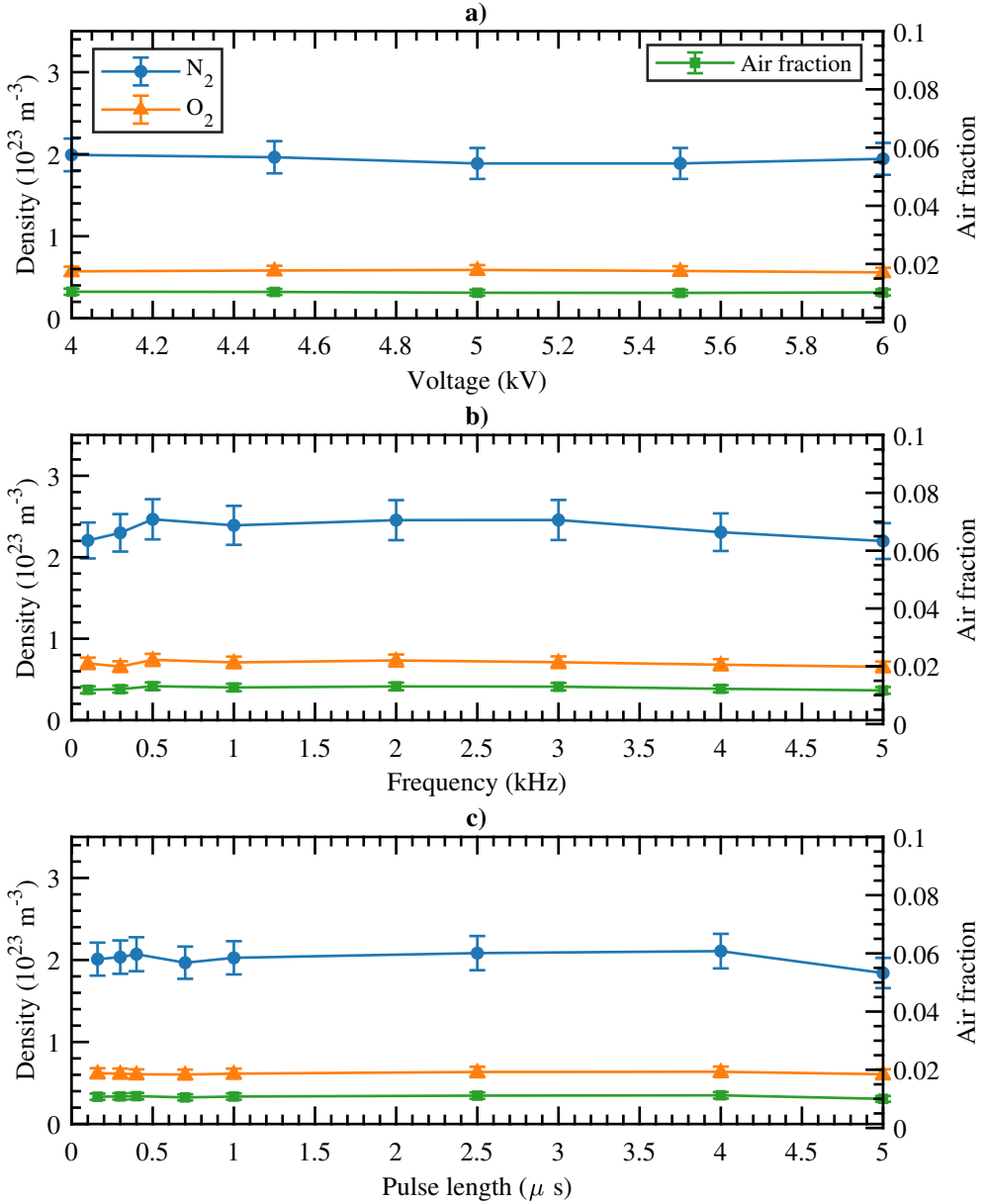
Figure 5.15: Number densities of N_2 and O_2 at $z = 8.7$ mm and $r = 0$ mm with $Q_{He} = 1500$ sccm measured by Raman scattering, as function of a) voltage, b) frequency and c) pulse length.

respectively, when the amplitude, frequency and pulse length of the applied voltage are varied. The air fraction is approximately 1 % and also does not change with varying voltage pulse amplitudes, frequencies and lengths. The flow model shows an air fraction of approximately 0.4% at $z = 8.7$ mm and $Q_{He} = 1500$ sccm (figure 5.11(b)), which is slightly lower.Thus, the air fraction and the N_2 and O_2 densities are independent of the shape of the applied voltage pulse, in the range that was measured here and within the error bars of the Raman measurements. This corresponds to the results from figure 5.10, where was shown that the radial profile of these densities and the air fraction at different axial positions barely changes whether the plasma is on or off, i.e. whether there was an applied voltage or not.

5.4 Discussion

5.4.1 Comparison with literature

To place the results found here in perspective, they are compared to results reported in literature for jets with different geometries, applied voltages and flow rates.

Turbulence

The distance at which the turbulence starts in this thesis at a helium flow rate of 1500 sccm is compared with turbulent jets from literature of Xiong *et al.* [123], Oh *et al.* [128], Morabit *et al.* [127], Robert *et al.* [130], Papadopoulos *et al.* [125], Boselli *et al.* [131], Sobota *et al.* [28], Zheng *et al.* [143] and Xian *et al.* [145] and the result is summarized in figure 5.16, where closed symbols correspond to jets with plasma On and open symbols to plasma Off. All jets are operated vertically, except for the jet of Papadopoulos *et al.* which is operated horizontally. There is no quantitative relation that unifies all data points in this figure, which implies that the Reynolds number alone does not determine at which position the jet becomes turbulent. The Reynolds numbers in figure 5.16 are calculated with equation (5.17), but the used values for the gas velocity v, gas density ρ and dynamic gas viscosity μ are only valid at the exit of the capillary, since v depends on the position in the flow as was shown in [125] and both ρ and μ are temperature dependent [142]. To compare the results of the different jets more correctly, the Reynolds number could be plotted as function of axial position or as function of position where the turbulence starts. This is however not possible with the available data.

Still, some qualitative conclusions can be drawn from the current results in figure 5.16. The presence of a plasma shortens the laminar flow length when a laminar flow was present at plasma Off (which was not the case for $Re = 213.7$ of Robert *et al.*), as shown by the results of Papadopolous *et al.* , Robert *et al.* , Oh *et al.* , Zheng *et al.* , Sobota *et al.* , Boselli *et al.* and Xian *et al.* . An increase in Reynolds number leads to a shorter laminar flow length as shown by the results of Papadopolous *et al.* , Robert *et al.* , Boselli *et al.* and Xiong *et al.* , except for this particular case of Robert *et al.* again and for the plasma Off case of the horizontal jet Papadopoulos *et al.* where the impact of the buoyancy force is lowered at larger Reynolds numbers which leads instead to a longer laminar flow length. The jet used in this thesis is relatively stable compared to the other jets, because around the same Reynolds number, the jets of Papadopoulos *et al.* , Morabit *et al.* and Robert *et al.* at plasma On show turbulence closer to the capillary, meaning that they have a shorter laminar flow length. On the other hand, the jets of Robert *et al.* , Papadopoulos *et al.* and Zheng *et al.* at plasma Off have a longer laminar length than the jet of this thesis and are thus stable at a longer distance. The differences between
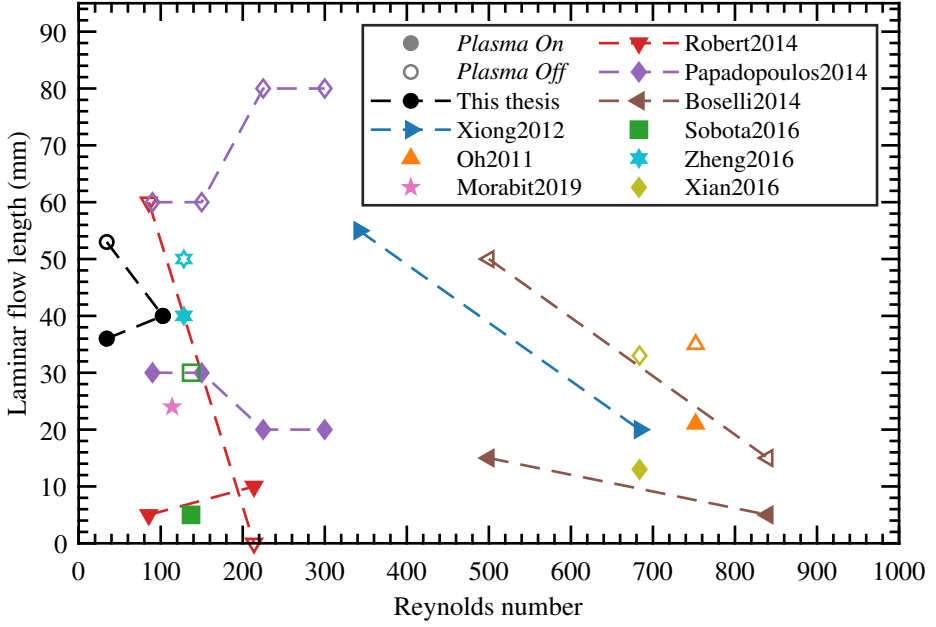
Figure 5.16: Position from the end of the capillary where the turbulence starts as function of the Reynolds number for different jets from literature and the jet from this thesis. Results for plasma Off cases are shown as open symbols and plasma On cases as closed symbols.
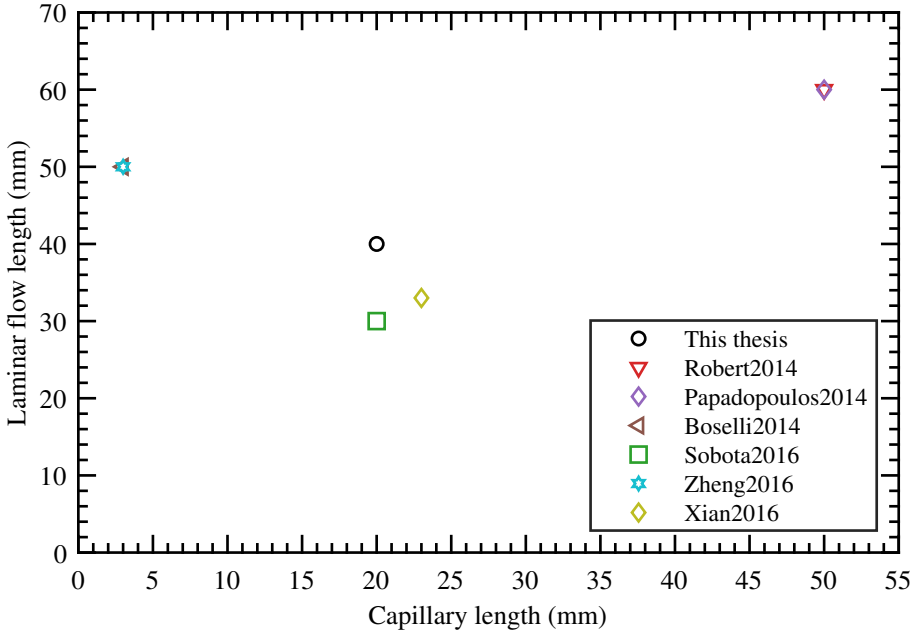
Figure 5.17: Laminar flow length at plasma Off as function of the capillary length for different jets from literature and the jet from this thesis.

the jets are that the jet of Papadopoulos *et al.* is operated horizontally and thus the buoyancy force of the helium species that are much lighter than the air species plays a significant role in the formation of the flow profile. Robert *et al.* have shown that the length of the capillary could have an influence on the laminar length of the jet, since the laminar length doubled for $Re = 85.47$ and $Re = 213.7$ both at plasma Off and at plasma On when the length of the capillary was increased from 5 cm to 15 cm. However, since in the case of the 15 cm long capillary also a metallic target was placed at 4.5 cm from the nozzle, this could have an influence on the flow too and thus the result is not unambiguous. For the jets of figure 5.16 from which the length of the capillary is known, the laminar flow length at plasma Off is shown in figure 5.17 as function of this capillary length. There are not enough data points to be certain of a direct relation between these two lengths, especially since the data points for Sobota *et al.* and Boselli *et al.* show merely the minimum laminar flow length, since the actual length was out of the range in the measurements [28, 131]. Nevertheless, it can be seen that long laminar flow lengths are achieved at both short capillary lengths (3 mm) and long lengths (50 mm), while intermediate capillary lengths (around 20 mm) yield a slightly shorter laminar flow. Furthermore, the jets of Boselli *et al.* and Zheng *et al.* have different Reynolds numbers, but a similar capillary length and a similar laminar flow length. The same holds for the jets of Xian *et al.* with respect to the jet of this thesis and Sobota *et al.* . This indicates that the length of the capillary indeed has an influence on the laminar flow length, but we are yet unable to quantify this influence as other circumstances could also play a role. Other differences between the jets that could have an influence are the amount of impurities in the applied helium flow, the humidity of the ambient air, the vertical orientation of the jet being upwards or downwards and the gas temperature of the jet and the surrounding air.

Air densities

Van Doremaele *et al.* [135] measured normalized air densities by Rayleigh scattering in a helium plasma jet, with inner diameter of the capillary of 2 mm and powered by 500 ns long pulses of 4.5 kV at 5 kHz with 1.5 slm helium, that interacts with a dielectric target at a distance of 5 mm and that has a metallic ground at the back. It can be calculated that the Reynolds number for this jet is $Re = 128.2$, which is slightly higher than for our jet at 1.5 slm He, due to their narrower capillary. The target may have an influence on the exact values and the flow profile, but the general shape of the obtained profiles are similar: the lowest air density in the center and an increase towards the sides. At plasma Off, their air fraction values are approximately 40 % lower than in our case, probably due to the high back reflection of the helium flow on the target that is placed very close to the capillary. However, at plasma On between $z/d = 0.75$ and $z/d = 2$, which are axial positions from the exit of the capillary normalized on the diameter d of the capillary, their normalized air density increases from around 0.05 at $r = \pm 0.5$ to around 0.5 at $r = \pm 2$ mm. This radial increase in value corresponds well to our air fraction between $z/d = 1.2$ and $z/d = 3.5$ from $r = \pm 0.5$ mm to $r = \pm 2$ mm. Thus in [135] the plasma has a larger impact than in our case, which can be explained by the applied power to the plasma that is almost three times higher in their case. The effect of the dissipated power on the behavior of the plasma jet is discussed in the next section.

Dünnbier *et al.* [136] have measured densities of N_2 and O_2 by molecular beam mass spectrometry (MBMS) in an argon plasma jet with an inner diameter of the capillary of 0.8 mm that is RF-powered at 1.1 MHz with 2 kV voltage and with a 3 slm argon flow. They have also obtained an increase in N_2 and O_2 densities as function of axial position, from around 4×10^{24} m^{-3} N_2 and 1×10^{24} m^{-3} O_2 at $z = 10$ mm (corresponds to $z/d = 12.5$) to around 12×10^{24} m^{-3} N_2

and 3×10^{24} m^{-3} O$_2$ at $z = 35$ mm (corresponds to $z/d = 44$). These values are higher than in our case and the increase is also less rapidly, but this might be due to differences in geometry, applied voltage (MHz AC vs. kHz pulsed), gas flow (argon vs. helium) and gas temperature between the jets. Helium is lighter than argon and air, thus it may diffuse easier upwards, which could be the reason why the increase in N$_2$ and O$_2$ density is steeper in the helium jet than in the argon jet.

5.4.2 Comparison with a sinusoidal (AC) jet

Sobota *et al.* have studied the influence of flow on plasma parameters in a jet with the same geometry as the jet in this thesis, but with an AC applied voltage with a peak-to-peak value of 4 kV at a frequency of 30 kHz [28]. We will now compare those published results to the results obtained for the pulsed jet of this thesis. It is important to point out that the lowest flow for the AC jet is 700 sccm helium, while 500 sccm is used for the pulsed jet. These are the closest low flow rates possible to compare, but this difference will be kept in mind during the comparison. Another difference between the AC and the pulsed jet is that the AC jet is operated downwards, while the pulsed jet is operated upwards for the discussed comparison. Similarly to the diagnostics in this thesis, but not in the exact same setups, ICCD imaging was used to determine the length of the visible plasma plume and Stark polarization spectroscopy to determine the electric field at the head of the ionization front, both for different helium flow rates.

Electric field

Figure 5.18 shows the electric field as function of axial position for different flow rates and for both jets. Within the corresponding measurement range, the electric field is the same in the AC jet as in the pulsed jet when the same helium flow is applied, even though the applied voltage is different: sinusoidal waves with an amplitude of 2 kV at a frequency of 30 kHz for the AC jet and square pulses with an amplitude of 6 kV, a length of 1 µs at a frequency of 5 kHz for the pulsed jet. This may seem surprising, but looking back at the results of section 4.3.3, we found a relation between the potential in the ionization front that is necessary to sustain the discharge propagation and the amount of oxygen present at that location (equations (4.2) and (4.3) and figure 4.14). In section 5.3.4 and figure 5.10(a) it was shown that, close to the exit of the capillary, the N$_2$ and O$_2$ densities in the jet do not vary with amplitude, frequency and length of the applied voltage pulse within the tested range or when the plasma is on or off. Therefore it is reasonable to assume that the AC jet and the pulsed jet have the same flow composition. Then, since the flow rates, thus flow velocities, and the flow composition within the measured range are the same for both jet cases, it can be expected that the same potential is necessary in the ionization front to sustain the plasma which explains why the electric fields are the same. The difference between the jets is then that the potential is supplied by different voltages: either by AC or by positive square pulses at different frequencies.

Visible plume length − observations

Another difference between the two jets is the visible length of the plasma plume. The plasma plume length is mainly determined by the emission from excited He and N$_2$ states. Since the ICCD setups used to determine the length of the plume of the AC jet and the pulsed jet are not the same, differences in the sensitivity of the camera, the sensitivity of the optics and the

exposure time can lead to uncertainties in the detected plume length. It is important to be aware of this, but it is not expected that this will influence the analysis below.

In figure 5.19 the length of the plasma plume (a) and the air fraction corresponding to this position (b), as well as the position of the maximum value of the electric field (c), the air fraction corresponding to this position (d) and the maximum value of the electric field (e) are shown for both jet cases as function of the applied helium flow rate. The air fractions are determined from the flow model results in figure 5.11(b). It must be noted that the position of the maximum electric field is also the maximum position possible to measure the electric field, since beyond this position the intensity of the plasma is too low to obtain spectra from which the electric field can be determined. Depending on the flow rate, the plasma plume is $2-3$ times longer for the pulsed jet than for the AC jet (figure 5.19a). Since the two jets have the same flow profile, the air fraction at which the plasma plume terminates is different (figure 5.19b) and there is not a specific value for the air fraction above which the plasma plume terminates in both jets. At $Q_{He} = 1500$ sccm, the pulsed jet has a length of 48 mm, which corresponds to an air fraction of 0.21 (figure 5.19b). Using this air fraction and equation (4.3), the potential that is needed in the ionization front to sustain the plasma is 3.85 kV. Looking back at the simulation results in figure 4.13, the pulsed jet can supply this potential in the ionization front when voltage pulses of 6 kV amplitude and 1 μs long are applied with $Q_{He} = 1500$ sccm, which is exactly the case now. We do not have similar simulations for the AC jet, but apparently the AC jet cannot supply such a potential since the ionization front does not propagate further than 15.5 mm (figure 5.19a).
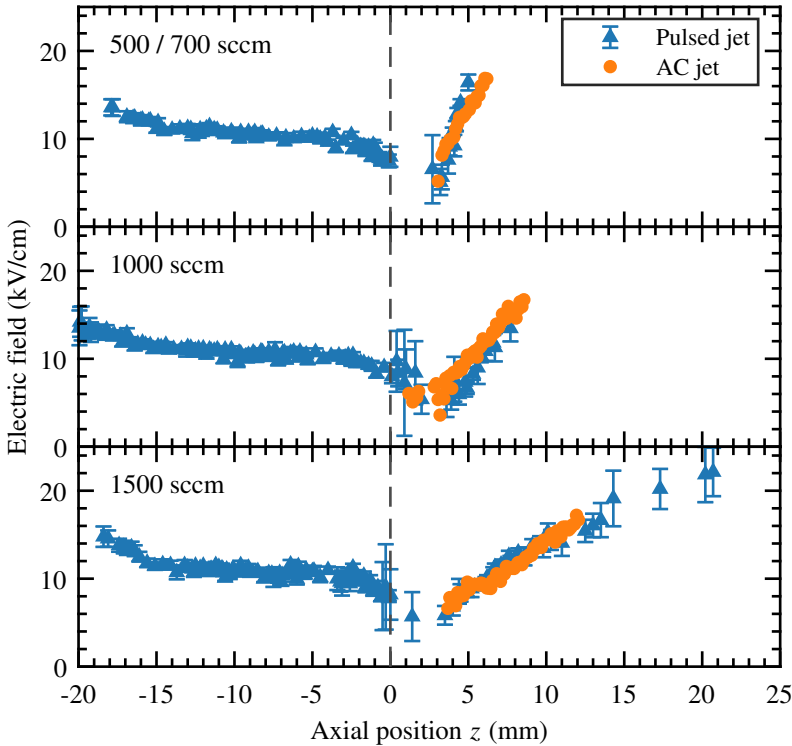
Figure 5.18: Electric field as function of axial position for the AC jet and the pulsed jet for different helium flow rates.

However, the potential in the front cannot exceed the applied potential, so in the AC jet this potential can be 2 kV at most. Streamers and jets have a limited conductivity of the channel that is formed between the front and the powered electrode [1] and thus the potential in the front has to be lower than the applied potential, which is also visible from the simulation results in figure 4.13. The fact that a certain potential is needed in the ionization front to sustain the plasma is also visible from results for the AC jet in figure 5.19: the same electric field (e) is measured for different flow rates at the same air fraction (d) because this air fraction corresponds to a different position in the jet (c) when the flow rate is changed.

Visible plume length − analysis and discussion

To analyze the different plume length of the AC and the pulsed jet, we can make a separation between, on the one hand, what happens during the time between one ionization wave and the next one and, on the other hand, what happens during the time of one particular ionization wave. In between two voltages pulses, thus ionization waves, there is the memory effect of leftover excited or charges species from the previous pulse. This can be affected by the frequency of the applied voltage pulses, if the amount of energy per pulse is the same, since then the time between pulses is different. As will be shown in chapter 6, the energy per voltage pulse stays constant in the frequency range of $0.5 − 5$ kHz. Thomson scattering measurements on the pulsed plasma jet (explained in section 2.5 and applied in chapter 4) reveal that a variation in the frequency of the applied voltage pulse between 0.5 kHz and 5 kHz has no influence on the electron density and also the plume length and velocity of the ionization front are found to change negligibly. In our conditions, the influence of the frequency on the memory effect is thus not that important. The gas flow rate could also affect the memory effect, since an increase in the flow rate leads to an increased dilution of the excited or charged species that remain from one pulse to the next one. For the comparison of the pulsed and the AC jet, however, this has no influence since we compare results at the same flow rates.

The gas flow rate also directly affects every single pulse (ionization wave), as we have shown (figure 5.11(b)) that the air fraction in the jet at a certain axial position changes with the gas flow rate. But again, this does not influence the comparison between the pulsed and the AC jet.

Influence of voltage pulse and power
The amplitude and duration of the voltage pulse have the most impact on what happens during one ionization wave. As shown in figures 4.12 and 5.18, the electric field measured in the ionization front is, at a single flow, the same for different amplitudes and durations of the voltage pulse and even the same for AC and pulsed applied voltage. The electric field in the front only depends on the gas composition at a given position, which in turn depends on the applied helium gas flow. The visible plume length, which is mainly determined by the emission of excited states of He and N_2, increases with amplitude and duration of the applied voltage pulse (as shown in figure 5.19a) and is in particular much longer in the pulsed jet than in the AC jet. Since the plume length corresponds to the emission of electronically excited states, it can depend on the electron density and the electron energy. As the electric field is shown to be the same in these different cases, the difference in plume length is probably related to the number of produced electrons. In fact, a decrease of around 0.2×10^{19} m^{-3} in electron density is found, which corresponds to around 14%, when the amplitude of the applied voltage pulse is decreased from 6 kV to 4 kV. An even lower electron density can therefore be expected in the AC jet, which has a voltage amplitude of 2 kV. At the same decrease in voltage amplitude of 6 kV to 4 kV, the plume length and the maximum velocity of the ionization wave in the plasma plume decrease, respectively,

from 48 mm to around 22 mm and from 1.2×10^5 m/s to 0.6×10^5 m/s. The energy per pulse also decreases with voltage amplitude, as will be shown in chapter 6: from 36 μJ at 6 kV to 15 μJ at 4 kV.

The AC jet and the pulsed jet have a different input voltage and current and thus also a differ-
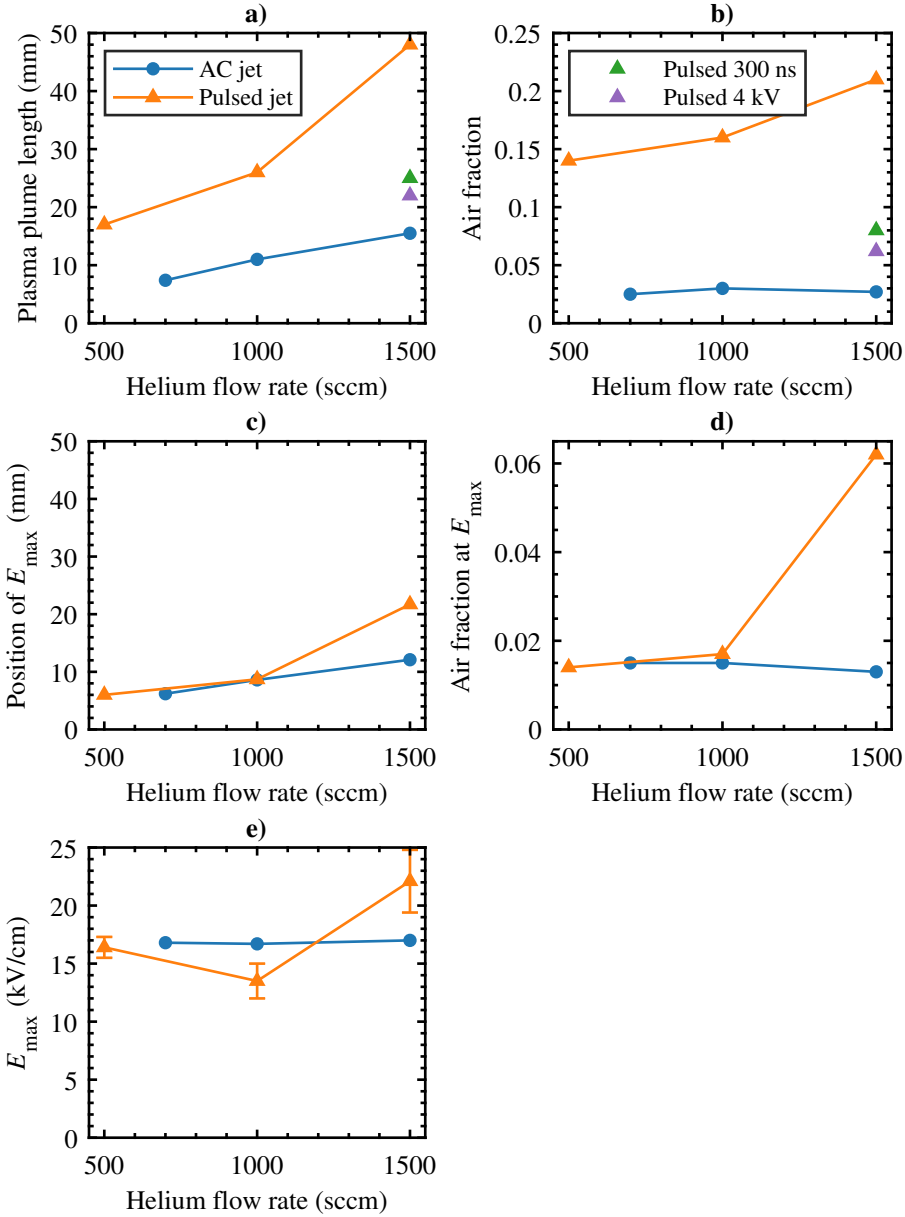
Figure 5.19: Different properties of the AC jet and the pulsed jet for different flow rates: a) plasma plume length, b) air fraction at the plasma plume length, c) position of the maximum electric field E_{max}, d) air fraction at the position of E_{max}, e) value of E_{max}. In a) and b) results of the pulsed jet with $V_P = 6$ kV and $t_f = 300$ ns (in green) and $V_P = 4$ kV and $t_f = 1000$ ns (in purple) are also included.

ent power that is dissipated in the plasma. At 4 kV, the lowest measurement voltage amplitude, the energy per pulse is 14.5 μJ, which corresponds to a power of 14.5 W since the pulse duration is 1 μs. This is two orders of magnitude larger than the dissipated power of 0.2 W [5] in the AC jet.

The length of the plasma plume can then be controlled by two parameters: the number of electrons that are produced in proportion to the dissipated power and the potential in the ionization front.

Influence of potential in the front
According to equations (4.2) and (4.3) the potential in the front depends on two parameters: the first is the slope parameter in combination with the air fraction at the given position, which is thus controlled by the gas composition, and the second is the offset parameter, which is related to the potential applied to the powered electrode during the propagation of the ionization wave. To discuss the potential in the front, we first repeat the streamer propagation principle as explained in [1] for example, for a regular streamer in a homogeneous gas and with a homogeneous applied electric field. The electric field that sustains the potential in the ionization front and hence the propagation of the streamer results from the sum of the applied electric field and the electric field induced by the charge separation at the front. The conductivity of the channel that is formed behind the ionization front depends on the earlier by the streamer produced charges and is thus limited. Therefore, only a part of the potential that is applied to the electrode is transferred to the ionization front. This also means that the peak electric field in the front slowly decreases when the streamer moves further away from the powered electrode, until the sum of the transferred potential from the electrode and the induced potential at the front becomes insufficient to sustain ionization and thus propagation.

The plasma jet is therefore a peculiar case of a streamer, since the electric field needed to sustain ionization is controlled by the change of the gas composition along its propagation. Since the amount of air in the helium flow increases along the propagation, the electric field is forced to increase in order to sustain ionization as well as the slope parameter as function of the air content in equations (4.2) and (4.3). The duration of the applied voltage pulse probably plays a role in the offset parameter in these equations. When the duration of the applied voltage pulse is longer than the propagation lifetime of the ionization wave, as discussed in chapter 4, a larger part of the applied potential can be transferred to the front, and thus the potential in the front and the offset parameter are higher. On the other hand, a shorter duration of the applied voltage pulse leads to a shorter time over which the applied potential can be transferred to the front and thus the potential in the front and the offset parameter are lower.

As shown in [5, 26], the plasma in the AC jet forms at the polarity change of the applied voltage, where the voltage is almost zero, because a high amount of electrons that sit on the capillary wall around the electrodes experience a large potential difference when the applied voltage, and thus the electric field between the electrodes, changes polarity. These electrons are present on the inner wall of the capillary due to the previous half period of the applied voltage. The principle of a DBD is thus well harvested in the plasma operation of the AC jet. The velocity of the ionization wave is $1.5 - 2.0 \times 10^4$ m/s, which is an order of magnitude lower than the pulsed jet. While the ionization wave propagates, the voltage rises from approximately 500 V to 1 kV, which is very low compared to the pulsed jet. The extra potential transferred to the front and hence the offset parameter are thus basically zero in the AC jet with respect to the pulsed jet.

The difference in plume length of the pulsed and the AC jet can therefore not be explained by the difference in time between the duration of the applied voltage and the propagation duration

of the ionization wave, as is the case for shorter pulses in the pulsed jet. Instead, the offset parameter for the AC jet is zero and thus the potential in the front is lower. From figure 5.19b it can be seen that the AC jet stops propagating at an air fraction of around 3 %, at a helium flow rate of 1500 sccm. Returning to figure 4.13 while keeping in mind that the potential in the front is at most 2 kV, this point falls well between the lines in this figure and thus the findings on the plasma plume length seem consistent.

5.4.3 Quantitative schlieren imaging

Schlieren imaging itself is an easy to implement diagnostic to visualize the flow in a system, in this case the plasma jet, and as such it has been widely used in literature [28, 32, 125, 128–131]. Quantitative schlieren, however, is not so widely used and has been proven to be difficult for the plasma jet of this thesis.

From the radial profiles of the contrast in figure 5.6 it can be seen that the profiles are not symmetric, as the peak values of the left and right side of the profiles are not equal. The profiles should be symmetric, because to calculate the integral for the refractive index, we assume axial symmetry. The correct peak value of the contrast is probably close to the average of the peak at the left hand side and the peak on the right hand side of the shown profiles. However, due to the artifacts at larger radial positions on the right hand side of the profile, we cannot take the average contrast of both sides and use this to calculate the refractive index, since that would induce another error. The maximum error in the contrast values is therefore estimated as the difference between the peak value on the left hand side and the average of the peak values of the left and right hand sides, which then corresponds to a maximum error of 0.1 in the contrast values (which generally have values between -0.5 and 0.5). A possible reason for the asymmetry in the contrast profiles is that the knife edge is not positioned exactly in the focal point of the lens in front of it (L_3 in figure 2.16).

Another parameter that yields uncertainty in the calculated refractive index, and thus in the air fraction, is the sensitivity, which is equal to $S = f_3 A'(h)/(DA(h))$ according to equation (5.6). The error in $A(h)$ is already minimized by using the trigonometrical expression instead of calculating it from the measured I_k and I_0. However, it still depends on h. From figure 5.3 and the determination of the knife edge positions that corresponds to $h = 0$ and $h = 1$, we estimate the error in h to be 0.05. Since this determination defines the diameter of the beam D, the corresponding error in D is then 0.07 mm (or 5 %). The error in the focal length f_3 would be expected to be negligible, but it was found out that the lens has an asymmetric behavior if it is rotated 180 º around its vertical axis, which makes us believe that f_3 has a non-negligible error due to the imperfection of the large diameter lenses. We do not know the exact value of the error, but we estimate that it cannot be larger than 1 cm (with respect to $f_3 = 45$ cm), which corresponds to an error of 2 %. In total, these individual error yield an error of 80.6 in S that corresponds to around 12 %.

The total error in the refractive index is estimated as

$$S_n = \sqrt{\left(\frac{\partial n}{\partial C}\right)^2 S_C^2 + \left(\frac{\partial n}{\partial S}\right)^2 S_S^2} \approx \sqrt{\left(\frac{1}{S}\right)^2 S_C^2 + \left(\frac{C}{S^2}\right)^2 S_S^2}$$

where S_i is the error in property i and the approximation $n \propto C/S$ is used for the error estimation, i.e. not to calculate n. This calculation yields an error value for every position in the contrast image and hence for every position in the refractive index image. These errors in the refractive index have a magnitude of $50 - 100$ %. The calculated refractive index also depends on the

reference value of the refractive index (n_∞) at $r = 5$ mm, but the error in this value is expected to be significantly lower than the errors discussed above and is therefore neglected. Since the air fraction scales linearly with the refractive index (equation (5.16)), the total errors in the air fraction are also $50 - 100$ %.

These large error bars are of course a disadvantage to the quantitative schlieren method, but with even more precise alignment, checking of the optical components and calibration of the setup, it can be a valuable method to determine the flow profile and composition in the plasma jet, since this information of the whole jet region is basically captured in one image. Compared to rotational Raman scattering, quantitative schlieren imaging has a couple of advantages. In principle, no expensive or extensive equipment such as a short-pulsed laser, high resolution spectrometer or ICCD camera are needed. A high frame rate camera is only needed when a large temporal resolution is desired. Quantitative schlieren imaging is also non-intrusive, which makes it especially suitable for plasma jets that are susceptible to influences from the environment.

A larger contrast, especially in the region around $r = 0$ mm, would also improve the calculation of the refractive index and the air fraction in the jet. This can probably be achieved by increasing the sensitivity of the system, because a higher sensitivity means that the system is more susceptible to small gradients of the refractive index, such as at the center of the jet where there is only little mixing of the helium with the ambient air.

5.5 Conclusions

In this chapter, the air entrainment in the free helium jet is studied and especially the influence of the plasma on this entrainment. Rotational Raman scattering has been used to determine the N_2 and O_2 densities in the jet in axial and radial direction. It has been found that, close to the exit of the capillary, there is a negligible difference in these densities whether the plasma is applied to the helium flow or not. Similarly, measurements at one location ($z = 8.7$ mm, $r = 0$ mm) have shown no influence of a different amplitude, length or frequency of the applied voltage pulse on the N_2 and O_2 densities.

Qualitative schlieren imaging has been used to visualize the flow profile of the jet for different helium flow rates. At a large flow of 1500 sccm, turbulence is visible around $z = 40$ mm, while no turbulence was visible at lower flows. The addition of plasma to the helium flow leads to the appearance of turbulent structures also at lower flows. It was shown that the plasma plume is shorter than the flow profile and because little turbulence is present at low flows, the length of the plasma plume is not solely determined by the onset of turbulence. Comparison of the laminar flow length of the plasma jet with those in literature has shown that in most cases the presence of the plasma decreases the laminar flow length, but no direct relation between this length and the Reynolds number could be found. Instead, other differences between the studied jets, such as the length of the capillary, the amount of impurities and the gas temperature, are believed to contribute to the differences in laminar flow length.

The negligible difference between plasma Off and plasma On on the N_2 and O_2 densities and thus the air fraction in the plasma jet has also been shown as a result from the quantitative schlieren measurements. From the schlieren images, the refractive index can be calculated according to the shown method and using the results from the Raman measurements as calibration, the air fraction in the whole region of the plasma plume has been calculated. Due to difficulties and uncertainties in the analysis process, the exact values were found to have an uncertainty of $50 - 100$ % which does not allow quantitative comparison to the simulations and Raman results,

but the order of magnitude and slope of the profiles were found to be comparable. More precise alignment, optics and measurements are needed to reach the full potential of the quantitative schlieren technique, because then it would yield full 2D maps of the air fraction in one measurement, which is a large advantage over rotational Raman scattering where a measurement would be required for every point, which is much more complicated and time consuming.

Comparison of different parameters in the pulsed jet and a jet with the same geometry but powered by 20 kHz AC with 2 kV amplitude have contributed to the understanding of what determines the length of the plasma plume. The length of the plasma plume shows a 2-3 times difference, where the pulsed jet is the longest. It is found that the electric field does not cause this difference, since at three flow rates, the axial electric field profiles were found to be the same for the pulsed and the AC jet even though the plasma is supplied with a different voltage form. Following the Raman results, that show similar N_2 and O_2 densities for different voltage pulses and at plasma On and plasma Off, we assume that the flow profile is the same in the AC and pulsed jet. According to the results in chapter 4 the plasma length is determined by the local air concentration, since a linear relation exists between the needed potential in the head and the local O_2 concentration. Thus, a similar potential is needed in the front of both jets, because the air density profile is the same, and hence the measured electric field is the same. The AC jet can, however, sustain this potential over a shorter distance than the pulsed jet. Based on measurements of the electron density and energy and simulations in the pulsed jet, and literature on the AC jet, we argue that this is caused by an energy per voltage pulse or cycle that is two orders of magnitude lower, thus less electrons are produced, and because less potential from the powered electrode to the ionization front is transferred during the propagation of the ionization wave. Therefore, the plasma plume in the AC jet is shorter than in the pulsed jet.

6

Gas temperature in a free helium jet

Abstract: Different diagnostics are used to determine the gas temperature in a free helium plasma jet. Rotational Raman scattering is used that yields the rotational temperature of N_2 and O_2 , but comparing these results to measurements by a fiber-optical temperature probe shows that the obtained gas temperatures from rotational Raman scattering are only valid if the corresponding densities of N_2 and O_2 are sufficiently high. A lower limit for these densities to yield reliable temperature results is set to 10^{23} m^{-3}, which corresponds to 1 % of air inside the helium jet. When only a helium flow is applied, heating of a few degrees is observed along the axis of the jet, while cooling of a few degrees is observed around this heated channel. Application of the plasma to the helium flow yields an overall temperature increase of around 12 $^{\mathrm{o}}$C with a maximum temperature of 40 $^{\mathrm{o}}$C. Changing the amplitude, length or frequency of the applied voltage pulses leads to (slight) increases in the temperature as expected from the measured energy per pulse that is supplied to the plasma. The main heating mechanism in the plasma jet is found to be ion Joule heating due to elastic collisions between ions and neutrals. It is also found that, in the studied jet, not gas heating but momentum transfer between charged and neutral particles, in the shape of the electrohydrodynamic force that induces an electric wind, causes a doubling of the gas flow velocity and thus is the main cause for disturbances or turbulence in the jet as reported in chapter 5.

6.1 Introduction

In chapter 5 we have shown that when the plasma was applied to the helium flow, more turbulence was induced than when only the helium flow was applied, while the air entrainment stayed approximately constant close to the nozzle. Another parameter in the jet that is expected to be influenced by the plasma is the temperature of the heavy species (ions and neutrals). This chapter therefore assesses the gas temperature in the plasma jet and focuses on the difference in temperature with and without the presence of the plasma.

Since the electrons and the heavy species in cold atmospheric pressure plasma jets are not in thermal equilibrium, these plasma jets are particularly useful for the treatment of sensitive targets, which is for example the case in most biomedical applications. Weltmann *et al.* [146] have shown that human cells and tissue are extremely temperature sensitive. A temperature of $37 - 38.5\ ^{\circ}$C stimulates keratinocyte proliferation [147], which is the multiplication or reproduction of epidermal cells, thus it supports wound healing and tissue regeneration. For these effects to be beneficial, the tissue temperature should stay below $40\ ^{\circ}$C [146]. If the temperature is $40 - 50\ ^{\circ}$C, local overheating can occur which results in changes in the cell membrane and molecular structures and can even cause cell death. A higher temperature ($> 50\ ^{\circ}$C) causes protein and collagen to lose their structure (denaturation), but also the destruction of cell membranes and the evaporation of the cell liquid [146]. It is important to mention that these temperature influences are valid when the cells and tissue are at these temperatures, meaning that the temperature of the plasma can actually be higher, as long as it does not heat the cells and tissue to their limit temperatures. This can be achieved by adapting the time of interaction between the plasma and the surface, for instance by moving the plasma over the surface to be treated or by operating the plasma in burst mode instead of continuously, as was shown in [146]. It is therefore important to know the temperature of the gas accurately, since a temperature difference of only $10\ ^{\circ}$C can already have a major impact on the subjected target.

Different diagnostics have been used in literature to obtain the gas temperature in a plasma jet. Emission spectroscopy has been used, where fitting of for example the N_2 (C-B) rovibrational band [135, 148–150] or the OH radial [149, 151, 152] yield the rotational temperature of N_2 or OH, respectively. Laser scattering has also been applied, with Rayleigh scattering [45, 149, 152] and rotational Raman scattering [30, 45, 149] yielding the rotational temperature of N_2 or O_2 that corresponds to the gas temperature. Furthermore, a fiber-optical probe [103, 146] has been used to determine the gas temperature in the plasma jet.

In this chapter, the gas temperature at plasma Off and plasma On is determined using two diagnostics. Rotational Raman scattering is used to measure the rotational temperature of N_2 and O_2 in the jet and these results are compared to measurements by a temperature probe (section 6.3.2). Electrical measurements are performed to obtain the energy per voltage pulse that goes into the plasma and these results are used to explain the influence of the amplitude, length and frequency of the applied voltage pulse on the gas temperature (section 6.3.3). We also show the influence of a floating metallic target on the temperature in the plasma jet (section 6.3.4). Similar to the discussion in chapter 5, the gas temperature results of the pulsed jet of this thesis are compared to the results of the AC powered jet of [28] (section 6.4.3). Based on the results of chapters 4 and 5 and this chapter, we are able to determine the main mechanism that causes the heating of the gas when the plasma is applied (section 6.4.2). The chapter is concluded with the estimation of the influence of the gas heating and the momentum transfer between charged and neutral particles, thus causing the electrohydrodynamic force, on the flow structure of the jet (section 6.4.6). Using all obtained results, we are able to determine which of these two mechanisms is the main cause in our conditions for the change in flow structure as reported in chapter 5

when plasma is applied to the flow in the jet.

6.2 Experimental setup

The same cold atmospheric pressure plasma jet is used as before, with dimensions as shown in figure 2.1. Positive, unipolar pulses with an amplitude V_P of $4 - 6$ kV, a length t_f of $0.16 - 5$ μs and a repetition rate f of $0.1 - 5$ kHz are used to power the jet. The jet is operated vertically downwards with a helium flow of 1500 sccm.

6.2.1 Rotational Raman scattering

The same Thomson and rotational Raman scattering setup as in chapters 4 and 5 that is described in more detail in section 2.5 is used to determine the gas temperature in the jet from the rotational temperatures of N_2 and O_2 . In this chapter a fit of the Raman signal yields the gas temperature, while the Thomson signal is not used. Initially the error of the fit is used as an estimate for the uncertainty in the gas temperature, since it is of the same magnitude as the spread in temperatures measured at the same settings on different days.

Measurements are done at the center of the jet along the jet axis and at two axial positions while varying the radial position, as well as measurements at one position ($z = 8, 7$ mm, $r = 0$ mm) while varying the amplitude, length and frequency of the applied voltage pulse.

6.2.2 Temperature probe

To verify the gas temperature results as measured with the rotational Raman scattering setup, the gas temperature is also measured using a temperature probe. The setup in which the plasma jet is placed to perform these measurements, was explained in section 2.6 and shown in figure 2.12. Temperature maps are made in the axial plane at the center of the jet ($y = 0$) over a range of 16 mm in x-direction and 45 mm z-direction at a step size of 0.5 mm and by taking the mean temperature during 1 s at every position. Measurements are done at plasma Off and On and for different settings of the applied voltage pulse.

6.2.3 Energy measurements

As is explained in the next section, the energy that is applied to the plasma by the applied voltage pulses is related to the heating of the gas. Therefore, we measure the energy per pulse that goes into the plasma using the setup that is shown in figure 2.3 and explained in more detail in section 2.2. Measurements are performed for different values of the amplitude, length and frequency of the applied voltage.

## 6.3 Results

6.3.1 Influence of plasma

First, we study the influence of the plasma on the temperature of the gas. A vertical cross section of the gas temperature as measured with the temperature probe at $y = 0$ mm is shown in figure 6.1(a) for the plasma Off and the plasma On cases. At plasma Off, the profile of the helium flow is visible as a channel as wide as the inner diameter of the capillary (2.5 mm) with

a slightly higher temperature ($+5$ °C) than the ambient air ($20 - 23$ °C) at $|r| > 5$ mm that continues in the axial direction over a few cm. On both sides of this channel the temperature is below that of the ambient air over a radial width of around 2 mm, which makes the total width of the two channels slightly wider than the outer diameter of the capillary (4 mm). For the plasma On case, we can see that the temperature in the center channel is higher than at plasma Off, which is expected since energy is dissipated in the gas because of the applied voltage. The outer channel with lower temperature than the surroundings is still present, although the temperatures there are not as low as at plasma Off. The other clear difference is that the increased temperature in the helium channel is present over a twice as long axial distance at plasma On than at plasma Off. At these positions of $z > 25$ mm the profile looks wider and more scattered, because the end of the plasma plume is reached at $z = 40$ mm and the flow is unstable here due to the helium gas that tends to drift upwards since it is much lighter than the air. Figure 6.1(b) shows the difference between the temperature profiles of figure 6.1(a), which represents the heating induced by the plasma. In the central helium channel, the plasma induces a temperature increase of $10 - 15$ °C.

The influence of the plasma on the gas temperature is also clearly visible from figure 6.2, where the axial profile at $r = 0$ mm of the temperature is given for when the plasma is on and when the plasma is off. Overall, an offset of about 12 °C is visible, where the temperature is higher when the plasma is on. For both plasma Off and plasma On, the temperature increases over $8 - 10$ mm for increasing axial position, reaches a maximum that is approximately 3 °C higher than the initial value at $z = 0$ and then decreases until the end of the measurement range. This decrease starts a few millimeter sooner at plasma Off than at plasma On.

(a)   (b)
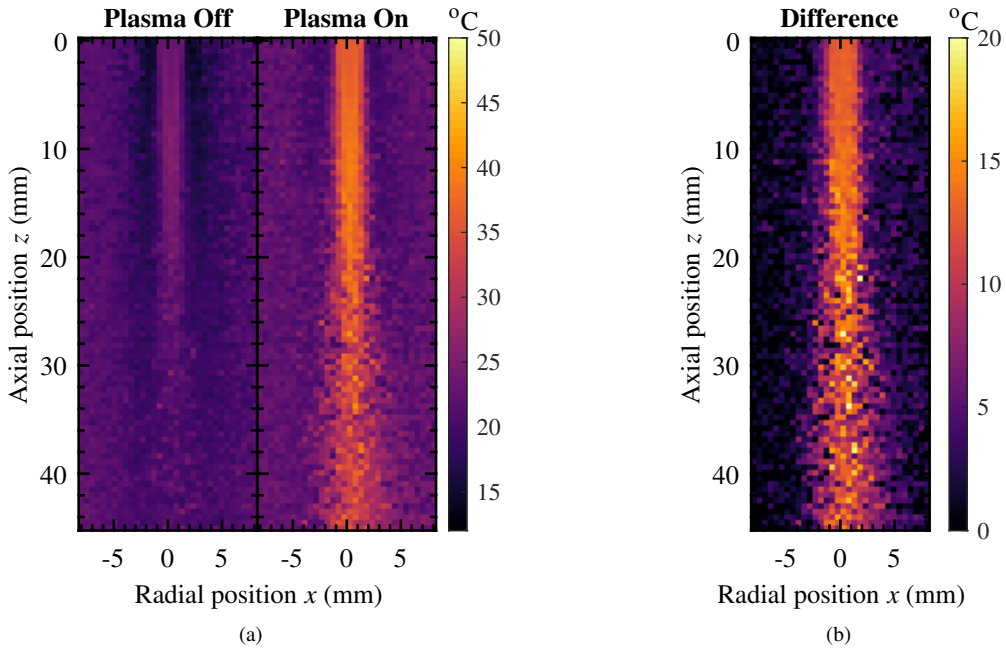
Figure 6.1: Gas temperature as measured with the temperature probe at $y = 0$ mm for a helium flow of 1500 sccm, a) with the plasma Off (left) and the plasma On (right) and b) the temperature difference between plasma On and Off. The temperature scale in b) is smaller for better visibility.
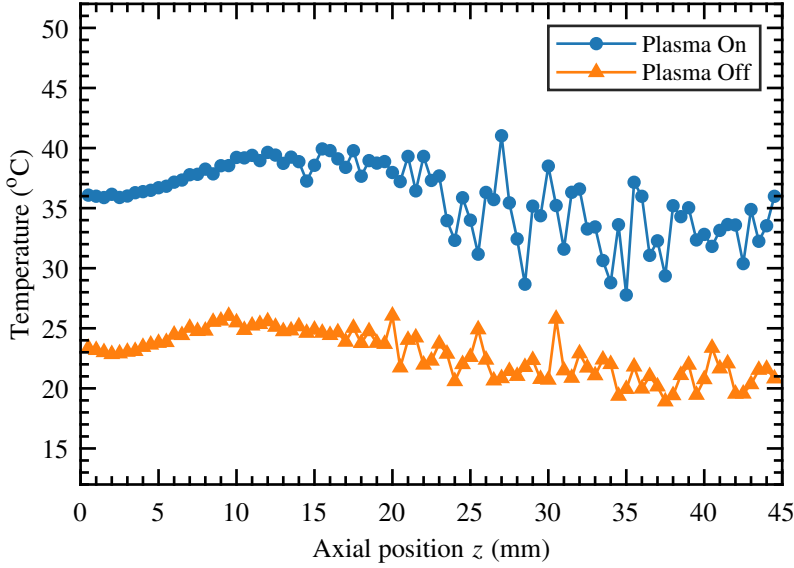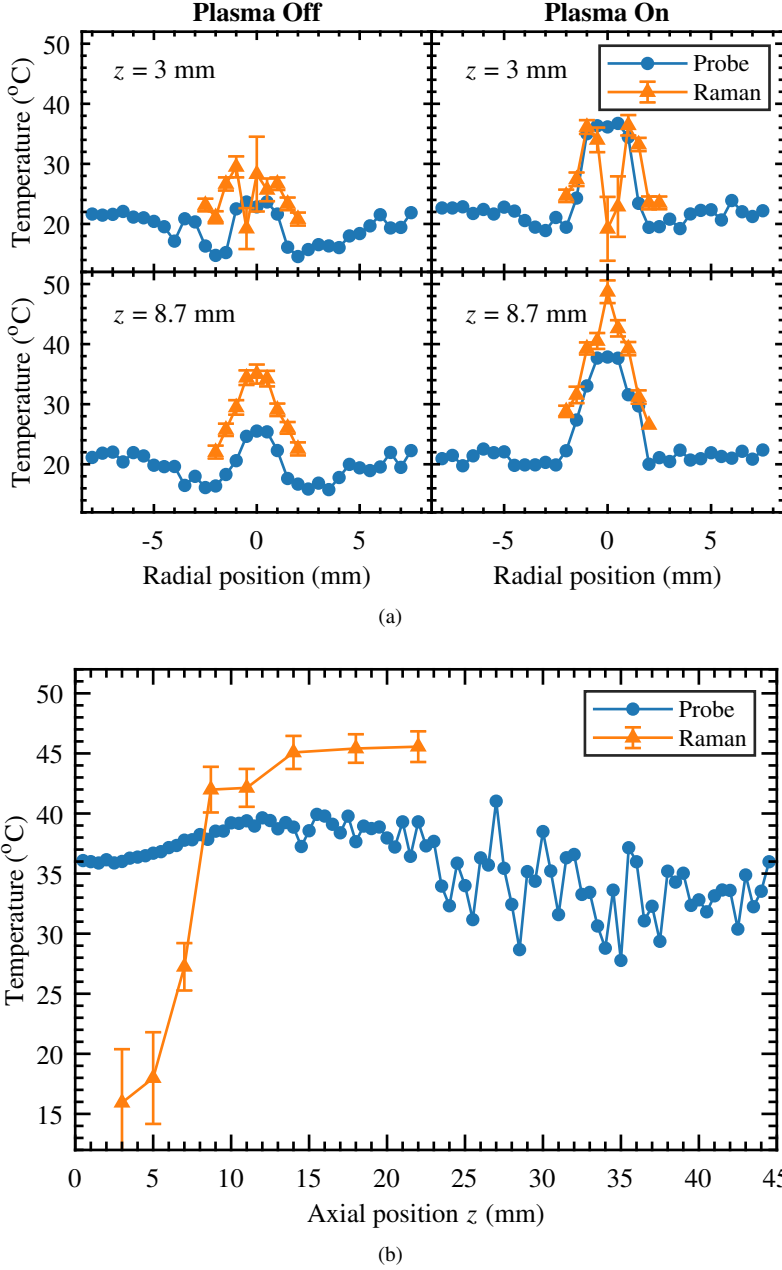
Figure 6.2: Gas temperature at $r = 0$ mm as function of axial position, measured with the temperature probe with the plasma On and Off.

6.3.2 Comparison of measurement techniques

Apart from using a temperature probe, the gas temperature is also measured by rotational Raman scattering. To compare the two techniques, the radial profiles of the gas temperature, measured with Raman scattering and with the temperature probe are shown in figure 6.3(a) for $z = 3$ mm and $z = 8.7$ mm and for plasma On and plasma Off. It can be seen that the agreement between the two measurement methods is better at plasma On than at plasma Off. At the center of the jet, the Raman data are most off with the probe data: at $z = 3$ mm the temperature is too low compared to the probe data and at $z = 8.7$ mm the temperature is too high. As we have seen from figures 5.10 and 5.11, there are significant gradients in the N_2 and O_2 densities both in radial and in axial direction, and the densities are especially low at the center of the jet. The number density of the molecular species is proportional to the scattering intensity of a rotational Raman transition [44], and since it is independent of the transition itself, it is also proportional to the total scattering intensity. The gas temperature, however, is inversely proportional to minus the natural logarithm of the scattering intensity of a rotational Raman transition [44], thus for very low densities and scattering intensities, the gas temperature is not easy to fit. We can therefore set a limit to the number densities of 10^{23} m^{-3}, which is the density corresponding to the position in figure 6.3(b) where the gas temperature from Raman increases rapidly by around 25 °C. If the N_2 and O_2 densities are above this limit, the values for the gas temperature can be considered reliable, while if the densities are below this limit, the temperature are considered not reliable. This is the reason for the substantial difference in temperature between the probe measurements and the Raman measurements in figure 6.3(b), where the axial temperature profile is shown at $r = 0$ mm. Using the results from this figure, we adapt in the next figures the error bars for the Raman results that originate from the fitting procedure of the spectra to ± 20 °C if the densities at the corresponding position are below the limit of 10^{23} m^{-3} and to ± 10 °C if the densities are above the limit.

Van Gessel *et al.* [45] have also measured the gas temperature with Raman scattering in a

plasma jet and have shown that in the center of the jet the measurements do not agree with the gas temperature as measured with Rayleigh scattering, because the gas temperature is hard to fit when the density of N_2 and O_2 is low. Their measured temperatures are higher than in our case

(a)

(b)

Figure 6.3: Gas temperature as measured with Raman scattering and with the temperature probe for a) plasma Off and plasma On at $z = 3$ mm and $z = 8.7$ mm as function of radial position and b) for plasma On at $r = 0$ mm as function of axial position.

(above 100 °C in the center of the jet), since they use an RF-powered jet that gives a continuous discharge and a higher input power, but the shape of the radial profiles is similar: the highest temperature in the center and then a gradual decrease towards the sides.

6.3.3 Influence of the applied voltage pulse

To get a better insight in the mechanisms that induce gas heating in the plasma, we study the influence of the applied voltage pulse on the gas temperature. In figure 6.4 the dependency of the gas temperature on the a) amplitude, b) frequency and c) pulse length of the applied voltage is shown as measured by Raman scattering at $z = 8.7$ mm and $r = 0$ mm. Added to these figures with blue markers are the results from measurements with the temperature probe, that are also performed at different settings of the applied voltage shape, although not for as many settings as for Raman scattering. From the results for the N_2 and O_2 densities in figure 5.15, the error bars for the temperature from Raman are adapted correspondingly to ± 20 °C. The results from the probe are within the error bars of the results from Raman scattering. Although the N_2 and O_2 densities were shown to be constant within the measured range of the amplitude, frequency and pulse length of the applied voltage (figure 5.15), the gas temperature shows not to be independent of these properties. The measurements are not precise enough (Raman scattering) or are not consisting of a sufficient amount of data points (temperature probe) to draw quantitative conclusions from the results, but still some qualitative relations can be discussed.

From figure 6.4a it can be seen that the gas temperature increases when applying a higher voltage. At an increased applied voltage, more energy is dissipated by the plasma, as can be seen in figure 6.5a, where the energy per pulse is plotted as function of the applied voltage. As discussed in chapter 5, the electric field and electron temperature are the same for higher voltages, but the electron density is probably higher. Therefore, more collisions can take place between the charged species and the neutral background species, such as helium atoms and air molecules (N_2 and O_2). The subsequent energy transfer during these collisions leads to an increased gas temperature.

As function of the frequency of the applied voltage pulse (figure 6.4b), the temperature also shows a slight increase, whilst the energy per pulse (figure 6.5b) stays constant. In this case, the raise in temperature can be explained by looking at the amount of ionization waves per second, which increases from 100 to 5000 in the measured range. Since each wave transfers a similar amount of energy to the background species, the total amount of energy used per second to heat the gas increases. Therefore, the measured gas temperature is higher.

Finally, also the pulse length has a positive effect on the gas temperature (figure 6.4c), i.e. the gas temperature increases as the duration of the applied voltage pulse becomes longer. Following the same reasoning as for the influence of the voltage amplitude, an increased pulse length leads to a higher energy per pulse as can be seen in figure 6.5c, due to the fact that more electrons and ions are produced. Meanwhile, the electric field and the electron temperature remain the same. Therefore, the plasma will transfer more energy to the gas during collisions, causing the gas temperature to rise.
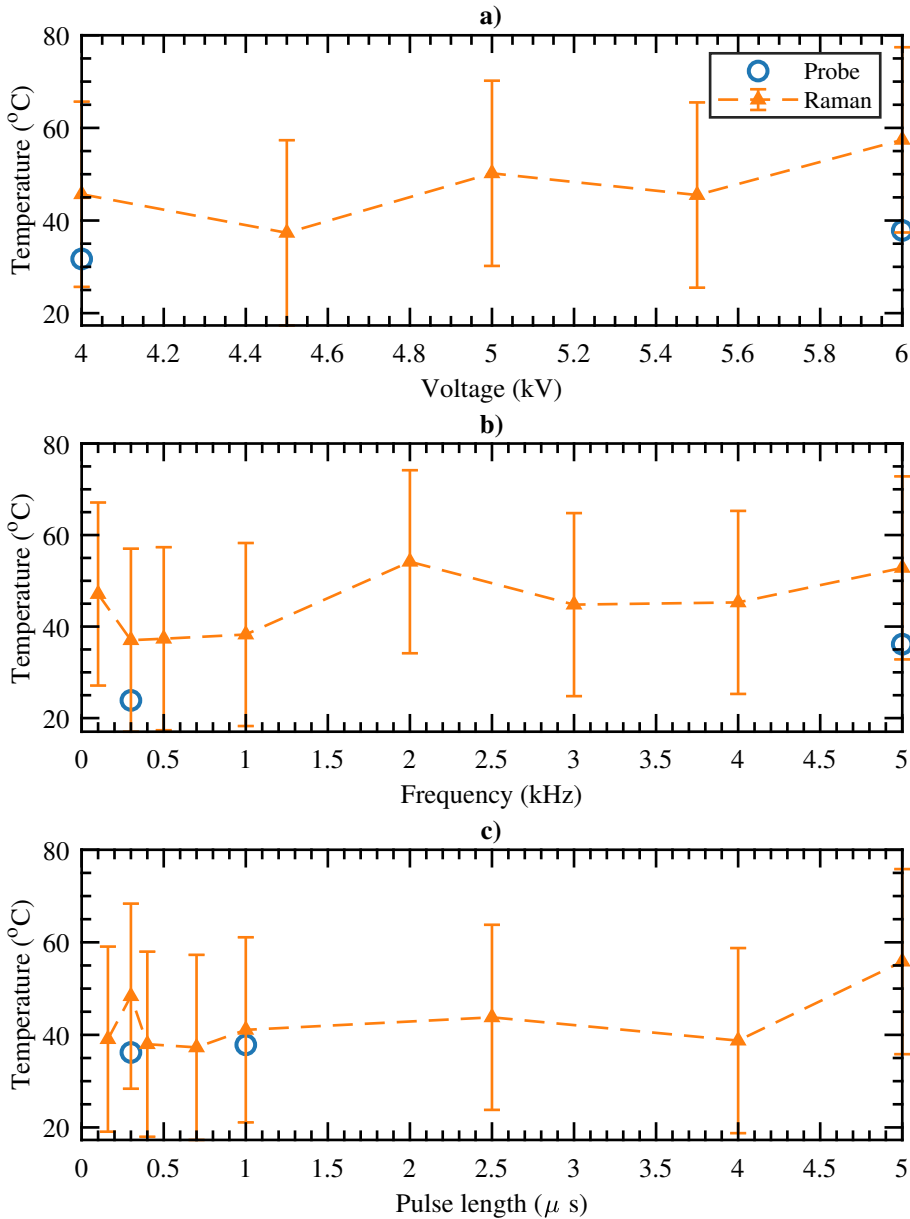
Figure 6.4: Gas temperature at $z = 8.7$ mm and $r = 0$ mm measured by Raman scattering and with the temperature probe as function of a) the applied voltage, b) the frequency and c) the pulse length. The helium flow is 1500 sccm.
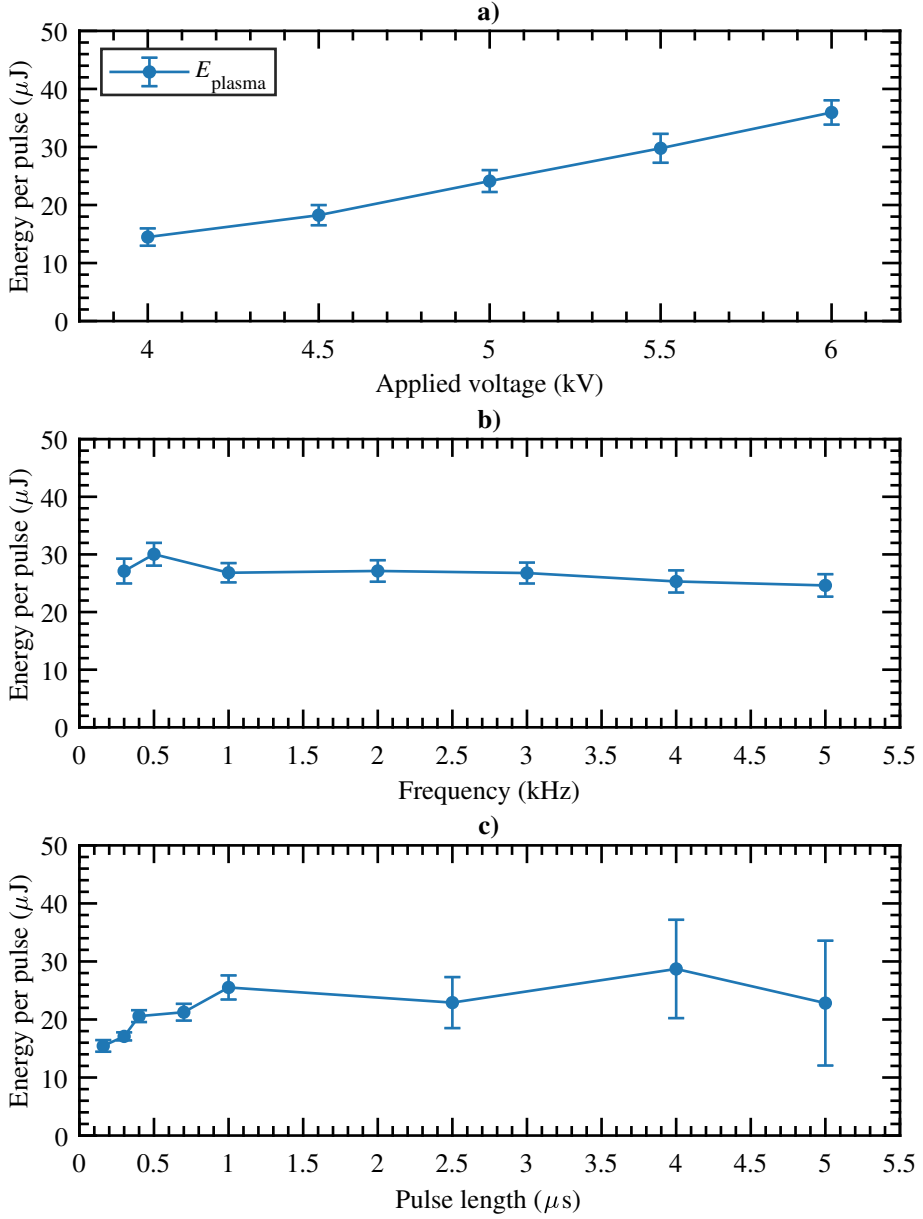
Figure 6.5: The energy that is dissipated in the plasma as function of a) the applied voltage, b) the frequency and c) the pulse length. In b) and c) the applied voltage is 5 kV. The helium flow is 1500 sccm.

6.3.4 Influence of a target on the gas temperature profile

After investigating the temperature profiles in a free helium plasma jet, we can also look at the influence of a target on the gas temperature. Therefore, a floating metallic target (copper) is placed at 10 mm from the exit of the capillary and the temperature is measured as before with the temperature probe at $y = 0$ and over a range of 9 mm in z-direction and 21 mm in y-direction. The results of these measurements are shown in figure 6.6 for plasma Off and plasma On. Similar to the free jet temperature maps in figure 6.1, the helium flow can be seen as a heated central channel of approximately 2 mm in diameter with a cooling channel around it at the boundary where the helium flow mixes with the ambient air. At the target interface, Schlieren measurements in a similar setup performed by Kovačević *et al.* [32], have shown the existence of a re-circulation flow, as the helium flow hits the target, disperses over a distance of around $6 - 10$ mm from the center of the jet along the target surface and then returns in negative z-direction. This re-circulation of the supplied helium flow from the target located at $z = 10$ mm can also be seen in the temperature maps of figure 6.6. Here, at similar radial positions ($|r| = 5 - 10$ mm), secondary bright areas can be observed that are warmed by the heated helium flow.

Comparing the values of the temperatures measured in the presence of a target with those in the free jet, we see a similar temperature in the central channel in case the plasma is off. However, when the plasma is turned on, we see an increase of around $8 - 10$ °C at the center of the jet between the exit of the capillary and the surface of the target. In chapter 7 will be shown that the electron density in the plasma increases when a floating metallic target is placed at 1 cm from the exit of the capillary. The gas temperature increases due to electron-neutral as well as ion-neutral collisions scale linearly with the electron density (equations (6.8) and (6.11)), which is then the reason why higher gas temperatures are measured in the jet when the metallic target is present.
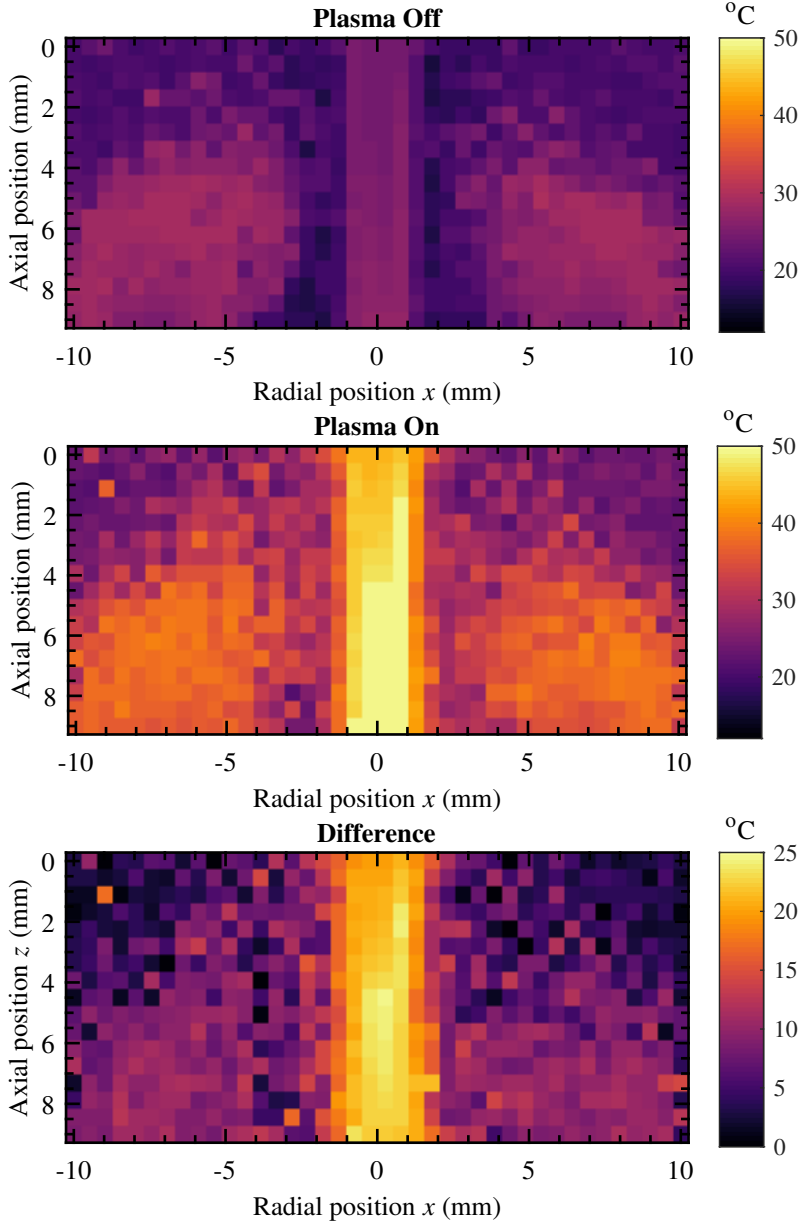
Figure 6.6: Gas temperature as measured with the temperature probe at $y = 0$ mm for a helium flow of 1500 sccm and a floating copper target at $z = 10$ mm with the plasma Off (top) and the plasma On (center). The temperature difference between plasma Off and On is shown in the bottom figure, where the temperature scale is smaller for better visibility.

6.4 Discussion

6.4.1 Gas heating processes

To determine the heating source of the gas temperature it is important to look at the different processes that play a role in gas heating in the plasma jet. It starts with the energy supplied to the helium flow by the applied voltage pulses, which ionizes the gas, thereby generating electrons and ions. Both of these species are subsequently accelerated in the induced electric field, causing them to gain energy, quantified by the electron temperature T_e and the ion temperature T_i, respectively.

The electrons lose their energy in elastic and inelastic collisions with the heavy species, the latter of which results in the vibrational and electron excitation of the heavy particles. Vibrational excitations are only present in molecular gases, meaning that the inelastic collisions have a relatively small impact at the center of the jet, especially close to the exit of the capillary, as the presence of N_2 and O_2 here is relatively low. More towards the outside of the jet at the interface between the helium flow and the ambient air or further downstream, where gas mixing causes the concentration of the molecular species (N_2 and O_2) to increase, as was shown in chapter 5, this process could in principle be significant. In order to contribute to the heating of the background gas, the vibrationally excited species need to transfer their energy to thermal energy which takes place via vibrational-translational relaxation, which is a process that has a characteristic timescale of microseconds for vibrationally excited N_2 and O_2 [1]. The relaxation length of these vibrational-translational processes is very short at atmospheric pressure [1], hence if this would be the dominating heating mechanism, a higher gas temperature would be expected at the boundary between the helium flow and the ambient air where the air admixing rapidly increases. However, from the temperature profile at plasma Off we can see that most heating occurs along the axis of the jet, thus in the helium channel. The gas heating due to the vibrational-translational relaxation of vibrationally excited particles can therefore be neglected.

The ions collide with the particles from the neutral background gas and lose their energy in this process that is called Ohmic or Joule heating. The electrons and ions can also recombine, forming neutral particles with a higher energy. This process can also contribute to the heating of the gas.

In the plasma, metastable states of helium are also present, that mainly lose their energy via collisions and not via radiation, thus contributing to the increased gas temperature.

The change in gas temperature T_{gas} can be calculated with the heat transport equation [153]

$$\rho c_P \frac{\partial T_{\text{gas}}}{\partial t} = \nabla \cdot (\lambda_{\text{gas}} \nabla T_{\text{gas}}) + P_{e-n} + P_{i-n} + P_{e-i} + P_{\text{He}^*} \tag{6.1}$$

where ρ is the density of the helium gas, c_p the specific heat coefficient at constant pressure for helium, λ_{gas} the thermal conductivity of the helium gas and P_{e-n}, P_{i-n}, P_{e-i} and P_{He^*} the dissipated power density as gas heating due to the elastic electron-neutral and ion-neutral collisions, electron-ion recombination and collisional relaxation of helium metastables, respectively. P_{e-n} is given by [153]

$$P_{e-n} = 3 \frac{m_e}{M_n} n_e \nu_{e-n} (T_e - T_{\text{gas}}) k_B \tag{6.2}$$

with m_e the electron mass, M_n the mass of the neutral gas atoms (helium), n_e the electron density and ν_{e-n} the electron-neutral collision frequency. On the other hand, P_{i-n} is given by [153]

$$P_{i-n} = \sum_i \vec{j}_i \cdot \vec{E} = \sum_i e \vec{\Gamma}_i \cdot \vec{E} = e \sum_i (-D_i \nabla n_i + \mu_i \vec{E} n_i) \cdot \vec{E} \tag{6.3}$$

where the sum goes over all ions i, $\vec{j}_i$ is the ion current density, $\vec{\Gamma}_i$ is the ion flux for a drift-diffusion approximation, D_i is the ion diffusion coefficient, μ_i the ion mobility, n_i the ion density and $\vec{E}$ the electric field. Similar to [143], we neglect the heat conduction term in order to calculate the maximum increase in gas temperature. For P_{e-i} we use the electron-ion recombination reaction [154]

$$e^- + \mathrm{He}^+ \rightarrow \mathrm{He} \tag{6.4}$$

so that P_{e-i} is given by [155]

$$P_{e-i} = n_e n_{\mathrm{He}^+} k_{e-i} \Delta E_{e-i} \tag{6.5}$$

where n_{He^+} is the density of He^+, $k_{e-i} = 6.76 \times 10^{-19} T_e^{0.5}$ m^3/s [154] the rate coefficient for the reaction in equation (6.4) and ΔE_{e-i} the energy difference between the left hand side and the right hand side of the reaction equation. Similarly, we estimate the maximum contribution of P_{He^*} from the energy transfer in collisions between He^* and He:

$$P_{\mathrm{He}^*} = n_{\mathrm{He}^*} n_{\mathrm{He}} k_{\mathrm{He}^*} \Delta E_{\mathrm{He}^*} \tag{6.6}$$

in which n_{He^*} and n_{He} are the densities of He^* and He, respectively, ΔE_{He^*} is the energy transferred between He^* and He, and k_{He^*} is the rate coefficient for this reaction, estimated from [40]

$$k_{\mathrm{He}^*} = \sigma v_n = \pi \alpha_{\mathrm{He}}{}^2 v_n \tag{6.7}$$

with σ the corresponding cross section, α_{He} the radius of the helium atom and v_n the velocity of the neutral species He^* and He.

The different contributions to the increase in gas temperature are then as follows. The gas temperature increase due elastic electron-neutral collisions $\Delta T_{\mathrm{gas},e-n}$ is

$$\Delta T_{\mathrm{gas},e-n} = \frac{3}{\rho c_P} \frac{m_e}{M_n} n_e \nu_{e-n} (T_e - T_{\mathrm{gas}}) k_{\mathrm{B}} \tau_e \tag{6.8}$$

with the duration of these collisions equal to the electron lifetime τ_e, which can be calculated from [40]

$$\tau_e = \frac{1}{\pi N_n a_{\mathrm{He}}{}^2 v_e} \tag{6.9}$$

where N_n is the total gas density and v_e the electron velocity as given by [40]

$$v_e = \mu_e E \tag{6.10}$$

in which μ_e is the electron mobility and E the electric field. Likewise, the gas temperature increase due to ion Joule heating (elastic ion-neutral collisions) $\Delta T_{\mathrm{gas},i-n}$ is then

$$\Delta T_{\mathrm{gas},i-n} = \frac{e t_1}{\rho c_P} \sum_i (-D_i \nabla n_i + \mu_i \vec{E} n_i) \cdot \vec{E} \tag{6.11}$$

with the ion Joule heating time equal to the duration of the plasma t_1. For the electron-ion recombination, the increase of the gas temperature $\Delta T_{\mathrm{gas},e-i}$ is

$$\Delta T_{\mathrm{gas},e-i} = \frac{\tau_e}{\rho c_P} n_e n_{\mathrm{He}^+} k_{e-i} \Delta E_{e-i} \, . \tag{6.12}$$

The gas temperature increase due to relaxation collisions of He^*, $\Delta T_{\mathrm{gas},\mathrm{He}^*}$, is then

$$\Delta T_{\mathrm{gas},\mathrm{He}^*} = \frac{t_2}{\rho c_P} n_{\mathrm{He}^*} n_{\mathrm{He}} k_{\mathrm{He}^*} \Delta E_{\mathrm{He}^*} \tag{6.13}$$

with t_2 the lifetime of the helium metastables He^*.

6.4.2 Determination of main heating mechanism

As explained in section 6.4.1, the mechanisms that contribute to the heating of the gas by the plasma are elastic collisions between electrons and neutrals, elastic collisions between ions and neutrals, electron-ion recombination collisions and the collisional relaxation of helium metastables. The temperature increase that these collisions cause can be calculated from equation (6.8) for the electron-neutral interaction, from equation (6.11) for the ion-neutral interaction, from equation (6.12) for the electron-ion interaction and from equation (6.13) for the He^*-He interaction. We can further separate the temperature increase into a contribution from the ionization front and the channel behind the front, since some parameters of equations (6.8) and (6.11) to (6.13) have different values in these regions. From the results in this chapter and chapter 4, measured values (instead of estimated values as in [143]) can be taken for E, n_e, T_e and T_{gas}. $T_{gas} = 23\,°C$ and values for the other parameters are given in table 6.1. Bolsig+ [105] with cross sections from LXCat [106] is used to calculate μ_e, D_e and ν_{e-n}. Input values of $T_{gas} = 23\,°C$ and $E/N = 60.5$ Td with $N = N_n = 2.48 \times 10^{25}$ m^{-3} from the ideal gas law at atmospheric pressure and $T_{gas} = 23\,°C$ yield $\mu_e = 0.0965$ $m^2V^{-1}s^{-1}$, $D_e = 0.644$ m^2s^{-1} and $\nu_{e-n} = 1.92 \times 10^{12}$ s^{-1}. Subsequently, τ_e is calculated from equation (6.9) using μ_e to yield $\tau_e = 9.23 \times 10^{-11}$ s.

According to [34, 95, 143, 156], the electron impact ionization of helium molecules is considered as the main ionization process with reaction equation

$$He + e^- \rightarrow 2e^- + He^+$$
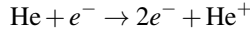
and these produced He^+ ions are considered to dominate in the ionization front. Using the expressions $\mu_{He^+} = 3.25 \times 10^{22}/N_n$ $m^2s^{-1}V^{-1}$ and $D_{He^+} = \mu_{He^+}T_{gas}k_B/e$ m^2s^{-1} from [153] yields $D_{He^+} = 3.34 \times 10^{-5}$ m^2s^{-1}. Based on the quasi-neutrality principle, $n_i \approx n_e$, while the spatial gradient of ∇n_i can be approximated as n_i/s [143] with s the length of the ionization front, estimated from figures 4.5 and 4.10, or the length of the ionization channel, taken from figure 4.6(a). Both values are given in table 6.1. t_1 for the ionization front is the time the front is present at a certain location, which is calculated from s/v_{front} with $v_{front} = 12 \times 10^4$ m/s from figure 4.6(b). For the ionization channel, t_1 is taken as the time it takes to reach the maximum length of the plasma plume and this values is taken from figure 4.6(a). The values for t_1 are also shown in table 6.1.

For the electron-ion recombination, we take the density of He^+ from simulations of [34] on the same jet as used in this thesis, to be $n_{He^+} \propto 10^{18}$ m^{-3} in the front and $n_{He^+} \propto 10^{15}$ m^{-3} in the channel. From the same simulations, we take $n_{He^*} \propto 10^{18}$ m^{-3} in the front and $n_{He^+} \propto 10^{17}$ m^{-3} in the channel. We approximate the velocity of the neutral helium species by the velocity of the ions: $v_n \approx v_{He^+} = \mu_{He^+}E$. The maximum energy that can be transferred in the electron-ion recombination reaction is the ionization energy, thus $\Delta E_{e-i} = 24.58$ eV. In the collisions

Table 6.1: Values for different parameters in the ionization front and the channel behind.

	Front	Channel
n_e (m^{-3})	1.5×10^{19}	0.5×10^{19}
T_e (eV)	1	0.25
E (kV/cm)	15	1.5
s (mm)	0.5	40
t_1 (ns)	4	600

between He* and He, the maximum energy transfer corresponds to the excitation energy of the metastable state He (2 ^{3}S), thus $\Delta E_{\text{He}^*} = 19.80$ eV. The lifetime of the helium metastables is estimated to be in the order of µs [34, 157].

The remaining parameter values are $\rho_{\text{He}} = 0.1618$ kg/m^3 at $T_{\text{gas}} = 23$ °C and $c_p = 5.19 \times 10^3$ J kg^{-1}K^{-1}.

Substituting these values into equations (6.8) and (6.11) to (6.13) yields a temperature increase of $\Delta T_{\text{gas},e-n} = 2.0 \times 10^{-4}$ °C for the gas heating due to electron-neutral collisions in the ionization front and $\Delta T_{\text{gas},e-n} = 1.5 \times 10^{-4}$ °C in the ionization channel. The ion-neutral collisions cause an increase of $\Delta T_{\text{gas},i-n} = 0.034$ °C in the front and $\Delta T_{\text{gas},i-n} = 0.017$ °C in the channel. The temperature increase due to electron-ion recombination is $\Delta T_{\text{gas},e-i} = 4.4 \times 10^{-12}$ °C in the front and $\Delta T_{\text{gas},e-i} = 7.3 \times 10^{-15}$ °C in the channel. The relaxation collisions of He* cause an increase of $\Delta T_{\text{gas},\text{He}^*} = 2.2 \times 10^{-8}$ °C in the front and $\Delta T_{\text{gas},\text{He}^*} = 2.2 \times 10^{-13}$ °C in the channel. In all cases, the heating is mostly caused by the ionization front and not by the ionization channel. It can also be seen that the heating caused by electron-neutral collisions, electrion-ion recombination and helium metastable relaxation is negligible with respect to the ion-neutral collisions. The total temperature increase is then $\Delta T_{\text{gas,tot}} = 0.051$ °C, which is much lower than the measured temperature increase of around 12 °C.

The calculated estimations for the estimated temperature increase are based on measured and simulated values, hence they should be relatively accurate. Nevertheless, the estimated gas heating is not of the same order as the measured one. A possible influence, that has not been taking into account in the estimations, is the presence of molecular impurities in the helium gas flow. The molecular species will get vibrationally excited and the subsequent relaxation will cause an increase in the gas temperature. These species then do not come from the admixed air, but instead it is mainly N$_2$ from the gas bottle and gas line. It is also possible that a large part of the gas heating takes place in a region of the plasma that has not been diagnosed (and for which we thus do not have the exact plasma parameters), namely the region between the electrodes where a pseudo-sheath is formed at the metal powered electrode and also under the grounded electrode. During the phase where charge builds up before the ionization wave starts, in which the plasma behaves similarly to a glow-like discharge until the electric field is shielded in front of the ground, the plasma in this region could heat significantly. Wang *et al.* [153] have shown by simulations of a direct current helium plasma at atmospheric pressure that the sheath region has a strong contribution to the gas heating. Since they found that their discharge resembles a glow discharge, it is possible that in our case this sheath region also has a significant influence on the gas temperature.

6.4.3 Comparison to AC jet

Similar to the comparison in section 5.4.2 of the electric field, air fraction and plasma plume length between the AC jet of [28] and the pulsed jet of this thesis, we can compare the gas temperature in these jets. In figure 6.7 the axial profile of the gas temperature is shown for the two jets, in both cases measured with a temperature probe. Since no results of a helium flow rate of 1500 sccm are shown in [28], we compare the results to the closest flow rates shown there, which are 1250 sccm and 1750 sccm. The temperature profiles of the AC jet are shorter, because the plasma plume has a length of 13.2 mm at 1250 sccm and 15.6 mm at 1700 sccm, which is $2.5-3$ times smaller than the length of the pulsed jet of 40 mm (shown in figure 4.6(a)). Both jets show an increase in temperature over axial position, but the temperature increase at the AC jet is steeper than at the pulsed jet because it takes place over a shorter distance. The temperature in the pulsed jet is everywhere $5-10$ °C higher than in the AC jet. The power

that is dissipated by the plasma in the AC jet is around 0.2 W [5], while in the pulsed jet this is around 36 W (calculated from figure 6.5a), which is around 180 times larger. However, the temperature difference in the two jets is much lower than a factor 180, which means that the temperature difference is not proportional to the power difference.

In chapter 5 we have argued that the electron and ion density can be expected to be significantly lower in the AC jet and since the gas heating due to electron-neutral collisions (equation (6.8)) and ion-neutral collisions (equation (6.11)) depend both linearly on these densities, this can explain the lower gas temperature in the AC jet compared to the pulsed jet.

From the results for the AC jet it can be seen that the gas temperature from the exit of the capillary until the end of the plume is higher for a lower applied flow. Since the heating depends on the energy density, thus on the amount Joules applied per liter of the gas, this is lower at larger flow rates.
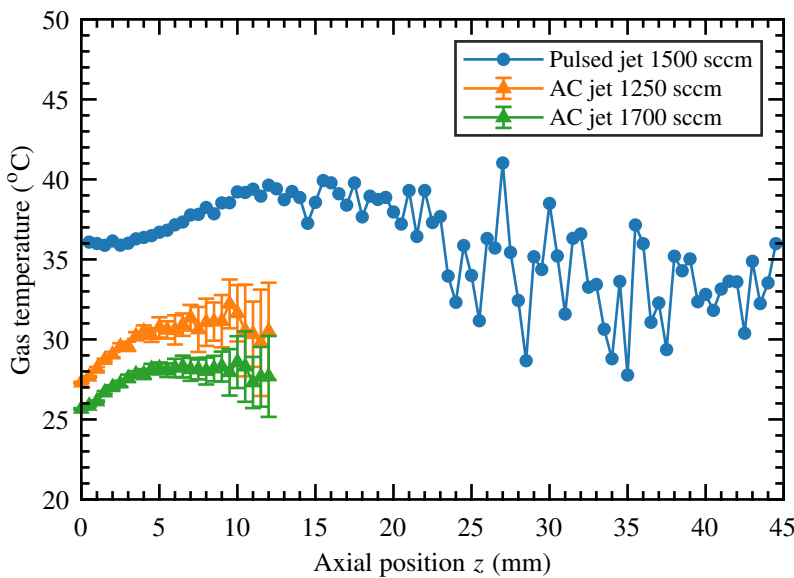
Figure 6.7: Gas temperature as function of axial position for the pulsed jet at 1500 sccm and the AC jet at 1250 sccm and 1700 sccm.

6.4.4   Increasing temperature in the effluent

The increase in temperature as function of axial position is visible both when the plasma is on as when the plasma is off, and therefore it cannot only be caused by gas heating due to the plasma. The gas temperature at plasma Off has been measured by Slikboer *et al.* [39] for different gas types at a flow rate of 700 sccm in a jet with the same geometry as used in this thesis, but operated horizontally. For a helium flow, similar results have been obtained: a heating of up to 5 °C in the central channel of the flow and a cooling of up to −5 °C in the channel around. Argon, on the contrary, has shown a cooling of up to −5 °C in the central channel and a heating of up to 2 °C in the channel around, while flows of N_2 , O_2 and air have shown no change in the gas temperature.

In an argon plasma jet with inner diameter of the capillary of 1.6 mm and powered by a 2.1 kV peak-to-peak voltage at 0.9 MHz with an argon flow of 3 slm, Schmidt-Bleker *et al.* [104]

measured by a fiber-optics probe and schlieren imaging a temperature increase in the central channel as well, of about 2 °C and 3 °C, respectively, from $z = 0$ to $z = 4$ mm. Using z/d as the axial position normalized on the diameter of the capillary, this corresponds to a temperature increase from $z/d = 0$ to $z/d = 2.5$. In our case, a similar temperature increase takes place from $z/d = 0.8$ to $z/d = 4.8$, which means that the gas temperature in our jet increases less rapidly. This difference could be caused by the difference in gas velocity, which is 24.9 m/s at the exit of the capillary in the jet of Schmidt-Bleker *et al.* and 5.1 m/s in our jet.

An increase of about 8 °C from $z/d = 0$ to $z/d = 4$, was observed through schlieren imaging by Chamorro *et al.* [134] in a 50 Hz oxygen plasma jet. This is again a steeper temperature increase than in our jet, approximately twice as steep, but the difference in gas velocity (212 m/s vs. 5.1 m/s) is significant and also oxygen is used instead of helium. As cause for the temperature increase a fast heating mechanism was suggested by Chamorro *et al.* , but their suggestions ([158, 159]) only take place in the presence of a plasma. A possible fast heating mechanism that present in a gas flow without plasma is the Joule-Thomson effect. The Joule-Thomson effect takes place when a gas at a certain temperature and pressure is passed through a membrane, porous plug or valve in a thermally insulated tube, where it expands and obtains a lower pressure [160, 161]. The temperature after the passing can either be lower or higher than before, depending on the Joule-Thomson coefficient of the gas:

$$\mu = \left(\frac{\partial T}{\partial P} \right)_H \tag{6.14}$$

that gives the temperature per unit change in pressure when the enthalpy is constant. Since ∂P is always negative for an expansion [160], a negative μ leads to heating and a positive μ to cooling of the gas. For helium at 1 atmosphere pressure and 25 °C, $\mu = -6.01 \cdot 10^{-2}$ °C/atm [162]. For the temperature increase of around 3 °C that is visible in figure 6.2, equation (6.14) yields a pressure drop of about 50 bar. Such a pressure drop is in the setup only possible at the pressure reducer that reduces the high pressure of the gas from the gas bottle to about 1 bar before the gas is fed to the mass flow controller. However, the travel distance of the gas from the pressure reducer to the exit of the capillary is more than a meter, a distance over which the gas will be thermalized. Non-thermalization is a prerequisite for the Joule-Thomson effect and therefore it seems not a plausible explanation in this case.

The temperature increase has also been observed at plasma On in an argon jet [104] and in an oxygen jet [134], as discussed before, while according to their positive Joule-Thomson coefficients (e.g. $\mu = 0.3590$ °C/atm for argon [163] at 1 atm and 25 °C), the Joule-Thomson effect would yield a decrease in temperature. However, the temperature increase in the argon jet could also be caused by the heating due to the plasma, since the cooling in the argon jet of Slikboer *et al.* [39] at plasma Off was only 2 °C below the ambient temperature, while the temperature in the argon jet of [104] rises up to 25 °C above the ambient temperature, which is significantly larger.

The axial position of the temperature increase corresponds to the position of the velocity increase of the ionization wave after it exits the capillary. This could be the cause for the temperature increase starting a few millimeters later at plasma On than at plasma Off. However, since there are no ionization waves at plasma Off, it cannot explain the existence of the temperature increase. The cause for the temperature increase remains therefore unknown.

6.4.5 Estimation of the electrohydrodynamic force

Apart from gas heating, collisions between neutral particles and charged particles also cause momentum exchange that can significantly impact processes in the plasma jet [164]. The associated force with this momentum transfer is the electrohydrodynamic (EHD) force, which is only significant in the non-neutral region in the plasma [165]. Following the streamer principle for the propagation of the ionization wave in the plasma jet, charged species in the ionization wave are accelerated by the electric field and transfer their momentum to neutrals via high-frequency collisions [164]. Since the densities of charged species are high in both the ionization front and the ionization channel behind the front, we can separate the contribution of both to the EHD force. Following the estimations in [125, 165], the EHD force acting on one ionization wave can be estimated as

$$F_{\text{EHD}} \approx n_i e E \tag{6.15}$$

where n_i is the ion density, e the elementary charge and E the local electric field. The ion density built up at the front should be of the same order as the electron density in the ionization wave [125] and the channel is quasi-neutral, thus $n_i \approx n_e$. Averaged in time, the EHD force becomes

$$F_{\text{EHD,mean}} \approx F_{\text{EHD,str}} f \delta t = n_e e E f \delta t \tag{6.16}$$

where f is the frequency of the applied pulse and δt is the time interval in which the ionization front or channel interacts with the neutrals from the background gas. For the front, δt is equal to s/v_{front} with s the length of the ionization front and v_{front} the velocity of the ionization front, while for the channel δt is equal to the time it takes to reach the given position in the plasma plume. Instead of making assumptions for (part of) these properties as in [125, 165], we can take the values for n_e, E, v_{front} and $\delta t_{\text{channel}}$ directly from the results of chapter 4 and estimate s from figures 4.5 and 4.10 to be 0.5 mm. At $z = 8.7$ mm, this yields $F_{\text{EHD,mean}}^{\text{front}} = 77.9 \pm 17.9$ N/m^3 for the ionization front and $F_{\text{EHD,mean}}^{\text{channel}} = 163 \pm 63.7$ N/m^3 for the ionization channel, which is close to the lower bound values calculated for a surface DBD in [165] ($F_{\text{EHD,mean}} \approx 5 \times 10^2 - 5 \times 10^4$ N/m^3) and lower than for a horizontally operated AC plasma jet in [125] ($F_{\text{EHD,mean}} \approx (1.4 - 4.8) \times 10^3$ N/m^3). In the case of the AC plasma jet, constant values have been taken for n_e, E and v over the whole propagation length and for s the length of the plasma plume is taken, meaning that the mean EHD force has also been averaged over the length of the plasma plume, while in our case the mean EHD force can be given at different axial positions and we can distinguish the contribution of the ionization front and the ionization channel. If we also take the average over the plasma plume length of the mean EHD force, $n_e \approx 1.25 \times 10^{19}$ m^{-3}, $E \approx 15$ kV/cm and $\delta t = 620$ ns, yielding $F_{\text{EHD,mean}} \approx 9.3 \times 10^3$ N/m^3, which is of the same order as $F_{\text{EHD,mean}}$ of the AC jet in [125].

Since we also have data of n_e, E, v_{front} and $\delta t_{\text{channel}}$ as function of the amplitude and pulse length of the applied voltage, we can study the influence of these parameters on the EHD force. The resulting mean EHD force, with the separate contributions of the front and the channel, is shown in figure 6.8 as function of applied voltage (a) and pulse length (b) at $z = 8.7$ mm. The error bars are calculated from the corresponding error bars of the parameters in equation (6.16). It can be seen that the contribution of the ionization channel to the mean EHD force is always larger than the contribution of the ionization front. On the one hand, the charged species density and the electric field in the channel are lower, but on the other hand the interaction time with the neutral species is higher, which yields net a higher mean EHD force. As function of the applied voltage, the mean EHD force of the channel and the front decreases with increasing voltage, because the increase in charged species density cannot cancel the decrease in interaction

time. At constant applied voltage, the mean EHD force of the ionization channel increases to a maximum with pulse duration until the pulse duration exceeds the propagation time of the ionization wave (as shown in chapter 4), because the interaction time is constant while the charged species density increases. Then, it decreases and increases again slightly, probably due to the extra potential that can be transferred from the powered electrode to the front (as discussed in chapter 5). The mean EHD force of the ionization front decreases until the pulse duration exceeds the propagation time of the ionization wave, because the velocity of the front increases thus the interaction time decreases while the charged species density increases. After this, it increases at the same rate as the EHD force of the channel due to the extra transferred potential.

6.4.6 Main mechanism that induces turbulence in the flow

It was shown in chapter 5 and in literature [32, 125, 127, 129, 164] that the presence of the plasma has an influence on the flow profile in the jet, since turbulent structures appear. Additionally, in this chapter we have estimated that energy supplied to the gas by the plasma heats the gas mainly due to ion-neutral collisions. We have also estimated the magnitude of the electrohydrodynamic force induced by the plasma in the ionization front and channel that causes momentum transfer between charged and neutral particles. To determine which of these mechanisms has the largest impact on the flow of the jet, we calculate the change in flow velocity that they both cause, since an increase in flow velocity can lead to an increase in turbulence in the jet [32, 124, 125, 127].

For the influence of the gas heating, the continuity equation for the mass flow rate at laminar flows can be considered [143, 166]:

$$\rho_{On}v_{On}A_{On} = \rho_{Off}v_{Off}A_{Off} \tag{6.17}$$

in which ρ is the helium mass density, v the flow velocity and A the cross-sectional area of the helium channel that is considered equal to the cross-sectional area of the capillary and thus is constant at plasma Off and plasma On. The subscripts Off and On refer, respectively, to the cases plasma Off with corresponding temperature $T_{gas,Off} = 23\ °C$ and plasma On with maximum temperature $T_{gas,On} = T_{gas,Off} + \Delta T_{gas,tot} = 36.7\ °C$. The flow velocity at plasma Off is calculated at the end of the capillary with the helium flow rate of 1500 sccm and inner diameter 2.5 mm to yield $v_{Off} = 5.09$ m/s. Using equation (6.17) with the helium mass densities at the corresponding temperatures then yields a flow velocity at plasma On of $v_{On} = 5.32$ m/s, which is an increase in velocity of $\Delta v_{heat} = 0.23$ m/s at the capillary exit. Until $z = 8.7$ mm, we have seen in chapter 5 that the width of the helium channel stays constant at plasma Off and On, but at positions even further down the plasma plume, a difference may occur. This diameter difference should then be taken into account in equation (6.17), which then can lead to a higher velocity increase if the diameter decreases at plasma On. For example, a decrease in diameter of the channel at plasma On of 10 % with respect to plasma Off, gives $A_{On} = 0.81A_{Off}$ and, keeping all other parameters the same, $v_{On} = 6.57$, which yields an increase of $\Delta v_{heat} = 1.48$ m/s.

The electric wind that is caused by the EHD force has an associated velocity v_E of [164]

$$v_E = \sqrt{\frac{2p_{dyn}}{\rho_{He}}} \tag{6.18}$$

in which ρ_{He} is the mass density of the neutral background gas (helium) and p_{dyn} is the dynamic pressure, corresponding to the integral of the EHD force over the length of the plasma plume L

(a)

(b)
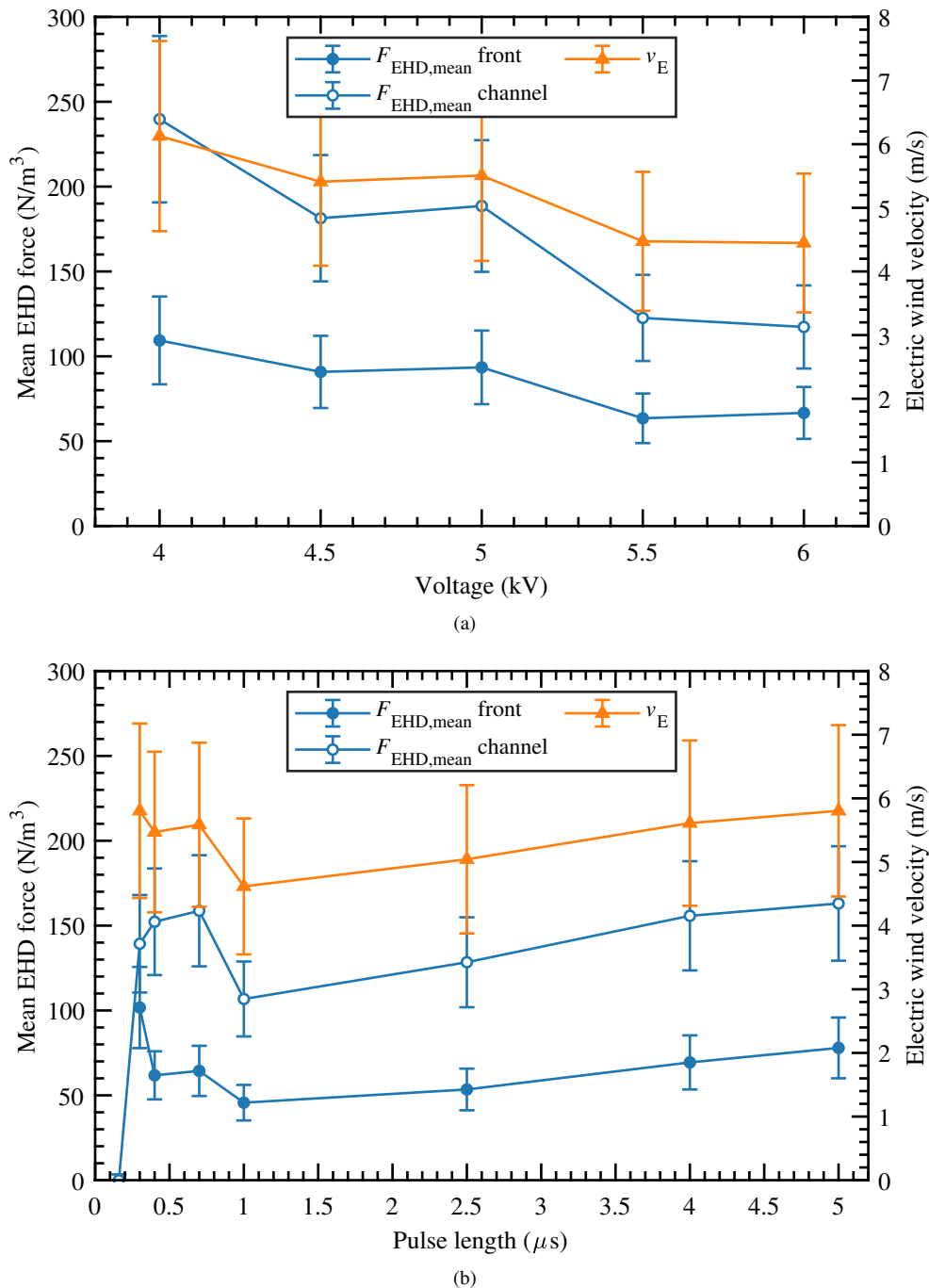
Figure 6.8: Mean EHD force at $z = 8.7$ mm as function of a) applied voltage (at 1 μs pulse length) and b) pulse length (at 6 kV applied voltage).

[164]:

$$p_{\text{dyn}} = \int_0^L F_{\text{EHD,mean}}^{\text{tot}} dz = \int_0^L \left(F_{\text{EHD,mean}}^{\text{front}} + F_{\text{EHD,mean}}^{\text{channel}} \right) dz \qquad (6.19)$$

with $F_{\text{EHD,mean}}$ as in equation (6.16) and L (from figure 4.11) the length of the plasma plume at the position where $F_{\text{EHD,mean}}$ is calculated. At $z = 8.7$ mm, the velocity of the electric wind is then calculated to be $v_E = 4.5 \pm 1.1$ m/s.

The plasma plume length and the EHD force depend on the amplitude and length of the applied voltage pulses and thus we can also calculate the velocity of the electric wind as function of this amplitude and pulse length. The results are shown in figure 6.8 next to the results for the mean EHD force. It can be seen that the electric wind velocity slightly follows the trends of the mean EHD force, although within the error bars we can say that the electric wind velocity stays approximately constant as function of applied voltage or pulse length around a value of $v_E \approx 5.3 \pm 0.8$ m/s. This means that the gas velocity is almost doubled.

Thus, comparing v_E and Δv_{heat} we see that $v_E > \Delta v_{\text{heat}}$. The main mechanism in our jet that increases the turbulence in the jet when the plasma is turned on is therefore probably the momentum exchange between the charged particles and the neutrals, and not the gas heating. Furthermore, adding $v_E \approx 5.3 \pm 0.8$ m/s to the initial gas velocity $v_{\text{Off}} = 5.09$ m/s yields an increase in Reynolds number (equation (5.17)) from 102.6 to 209.2, which corresponds to a turbulent regime according to [124].

In [143], Zheng *et al.* estimate the velocity increase due to heating to be 9 % of the initial flow velocity, which is larger than in our case but of the same order, and the velocity increase due to ion-neutral collisions five orders of magnitude lower than the initial flow velocity. They then conclude that heating is the main cause for the change in gas velocity and hence the increased turbulence. However, this estimate of the velocity increase due to ion-neutral collisions is not based on the electric wind and the EHD force, but on the calculated increase in helium ion velocity due to momentum conservation in such a collision. No contribution of the ionization channel is taken into account, which in our case accounts for a large part of the EHD force and thus the electric wind velocity. Since the timescale on which the channel contributes is larger than that of the front, this may be a reason why the estimated influence of momentum exchange between charged and neutral particles in [143] is lower than in our case.

6.5 Conclusions

In this chapter we have shown the gas heating that takes place in the plasma jet. The gas temperature has been measured with rotational Raman scattering and with a temperature probe. It was shown that at too low densities of air species in the gas, the gas temperature as obtained from Raman scattering is not reliable. A reliability limit for the temperatures obtained from Raman scattering was therefore set at a corresponding density of 10^{23} m^{-3}, which corresponds to an air fraction of around 1 %. The gas temperature was determined at different axial and radial positions in the jet for plasma Off and plasma On. At plasma Off, the temperature in the central helium channel was found to be around 5 °C higher than the surrounding air at $20-23$ °C, while a cooling of also around 5 °C was visible around this heated helium channel. At plasma On, the gas temperature in the helium channel was around 12 °C higher than at plasma Off, while the cooling around this channel was still present, although with a lower temperature difference with respect to the surrounding air. As function of axial position, the temperature shows an increase over the first $10-12$ mm from the exit of the capillary, both at plasma On and plasma Off. This increase has also been observed in literature with plasma jets fed by argon or oxygen. We have

calculated that it cannot be due to Joule-Thomson heating, because there is no sufficiently high pressure drop present in the setup of the plasma jet. Gas heating due to the plasma itself also cannot be the cause, because the temperature increase is also present when the plasma is absent. The exact cause of this increase remains therefore still unknown.

In chapter 5 we have shown that the amplitude, duration and frequency of the applied voltage pulses do not change the air fraction in the plasma jet. In this chapter however, we have shown that the gas temperature changes under the influence of the applied voltage pulse. We have explained these changes by the dependency of the measured energy per pulse on these parameters. The gas temperature increases with increasing amplitude of the applied voltage, because more energy per pulse is supplied, which increases the electron density while the electric field and electron temperature stay the same. Therefore, more collisions and thus more energy transfer can take place between electron, ions and neutrals, which increases the temperature of the gas. The length of the applied voltage pulse also has a positive influence on the gas temperature, since it also causes an increase in the energy per pulse and thus in the energy transfer in the plasma. As function of the frequency of the voltage pulses, the gas temperature also slightly increases, while the energy per pulse stays constant. Because every pulse supplies the same amount of energy, effectively more energy per unit of time is supplied and thus the gas temperature increases too.

The placement of a floating copper target at 1 cm from the exit of the capillary has shown to lead to higher gas temperatures in the region between the target and the capillary. This increase has been attributed to the increased electron density and temperature in the plasma, which will be shown in chapter 7. Furthermore, the gas flow structure was visible from the temperature map as regions with increased temperatures, since the helium flow formed rotating structures on the surface of the target at a few millimeter from the axis of the jet.

The results of both this chapter and chapters 4 and 5 have been used to determine the mean gas heating mechanism in the plasma jet and the main mechanism that induces turbulence in the jet. A heat transport equation was used to estimate the increase in gas temperature when the plasma is On with respect to when the plasma is Off. It was found that the contribution from ion joule heating due to elastic ion-neutral collisions dominates the increase in gas temperature. The calculated temperature increase of $\Delta T_{\text{gas,tot}} = 0.051$ °C is however much lower than the measured temperature increase of around 12 °C and thus some gas heating mechanisms may still be missing. Following the continuity equation for the mass flow rate, the change in flow velocity due to this gas heating was calculated to be $\Delta v_{\text{heat}} = 0.23$ m/s. The other mechanism that is present when the plasma is turned On is the electrohydrodynamic force due to the momentum exchange between the charged and neutral species. This EHD force induces an electric wind with a calculated velocity of $v_E = 5.3 \pm 0.8$ m/s. The electron wind velocity changes the Reynolds number from 103 to 209, which is above the threshold for the onset of vortices. Since this induced velocity is an order of magnitude larger than the velocity changed due to gas heating, it has been concluded that the electric wind from the EHD force is the main mechanism that causes turbulence in the studied jet.

7

Interaction of a plasma jet with grounded and floating metallic targets: simulations and experiments

Abstract: The interaction of kHz μs-pulsed atmospheric pressure He jets with metallic targets is studied through simulations and experiments, focusing on the differences between floating and grounded targets. It is shown that the electric potential of the floating target is close to the one with grounded target in the instants after the impact of the discharge, but rises to a high voltage, potentially more than half of the applied voltage, at the end of the 1 μs pulse. As a result, a return stroke takes place after the discharge impact with both grounded and floating targets, as a redistribution between the high voltage electrode and the low voltage target. Electric field, electron temperature and electron density in the plasma plume are higher during the pulse with grounded target than with floating target, as gradients of electric potential progressively dissipate in the latter case. Finally, at the fall of the pulse, another electrical redistribution takes place, with higher intensity with the highly-charged floating target than with the grounded target. It is shown that this phenomenon can lead to an increase in electric field, electron temperature and electron density in the plume with floating target.

7.1 Introduction

The interactions between non-thermal plasmas at intermediate to high pressures and surfaces is of great interest due to an increasing number of applications. These include biomedical treatment [12–14, 80], surface modification [18–20], catalysis [167, 168], and nitrification of liquids [21]. As shown in chapter 1, plasma jets are very useful tools for the study of those interactions, as they are able to repetitively deliver in remote locations a wide range of reactive and charged species, high electric fields and UV photons, at atmospheric pressure and while keeping low gas temperature. In chapter 6 we have shown that the gas temperature in a free helium jet does not exceed 40 °C in the measured range of the amplitude, length and frequency of the applied voltage pulses. However, when a floating metallic target was placed at 1 cm from the exit of the capillary, the temperature of the gas increased with around 5 °C in the helium channel between the capillary and the target. It was also shown that the helium flow distributed this heat over a larger radial area above the target.

In this chapter, we use the same diagnostics as for the free jet in chapter 4 to determine plasma parameters such as the electric field, electron density and electron temperature, but now with the presence of a metallic target underneath the plasma jet. Additionally, the potential in a floating metallic target is measured when interacting with the plasma jet. All results are compared to results from the two-dimensional fluid model that was also shown in chapter 4, but is now adapted to the case where a target is present. The results from this model are also used to explain the influence of grounding on a metallic target.

Several works have studied interactions of jets with targets, finding not only that the plasma affects the surface, but also that discharge dynamics can vary dramatically when interacting with surfaces with different electrical properties [84, 169, 170]. As such, in the last years there have been several investigations of jet interactions with targets of different electrical character: dielectric at floating electric potential [17, 26, 27, 29, 30, 36–38, 89, 91, 101, 108, 109, 116, 171–175]; dielectric attached to a grounded plate [26, 91, 101, 131, 176–183]; conductive at floating potential [30, 91, 109, 116, 174, 184–187]; conductive grounded [17, 35, 91, 116, 131, 176, 178, 180–183, 185–188].

These studies have distinguished the effect of dielectric targets of different relative permittivities ε_r and conductivities and of metallic targets on discharge dynamics. With low values of ε_r (approximately $\varepsilon_r \leq 20$) and conductivity and low capacitance, after the impact of the discharge on the target, the surface of the target is charged locally in a short time, which quickly leads to the depletion of the axial component of electric field and the rise of the radial component that sustains the propagation of the discharge on the surface [30, 101, 178–181]. With high values of ε_r or conductivity (liquid water-based surfaces) and with metallic targets, the charging of the surface is slower or inexistent, there is no radial component of electric field and no discharge propagation on the surface. Instead, a higher voltage drop remains in the gap, which promotes a return stroke and the formation of a conductive channel [1, 30, 35, 109, 116, 178, 180, 181, 188–190]. The return stroke is an ionization wave that propagates with reverse polarity with respect to the first ionization front [188–190]. It starts at the target where electron emission takes place and propagates in an already ionized channel towards the powered electrode, provoking charge separation of opposite sign to that generated by the first wave, thus partially neutralizing the plasma channel [1, 34]. The return stroke is driven by the gradient of electric potential between the target and the powered electrode.

Despite some recent studies, the difference between grounded and floating conductive targets is less characterized. It has been reported by experiments that the He flow channeling in jets is stronger over grounded metallic targets than over those at floating potential [185]. More-

over, in [91], experiments and simulations of He jets have been used to compare the discharge dynamics with floating and grounded dielectric and metallic targets, obtaining higher velocities of propagation, maximum electric fields, higher species production and higher *E. coli* cell inactivation with the grounded targets. The faster discharge propagation towards grounded targets has also been observed in [91, 101, 116, 187]. The simulation results in [116] have also shown higher ionization source term during propagation and higher electric field and electron density after impact on a conductive grounded target than on a conductive floating target. The experiments in [181, 186] have also observed higher production of reactive species in jets interacting with grounded conductive targets than in jets interacting with dielectric or floating conductive targets. [186] have reported lower viability of cancer cells when using a grounded substrate under the cells during plasma jet treatment. Furthermore, it has been shown through simulations in [101] that a dielectric target attached to a ground is significantly more charged by a He jet than the same target at floating potential. These differences suggest the importance of grounding or not the target for applications.

Another subject not fully understood in jet-target interaction is the discharge dynamics at the fall of the applied voltage. In jet experiments with dielectric targets using AC voltages a faint back discharge has been reported at the reversion of applied voltage polarity [27, 172]. In pulsed jets, similar phenomena have been reported at the fall of the pulse. In [178] the dynamics of charges at the fall of the voltage pulse has been described through simulations, not as a new discharge but as a balance between remaining positive and negative charges in the plasma and on the target surface. In [180] simulations of jets with grounded dielectric and conductive targets have observed an electric field reversal and a brief heating of electrons at the fall of the applied voltage. In the free jet experiments in [66] a secondary discharge has been observed at the end of the pulse and it has been attributed to the residual charges left from the first discharge. It has been found to have opposite polarity with respect to the first discharge and to be associated to an electric field below 6 kV/cm. Moreover, in [30, 181] a faint discharge at the fall of the voltage pulse has been reported, observed in the whole plasma channel, more pronounced with metallic target at floating potential than with dielectric or grounded metallic targets. The faint glow has been attributed to the neutralization of the space charge in the plasma channel in [181]. In fact, in [191] the electric field reversal at the falling edge of a positive voltage pulse and consequent secondary ionization have been investigated with a full kinetic treatment in argon discharges between planar electrodes on nanosecond time scales. It is claimed that the secondary ionization is induced by charge transport in the bulk plasma region. In our previous works on pulsed jets with dielectric targets [36, 38, 101], we have shown through comparisons between experiments and simulations on the electric field in the target induced by surface charges that the electrical redistribution at the fall of the pulse neutralizes the positive charge on the target surface and in some cases charges the target negatively.

In chapter 4 we have characterized a kHz atmospheric pressure He plasma jet without target powered by pulses of positive applied voltage through quantitative comparisons on several key parameters of plasma jet dynamics (i.e. length and velocity of discharge propagation, gas mixture composition, electron temperature and density and peak electric field) between experimental measurements combining different diagnostic techniques and two-dimensional numerical results. Excellent agreement has been obtained between experiments and simulations on the length and velocity of discharge propagation, the gas mixture distribution and the peak electric field in the discharge front, as well as a qualitative agreement on the electron density and temperature measured behind the high field front. Moreover, we have shown how the fall of the pulse of applied voltage leads to lowering the electric potential in the plasma and, in the case of short pulses, to stopping discharge propagation. In this chapter we combine different experimental di-

agnostic techniques (imaging, Stark polarization spectroscopy peak electric field measurements, Thomson scattering measurements of electron properties in the plasma plume and high-voltage probe measurements of the temporal evolution of electric potential of a floating target) and 2D fluid simulations to study the interaction of a positive pulsed He plasma jet with metallic targets and the influence of grounding or not the target on discharge dynamics before the impact, after the impact and after the end of the pulse. Moreover, we compare discharge parameters with metallic targets with those from the jets in chapter 4 without target.

Firstly, both the experimental and numerical setups for free jet, jet with metallic target at floating potential and jet with grounded metallic target are described in section 7.2. A set of assumptions to describe the floating metallic target in the model is proposed. Then, section 7.3.1 describes the general discharge dynamics with the three jet configurations in both experiments and simulations, focusing on discharge propagation and the associated peak electric field. Finally, section 7.3.2 describes in detail the charging of the floating metallic target and shows the influence it has on plasma parameters after the impact of the discharge on the target and after the fall of the pulse. As a result, the electrical redistribution associated to the fall of the pulse and its dependence on the target are characterized.

7.2   Setup

7.2.1   Experimental setup

As before, the geometry of the plasma jet is shown in figure 2.1 and a detailed description is given in section 2.1. The jet is powered by positive square high voltage pulses at a repetition rate of 5 kHz and with a helium flow of 1500 sccm. The width t_f and amplitude V_P of the pulses are varied to be 1 or 10 μs and 4, 5 or 6 kV, respectively. Three jet configurations are used: free jet, jet with metallic target at floating potential and jet with grounded metallic target.

As target, a copper plate of 8 mm × 8 mm with a thickness of 1 mm is used. For the measurements with target, the target is placed on a plastic, insulated plate that is connected to the holder of the jet itself. The distance between the target and the nozzle of the jet is set to 1 cm. In general, the distance between the target and the closest grounded plane, which is a table, is around 30 cm. The target can be grounded by connecting a cable to the ground on one end and to the target on the other end.

The same diagnostics as in chapter 4 are used to study various parameters in the plasma jet itself. An overview of these diagnostics with the parameters they provide is given in table 7.1. More information about the used diagnostics is given in the sections of this thesis that are mentioned in the table. The voltage and current that are applied to the jet are measured at the anode as described in section 2.2 using the setup of figure 2.3. Figure 7.1 shows the applied voltage as function of time, as well as the capacitive current I_{cap} in the top figure and the conductive current I_{con} in the bottom figure, for the three jet configurations: free jet, jet with floating metallic target and jet with grounded metallic target. I_{tot} is not represented for conciseness, but it can be found by adding I_{con} to I_{cap}. It can be seen that the capacitive current is basically the same in the three cases, as expected, but a difference is visible at the conductive current, namely just before the negative current peak. The implications of these differences will be analyzed in section 7.3.2.

Additionally, the potential of a floating metallic target is measured as described in more detail in section 2.8 with the setup that is shown in figure 2.17. Measurements of the potential of the target are performed with the floating metallic target placed at 1 cm from the exit of the capillary.

(a)

(b)
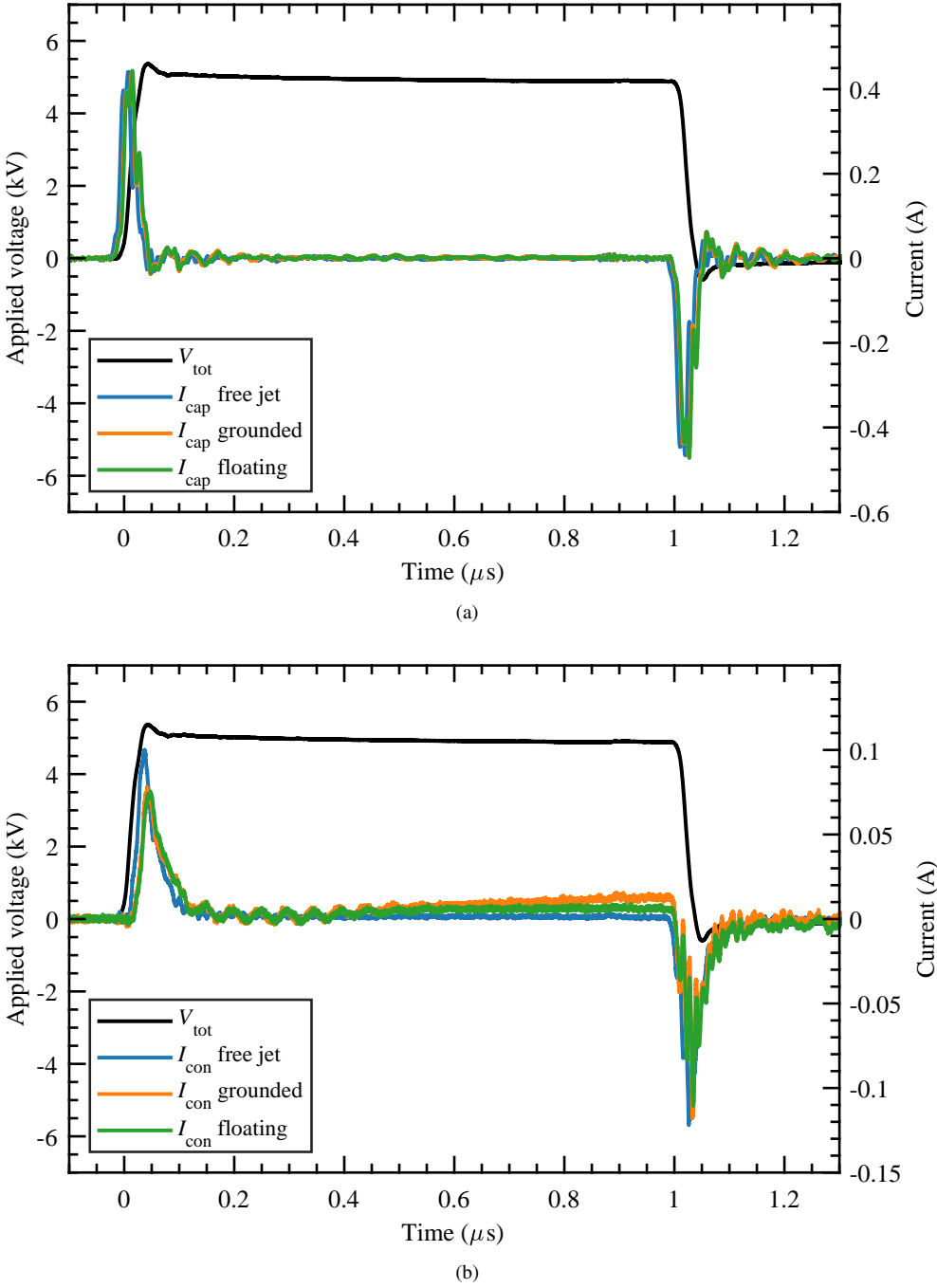
Figure 7.1: Applied voltage pulse together with a) the capacitive current and b) the conductive current for the free jet, grounded target and floating target cases. The *y*-axis for the conductive current has a smaller scale than for the capacitive current for better visibility.

Table 7.1: Used diagnostics, the resulting parameters of the plasma that are discussed in this work and references to the sections in this thesis with more detailed explanations of the diagnostics.

Diagnostic	Resulting parameter(s)	Reference
Electrical measurements	Voltage and current applied to the jet	section 2.2
ICCD imaging	Position and velocity of ionization front	section 2.3
Stark polarization spectroscopy	Electric field	section 2.4
Thomson scattering	Electron density and temperature	section 2.5
Rotational Raman scattering	Number density of oxygen and nitrogen	section 2.5

7.2.2   Numerical setup

We use the same two-dimensional axisymmetric fluid model as described in chapter 4 and our previous works [36, 101, 192]. The numerical setup is shown in figure 7.2. The model assumes in the whole domain atmospheric pressure and room-temperature $T = 300$ K. The geometries taken are as close as possible as in the experiments. A dielectric pyrex tube with a relative permittivity of $\varepsilon_r = 4$, length 3.3 cm (between $z = 0.0$ cm and $z = -3.3$ cm), internal radius $r_{in} = 1.25$ mm and outer radius $r_{out} = 2.0$ mm is used. Helium flows through the tube with a 1500 sccm flux as in the experimental conditions. A ring electrode is set inside the tube between $z = -2.8$ cm and $z = -3.3$ cm with inner radius 0.4 mm and outer radius 1.25 mm and a grounded ring is wrapped around the tube between $z = -2.0$ cm and $z = -2.3$ cm. The inner ring is powered by a positive applied voltage that increases from zero at $t_0 = 0$ ns during 50 ns until it reaches a plateau voltage V_P. It is then constant until $t = t_f$ and decreases until $t_f + 50$ ns, when it reaches zero, as in figure 4.1.

Three geometries are studied: 1) A free jet with no target present, but with a grounded plane set far from the tube at $z = 20$ cm. This is the same jet configuration as in chapter 4; 2) A jet with conductive metallic target at floating potential placed at $z = 1$ cm with 1 mm thickness and $\sim$64 cm^2 surface ($\sim$4.5 cm radius) as in the experiments, with a grounded plane set at $z = 20$ cm. This is the case represented in figure 7.2; 3) A jet with conductive metallic target at grounded potential placed at $z = 1$ cm.

The metallic targets are modelled as in [34], with infinite conductivity. To model the conductive target at a floating potential, we assume a very high relative permittivity $\varepsilon_r = 1000$, which guarantees that the target is isopotential. Unlike the grounded metal, the floating target charges and uncharges through the interaction with the plasma. However, unlike the case with dielectric surfaces, we consider that charges are conducted instantaneously inside the metallic material. Thus, we integrate the fluxes of inwards- and outwards-directed charged particles in time, to obtain the total net charge in the target Q and we distribute this charge instantaneously and homogeneously in the target as net volume charge density ρ. This approach is similar to the one recently used in [116], describing a floating metal as a material with $\varepsilon_r = 80$ and high conductivity. Finally, we consider the target as an ideal metal, i.e. a perfect absorber and perfect emitter, where an infinite number of free conducting charges can be exchanged with the plasma by mediation of the electric field. Therefore, we consider as for the grounded metallic target and the inner ring electrode, that electrons are emitted and absorbed and that ions are neutralized following a Neumann boundary condition for their fluxes through electric drift.

Figure 7.2 shows that in the model, the discharge setup is placed inside a grounded cylinder with a radius of 10 cm, to clearly define boundary conditions. The discharge dynamics is simulated through drift-diffusion-reaction equations for mean electron energy, electrons, posi-

tive ions and negative ions, and reaction equations for neutral species, coupled with Poisson's equation in cylindrical coordinates given by equations (4.1a) to (4.1f) At the surface of the tube, secondary emission of electrons by ion bombardment ($\gamma = 0.1$ for all ions) is taken into account. The surface charge density σ on the surface of the dielectric is obtained by integrating in time charged particle fluxes through electric drift to the surface. We consider that these charges then remain immobile on the surface of the dielectric.

In the experiments there is a high repetition rate ($f = 5$ kHz). However, there is uncertainty on what the exact initial conditions should be to reproduce the repetitive discharges [94]. To take this into account, we consider, as in our previous works [35, 36, 38, 101, 192], a standard uniform initial preionization density $n_{init} = 10^9$ cm^{-3} of electrons and O_2^+. However, no initial surface charges are considered on the surfaces. As in our previous works, the static flow is precalculated using [34, 102, 193]. In chapter 4 (figure 4.3) , the flow calculation from [28] with 1500 sccm of helium with 1000 ppm of air impurities flowing through the tube into air has been used and compared with radially-resolved Raman scattering measurements of air density ($N_2 + O_2$) in free jet configuration, yielding a good agreement. In this work, we use the same flow calculation for the free jet. For the cases with target, we use the same model to recalculate the flow for the geometry in figure 7.2 with a flow rate of 1500 sccm. Then, to use the local gas mixture compositions in the plasma model, we consider that helium contains O_2 impurities and flows downstream into an O_2 environment, as an approximation to air, as in chapter 4 and [192]. The spatial distribution of O_2 in the He-O_2 mixture obtained from the flow calculation with target is presented in figure 7.2.

The reaction scheme proposed in [101] is used to describe the kinetics in the He-O_2 plasma, including a total of 55 reactions with 10 species. All the parameters related to electron kinetics are calculated with the electron Boltzmann equation solver BOLSIG+ [105], using the
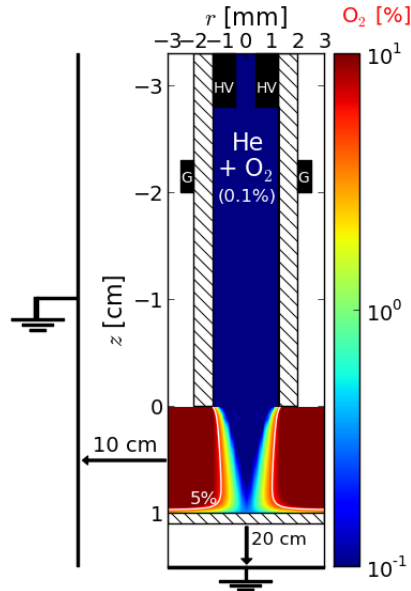
Figure 7.2: Side view schematics of the discharge setup used in the simulations in the case with metallic target at floating potential. The colour plot and the contour curves show the O_2 spatial distribution in the He-O_2 mixture (percentage over a total of 2.45×10^{19} cm^{-3} gas density).

IST-Lisbon database of cross sections in LXCat [106, 107], as functions of both the local gas mixture and the local mean electron energy ε_m. We describe photoionization using the approach described in [36, 90]. The ionizing radiation is assumed to be proportional to the excitation rate of helium atoms by electron impact and the photoionization source term is taken as proportional to the amount of O_2 (X_{O_2}) and thus we use as photoionization proportionality coefficient $A_{ph} = 100 \times X_{O_2}$ [90].

A finite volume approach and a Cartesian mesh are used in the model. The mesh size is 10 μm, axially between $z = -3.3$ cm and $z = 5.0$ cm (free jet case) or $z = 1.1$ cm (floating target case) or $z = 1.0$ cm (grounded target case) and radially between $r = 0$ and $r = 3.0$ mm. Then, in the rest of the domain the mesh size is expanded using a geometric progression. The average computational time required for a 2 μs simulation run to obtain the results presented in this paper was of four days with 64 MPI processes on a multicore cluster "Hopper" (32 nodes DELL C6200 bi-pro with two 8-core processors, 64 GB of memory and 2.6 GHz frequency per node). Further details on the numerical schemes and other characteristics of the simulations are given in [34].

7.3 Results and discussion

7.3.1 Characterization of discharge propagation and peak electric field

In this section, $V_P = 5$ kV and $t_f = 1$ μs are used. Firstly, we compare discharge propagation with metallic targets at floating potential and at grounded potential. Figure 7.3 presents the experimental imaging from light emission in the two cases at different instants: during discharge propagation, at discharge impact on the target, before the fall of the pulse at $t_f = 1000$ ns and after the fall of the pulse. These emission images are wavelength integrated and show mostly emission in the range of $200 - 600$ nm, since the sensitivity of the camera drops exponentially outside this wavelength range. From the emission spectra (not shown here) it is visible that the main sources are atomic helium (He I), the second positive system of N_2 and the first negative system of N_2^+.

Figure 7.3 shows a similar propagation towards the floating and grounded targets. However, the discharge propagates faster towards the grounded target, as impact takes place at around 300 ns after the start of the pulse, which is about 60 ns earlier than in the case with the target at floating potential. Then, both cases in figure 7.3 show a return stroke shortly after the impact on the target. In the grounded case, light emission from the plasma persists until the end of the pulse, and is particularly high in the plume region between the tube and the target, which suggests that reactivity in the plasma persists during that time. Conversely, with the target at floating potential, the emission intensity severely decreases until the end of the pulse in the whole plasma but especially in the plume. As the applied voltage falls to zero from 1000 to 1050 ns, the emission intensity progressively decreases in the whole plasma in the grounded case, while in the floating case it increases near the inner ring electrode from $t = 900$ ns to $t = 1060$ ns, which suggests an electric redistribution in that region. A light emission event at the end of the pulse has also been observed experimentally in [30, 36, 181] for jets with different targets. The results of experimental imaging are compared to the simulation results shown in figure 7.4. This figure presents the spatial distribution of the electron-impact ionization rate S_e, driven by the electric field, for the same two cases as in figure 7.3 and also at different instants. In fact, the numerical electron-impact ionization source term and the experimental light emission can be qualitatively compared, as is common approach [194].
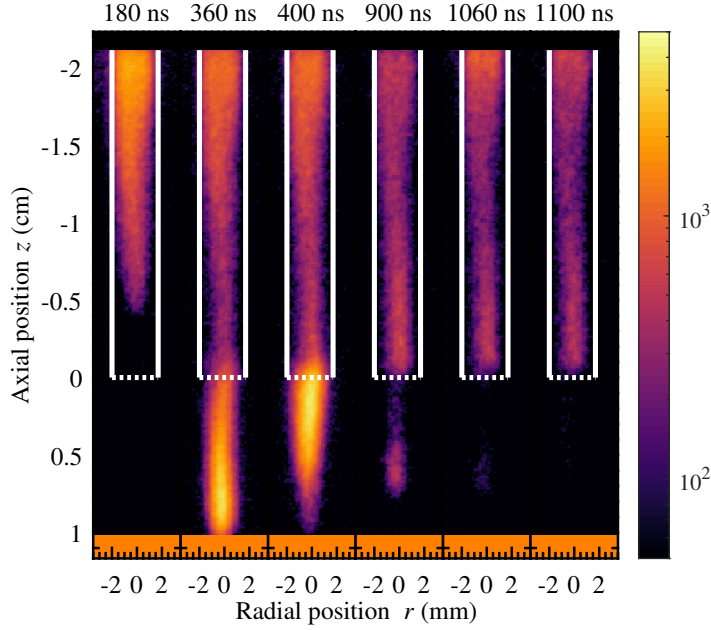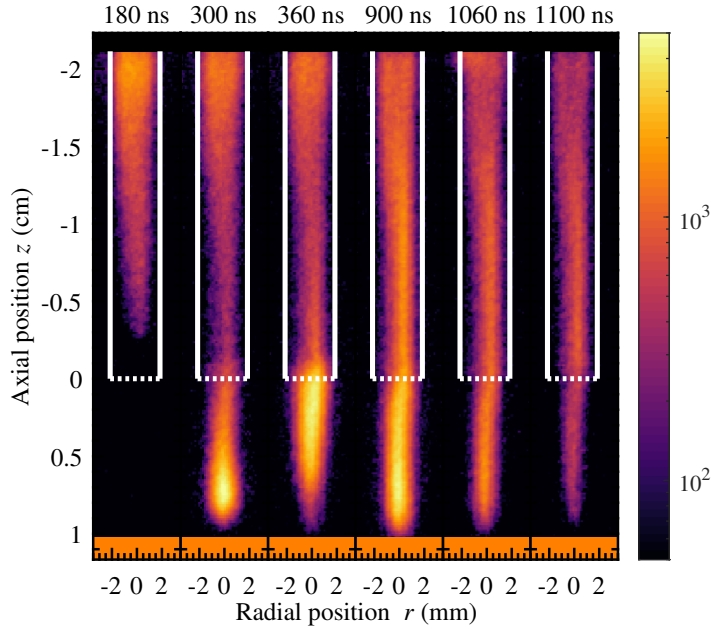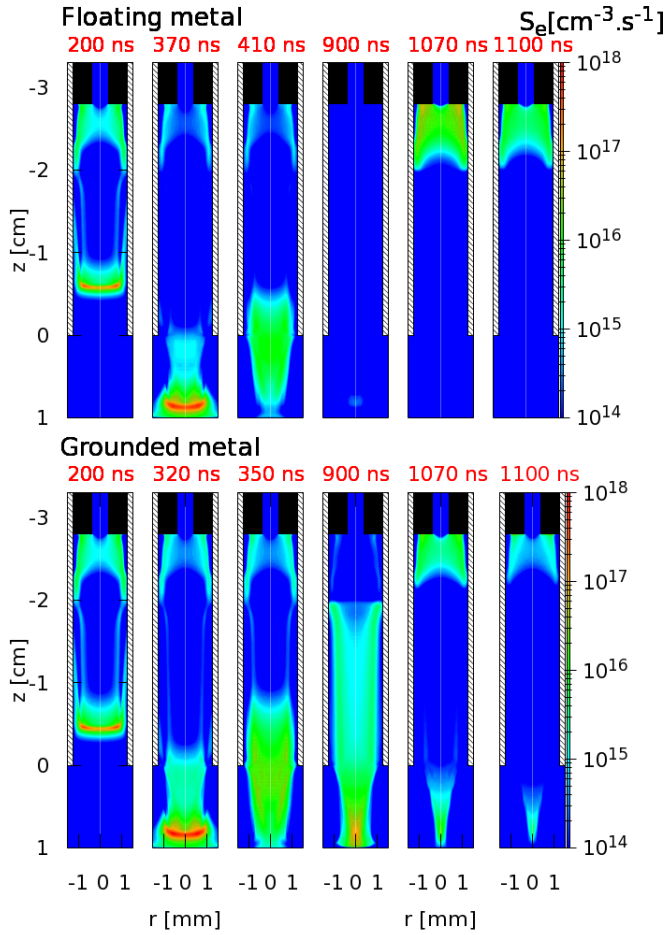
Figure 7.3: Imaging from the experiments with $V_P = 5$ kV and $t_f = 1$ μs, at different times, for the case with a metallic target at floating potential (a) and with a grounded metallic target (b). The colors represent the intensity of light emission in arbitrary units and are plotted on the same logarithmic scale in all images.

Figure 7.4 shows that in the simulations, as in the experiments, discharge propagation is faster towards the grounded target than towards the target at floating potential. The difference in time of impact between the two cases is approximately 50 ns, which is very close to the experimental one of 60 ns. For each case, the discharge impact on the target takes place around 10 to 20 ns later in the simulations than in the experiments. It has been shown in chapter 4 that this difference is mostly due to the time of ignition of the discharge.The difference in ignition time is attributed to the uncertainty in memory effects, such as the possibility of leftover surface charges between pulses (repetition rate of 5 kHz) on the inner surface of the dielectric tube, that are not taken into account in the simulations containing only one pulse. Indeed, it has been shown in that work that the propagation velocity in a free jet is the same in experiments and simulations. With both targets, the plasma structure is similar in the experiments and the simulations. However, close to the electrodes ($z \simeq -2$ cm), the plasma appears to be more centered in the experiments than in the simulations, in which case S_e has its maximum close to the tube walls. Conversely, close to the nozzle, it is shown that the discharge propagates with a

Figure 7.4: Cross section of the spatial distribution of the electron-impact ionization source term, from the simulations, with $V_P = 5$ kV and $t_f = 1$ μs at different times, for the case with a metallic target at floating potential (on top) and with a grounded metallic target (on bottom).

wider structure in the experiments than in the simulations.

As in the experiments, figure 7.4 shows a return stroke after the impact with both the floating and grounded targets, with values of S_e around 10^{16} cm^{-3} s^{-1} in the floating target case at $t = 410$ ns and up to 10^{17} cm^{-3} s^{-1} with grounded target at $t = 350$ ns. The return stroke is driven by the gradient of electric potential between the target and the powered electrode that transports electrons emitted from the metallic targets, as will be shown in section 7.3.2. Its presence with the target at floating potential suggests that the target has a low potential immediately after the impact of the discharge. With the floating target, it is visible that S_e in the plasma in the simulations decreases from the time of impact to the end of the pulse. Indeed, S_e is no longer visible at $t = 900$ ns in the floating target case. Conversely, with the grounded target, S_e remains visible until the end of the pulse, with higher intensity in the plume than in the tube, with values up to 10^{17} cm^{-3} s^{-1}. Both results agree with the experimental observations in figure 7.3 and the simulation results in [116]. These results imply that an electric field remains in the plasma between the powered electrode and the grounded target, while in the case of the target at floating potential the potential gradients in the plasma dissipate as the target is charged, as will be shown in section 7.3.2.

After the end of the pulse, as the voltage of the inner ring electrode falls to zero, a new dynamics takes place. Indeed, as happens with light emission from experiments, S_e increases close to the inner electrode, which requires the presence of an electric field in that region, between the grounded inner ring and the plasma. S_e after the fall of the pulse is more intense with the charged target at floating potential, reaching 10^{17} cm^{-3} s^{-1}, than with the grounded target. During the pulse, as the floating target is charged, its electric potential can rise to values of the same order of the applied voltage, which is not the case with the grounded target, as will be shown in section 7.3.2. Then, when the applied voltage falls to zero, the gradient of potential between the new grounded electrode and the plasma is higher in the case with floating target than with grounded target.

In order to deepen the understanding on discharge propagation and quantitatively compare simulations and experiments, in figure 7.5 we follow the position of the discharge front in time in experiments and simulations. Besides the two cases presented in figures 7.3 and 7.4, the results with free jet (no target) and $V_P = 5$ kV are also shown and compared. In the experiments, the position of the discharge front is obtained from the maximum of the light emission intensity, with an errorbar of 0.07 cm, while in the simulations it is obtained from the maximum of the axial component of electric field $E_{z\text{MAX}}$. That approach allows to follow the propagation of the first ionization wave in both experiments and simulations and of the return stroke in simulations but not in experiments. The numerical result is shifted by 30 ns to account for the difference in time of ignition with respect to the experiments.

Figure 7.5 shows, as in chapter 4, a small difference between the ignition time in experiments and simulations of about 30 ns and an excellent agreement in discharge propagation for every case. In both experiments and simulations, the discharge propagating towards the grounded target is faster than in the other cases, all along the propagation, due to the proximity of the ground, as has also been shown in experiments and simulations in [91, 101, 116, 187]. Conversely, the discharge propagates faster towards the floating target than in the free jet case only when the discharge is close to the target. The ground is placed at $z = 20$ cm in both cases and thus does not justify the difference. Indeed, the difference in velocity is due to the influence of ε_r on propagation ($\varepsilon_r = 1000$ in the floating target case and $\varepsilon_r = 1$ in air in the free jet case). It has been shown in [101] that ε_r does not significantly change the velocity of discharge propagation, except when the discharge front is very close to the target surface, mostly in the last 5 mm of propagation. There, the velocity of propagation increases with ε_r. A difference between dif-

ferent targets on electron density and peak electric field only at a few mm from the surface has also been measured in [29, 30] and simulated in [91, 186]. Finally, the simulation results in


(a)

(b)
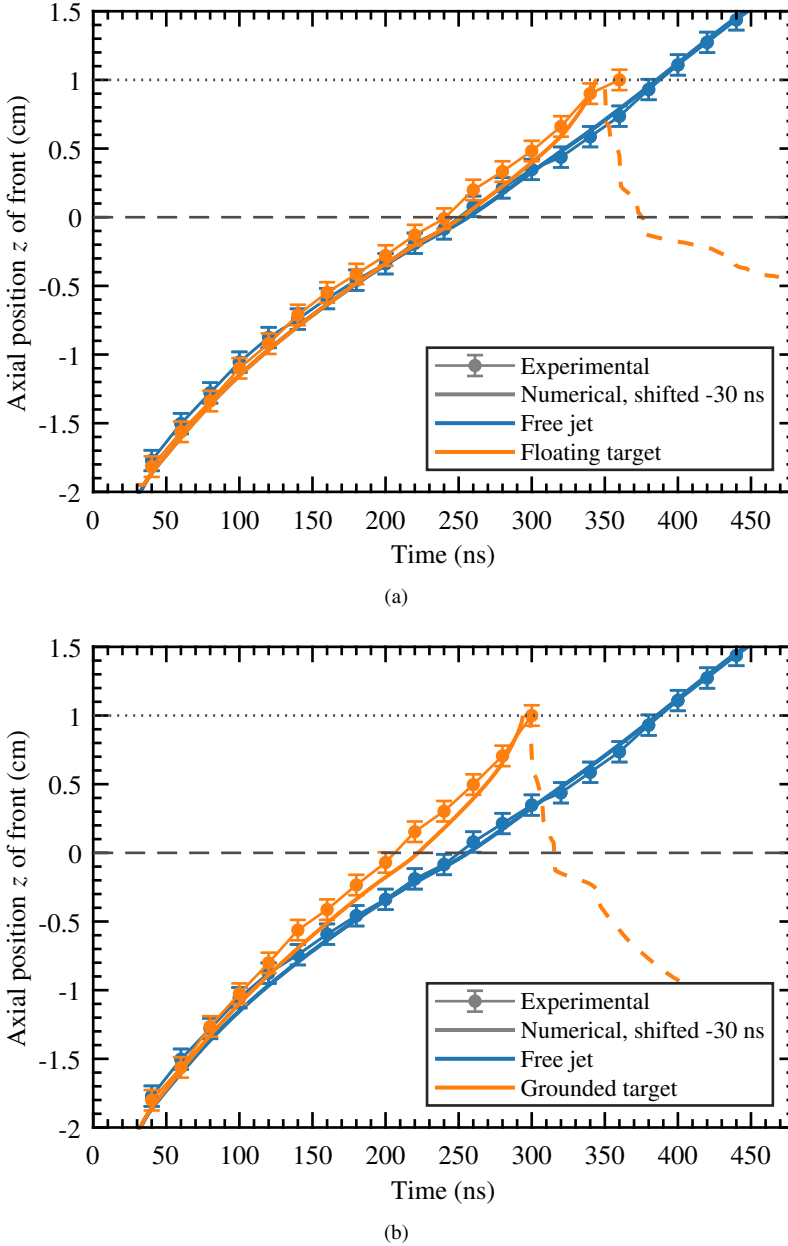
Figure 7.5: Temporal evolution of the position of the discharge front during propagation and after impact, from simulations and experiments, with $V_P = 5$ kV and for the three different configurations. a) Free jet (no target) and metallic target at floating potential. b) Free jet and grounded target. The return stroke from the simulations is represented with dashed lines. The horizontal dotted line indicates the position of the target and the horizontal dashed line the capillary exit.

figure 7.5 show the return stroke propagating from the target towards the inner electrode, with both grounded and floating targets. The return stroke propagates faster than the first ionization wave, in agreement with the cases in [35, 188] for grounded target and both positive and negative polarities of applied voltage.

In figure 7.6, the value of $E_{z\text{MAX}}$ along the propagation is presented for the three previously described cases. Both experimental Stark shift measurements and simulation results are shown. In both cases, $E_{z\text{MAX}}$ is the peak electric field in the center of the front [109], with a radial uncertainty of the size of the slit width of 100 μm. As explained in [109], $E_{z\text{MAX}}$ in the experiments comes from the distance between the allowed and forbidden lines of the studied helium band, where the position of the forbidden line changes the most due to the high electric field. The error in the electric field values is taken as the uncertainty of the fit in determining the wavelength position of both lines, yielding values of around ± 1 kV/cm, as can be seen in figure 7.6. Hence, the measured $E_{z\text{MAX}}$ might not be the highest at the measured position, but actually an average value within a range of ± 1 kV/cm. This range of ± 1 kV/cm around the maximum of E_z corresponds to a distance of around $z \pm 0.1$ mm around its position, according to the simulations. Therefore, we take the average E_z within a distance of $z \pm 0.1$ mm around the maximum of E_z found in the center for $r < 0.1$ mm, accounting for the slit width. The axial averaging of E_z has been shown in chapter 4 to be a more accurate way to compare simulation results with Stark shift electric field measurements than taking the local maximum of E_z. Moreover, we have verified that the difference between the maximum of E_z for $r < 0.1$ mm and its radial average within $r < 0.1$ mm is negligible.

Between the three different jet configurations, in both experiments and simulations, there are
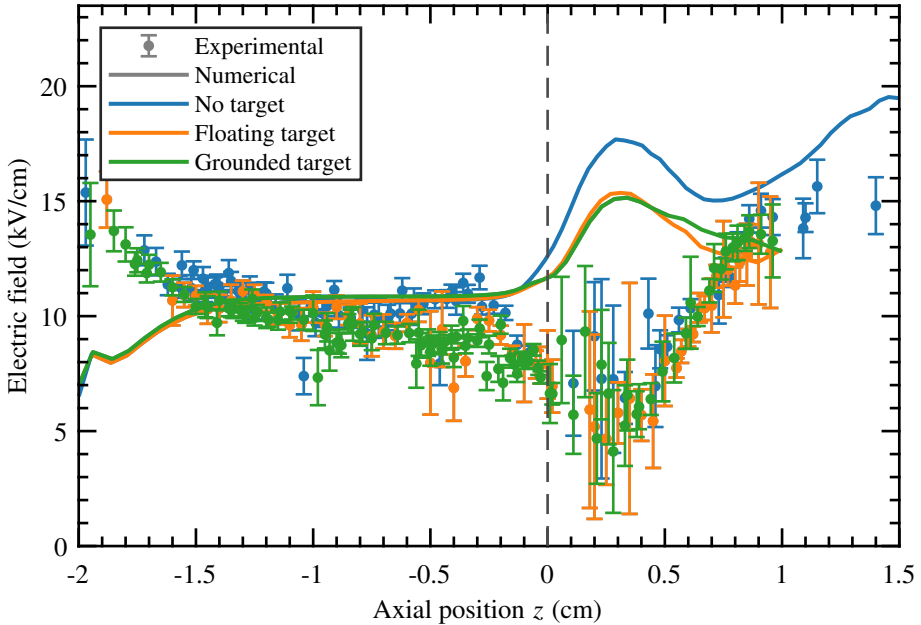
Figure 7.6: Evolution of the peak electric field along discharge propagation, from simulations and experiments, with $V_P = 5$ kV and for three different configurations: free jet (no target), metallic target at floating potential and grounded. Average within $z \pm 0.1$ mm of $E_{z\text{MAX}}$ for $r < 0.1$ mm. The vertical dashed line indicates the capillary exit.

only small differences in $E_{z\text{MAX}}$. That is also the case for the propagation shown in figure 7.5 and in the electric field measurements with different targets in [29]. $E_{z\text{MAX}}$ obtained from the experiments and from the simulations presents a good agreement, with $E_{z\text{MAX}}$ around 10 kV/cm in the tube, between $z = -1.5$ cm and $z = -0.5$ cm, and rising to higher values (< 20 kV/cm) outside the tube. However, as both experiments and simulations assess $E_{z\text{MAX}}$ in the center, the agreement between numerical and experimental results decreases in the regions where the discharge structure is different in experiments and simulations (see figures 7.3 and 7.4), as was already the case in chapter 4 with free jets: close to the electrodes ($z < -1.5$ cm) and to the nozzle ($z \simeq 0$). As the experimental discharge is tendentiously wider close to the nozzle, the electric field is more off-centered than in the simulations and thus its value at the center is lower in the experiments. Likewise, close to the electrodes, as the discharge is more centered in the experiments, $E_{z\text{MAX}}$ is higher at the center than in the simulations. Moreover, the increase of $E_{z\text{MAX}}$ just outside the tube in the simulations may be due to the change of permittivity between the tube with $\varepsilon_r = 4$ and the ambient air with $\varepsilon_r = 1$ [114]. The fact that the tube edges are sharp in the model, while they are rounded in the experiments, might contribute to the difference. However, as shown in figure 7.5, the differences between simulations and experiments in discharge structure and $E_{z\text{MAX}}$ do not lead to a significant difference in discharge propagation velocity. Indeed, we have shown in chapter 4, through comparisons of discharge dynamics with different applied voltages, that $E_{z\text{MAX}}$ profiles are not directly related to discharge propagation velocities, in agreement with studies in air streamer discharges [96]. Velocities are dependent on geometry and on the magnitude of applied voltage, while the electric field is related to the local charge separation.

7.3.2 Jet-target interaction

In this section, we study the dynamics taking place after the impact of the discharge on the target. Firstly, figure 7.7 presents the temporal evolution of the electric potential in the conductive metallic target at floating potential. Experimental and numerical results are shown for three cases of V_P: 4, 5 and 6 kV. In the experiments, two different lengths of pulse are used for each case: $t_f = 1$ µs and $t_f = 10$ µs. In the simulations, only $t_f = 1$ µs is used.

Figure 7.7 shows that the target potential in the experiments for pulses with $t_f = 10$ µs starts increasing at the impact of the discharge and slowly rises due to electron emission and ion neutralization until saturation is reached after some µs at a potential slightly below V_P. It is visible that both the time of impact of the discharge and the time of saturation are inversely proportional to V_P. Thus, the pulse width and the applied voltage allow to control the charging of the floating target, as shown also in [36] for a dielectric target. With short pulses of $t_f = 1$ µs, the charging of the target is interrupted. As the applied voltage in the inner ring electrode is dropped, the target changes from cathode to anode and the electric potential slowly decreases by electron absorption, reaching almost zero at $t = 2$ µs. Negative charge deposition after the fall of the pulse due to reversal of electric field direction has also been observed in experiments and in simulations with different dielectric targets [36, 38, 101]. However, even with short pulses of $t_f = 1$ µs, the target potential reaches non-negligible values at the end of the pulse, of almost 2/3 of V_P when $V_P = 6$ kV, 1/2 of V_P when $V_P = 5$ kV and 1/4 of V_P when $V_P = 4$ kV. Conversely, in the simulations the target potential has a first increase with the approach of the discharge, mostly due to electron emission by effect of the electric field. Then, the potential increases faster after the discharge impact. Indeed, it rises faster than in experiments and saturates at about 2 kV below V_P. In the cases with $V_P = 5$ and 6 kV, the saturation takes place during the 1 µs pulse, approximately 400 ns after the impact with $V_P = 6$ kV and 600 ns after the impact in the

$V_P = 5$ kV case. After the end of the pulse, the potential also decreases faster in simulations than in experiments, decreasing to half its value in about 150 ns, instead of 400 to 700 ns registered in experiments. In both experiments and simulations the rate of charging and uncharging grows with V_P. The difference between the experimental and numerical results of charging of the target will be discussed in section 7.3.3.

The total charge in the target can also be obtained from the simulations. Although not shown here, it follows approximately the same temporal profile as the electric potential in the target, reaching values of around 2.0, 3.6 and 4.0 nC at the end of the pulse, respectively for $V_P = 4$, 5 and 6 kV. These values agree with those presented in [101] for $V_P = 6$ kV, where it has been shown through simulations that a floating dielectric target of $\varepsilon_r = 80$ charges up to 2 nC in about 400 ns and a grounded dielectric target of $\varepsilon_r = 56$ charges up to 10 nC in the same timescale. As expected for a floating conductive target, the value obtained here for $V_P = 6$ kV stands between those two cases. However, as the charge is distributed in the large metallic target, 4.0 nC corresponds to only ~ 0.06 nC cm^{-2} of surface charge density. This value is much lower than those in dielectric targets that charge locally up to 70 nC cm^{-2} [36, 101]. As the target is charged in the model through ion neutralization and electron emission, both driven by the electric field, and considering that electrons are approximately 100 times more mobile than ions, we can conclude that the number of electrons emitted during the charging is of the order of 10^{10} (1 nC corresponding to approximately 6×10^9 elementary charges). Considering the case with $V_P = 6$ kV, where the target charges approximately 1 nC per 100 ns, we can calculate a flux of electron emission through the discharge cross section of ~ 0.05 cm^2 of approximately 0.2 nC ns^{-1} cm^{-2} or 10^9 ns^{-1} cm^{-2} electrons. Likewise, electrons are absorbed after the fall of the pulse with a flux ~ 0.3 nC ns^{-1} cm^{-2}. Finally, we calculate the self-capacitance of the target as $C = Q/V$ to be between 1.0 and 1.2 pF, where Q is the total charge in the target and V is its
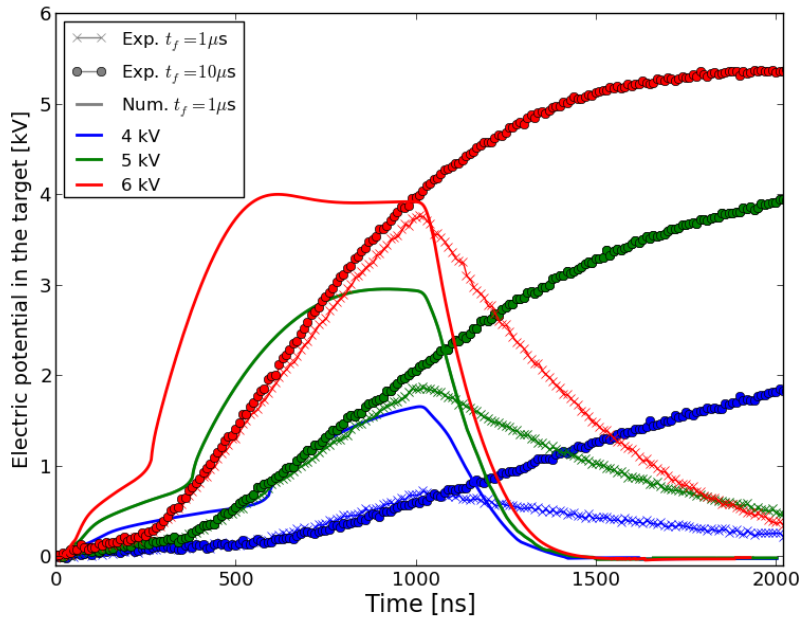
Figure 7.7: Temporal evolution of the electric potential in the metallic target at floating potential, from simulations and experiments, with $V_P = 4$, 5 and 6 kV.

potential. In [184], with a jet powered by a voltage with peak of 6-7 kV impacting on a copper target with an imposed capacitance in the order of a few pF, the charge accumulated in the target has been measured through time integration of the discharge current to have a maximum of $4 - 5$ nC, in agreement with our results.

Despite the differences, both experimental and numerical results in figure 7.7 support the conclusion that the metallic target at floating potential has a voltage close to zero at the time of discharge impact, which allows it to behave approximately like a grounded target in the instants after the impact. However, at the end of the pulse the target is charged and thus its interaction with the plasma is expected to be different from that of a grounded target. Then, we analyze the consequences of jet-target interaction on the plasma. In the experiments, the temporal evolution of electron temperature T_e and electron density n_e has been measured through Thomson scattering in a jet with $V_P = 6$ kV and floating copper target, in the center at $r = 0$ and at $z = 8.7$ mm, at only 1.3 mm from the target. This is represented in figures 7.8(a) and 7.8(b).

In the experiments, T_e first increases to 4 eV as the discharge arrives. As the position assessed is very close to the target, the propagation of the return stroke is not distinguishable from this first peak of T_e. Then, as the return stroke propagates further into the tube, T_e decreases close to the target. However, T_e returns to 4 eV and stays with that value until the end of the pulse, which suggests a continuous reactivity in the plume. This would not be the case if the target would charge up to $V_P = 6$ kV, in which case the plasma would tend to be a quasineutral channel. Then, as the applied voltage falls, there is an increase in T_e to almost 5 eV, to which follows a slow decrease. The experimentally-measured n_e follows the same evolution, remaining close to 10^{14} cm^{-3} during the pulse and then increasing after the fall of the pulse. The increase of n_e after the fall of the pulse shows that the electrical redistribution taking place between the inner electrode (now cathode) and the plasma, limited by a target charged at 4 kV (figure 7.7), can effectively transport or produce a significant amount of electrons. The experimental values of T_e and n_e in this work agree with already published results [30], where the same jet has been used, but add the increase in n_e after the fall of the pulse.

The experimental T_e and n_e are compared with the simulation results in the same figures (figures 7.8(a) and 7.8(b)) for the same case. The simulation results of T_e and n_e have been retrieved every 10 ns without temporal averaging, as 10 ns is also the duration of each measurement. The numerical results are presented both locally at $r = 0$ and $z = 8.7$ mm and averaged within the volume of the laser beam in the Thomson scattering measurements, i.e. within a cylinder of 50 μm radius and 100 μm length centered at $r = 0$ and $z = 8.7$ mm. The temporal evolution of the axial component of electric field E_z is also presented, in figure 7.9, at the same position and in the middle of the plume, at $r = 0$ and $z = 5$ mm. This quantity is not accessible in experiments and therefore is represented exclusively as a simulation result with a resolution of 1 ns.

The numerical result for the case with floating target and $V_P = 6$ kV (blue curves) qualitatively agrees with the experimental measurements. Firstly, the comparison of the two numerical curves of T_e and n_e allows to conclude that although the averaging affects n_e by about 20%, its effect is invisible on T_e and it is not a fundamental factor when analyzing the data in this case, due to the relatively small volume of the laser beam. T_e has a peak as the discharge front impacts the target, within the errorbar of the experimental one. The peak takes place 40 ns later than in the experiments due to the difference in time of impact. Then, T_e falls to 2 eV and increases slowly during the pulse until 3 eV. At the end of the pulse, the numerical T_e has a sudden drop and a sudden increase. Although the drop is not obtained by the measurements, the increase is in agreement between simulations and experiments. The numerical values of T_e are generally lower than the experimental ones. We should notice that T_e is obtained from Thomson scattering measurements assuming that the lowest energy electrons (most of the population) follow a
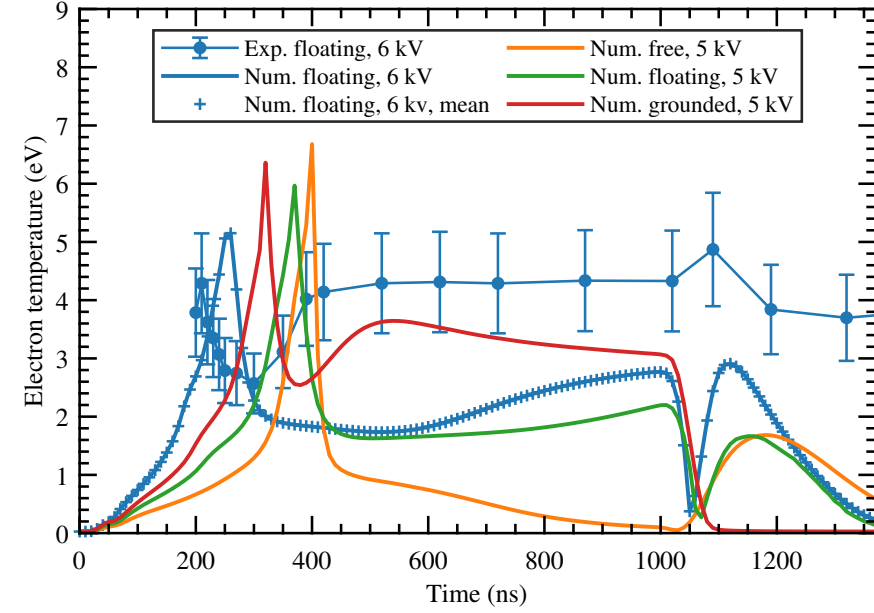
(a)
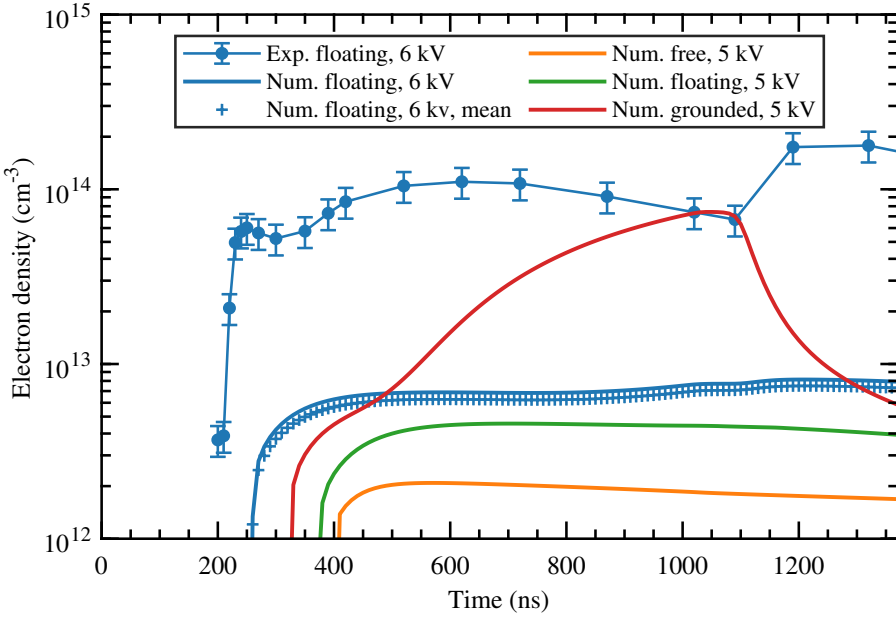
(b)

Figure 7.8: Temporal evolution of the electron temperature (a) and the electron density (b) at $r = 0$ and $z = 8.7$ mm with results from the experiments and simulations with the metallic target at floating potential and $V_P = 6$ kV and also from the simulations with $V_P = 5$ kV and the three different configurations. The plus-sign markers correspond to the numerical results averaged over $z \pm 50$ µm and $r \to 50$ µm.

Boltzmann EEDF. However, the EEDFs calculated from Bolsig+ present deviations from the Boltzmann EEDFs. Indeed, the EEDFs have more populated bulk and less populated tail than the equilibrium solution. Thus, the Boltzmann assumption potentially leads to an overestimation of T_e from Thomson scattering measurements. This effect has been quantified for argon microwave discharges in [195], leading to differences in T_e up to a factor 4. For the same case with floating target and $V_P = 6$ kV (black and grey curves), n_e follows approximately the same evolution in simulations and experiments, but is more than one order of magnitude lower in simulations than in experiments. This difference has already been observed in chapter 4 in a free jet case and is discussed in that chapter, along with the values of n_e and T_e in experiments and simulations. There, we have verified that the difference between simulations and experiments is in agreement with literature and that it is not expected to be due to any perturbation of the studied discharge by the laser used in the experiments. Then, as in chapter 4, we assume that the difference may be related to the assumption of oxygen instead of air in the model and to the unknown memory effects of discharge repetition.

E_z presented in figure 7.9 for the floating target case at $z = 8.7$ mm and $z = 5.0$ mm with $V_P = 6$ kV (black curve) confirms the conclusions taken from the analysis of the temporal evolution of T_e. In addition, figure 7.9 allows to observe the direction of the electric field at each stage. Firstly, we observe the peak of E_z in the direction of propagation with amplitude 14 kV/cm associated to the arrival of the discharge front. Then, the return stroke propagates from the target towards the powered electrode as a wave of opposite polarity, with a second peak of E_z that is also positive, as shown in [35, 188]. At $z = 8.7$ mm, at only 1.3 mm from the target, the second peak of E_z is very close in time to the first peak and thus is not identifiable. At $z = 5$ mm, the return stroke is associated with a peak of E_z of ~ 4 kV/cm. During the rest of the pulse, the electric field in the plasma remains directed downwards with a much lower amplitude close to 1 kV/cm. After the fall of the applied voltage, E_z reverses sign and then is directed from the charged target towards the inner grounded electrode and tends to neutralize the net charge in the plasma. The reversal of direction causes E_z to pass by zero, which explains the drop of T_e around $t = 1050$ ns in figure 7.8(a). Then, E_z has a peak at $t = 1100$ ns in both axial positions of around -2 kV/cm, which results in a small increase in n_e. The similar peak of E_z in both positions shows that the electrical redistribution at the end of the pulse has a diffusive character and not that of a wave, as suggested by the observations of faint emission in [30, 181]. Its direction and value below 6 kV/cm agree with the findings in [66].

Besides the cases already discussed, the numerical temporal evolutions of T_e, n_e and E_z are represented in figures 7.8(a), 7.8(b) and 7.9, respectively, for three different jet configurations with $V_P = 5$ kV: free jet, jet with floating target and jet with grounded target. The results for these cases are represented only locally, and not averaged. The simulation results for floating target and $V_P = 5$ kV are very similar to those with $V_P = 6$ kV. Nevertheless, these are significantly different from the results with free jet and with grounded target. For all the cases, the peak T_e and E_z at the arrival of the discharge front at $z = 8.7$ mm stand between 5 and 7 eV and between 12 and 16 kV/cm, respectively. Then, with free jet, as there is no return stroke and a quasineutral plasma is formed behind the discharge front, T_e and E_z decrease to low values close to zero after the propagation, in agreement with the experimental observation in [30]. n_e in the channel is lower in free jet than with metallic targets, also in agreement with [30]. As figures 7.6 and 7.9 show that the peak electric field during discharge propagation is not lower in the case without target, we attribute the lower n_e to the absence of the target and of the return stroke. The influence of the return stroke on the increase of n_e has been demonstrated experimentally in [30] and numerically in [34], supported by the measurements of helium metastable density in [188], and in [180].

Here we assess the origin of the increase of n_e during the return stroke. Figure 7.8(b) shows that n_e in the plume at $z = 8.7$ mm obtained from the simulations for the case with $V_P = 5$ kV and floating target reaches a value around 2×10^{12} cm^{-3} higher than in the case without target and
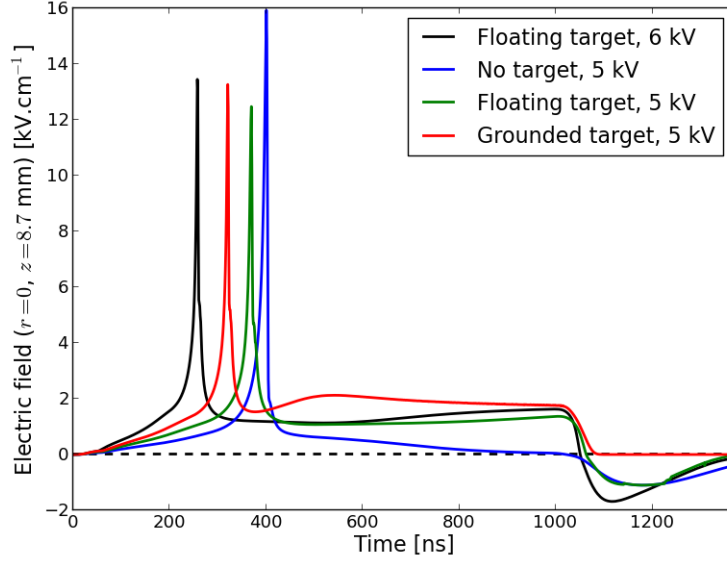
(a)
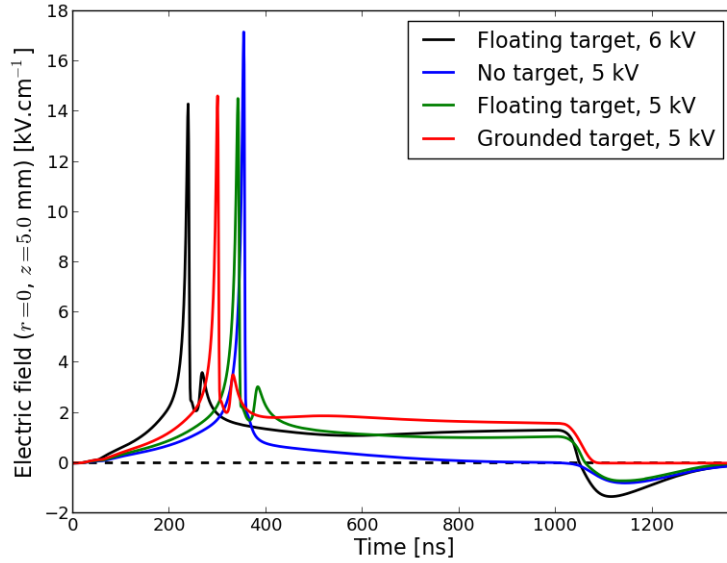
(b)

Figure 7.9: Temporal evolution of the electric field at $r = 0$, at $z = 8.7$ mm (a) and at $z = 5.0$ mm (b). Results are shown from the simulations, for $V_P = 5$ kV and the three different configurations and for $V_P = 6$ kV and the metallic target at floating potential. The horizontal dashed line signals $E_z = 0$.

thus without return stroke. This increase takes place mostly in the first 100 ns after the impact of the discharge on the target at around $t = 370$ ns. On the one hand, figure 7.4 shows that the electron-impact ionization source term S_e during those 100 ns does not exceed 10^{17} cm^{-3}.s^{-1} and thus cannot produce more n_e than 10^{10} cm^{-3}. Even though other ionization processes take place in volume (Penning ionization, photoionization, associative ionization [34]), they cannot justify an increase in n_e of the order of 10^{12} cm^{-3}. On the other hand, figure 7.7 shows that the potential of the target rises up to 1.5 kV until $t = 470$ ns, corresponding to a charging of approximately 2 nC and thus the emission of 1.2×10^{10} electrons. If these were homogeneously distributed through diffusive and convective transport in the plasma with 3.8 cm length and 0.125 cm radius (volume 0.19 cm^3), an increase in n_e of 6.4×10^{10} cm^{-3} (approximately one third of 2×10^{12} cm^{-3}) could be expected. This distribution is not homogeneous in the whole volume and thus the electron emission has a larger impact close to the target, where n_e has been assessed. These results allow to conclude that electron emission from the target and the subsequent transport of electrons in the plasma are the main source of the experimentally and numerically observed increase of n_e and are important aspects of the return stroke.

With grounded target, as a sharp potential gradient remains in the plasma during the pulse, a conductive channel is formed between the electrodes (with the possibility of a transition to an arc phase on longer timescales). T_e and E_z remain relatively high during the pulse, close to 3.5 eV and to 2 kV/cm, respectively, and n_e increases with time during the pulse up to 8×10^{13} cm^{-3}. This increase in n_e is also associated with electron emission from the target, since S_e presented in figure 7.4 could only account for an increase in n_e of the order of 10^{11} cm^{-3} in a few hundreds ns. In agreement, [116] have also reported higher E_z and n_e after discharge impact with grounded target than with floating target. This can explain the higher species production, higher *E. coli* cell inactivation and lower cancer cell viability with grounded targets reported in [91, 181, 186]. The difference between targets during the pulse is also visible in the experimental results of the conductive current at the inner electrode with $V = 5$ kV, presented in figure 7.1. Indeed, by integrating I_{con} in time, we have measured 6.0 nC in the case with grounded target during the pulse, excluding the positive and negative peaks. Conversely, only 1.1 nC and 1.9 nC have been measured with the free jet and with the floating target, respectively. These values agree in order of magnitude with the 3.6 nC simulated at the floating target (figure 7.7).

Then, as the applied voltage falls, the electrical redistribution between the inner ring and the plasma affects the plasma differently in each case. As in the case with floating target with $V_P = 5$ kV, the fall of the pulse in the free jet brings a rise in T_e up to 2 eV and in negative E_z up to -1 kV/cm, which results in approximately constant n_e. The electric field in these cases is directed from the plasma at positive potential towards the inner grounded ring. Conversely, with grounded target, the electrical redistribution takes place between a grounded inner electrode and a grounded plane. For that reason, its effects are weaker than in the case of a floating target charged at 3 kV in the $V_P = 5$ kV case. Indeed, with grounded target, T_e and E_z decrease to very low values after the pulse and n_e decreases in time. With grounded target, as $E_z \simeq 0$, transport through electric drift is excluded and thus the decrease in n_e after the pulse is attributed to diffusive and chemical losses. As such, we can conclude that in the other two jet configurations n_e is kept constant or increases (with floating target and $V_P = 6$ kV) after the fall of the pulse due to electron emission from the inner electrode and electron transport towards the target. This analysis is reinforced by the negligible values of S_e in the plasma plume after the fall of the pulse observed in figure 7.4 and by the decrease in electric potential of the target due to electron absorption observed in figure 7.7. In [191] the secondary ionization at the falling edge of a pulse of applied voltage is also claimed to be induced by charge transport. These results concerning the fall of the pulse constitute a major difference between grounding and not grounding the

target.

7.3.3 Discussion on the discrepancy of charging and uncharging the floating metallic target

The faster charging and uncharging of the floating metallic target in simulations than in experiments (figure 7.7) leads to questioning the conditions for comparison and the assumptions taken in the model. Firstly, both experiments and simulations have verified that changing the position of the grounded plate behind the target between $z = 15$ and $z = 31$ cm has no influence on the results. Then, we should consider that in [36] we have used the same model with secondary electron emission ($\gamma = 0.1$) instead of a perfect electron emitter assumption to describe the interaction between the discharge and a dielectric BSO target. We have found an excellent agreement with experiments on the electric field evolution inside the target, which is closely related to surface charge, for both charging (ion neutralization and electron emission) and uncharging (electron absorption) of the target. However, taking the same secondary electron emission assumption as in [36] for the metallic targets has a negligible effect (~ 0.2 kV) on the results of figure 7.7, although it removes the potential increase before the discharge impact. Furthermore, it decreases the agreement with experiments in figures 7.8(a) and 7.8(b).

The model describes metallic surfaces as perfect absorbers and perfect emitters of electrons, and thus ignores the cathodic sheath between the plasma and the metallic surface and simplifies the dynamics of charges between the plasma and the surface. In [196] a voltage drop of $0.2 - 0.3$ kV in the sheath between air streamers at atmospheric pressure and cathodes has been suggested. This value is too low to justify the different rate of charging in figure 7.7. However, a recent work [197] that highlights the importance of streamer-cathode sheaths has shown through numerical simulations a voltage drop of 1.5 kV over 50 μm when a nitrogen streamer at 26.7 kPa approaches a grounded cathode. [197] also suggest that the description of streamer-cathode sheaths lies outside the conditions for validity of both the drift-diffusion approximation used in fluid models and the two-term approximation for solution of the electron Boltzmann equation.

Furthermore, the works of Bronold and co-authors [198] have initiated a microscopic description of charge transfer across plasma walls leading to the calculation of electron absorption, backscattering and secondary emission coefficients. Other works [116, 199, 200] simulate the fluxes of electron emission from metallic surfaces from ion bombardment, thermionic emission, field emission or photo-emission processes. These factors point to potential improvements of the model that could lead to better agreement between numerical and experimental results in figure 7.7.

Finally, in the experiment a thin oxide layer is very likely to be formed on the copper surface interacting with the plasma and could be responsible for diminishing the conductivity of the target [16]. As the model supposes the conductivity to be infinite, this could justify the slower rise and fall of electric potential in the experiments.

7.4 Conclusions

This chapter has addressed the interaction of kHz μs-pulsed atmospheric pressure He jets with metallic targets through simulations and experiments, focusing on the differences between floating and grounded targets. Three jet configurations have been studied with positive polarity of applied voltage: free jet, jet with metallic target at floating potential and jet with grounded

metallic target. The same conditions have been taken in experiments and simulations. Experimentally, the jets have been studied through imaging and Stark polarization spectroscopy peak electric field measurements. In the case with floating copper target, electron properties in the plasma plume have been assessed through Thomson scattering measurements and the temporal evolution of electric potential of the target under plasma exposure has been measured with a high voltage probe. Numerically, an axisymmetric two-dimensional plasma fluid model has been used. A description of the floating metallic plate as an isopotential infinitely conductive surface where ions are neutralized and electrons are emitted and absorbed through effect of the electric field has been proposed.

Experiments and simulations have observed the same discharge dynamics. The discharge propagates faster towards the grounded target than in the other two configurations. With floating target, the discharge only propagates faster with respect to the free jet case in the last 5 mm of propagation. Moreover, experimental and numerical results both show that the peak electric field at the discharge front during the propagation is approximately the same between the three different configurations. With both grounded and floating targets, a return stroke has been observed after discharge impact on the target, as an ionization wave propagating from the target towards the powered electrode in an already ionized channel. With grounded target, reactivity stays in the plasma plume during the 1 µs pulse, while with floating target it severely decreases in a few hundred ns. At the fall of the applied voltage pulse, another electrical redistribution takes place between the now grounded inner electrode and the positive plasma. This has been shown to have higher intensity with floating target than with grounded target.

The explanations for the differences between grounded and floating targets have been found in the temporal evolution of electric potential of the floating target. The discrepancy between simulations and experiments in that temporal evolution has been discussed, taking into account that the model describes metallic surfaces as perfect absorbers and emitters of electrons. A more accurate description of electron absorption, backscattering and emission from the surfaces has been pointed as a potential future improvement of the model. However, both experiments and simulations have shown that the potential of the floating target after discharge impact increases a few kV per µs, depending on the amplitude of applied voltage. Thus, the pulse width and the applied voltage allow to control the charging of the target. After the pulse, the potential decreases at approximately those rates, until approaching zero. As such, during dozens of ns after the impact, the target is close to grounded but, at the end of the 1 µs pulse, it is at a high voltage, potentially more than half of the applied voltage. That explains the similar return stroke with floating and grounded targets. Furthermore, it justifies the decay in reactivity during the pulse with floating target as the target charges and potential gradients in the plasma dissipate. As a result, simulations have shown that the electron temperature and electric field remain high in the plasma with grounded target and the electron density in the plasma plume increases during the pulse with grounded target but not with floating target or without target. Finally, the charging of the floating target has shown that the redistribution at the end of the pulse takes place between a grounded inner electrode and a plasma limited by a charged surface in the floating target case, while with grounded target it takes place between two grounded electrodes. That justifies the stronger intensity of that redistribution with floating target. Experiments and simulations have shown an increase in electron temperature, magnitude of electric field and electron density in the plume with floating target after the pulse, which is not the case with grounded target. The increases in electron density in the plume after the pulse with floating target, during the return stroke with both floating and grounded targets and during the whole pulse with grounded target, have been shown to be mostly due to electron emission from metallic surfaces and charge transport in the plasma.

8

General conclusions and perspectives

Abstract: This chapter summarizes and combines the conclusions of the obtained results in this thesis. A perspective for future research on the plasma jet is also given.

8.1 Conclusions

In this thesis, we have studied a kHz pulsed atmospheric pressure helium plasma jet and focused on the propagation dynamics of the ionization waves in the jet and the influence of the plasma on the gas flow. Different optical, laser and electrical diagnostics have been used to assess different parameters of the plasma and the flow and, where possible, the results have been compared to those of a two-dimensional fluid model. The plasma has been studied when the jet operated freely and when it interacted with a metallic target. The main conclusions are summarized below.

8.1.1 Free jet

Propagation dynamics

We have studied the propagation of the ionization waves in the plasma jet by following the position and velocity of the ionization wave. Excellent agreement has been obtained between experiments and simulations on the propagation length and velocity of the ionization wave, for different values of the magnitude and pulse duration of the applied voltage. At an applied voltage pulse with a magnitude of 6 kV, duration of 1 µs, frequency of 5 kHz and helium flow of 1500 sccm, the ionization waves take around 620 ns to reach their maximum propagating distance of 40 mm from the exit of the capillary, with a velocity of around 10^5 m/s. The maximum axial electric field in the ionization front has been determined inside the tube, with a value of around 10 kV/cm, and in the plasma plume up to 2 cm from the exit of the capillary, where it rises up to 20 kV/cm. The results from the experiments and simulations agree well, with a maximum discrepancy of 11 %. Furthermore, the increase of the electric field in the plasma plume as measured in the experiments is shown to quantitatively agree with the simulations. Comparison of the electron density around the ionization front has provided the same trends in experiments and simulations, with an increase in the plasma plume, but no quantitative agreement. In the region of 3 mm to 10 mm from the capillary exit, the experiments have shown an increase in electron density from 0.4×10^{13} cm^{-3} to 2×10^{13} cm^{-3}, which is higher than the values from the simulations ($0.2 - 0.5 \times 10^{13}$ cm^{-3}) in the same region. The electron temperature has shown a decrease with values from the experiments of 3 eV near the capillary exit down to 0.5 eV at a 2 cm distance, which is lower than the simulations that have shown electron temperatures of 4 eV near the capillary exit down to 0.5 eV around a 3.5 cm distance. The divergence between the experiments and the simulations has been attributed to the uncertainty in memory effects between voltage pulses and in plasma chemistry coefficients.

The simulations have shown large gradients in the electron density and temperature, in both axial and radial direction. Their values depend therefore highly on the position in the jet where they are measured. The simulations have also suggested that the location where Thomson scattering measures the electron density and temperature is the quasi-neutral channel behind the ionization front and not inside the high field front. This is then the reason why the electron density is higher than in the front and increases along the plasma plume, while the electron temperature is lower and decreases along the plume.

It has been shown by both experiments and simulations that the propagation of the ionization wave stops during the applied voltage pulse for long pulses (≥ 1 µs) and by the action of the fall of the pulse for shorter pulses (< 1 µs). The propagation length of the ionization wave decreases with decreasing voltage amplitude or pulse duration. However, during these variations the electric field remained the same. For the same variation in parameter values, the temporal

evolution of the potential in the ionization front has been assessed by the simulations. It has been found that this potential slowly decreases during the propagation of the ionization wave and is forced to decrease faster at the end of the pulse. Furthermore, the propagation stops when the potential in the ionization front is below a certain threshold.

Results from the simulations have suggested that this threshold is defined by the gas mixture at the position of the front: a linear relation has been found between the necessary potential in the front and the local concentration of oxygen. The rise in the electric field in the plasma plume can therefore be explained by the necessary potential in the head that increases further down the plume, because the local oxygen concentration increases. The necessary potential in the front to sustain propagation depends on two parameters: a slope parameter that is defined by the gas composition at a given position and an offset parameter that is related to the potential applied to the powered electrode during the ionization wave propagation.

Comparison of the pulsed jet of this thesis with published results on a plasma jet with the same geometry, but powered by a 30 kHz AC voltage with an amplitude of 2 kV, has yielded more insight in the propagation dynamics in the plasma jet. Even though the shape of the applied voltage is different, it is found that the electric field in the ionization front in the two jets is the same, at equal helium flow rates. Measurements on the density of N_2 and O_2 in the pulsed jet, mixed from the ambient air into the helium, have shown that these densities change negligibly, profoundly close to the exit of the capillary, whether the plasma is turned off or on and also at different amplitudes, durations and frequencies of the applied voltage. It is therefore reasonable to assume that the flow composition in the AC jet and the pulsed jet are the same, which means that a a similar potential is needed in the ionization front to sustain propagation, and thus the electric field in the front is the same in the two jets.

The plasma plume, however, is $2 - 3$ times longer in the pulsed jet than in the AC jet. A difference in power that is dissipated in the plasma is measured of around two orders of magnitude, with the pulsed jet having the largest dissipated power. This difference is much larger than the length difference, meaning that the power difference can have an influence, but not a direct relation. Measurements on the electron density in the pulsed jet at different voltage amplitudes have yielded a decrease in electron density of 14 % from 6 kV to 4 kV. The AC jet is therefore expected to have a lower electron density. Since the electric field and hence the electron temperature are the same in the two jets, it is likely that the difference in electron density influences the length of the plasma plume, since it influences the amount of electrons that are produced. Furthermore, the potential in the ionization front in the AC jet does not benefit from the transferred potential from the powered electrode during propagation as the pulsed jet does, because the plasma in the AC jet is started mainly due to the polarity change of the applied potential instead of a large potential difference.

Influence of plasma on the gas flow

The structure of the flow profile in the plasma jet has been assessed through visualization of the flow and measurements of the N_2 and O_2 densities from the ambient air that have mixed with the helium flow. The air fractions in the helium flow are found to increase radially from almost zero at the center of the jet to 60 % at 2 mm from the center and axially from almost zero at the exit of the capillary to 20 % at 20 mm from this exit. At positions until 10 mm from the capillary exit, the air fractions are found to be constant at plasma On and Off.

From the flow visualization at different helium flow rates, the presence of turbulence was found at plasma Off only at a large flow rate (1500 sccm) and not at small flow rates (500 sccm and 1000 sccm), while turbulence appeared at all flow rates when the plasma was turned on. This

increased onset of turbulence due to the plasma corresponds to results in literature, although the precise location of the turbulence differs, which is attributed to differences in capillary length, impurities in the gas flow, humidity and room temperature between the jets.

The measured gas temperature at plasma Off and On is also not constant: the plasma increases the gas temperature generally by around 12 °C. Corresponding to measurements of the dissipated energy per pulse, the gas temperature is found to (slightly) increase with increasing amplitude, duration and frequency of the applied voltage pulses. Different mechanisms that can contribute to the gas heating in the plasma jet are elastic electron-neutral and ion-neutral collisions, inelastic collisions causing vibrational-translational relaxation, electrion-ion recombination and collisional relaxation of metastable states of helium. Using the measured values of among others the electric field, electron density and temperature and gas temperature, the main mechanism that leads to heating in the plasma jet of this thesis is estimated to be Joule heating due to ion-neutral collisions, even though some mechanisms seem to be still missing to fully explain the observed gas heating. The gas temperature in the pulsed jet has been measured to be higher than in the AC jet, which cannot be caused by the electric field or the electron temperature, but is similarly to the plasma plume length related to the electron density instead.

It has been shown in literature that turbulence can be caused by an increase in gas flow velocity. The increase in flow velocity due to the increase in gas temperature has been estimated to be one order of magnitude lower than the initial flow velocity. Momentum transfer between charged and neutral particles, in the form of the electrohydrodynamic force, can cause an electric wind with a certain velocity. The electric wind velocity is calculated to be twice as large as the initial flow velocity and thus we have estimated that the main mechanism that causes increased turbulence in the studied plasma jet is the electrohydrodynamic force and not the gas heating.

8.1.2 Jet with a metallic target

Influence on plasma

The propagation dynamics of the ionization wave when the plasma jet interacts with a floating and grounded metallic target have been found to be the same in the experiments and simulations. The ionization wave propagates faster towards the grounded target than to the floating target and in the free jet. With the floating target, the ionization wave propagates only faster than in the free jet in the last 5 mm before the target. However, the maximum axial electric field in the ionization front is measured to be approximately the same in both target cases with respect to the free jet. The gas temperature on the other hand increases with respect to the free jet with up to 25 °C in the plasma channel between the capillary and the floating metallic target. With the floating as well as the grounded target, a return stroke has been observed after the ionization wave impacts on the target, in the form of an ionization wave that propagates from the target back towards the powered electrode through an already ionized channel. This return stroke is therefore found to propagate at a larger velocity than the initial ionization wave and also has a lower electric field in the front. The reactivity (visible as the electron density and temperature for example) in the plasma plume after the impact on the target remains during the 1 μs long voltage pulse with the grounded target, while it severely decreases in a few hundred ns with the floating target. Apart from this return stroke, another electrical redistribution takes place at the fall of the applied voltage pulse, between the inner electrode that is now grounded and the positive plasma. The intensity of this redistribution has been shown to be higher with a floating target than with a grounded target.

Difference between floating and grounded target

The temporal evolution of the electric potential in the floating target has been found to be able to explain the differences between the floating and grounded target. Although discrepancies exist between the experiments and simulations, both have shown that the potential of the floating target increases a few kV per µs, depending on the amplitude of the applied voltage. The duration and the amplitude of the applied voltage thus allow to control the charging of the target. After the end of the pulse, the potential in the target decreases at approximately the same rates as it increased, until it approaches zero. During dozens of ns after the impact of the ionization wave on the target, the floating target is close to grounded, but at the end of the voltage pulse it is at a high potential, that can even be more than half of the applied voltage. The return stroke with the floating and grounded target is therefore similar. Furthermore, this justifies the decay in reactivity in the plasma during the voltage pulse with the floating target, as the target charges and potential gradients in the plasma dissipate. As a result of this, the electric field and electron temperature remain high in the plasma with a grounded target, as shown by the simulations, while the electron density increases during the voltage pulse, but this is not the case with a floating target or without a target. Finally, the charging of the floating target has shown that in this case the electrical redistribution takes place between a grounded inner electrode and a plasma limited by a charged surface, while in the case of the grounded target it takes place between two grounded electrodes. This then justifies the stronger intensity of the redistribution with the floating target.

After the end of the pulse, the electric field, electron density and temperature in the plasma plume, from both experiments and simulations, have shown an increase with the floating target, while this does not happen with the grounded target. The increased electron density in the plume in different situations (with floating target during the return stroke and after the end of the pulse, and with grounded target during the return stroke and during the full voltage pulse) has been shown to be mostly due to electron emission from the metallic surfaces and charge transport in the plasma.

8.2 Outlook

The electric field in the helium plasma jet has been measured by Stark polarization spectroscopy, a diagnostic from which the calibration depends on the approximation of the helium atom by the hydrogen atom. This diagnostic can therefore not be directly applied to plasmas with a different feed gas, such as argon. Using a mixture of helium and the desired gas, the wavelength shift of spectral lines of this gas could be calibrated to the helium lines. Another calibration method is determining the wavelength shift of this gas while using a plasma source with a known electric field. It must be noted that the calculated calibration method for Stark polarization for helium is only valid for electric fields with a minimum strength of 5 kV/cm, thus the plasma source for this suggested calibration method should be able to generate electric fields of this magnitude.

As already discussed in chapter 5, the schlieren setup needs to be improved to obtain more precise quantitative results. The knife edge should be aligned more precisely in the focal point of the corresponding lens, which will improve the sensitivity of the system.

An idea for future research would be to make a detailed study on the gas flow structure when the jet interacts with a target, as has been done for a free jet in this thesis. It would for example be interesting to see if the flow structure in the plasma jet is the same for a dielectric and a conductive target.

Also, since the plasma development mechanisms are now quite well understood in this particular jet configuration, it would be interesting to study if these characteristics remain valid in different plasma jet sources.

Bibliography

[1] Y. P. Raizer and J. E. Allen, *Gas Discharge Physics*, second edi. Springer Berlin, 1991.

[2] E. Timmermann, F. Prehn, M. Schmidt, H. Höft, R. Brandenburg, and M. Kettlitz, "Indoor air purification by dielectric barrier discharge combined with ionic wind: physical and microbiological investigations," *Journal of Physics D: Applied Physics*, vol. 51, no. 16, p. 164 003, 2018. DOI: 10.1088/1361-6463/aab48b.

[3] M. Bahri, F. Haghighat, S. Rohani, and H. Kazemian, "Impact of design parameters on the performance of non-thermal plasma air purification system," *Chemical Engineering Journal*, vol. 302, pp. 204–212, 2016. DOI: 10.1016/j.cej.2016.05.035.

[4] X. Lu, M. Laroussi, and V. Puech, "On atmospheric-pressure non-equilibrium plasma jets and plasma bullets," *Plasma Sources Science and Technology*, vol. 21, no. 3, p. 034 005, 2012. DOI: 10.1088/0963-0252/21/3/034005.

[5] A. Sobota, O. Guaitella, and A. Rousseau, "The influence of the geometry and electrical characteristics on the formation of the atmospheric pressure plasma jet," *Plasma Sources Science and Technology*, vol. 23, no. 2, p. 025 016, 2014. DOI: 10.1088/0963-0252/23/2/025016.

[6] M. Teschke, J. Kedzierski, E. Finantu-Dinu, D. Korzec, and J. Engemann, "High-speed photographs of a dielectric barrier atmospheric pressure plasma jet," *IEEE Transactions on Plasma Science*, vol. 33, no. 2, pp. 310–311, 2005. DOI: 10.1109/TPS.2005.845377.

[7] X. Lu and M. Laroussi, "Dynamics of an atmospheric pressure plasma plume generated by submicrosecond voltage pulses," *Journal of Applied Physics*, vol. 100, no. 6, p. 063 302, 2006. DOI: 10.1063/1.2349475.

[8] J.-P. Boeuf, L. L. Yang, and L. C. Pitchford, "Dynamics of a guided streamer ('plasma bullet') in a helium jet in air at atmospheric pressure," *Journal of Physics D: Applied Physics*, vol. 46, no. 1, p. 015 201, 2013. DOI: 10.1088/0022-3727/46/1/015201.

[9] D. Breden, K. Miki, and L. L. Raja, "Self-consistent two-dimensional modeling of cold atmospheric-pressure plasma jets/bullets," *Plasma Sources Science and Technology*, vol. 21, no. 3, p. 034 011, 2012. DOI: 10.1088/0963-0252/21/3/034011.

[10] B. L. Sands, B. N. Ganguly, and K. Tachibana, "A streamer-like atmospheric pressure plasma jet," *Applied Physics Letters*, vol. 92, no. 15, p. 151 503, 2008. DOI: 10.1063/1.2909084.

[11] N. Liu, S. Célestin, A. Bourdon, V. P. Pasko, P. Ségur, and E. Marode, "Application of photoionization models based on radiative transfer and the Helmholtz equations to studies of streamers in weak electric fields," *Applied Physics Letters*, vol. 91, no. 21, p. 211 501, 2007. DOI: 10.1063/1.2816906.

[12] K.-D. Weltmann and T. von Woedtke, "Plasma medicine—current state of research and medical application," *Plasma Physics and Controlled Fusion*, vol. 59, no. 1, p. 014 031, 2017. DOI: 10.1088/0741-3335/59/1/014031.

[13] G. Fridman, G. Friedman, A. Gutsol, A. B. Shekhter, V. N. Vasilets, and A. Fridman, "Applied Plasma Medicine," *Plasma Processes and Polymers*, vol. 5, no. 6, pp. 503–533, 2008. DOI: 10.1002/ppap.200700154.

[14] M. G. Kong, G. Kroesen, G. Morfill, T. Nosenko, T. Shimizu, J van Dijk, and J. L. Zimmermann, "Plasma medicine: an introductory review," *New Journal of Physics*, vol. 11, no. 11, p. 115 012, 2009. DOI: 10.1088/1367-2630/11/11/115012.

[15] J. Ehlbeck, R. Brandenburg, T. von Woedtke, U. Krohmann, M. Stieber, and K.-D. Weltmann, "PLASMOSE - antimicrobial effects of modular atmospheric plasma sources.," *GMS Krankenhaushygiene interdisziplinar*, vol. 3, no. 1, Doc14, 2008.

[16] N. D. Altieri, J. K.-C. Chen, L. Minardi, and J. P. Chang, "Review Article: Plasma–surface interactions at the atomic scale for patterning metals," *Journal of Vacuum Science & Technology A: Vacuum, Surfaces, and Films*, vol. 35, no. 5, p. 05C203, 2017. DOI: 10.1116/1.4993602.

[17] R. Wang, H. Xu, Y. Zhao, W. Zhu, K. K. Ostrikov, and T. Shao, "Effect of dielectric and conductive targets on plasma jet behaviour and thin film properties," *Journal of Physics D: Applied Physics*, vol. 52, no. 7, p. 074 002, 2019. DOI: 10.1088/1361-6463/aaf4c8.

[18] M. Noeske, J. Degenhardt, S. Strudthoff, and U. Lommatzsch, "Plasma jet treatment of five polymers at atmospheric pressure: surface modifications and the relevance for adhesion," *International Journal of Adhesion and Adhesives*, vol. 24, no. 2, pp. 171–177, 2004. DOI: 10.1016/j.ijadhadh.2003.09.006.

[19] C. Cheng, Z. Liye, and R.-J. Zhan, "Surface modification of polymer fibre by the new atmospheric pressure cold plasma jet," *Surface and Coatings Technology*, vol. 200, no. 24, pp. 6659–6665, 2006. DOI: 10.1016/j.surfcoat.2005.09.033.

[20] F. Fanelli and F. Fracassi, "Atmospheric pressure non-equilibrium plasma jet technology: general features, specificities and applications in surface processing of materials," *Surface and Coatings Technology*, vol. 322, pp. 174–201, 2017. DOI: 10.1016/j.surfcoat.2017.05.027.

[21] A. Lindsay, B. Byrns, W. King, A. Andhvarapou, J. Fields, D. Knappe, W. Fonteno, and S. Shannon, "Fertilization of Radishes, Tomatoes, and Marigolds Using a Large-Volume Atmospheric Glow Discharge," *Plasma Chemistry and Plasma Processing*, vol. 34, no. 6, pp. 1271–1290, 2014. DOI: 10.1007/s11090-014-9573-x.

[22] M. Ito, J.-S. Oh, T. Ohta, M. Shiratani, and M. Hori, "Current status and future prospects of agricultural applications using atmospheric-pressure plasma technologies," *Plasma Processes and Polymers*, vol. 15, no. 2, p. 1 700 073, 2018. DOI: 10.1002/ppap.201700073.

[23] H. Hülsheger and E. G. Niemann, "Lethal effect of high-voltage pulses on E. coli K12," *Radiation and environmental biophysics*, vol. 18, p. 281, 1980.

[24] H. Hülsheger, J Potel, and E. G. Niemann, "Electric field effects on bacteria and yeast cells," *Radiation and Environmental Biophysics*, vol. 22, no. 2, pp. 149–162, 1983. DOI: 10.1007/BF01338893.

[25] P.-M. Girard, A. Arbabian, M. Fleury, G. Bauville, V. Puech, M. Dutreix, and J. S. Sousa, "Synergistic Effect of H2O2 and NO2 in Cell Death Induced by Cold Atmospheric He Plasma," *Scientific Reports*, vol. 6, no. 1, p. 29 098, 2016. DOI: 10.1038/srep29098.

[26] O. Guaitella and A. Sobota, "The impingement of a kHz helium atmospheric pressure plasma jet on a dielectric surface," *Journal of Physics D: Applied Physics*, vol. 48, no. 25, p. 255 202, 2015. DOI: 10.1088/0022-3727/48/25/255202.

[27] A. Sobota, O. Guaitella, and E. Garcia-Caurel, "Experimentally obtained values of electric field of an atmospheric pressure plasma jet impinging on a dielectric surface," *Journal of Physics D: Applied Physics*, vol. 46, no. 37, p. 372 001, 2013. DOI: 10.1088/0022-3727/46/37/372001.

[28] A. Sobota, O Guaitella, G. B. Sretenović, I. B. Krstić, V. V. Kovačević, A Obrusník, Y. N. Nguyen, L Zajíčková, B. M. Obradović, and M. M. Kuraica, "Electric field measurements in a kHz-driven He jet—the influence of the gas flow speed," *Plasma Sources Science and Technology*, vol. 25, no. 6, p. 065 026, 2016. DOI: 10.1088/0963-0252/25/6/065026.

[29] A. Sobota, O. Guaitella, G. B. Sretenović, V. V. Kovačević, E. Slikboer, I. B. Krstić, B. M. Obradović, and M. M. Kuraica, "Plasma-surface interaction: dielectric and metallic targets and their influence on the electric field profile in a kHz AC-driven He plasma jet," *Plasma Sources Science and Technology*, vol. 28, no. 4, p. 045 003, 2019. DOI: 10.1088/1361-6595/ab0c6a.

[30] B. L. M. Klarenaar, O. Guaitella, R. Engeln, and A. Sobota, "How dielectric, metallic and liquid targets influence the evolution of electron properties in a pulsed He jet measured by Thomson and Raman scattering," *Plasma Sources Science and Technology*, vol. 27, no. 8, p. 085 004, 2018. DOI: 10.1088/1361-6595/aad4d7.

[31] G. B. Sretenović, O. Guaitella, A. Sobota, I. B. Krstić, V. V. Kovačević, B. M. Obradović, and M. M. Kuraica, "Electric field measurement in the dielectric tube of helium atmospheric pressure plasma jet," *Journal of Applied Physics*, vol. 121, no. 12, p. 123 304, 2017. DOI: 10.1063/1.4979310.

[32] V. V. Kovačević, G. B. Sretenović, E. Slikboer, O. Guaitella, A. Sobota, and M. M. Kuraica, "The effect of liquid target on a nonthermal plasma jet—imaging, electric fields, visualization of gas flow and optical emission spectroscopy," *Journal of Physics D: Applied Physics*, vol. 51, no. 6, p. 065 202, 2018. DOI: 10.1088/1361-6463/aaa288.

[33] E. Slikboer, "Investigation of Plasma Surface Interactions using Mueller Polarimetry," Ph.D. dissertation, Eindhoven University of Technology, 2018.

[34] P. Viegas, "Electric field characterization of atmospheric pressure helium plasma jets through numerical simulations and comparisons with experiments," Ph. D. thesis, École Polytechnique, France, 2018.

[35] P. Viegas, F. Péchereau, and A. Bourdon, "Numerical study on the time evolutions of the electric field in helium plasma jets with positive and negative polarities," *Plasma Sources Science and Technology*, vol. 27, no. 2, p. 025 007, 2018. DOI: 10.1088/1361-6595/aaa7d4.

[36] E. Slikboer, P. Viegas, Z. Bonaventura, E. Garcia-Caurel, A. Sobota, A. Bourdon, and O. Guaitella, "Experimental and numerical investigation of the transient charging of a dielectric surface exposed to a plasma jet," *Plasma Sources Science and Technology*, vol. 28, no. 9, p. 095 016, 2019. DOI: 10.1088/1361-6595/ab3c27.

[37] E. Slikboer, A. Sobota, O. Guaitella, and E. Garcia-Caurel, "Electric field and temperature in a target induced by a plasma jet imaged using Mueller polarimetry," *Journal of Physics D: Applied Physics*, vol. 51, no. 2, p. 025 204, 2018. DOI: 10.1088/1361-6463/aa9b17.

[38] P. Viegas, E. Slikboer, A. Obrusník, Z. Bonaventura, A. Sobota, E. Garcia-Caurel, O. Guaitella, and A. Bourdon, "Investigation of a plasma–target interaction through electric field characterization examining surface and volume charge contributions: modeling and experiment," *Plasma Sources Science and Technology*, vol. 27, no. 9, p. 094 002, 2018. DOI: 10.1088/1361-6595/aadcc0.

[39] E. Slikboer, K. Acharya, A. Sobota, E. Garcia-Caurel, and O. Guaitella, "Revealing Plasma-Surface Interaction at Atmospheric Pressure: Imaging of Electric Field and Temperature inside the Targeted Material," *Scientific Reports*, vol. 10, no. 1, p. 2712, 2020. DOI: 10.1038/s41598-020-59345-0.

[40] M. A. Lieberman and A. J. Lichtenberg, *Priciples of Plasma Discharges and Materials Processing*. 2005.

[41] H. C. J. Mulders, "Spectroscopic investigation of Indium Bromide for lighting purposes," PhD thesis, Eindhoven University of Technology, 2010.

[42] M. Hofmans, "Spectroscopic measurement of the electric field of a helium plasma jet," Master, Eindhoven University of Technology, 2017.

[43] B. L. M. Klarenaar, F. Brehmer, S. Welzel, H. J. van der Meiden, M. C. M. van de Sanden, and R. Engeln, "Note: Rotational Raman scattering on CO 2 plasma using a volume Bragg grating as a notch filter," *Review of Scientific Instruments*, vol. 86, no. 4, p. 046 106, 2015. DOI: 10.1063/1.4918730.

[44] B. L. M. Klarenaar, M Grofulović, A. S. Morillo-Candas, D. C. M. van den Bekerom, M. A. Damen, M. C. M. van de Sanden, O. Guaitella, and R. Engeln, "A rotational Raman study under non-thermal conditions in a pulsed CO 2 glow discharge," *Plasma Sources Science and Technology*, vol. 27, no. 4, p. 045 009, 2018. DOI: 10.1088/1361-6595/aabab6.

[45] A. F. H. van Gessel, E. A. D. Carbone, P. J. Bruggeman, and J. J. A. M. van der Mullen, "Laser scattering on an atmospheric pressure plasma jet: disentangling Rayleigh, Raman and Thomson scattering," *Plasma Sources Science and Technology*, vol. 21, no. 1, p. 015 003, 2012. DOI: 10.1088/0963-0252/21/1/015003.

[46] G. Settles, "High-speed Imaging of Shock Waves, Explosions and Gunshots," *American Scientist*, vol. 94, no. 1, p. 22, 2006. DOI: 10.1511/2006.1.22.

[47] E. Traldi, M. Boselli, E. Simoncelli, A. Stancampiano, M. Gherardi, V. Colombo, and G. S. Settles, "Schlieren imaging: a powerful tool for atmospheric plasma diagnostic," *EPJ Techniques and Instrumentation*, vol. 5, no. 1, p. 4, 2018. DOI: 10.1140/epjti/s40485-018-0045-1.

[48] J. Stark, "Beobachtungen über den Effekt des elektrischen Feldes auf Spektrallinien. I. Quereffekt," *Annalen der Physik*, vol. 348, no. 7, pp. 965–982, 1914. DOI: 10.1002/andp.19143480702.

[49] A. Lo Surdo, "Sul Fenomeno Analogo A Quello Di Zeeman Nel Campo Elettrico," *Il Nuovo Cimento*, vol. 7, no. 1, pp. 335–337, 1914. DOI: 10.1007/BF02958602.

[50] H. Haken and H. C. Wolf, *The Physics of Atoms and Quanta - Introduction to Experiments and Theory*, fifth edit. Springer-Verlag Berlin Heidelberg, 1996.

[51] P. Heckmann and E. Träbert, *Introduction to the spectroscopy of atoms*, second edi. Amsterdam: Elsevier Science Publishers B.V., 1989.

[52] I. I. Sobelman, *Atomic Spectra and Radiative Transitions*, 2nd. Springer-Verlag Berlin Heidelberg, 1996.

[53] W. Hanle and H. Kleinpoppen, Eds., *Progress in Atomic Spectroscopy*. Boston, MA: Springer US, 1979. DOI: 10.1007/978-1-4613-3935-9.

[54] H. A. Bethe and E. E. Salpeter, *Quantum Mechanics of One- and Two-Electron Atoms*. Berlin, Heidelberg: Springer Berlin Heidelberg, 1957. DOI: 10.1007/978-3-662-12869-5.

[55] M. Kuraica, N. Konjević, and I. Videnović, "Spectroscopic study of the cathode fall region of Grimm-type glow discharge in helium," *Spectrochimica Acta Part B: Atomic Spectroscopy*, vol. 52, no. 6, pp. 745–753, 1997. DOI: 10.1016/S0584-8547(96)01640-0.

[56] M. M. Kuraica and N. Konjević, "Electric field measurement in the cathode fall region of a glow discharge in helium," *Applied Physics Letters*, vol. 70, no. 12, pp. 1521–1523, 1997. DOI: 10.1063/1.118606.

[57] J. S. Foster, "Stark patterns observed in helium," *Proceedings of the Royal Society of London. Series A, Containing Papers of a Mathematical and Physical Character*, vol. 114, no. 766, pp. 47–66, 1927.

[58] B. Obradović and M. Kuraica, "On the use of relative line intensities of forbidden and allowed components of several HeI lines for electric field measurements," *Physics Letters A*, vol. 372, no. 2, pp. 137–140, 2008. DOI: 10.1016/j.physleta.2007.06.043.

[59] N. Cvetanović, M. M. Martinović, B. M. Obradović, and M. M. Kuraica, "Electric field measurement in gas discharges using stark shifts of He I lines and their forbidden counterparts," *Journal of Physics D: Applied Physics*, vol. 48, no. 20, p. 205 201, 2015. DOI: 10.1088/0022-3727/48/20/205201.

[60] S. S. Ivković, B. M. Obradović, N. Cvetanović, M. M. Kuraica, and J Purić, "Measurement of electric field development in dielectric barrier discharge in helium," *Journal of Physics D: Applied Physics*, vol. 42, no. 22, p. 225 206, 2009. DOI: 10.1088/0022-3727/42/22/225206.

[61] S. S. Ivković, B. M. Obradović, and M. M. Kuraica, "Electric field measurement in a DBD in helium and helium–hydrogen mixture," *Journal of Physics D: Applied Physics*, vol. 45, no. 27, p. 275 204, 2012. DOI: 10.1088/0022-3727/45/27/275204.

[62] B. M. Obradović, S. S. Ivković, and M. M. Kuraica, "Spectroscopic measurement of electric field in dielectric barrier discharge in helium," *Applied Physics Letters*, vol. 92, no. 19, p. 191 501, 2008. DOI: 10.1063/1.2927477.

[63] G. B. Sretenović, I. B. Krstić, V. V. Kovačević, B. M. Obradović, and M. M. Kuraica, "Spectroscopic measurement of electric field in atmospheric-pressure plasma jet operating in bullet mode," *Applied Physics Letters*, vol. 99, no. 16, p. 161 502, 2011. DOI: 10.1063/1.3653474.

[64] G. B. Sretenović, I. B. Krstić, V. V. Kovačević, B. M. Obradović, and M. M. Kuraica, "The isolated head model of the plasma bullet/streamer propagation: electric field-velocity relation," *Journal of Physics D: Applied Physics*, vol. 47, no. 35, p. 355 201, 2014. DOI: 10.1088/0022-3727/47/35/355201.

[65] P. Olszewski, E. Wagenaars, K. McKay, J. W. Bradley, and J. L. Walsh, "Measurement and control of the streamer head electric field in an atmospheric-pressure dielectric barrier plasma jet," *Plasma Sources Science and Technology*, vol. 23, no. 1, p. 015 010, 2014. DOI: 10.1088/0963-0252/23/1/015010.

[66] Y. Lu, S. Wu, W. Cheng, and X. Lu, "Electric field measurements in an atmospheric-pressure microplasma jet using Stark polarization emission spectroscopy of helium atom," *European Physical Journal: Special Topics*, vol. 226, no. 13, pp. 2979–2989, 2017. DOI: 10.1140/epjst/e2016-60334-7.

[67] M. M. Kuraica, "Razvoj novih spektroskopskih metoda za dijagnostiku tinjavog pražnjenja," PhD thesis, University of Belgrade, 1998.

[68] J. Stark, "Beobachtungen über den Effekt des elektrischen Feldes auf Spektrallinien. VI. Polarisierung und Verstärkung einer Serie," *Annalen der Physik*, vol. 353, no. 18, pp. 210–235, 1915. DOI: 10.1002/andp.19153531805.

[69] W. Demtröder, *Atoms, Molecules and Photons*, ser. Graduate Texts in Physics. Berlin, Heidelberg: Springer Berlin Heidelberg, 2010. DOI: 10.1007/978-3-642-10298-1.

[70] P. Zeeman, "The Effect of Magnetisation on the Nature of Light Emitted by a Substance," *Nature*, vol. 55, no. 1424, pp. 347–347, 1897. DOI: 10.1038/055347a0.

[71] I. H. Hutchinson, *Principles of Plasma Diagnostics*, second edi. Cambridge University Press, 2005.

[72] D. J. Griffiths, *Introduction to Electrodynamics*, fourth edi. Pearson, 2013.

[73] D. J. Griffiths and E. G. Harris, *Introduction to quantum mechanics*, second edi. Pearson Prentice Hall, 2005.

[74] D. D. Fitts, *Principles of Quantum Mechanics*, first edit. Cambridge: Cambridge University Press, 1999. DOI: 10.1017/CBO9780511813542.

[75] D. C. Morton, Q. Wu, and G. W. Drake, "Energy levels for the stable isotopes of atomic helium (4He I and 3He I)," *Canadian Journal of Physics*, vol. 84, no. 2, pp. 83–105, 2006. DOI: 10.1139/p06-009#.WOOoaqJBq71.

[76] A. Kramida, "A critical compilation of experimental data on spectral lines and energy levels of hydrogen, deuterium, and tritium," *Atomic Data and Nuclear Data Tables*, vol. 96, no. 6, pp. 586–644, 2010. DOI: 10.1016/j.adt.2010.05.001.

[77] A. Fowler, *Report on series in line spectra*. Fleetway press, ltd., 1922.

[78] K. D. Bonin and V. V. Kresin, *Electric-dipole polarizabilities of atoms, molecules, and clusters*, English. Singapore: World Scientific, 1997.

[79] D. R. Lide, *CRC handbook of chemistry and physics*, 84th editi. CRC press, 2003.

[80] D. Graves, "Low temperature plasma biomedicine: A tutorial review," *Physics of Plasmas (1994-present)*, vol. 21, no. 8, p. 080 901, 2014. DOI: 10.1063/1.4892534.

[81] S. Hübner, J. S. Sousa, V. Puech, G. M. W. Kroesen, and N. Sadeghi, "Electron properties in an atmospheric helium plasma jet determined by Thomson scattering," *Journal of Physics D: Applied Physics*, vol. 47, no. 43, p. 432 001, 2014. DOI: 10.1088/0022-3727/47/43/432001.

[82] C. Jiang, J Miles, J. Hornef, C. Carter, and S. Adams, "Electron densities and temperatures of an atmospheric-pressure nanosecond pulsed helium plasma jet in air," *Plasma Sources Science and Technology*, vol. 28, no. 8, p. 085 009, 2019. DOI: 10.1088/1361-6595/ab2182.

[83] S. Hübner, J. S. Sousa, J. van der Mullen, and W. G. Graham, "Thomson scattering on non-thermal atmospheric pressure plasma jets," *Plasma Sources Science and Technology*, vol. 24, no. 5, p. 054 005, 2017. DOI: 10.1088/0963-0252/24/5/054005.

[84] Y. Sakiyama, D. B. Graves, and E. Stoffels, "Influence of electrical properties of treated surface on RF-excited plasma needle at atmospheric pressure," *Journal of Physics D: Applied Physics*, vol. 41, no. 9, p. 095 204, 2008. DOI: 10.1088/0022-3727/41/9/095204.

[85] Z. Xiong, E. Robert, V. Sarron, J.-M. Pouvesle, and M. J. Kushner, "Dynamics of ionization wave splitting and merging of atmospheric-pressure plasmas in branched dielectric tubes and channels," *Journal of Physics D: Applied Physics*, vol. 45, no. 27, p. 275 201, 2012. DOI: 10.1088/0022-3727/45/27/275201.

[86] R. Wang, C. Zhang, Y. Shen, W. Zhu, P. Yan, T. Shao, N. Y. Babaeva, and G. V. Naidis, "Temporal and spatial profiles of emission intensities in atmospheric pressure helium plasma jet driven by microsecond pulse: Experiment and simulation," *Journal of Applied Physics*, vol. 118, no. 12, p. 123 303, 2015. DOI: 10.1063/1.4931668.

[87] A. M. Lietz, E. Johnsen, and M. J. Kushner, "Plasma-induced flow instabilities in atmospheric pressure plasma jets," *Applied Physics Letters*, vol. 111, no. 11, p. 114 101, 2017. DOI: 10.1063/1.4996192.

[88] W. Ning, D. Dai, Y. Zhang, Y. Han, and L. Li, "Effects of trace of nitrogen on the helium atmospheric pressure plasma jet interacting with a dielectric substrate," *Journal of Physics D: Applied Physics*, vol. 51, no. 12, p. 125 204, 2018. DOI: 10.1088/1361-6463/aaafbf.

[89] C. Lazarou, C. Anastassiou, I. Topala, A. S. Chiper, I. Mihaila, V. Pohoata, and G. E. Georghiou, "Numerical simulation of capillary helium and helium-oxygen atmospheric pressure plasma jets: propagation dynamics and interaction with dielectric," *Plasma Sources Science and Technology*, vol. 27, no. 10, p. 105 007, 2018. DOI: 10.1088/1361-6595/aadeb8.

[90] A. Bourdon, T. Darny, F. Pechereau, J.-M. Pouvesle, P. Viegas, S. Iséni, and E. Robert, "Numerical and experimental study of the dynamics of a μ s helium plasma gun discharge with various amounts of N 2 admixture," *Plasma Sources Science and Technology*, vol. 25, no. 3, p. 035 002, 2016. DOI: 10.1088/0963-0252/25/3/035002.

[91] L. Ji, W. Yan, Y. Xia, and D. Liu, "The effect of target materials on the propagation of atmospheric-pressure plasma jets," *Journal of Applied Physics*, vol. 123, no. 18, p. 183 302, 2018. DOI: 10.1063/1.5024806.

[92]   P. Zhu, B. Li, Z. Duan, and J. Ouyang, "Development from dielectric barrier discharge to atmospheric pressure plasma jet in helium: experiment and fluid modeling," *Journal of Physics D: Applied Physics*, vol. 51, no. 40, p. 405 202, 2018. DOI: 10.1088/1361-6463/aadb12.

[93]   G. V. Naidis, "Modelling of streamer propagation in atmospheric-pressure helium plasma jets," *Journal of Physics D: Applied Physics*, vol. 43, no. 40, p. 402 001, 2010. DOI: 10.1088/0022-3727/43/40/402001.

[94]   G. V. Naidis, "Modelling of plasma bullet propagation along a helium jet in ambient air," *Journal of Physics D: Applied Physics*, vol. 44, no. 21, p. 215 203, 2011. DOI: 10.1088/0022-3727/44/21/215203.

[95]   D. Breden, K. Miki, and L. L. Raja, "Computational study of cold atmospheric nanosecond pulsed helium plasma jet in air," *Applied Physics Letters*, vol. 99, no. 11, p. 111 501, 2011. DOI: 10.1063/1.3636433.

[96]   N. Y. Babaeva and G. V. Naidis, "Two-dimensional modelling of positive streamer dynamics in non-uniform electric fields in air," *Journal of Physics D: Applied Physics*, vol. 29, no. 9, pp. 2423–2431, 1996. DOI: 10.1088/0022-3727/29/9/029.

[97]   A. A. Kulikovsky, "Positive streamer between parallel plate electrodes in atmospheric pressure air," *Journal of Physics D: Applied Physics*, vol. 30, no. 3, pp. 441–450, 1997. DOI: 10.1088/0022-3727/30/3/017.

[98]   N. Mericam-Bourdet, M. Laroussi, A. Begum, and E. Karakas, "Experimental investigations of plasma bullets," *Journal of Physics D: Applied Physics*, vol. 42, no. 5, p. 055 207, 2009. DOI: 10.1088/0022-3727/42/5/055207.

[99]   G. V. Naidis, "Modeling of helium plasma jets emerged into ambient air: Influence of applied voltage, jet radius, and helium flow velocity on plasma jet characteristics," *Journal of Applied Physics*, vol. 112, no. 10, p. 103 304, 2012. DOI: 10.1063/1.4766297.

[100] A. Shashurin, M. N. Shneider, and M. Keidar, "Measurements of streamer head potential and conductivity of streamer column in cold nonequilibrium atmospheric plasmas," *Plasma Sources Science and Technology*, vol. 21, no. 3, p. 034 006, 2012. DOI: 10.1088/0963-0252/21/3/034006.

[101] P. Viegas and A. Bourdon, "Numerical Study of Jet–Target Interaction: Influence of Dielectric Permittivity on the Electric Field Experienced by the Target," *Plasma Chemistry and Plasma Processing*, vol. 40, no. 3, pp. 661–683, 2020. DOI: 10.1007/s11090-019-10033-6.

[102] COMSOL, *CFD module user's guide, version 5.3*, www.comsol.com/cfd-module, 2016.

[103] J. Winter, J. S. Sousa, N. Sadeghi, A. Schmidt-Bleker, S. Reuter, and V. Puech, "The spatio-temporal distribution of He (2 3 S 1) metastable atoms in a MHz-driven helium plasma jet is influenced by the oxygen/nitrogen ratio of the surrounding atmosphere," *Plasma Sources Science and Technology*, vol. 24, no. 2, p. 025 015, 2015. DOI: 10.1088/0963-0252/24/2/025015.

[104] A. Schmidt-Bleker, S. Reuter, and K.-D. Weltmann, "Quantitative schlieren diagnostics for the determination of ambient species density, gas temperature and calorimetric power of cold atmospheric plasma jets," *Journal of Physics D: Applied Physics*, vol. 48, no. 17, p. 175 202, 2015. DOI: 10.1088/0022-3727/48/17/175202.

[105]   G. J. M. Hagelaar and L. C. Pitchford, "Solving the Boltzmann equation to obtain electron transport coefficients and rate coefficients for fluid models," *Plasma Sources Science and Technology*, vol. 14, no. 4, pp. 722–733, 2005. DOI: 10.1088/0963-0252/14/4/011.

[106]   S. Pancheshnyi, S. Biagi, M. Bordage, G. Hagelaar, W. Morgan, A. Phelps, and L. Pitchford, "The LXCat project: Electron scattering cross sections and swarm parameters for low temperature plasma modeling," *Chemical Physics*, vol. 398, pp. 148–153, 2012. DOI: 10.1016/j.chemphys.2011.04.020.

[107]   IST, *IST-Lisbon database*, www.lxcat.net, retrieved on January 2018, 2018.

[108]   E. Slikboer, E. Garcia-Caurel, O. Guaitella, and A. Sobota, "Charge transfer to a dielectric target by guided ionization waves using electric field measurements," *Plasma Sources Science and Technology*, vol. 26, no. 3, p. 035 002, 2017. DOI: 10.1088/1361-6595/aa53fe.

[109]   M. Hofmans and A. Sobota, "Influence of a target on the electric field profile in a kHz atmospheric pressure plasma jet with the full calculation of the Stark shifts," *Journal of Applied Physics*, vol. 125, no. 4, p. 043 303, 2019. DOI: 10.1063/1.5075544.

[110]   A. Begum, M. Laroussi, and M. R. Pervez, "Atmospheric pressure He-air plasma jet: Breakdown process and propagation phenomenon," *AIP Advances*, vol. 3, no. 6, p. 062 117, 2013. DOI: 10.1063/1.4811464.

[111]   D. Maletić, N. Puač, N. Selaković, S. Lazović, G. Malović, A. Đorđević, and Z. L. Petrović, "Time-resolved optical emission imaging of an atmospheric plasma jet for different electrode positions with a constant electrode gap," *Plasma Sources Science and Technology*, vol. 24, no. 2, p. 025 006, 2015. DOI: 10.1088/0963-0252/24/2/025006.

[112]   J. Jarrige, M. Laroussi, and E. Karakas, "Formation and dynamics of plasma bullets in a non-thermal plasma jet: influence of the high-voltage parameters on the plume characteristics," *Plasma Sources Science and Technology*, vol. 19, no. 6, p. 065 005, 2010. DOI: 10.1088/0963-0252/19/6/065005.

[113]   G. V. Naidis and J. L. Walsh, "The effects of an external electric field on the dynamics of cold plasma jets—experimental and computational studies," *Journal of Physics D: Applied Physics*, vol. 46, no. 9, p. 095 203, 2013. DOI: 10.1088/0022-3727/46/9/095203.

[114]   J. Jánský and A. Bourdon, "Simulation of helium discharge ignition and dynamics in thin tubes at atmospheric pressure," *Applied Physics Letters*, vol. 99, no. 16, p. 161 504, 2011. DOI: 10.1063/1.3655199.

[115]   G. B. Sretenović, I. B. Krstić, V. V. Kovačević, B. M. Obradović, and M. M. Kuraica, "Spatio-temporally resolved electric field measurements in helium plasma jet," *Journal of Physics D: Applied Physics*, vol. 47, no. 10, p. 102 001, 2014. DOI: 10.1088/0022-3727/47/10/102001.

[116]   N. Y. Babaeva, G. V. Naidis, V. A. Panov, R. Wang, S. Zhang, C. Zhang, and T. Shao, "Plasma bullet propagation and reflection from metallic and dielectric targets," *Plasma Sources Science and Technology*, vol. 28, no. 9, p. 095 006, 2019. DOI: 10.1088/1361-6595/ab36d3.

[117] A. M. Lietz and M. J. Kushner, "Molecular admixtures and impurities in atmospheric pressure plasma jets," *Journal of Applied Physics*, vol. 124, no. 15, p. 153 303, 2018. DOI: 10.1063/1.5049430.

[118] S. A. Norberg, E. Johnsen, and M. J. Kushner, "Helium atmospheric pressure plasma jets interacting with wet cells: delivery of electric fields," *Journal of Physics D: Applied Physics*, vol. 49, no. 18, p. 185 201, 2016. DOI: 10.1088/0022-3727/49/18/185201.

[119] C.-G. Schregel, E. A. D. Carbone, D. Luggenhölscher, and U. Czarnetzki, "Ignition and afterglow dynamics of a high pressure nanosecond pulsed helium micro-discharge: I. Electron, Rydberg molecules and He (2 3 S) densities," *Plasma Sources Science and Technology*, vol. 25, no. 5, p. 054 003, 2016. DOI: 10.1088/0963-0252/25/5/054003.

[120] A. Fridman, *Plasma Chemistry*. Cambridge University Press, 2008.

[121] E. Stoffels, Y. Sakiyama, and D. B. Graves, "Cold Atmospheric Plasma: Charged Species and Their Interactions With Cells and Tissues," *IEEE Transactions on Plasma Science*, vol. 36, no. 4, pp. 1441–1457, 2008. DOI: 10.1109/TPS.2008.2001084.

[122] S. Zhang, A. Sobota, E. M. Van Veldhuizen, and P. J. Bruggeman, "Temporally resolved ozone distribution of a time modulated RF atmospheric pressure argon plasma jet: Flow, chemical reaction, and transient vortex," *Plasma Sources Science and Technology*, vol. 24, no. 4, p. 45 015, 2015. DOI: 10.1088/0963-0252/24/4/045015.

[123] R. Xiong, Q. Xiong, A. Y. Nikiforov, P. Vanraes, and C. Leys, "Influence of helium mole fraction distribution on the properties of cold atmospheric pressure helium plasma jets," *Journal of Applied Physics*, vol. 112, no. 3, pp. 1–9, 2012. DOI: 10.1063/1.4746700.

[124] R. P. Satti and A. K. Agrawal, "Flow structure in the near-field of buoyant low-density gas jets," *International Journal of Heat and Fluid Flow*, vol. 27, no. 2, pp. 336–347, 2006. DOI: 10.1016/j.ijheatfluidflow.2005.10.012.

[125] P. K. Papadopoulos, P. Vafeas, P. Svarnas, K. Gazeli, P. M. Hatzikonstantinou, A. Gkelios, and F. Clément, "Interpretation of the gas flow field modification induced by guided streamer ('plasma bullet') propagation," *Journal of Physics D: Applied Physics*, vol. 47, no. 42, 2014. DOI: 10.1088/0022-3727/47/42/425203.

[126] P. O'Neill, J. Soria, and D. Honnery, "The stability of low Reynolds number round jets," *Experiments in Fluids*, vol. 36, no. 3, pp. 473–483, 2004. DOI: 10.1007/s00348-003-0751-5.

[127] Y. Morabit, R. D. Whalley, E. Robert, M. I. Hasan, and J. L. Walsh, "Turbulence and entrainment in an atmospheric pressure dielectric barrier plasma jet," *Plasma Processes and Polymers*, no. November, pp. 1–12, 2019. DOI: 10.1002/ppap.201900217.

[128] J.-S. Oh, O. T. Olabanji, C. Hale, R. Mariani, K. Kontis, and J. W. Bradley, "Imaging gas and plasma interactions in the surface-chemical modification of polymers using microplasma jets," *Journal of Physics D: Applied Physics*, vol. 44, no. 15, p. 155 206, 2011. DOI: 10.1088/0022-3727/44/15/155206.

[129] N. Jiang, J. Yang, F. He, and Z. Cao, "Interplay of discharge and gas flow in atmospheric pressure plasma jets," *Journal of Applied Physics*, vol. 109, no. 9, 2011. DOI: 10.1063/1.3581067.

[130] E. Robert, V. Sarron, T. Darny, D. Riès, S. Dozias, J. Fontane, L. Joly, and J. M. Pou-
       vesle, "Rare gas flow structuration in plasma jet experiments," *Plasma Sources Science
       and Technology*, vol. 23, no. 1, 2014. DOI: 10.1088/0963-0252/23/1/012003.

[131] M. Boselli, V. Colombo, E. Ghedini, M. Gherardi, R. Laurita, A. Liguori, P. Sanibondi,
       and A. Stancampiano, "Schlieren High-Speed Imaging of a Nanosecond Pulsed Atmo-
       spheric Pressure Non-equilibrium Plasma Jet," *Plasma Chemistry and Plasma Process-
       ing*, vol. 34, no. 4, pp. 853–869, 2014. DOI: 10.1007/s11090-014-9537-1.

[132] H.-H. Zong, Y. Wu, H.-M. Song, M. Jia, H. Liang, Y.-H. Li, and Z.-B. Zhang, "Inves-
       tigation of the performance characteristics of a plasma synthetic jet actuator based on
       a quantitative Schlieren method," *Measurement Science and Technology*, vol. 27, no. 5,
       p. 055 301, 2016. DOI: 10.1088/0957-0233/27/5/055301.

[133] D. A. Xu, M. N. Shneider, D. A. Lacoste, and C. O. Laux, "Thermal and hydrodynamic
       effects of nanosecond discharges in atmospheric pressure air," *Journal of Physics D:
       Applied Physics*, vol. 47, no. 23, p. 235 202, 2014. DOI: 10.1088/0022-3727/47/23/
       235202.

[134] J. C. Chamorro, L. Prevosto, E. Cejas, G. Fischfeld, H. Kelly, and B. Mancinelli, "Am-
       bient Species Density and Gas Temperature Radial Profiles Derived from a Schlieren
       Technique in a Low-Frequency Non-thermal Oxygen Plasma Jet," *Plasma Chemistry
       and Plasma Processing*, vol. 38, no. 1, pp. 45–61, 2018. DOI: 10.1007/s11090-017-
       9842-6.

[135] E. R. Van Doremaele, V. S. Kondeti, and P. J. Bruggeman, "Effect of plasma on gas
       flow and air concentration in the effluent of a pulsed cold atmospheric pressure helium
       plasma jet," *Plasma Sources Science and Technology*, vol. 27, no. 9, p. 95 006, 2018.
       DOI: 10.1088/1361-6595/aadbd3.

[136] M. Dünnbier, A. Schmidt-Bleker, J. Winter, M. Wolfram, R. Hippler, K.-D. Weltmann,
       and S. Reuter, "Ambient air particle transport into the effluent of a cold atmospheric-
       pressure argon plasma jet investigated by molecular beam mass spectrometry," *Journal
       of Physics D: Applied Physics*, vol. 46, no. 43, p. 435 203, 2013. DOI: 10.1088/0022-
       3727/46/43/435203.

[137] G. S. Settles, *Schlieren and Shadowgraph Techniques*. Springer, 2001.

[138] J. A. Stone and A. Stejskal, "Using helium as a standard of refractive index: Correcting
       errors in a gas refractometer," *Metrologia*, vol. 41, no. 3, pp. 189–197, 2004. DOI: 10.
       1088/0026-1394/41/3/012.

[139] J. Zhang, Z. H. Lu, and L. J. Wang, "Precision refractive index measurements of air, N_2,
       O_2, Ar, and CO_2 with a frequency comb," *Applied Optics*, vol. 47, no. 17, p. 3143, 2008.
       DOI: 10.1364/AO.47.003143.

[140] B. Edlén, "The Refractive Index of Air," *Metrologia*, vol. 2, no. 2, pp. 71–80, 1966. DOI:
       10.1088/0026-1394/2/2/002.

[141] J. R. Welty, G. L. Rorrer, and D. G. Foster, *Fundamentals of Momentum, Heat and Mass
       Transfer*, sixth. John Wiley & Sons, Ltd, 2015.

[142] H. Petersen, "The properties of helium: Density, specific heats, viscosity, and thermal
       conductivity at pressures from 1 to 100 bar and from room temperature to about 1800
       K," Risø National Laboratory, Roskilde, Denmark, Tech. Rep. 224, 1970, pp. 1–42.

[143] Y. Zheng, L. Wang, W. Ning, and S. Jia, "Schlieren imaging investigation of the hydrodynamics of atmospheric helium plasma jets," *Journal of Applied Physics*, vol. 119, no. 12, 2016. DOI: 10.1063/1.4944052.

[144] S. Wasik and K. McCulloh, "Measurements of gaseous diffusion coefficients by gas chromatography," *Journal of Research of the National Bureau of Standards*, vol. 73A, no. 2, pp. 207–211, 1968. DOI: 10.1021/ed049p565.

[145] Y. B. Xian, M. Hasnain Qaisrani, Y. F. Yue, and X. P. Lu, "Discharge effects on gas flow dynamics in a plasma jet," *Physics of Plasmas*, vol. 23, no. 10, 2016. DOI: 10.1063/1.4964784.

[146] K. D. Weltmann, E. Kindel, R. Brandenburg, C. Meyer, R. Bussiahn, C. Wilke, and T. von Woedtke, "Atmospheric pressure plasma jet for medical therapy: Plasma parameters and risk estimation," *Contributions to Plasma Physics*, vol. 49, no. 9, pp. 631–640, 2009. DOI: 10.1002/ctpp.200910067.

[147] P. Boukamp, R. T. Petrussevska, D Breitkreutz, J Hornung, A Markham, and N. E. Fusenig, "Normal keratinization in a spontaneously immortalized aneuploid human keratinocyte cell line.," *The Journal of Cell Biology*, vol. 106, no. 3, pp. 761–771, 1988. DOI: 10.1083/jcb.106.3.761.

[148] M. C. Garcia, C. Yubero Serrano, and A. Rodero, "Measuring the air fraction and the gas temperature in non-thermal argon plasma jets through the study of the air influence on the collisional broadening of some argon atomic emission lines," *Plasma Sources Science and Technology*, pp. 0–7, 2020. DOI: 10.1088/1361-6595/ab87b8.

[149] I. Sremački, A. Jurov, M. Modic, U. Cvelbar, L. Wang, C. Leys, and A. Nikiforov, "On diagnostics of annular-shape radio-frequency plasma jet operating in argon in atmospheric conditions," *Plasma Sources Science and Technology*, vol. 29, no. 3, p. 035 027, 2020. DOI: 10.1088/1361-6595/ab71f7.

[150] C.-Y. T. Tschang, R. Bergert, S. Mitic, and M. Thoma, "Effect of external axial magnetic field on a helium atmospheric pressure plasma jet and plasma-treated water," *Journal of Physics D: Applied Physics*, vol. 53, no. 21, p. 215 202, 2020. DOI: 10.1088/1361-6463/ab78d6.

[151] Z. Chang, X. Shao, Z. Zhang, and G. Zhang, "Diagnosis of gas temperature, electron temperature, and electron density in helium atmospheric pressure plasma jet," *Physics of Plasmas*, vol. 19, no. 7, p. 073 513, 2012. DOI: 10.1063/1.4739060.

[152] S. Hofmann, A. F. H. van Gessel, T. Verreycken, and P. Bruggeman, "Power dissipation, gas temperatures and electron densities of cold atmospheric pressure helium and argon RF plasma jets," *Plasma Sources Science and Technology*, vol. 20, no. 6, p. 065 010, 2011. DOI: 10.1088/0963-0252/20/6/065010.

[153] Q. Wang, D. J. Economou, and V. M. Donnelly, "Simulation of a direct current microplasma discharge in helium at atmospheric pressure," *Journal of Applied Physics*, vol. 100, no. 2, 2006. DOI: 10.1063/1.2214591.

[154] D.-X. Liu, M.-Z. Rong, X.-H. Wang, F. Iza, M. G. Kong, and P. Bruggeman, "Main Species and Physicochemical Processes in Cold Atmospheric-pressure He + O2 Plasmas," *Plasma Processes and Polymers*, vol. 7, no. 9-10, pp. 846–865, 2010. DOI: 10.1002/ppap.201000049.

[155] C. D. Pintassilgo, V. Guerra, O. Guaitella, and A. Rousseau, "Study of gas heating mechanisms in millisecond pulsed discharges and afterglows in air at low pressures," *Plasma Sources Science and Technology*, vol. 23, no. 2, p. 025 006, 2014. DOI: 10.1088/0963-0252/23/2/025006.

[156] X. Y. Liu, X. K. Pei, X. P. Lu, and D. W. Liu, "Numerical and experimental study on a pulsed-dc plasma jet," *Plasma Sources Science and Technology*, vol. 23, no. 3, 2014. DOI: 10.1088/0963-0252/23/3/035007.

[157] R. Zaplotnik, M. Bišćan, D. Popović, M. Mozetič, and S. Milošević, "Metastable helium atom density in a single electrode atmospheric plasma jet during sample treatment," *Plasma Sources Science and Technology*, vol. 25, no. 3, p. 035 023, 2016. DOI: 10.1088/0963-0252/25/3/035023.

[158] J. P. Boeuf and E. E. Kunhardt, "Energy balance in a nonequilibrium weakly ionized nitrogen discharge," *Journal of Applied Physics*, vol. 60, no. 3, pp. 915–923, 1986. DOI: 10.1063/1.337332.

[159] E. I. Mintoussov, S. J. Pendleton, F. G. Gerbault, N. A. Popov, and S. M. Starikovskaia, "Fast gas heating in nitrogen–oxygen discharge plasma: II. Energy exchange in the afterglow of a volume nanosecond discharge at moderate pressures," *Journal of Physics D: Applied Physics*, vol. 44, no. 28, p. 285 202, 2011. DOI: 10.1088/0022-3727/44/28/285202.

[160] B. N. Roy, *Principles of modern thermodynamics*, First. CRC press, 1995.

[161] P. Jacobs, *Thermodynamics*. Imperial College Press, 2013.

[162] J. R. Roebuck and H. Osterberg, "The Joule-Thomson Effect in Helium," *Physical Review*, vol. 43, no. 1, pp. 60–69, 1933. DOI: 10.1103/PhysRev.43.60.

[163] J. R. Roebuck and H. Osterberg, "The Joule-Thomson Effect in Argon," *Physical Review*, vol. 46, no. 9, pp. 785–790, 1934. DOI: 10.1103/PhysRev.46.785.

[164] S. Park, U. Cvelbar, W. Choe, and S. Y. Moon, "The creation of electric wind due to the electrohydrodynamic force," *Nature Communications*, vol. 9, no. 1, 2018. DOI: 10.1038/s41467-017-02766-9.

[165] J. P. Boeuf, Y. Lagmich, T. Unfer, T. Callegari, and L. C. Pitchford, "Electrohydrodynamic force in dielectric barrier discharge plasma actuators," *Journal of Physics D: Applied Physics*, vol. 40, no. 3, pp. 652–662, 2007. DOI: 10.1088/0022-3727/40/3/S03.

[166] M. Ghasemi, P. Olszewski, J. W. Bradley, and J. L. Walsh, "Interaction of multiple plasma plumes in an atmospheric pressure plasma jet array," *Journal of Physics D: Applied Physics*, vol. 46, no. 5, p. 052 001, 2013. DOI: 10.1088/0022-3727/46/5/052001.

[167] O. Guaitella, F. Thevenet, C. Guillard, and A. Rousseau, "Dynamic of the plasma current amplitude in a barrier discharge: influence of photocatalytic material," *Journal of Physics D: Applied Physics*, vol. 39, no. 14, pp. 2964–2972, 2006. DOI: 10.1088/0022-3727/39/14/015.

[168] E. C. Neyts, "Plasma-Surface Interactions in Plasma Catalysis," *Plasma Chemistry and Plasma Processing*, vol. 36, no. 1, pp. 185–212, 2016. DOI: 10.1007/s11090-015-9662-5.

[169] S. Bornholdt, M. Wolter, and H. Kersten, "Characterization of an atmospheric pressure plasma jet for surface modification and thin film deposition," *The European Physical Journal D*, vol. 60, no. 3, pp. 653–660, 2010. DOI: 10.1140/epjd/e2010-00245-x.

[170] K. Urabe, T. Morita, K. Tachibana, and B. N. Ganguly, "Investigation of discharge mechanisms in helium plasma jet at atmospheric pressure by laser spectroscopic measurements," *Journal of Physics D: Applied Physics*, vol. 43, no. 9, p. 095 201, 2010. DOI: 10.1088/0022-3727/43/9/095201.

[171] R. Wild, T. Gerling, R. Bussiahn, K.-D. Weltmann, and L. Stollenwerk, "Phase-resolved measurement of electric charge deposited by an atmospheric pressure plasma jet on a dielectric surface," *Journal of Physics D: Applied Physics*, vol. 47, no. 4, p. 042 001, 2014. DOI: 10.1088/0022-3727/47/4/042001.

[172] E. Slikboer, O. Guaitella, and A. Sobota, "Time-resolved electric field measurements during and after the initialization of a kHz plasma jet—from streamers to guided streamers," *Plasma Sources Science and Technology*, vol. 25, no. 3, 03LT04, 2016. DOI: 10.1088/0963-0252/25/3/03LT04.

[173] Z. Liu, D. Liu, D. Xu, H. Cai, W. Xia, B. Wang, Q. Li, and M. G. Kong, "Two modes of interfacial pattern formation by atmospheric pressure helium plasma jet-ITO interactions under positive and negative polarity," *Journal of Physics D: Applied Physics*, vol. 50, no. 19, p. 195 203, 2017. DOI: 10.1088/1361-6463/aa6915.

[174] A. Kone, F. P. Sainct, C. Muja, B. Caillier, and P. Guillot, "Investigation of the Interaction between a Helium Plasma Jet and Conductive (Metal)/ Non-Conductive (Dielectric) Targets," *Plasma Medicine*, vol. 7, no. 4, pp. 333–346, 2017. DOI: 10.1615/PlasmaMed.2018019503.

[175] E. Slikboer, A. Sobota, O. Guaitella, and E. Garcia-Caurel, "Imaging axial and radial electric field components in dielectric targets under plasma exposure," *Journal of Physics D: Applied Physics*, vol. 51, no. 11, p. 115 203, 2018. DOI: 10.1088/1361-6463/aaad99.

[176] S. Hofmann, K. van Gils, S. van der Linden, S. Iseni, and P. Bruggeman, "Time and spatial resolved optical and electrical characteristics of continuous and time modulated RF plasmas in contact with conductive and dielectric substrates," *The European Physical Journal D*, vol. 68, no. 3, p. 56, 2014. DOI: 10.1140/epjd/e2014-40430-3.

[177] D. Breden and L. L. Raja, "Computational study of the interaction of cold atmospheric helium plasma jets with surfaces," *Plasma Sources Science and Technology*, vol. 23, no. 6, p. 065 020, 2014. DOI: 10.1088/0963-0252/23/6/065020.

[178] S. A. Norberg, E. Johnsen, and M. J. Kushner, "Helium atmospheric pressure plasma jets touching dielectric and metal surfaces," *Journal of Applied Physics*, vol. 118, no. 1, p. 013 301, 2015. DOI: 10.1063/1.4923345.

[179] L. Wang, Y. Zheng, and S. Jia, "Numerical study of the interaction of a helium atmospheric pressure plasma jet with a dielectric material," *Physics of Plasmas*, vol. 23, no. 10, p. 103 504, 2016. DOI: 10.1063/1.4964482.

[180] W. Yan and D. J. Economou, "Simulation of a non-equilibrium helium plasma bullet emerging into oxygen at high pressure (250–760 Torr) and interacting with a substrate," *Journal of Applied Physics*, vol. 120, no. 12, p. 123 304, 2016. DOI: 10.1063/1.4963115.

[181] Y. Yue, X. Pei, D. Gidon, F. Wu, S. Wu, and X. Lu, "Investigation of plasma dynamics and spatially varying O and OH concentrations in atmospheric pressure plasma jets impinging on glass, water and metal substrates," *Plasma Sources Science and Technology*, vol. 27, no. 6, p. 064 001, 2018. DOI: 10.1088/1361-6595/aac618.

[182] I. V. Schweigert, S. Vagapov, L. Lin, and M. Keidar, "Enhancement of atmospheric plasma jet–target interaction with an external ring electrode," *Journal of Physics D: Applied Physics*, vol. 52, no. 29, p. 295 201, 2019. DOI: 10.1088/1361-6463/ab1319.

[183] E. Simoncelli, A. Stancampiano, M. Boselli, M. Gherardi, and V. Colombo, "Experimental Investigation on the Influence of Target Physical Properties on an Impinging Plasma Jet," *Plasma*, vol. 2, no. 3, pp. 369–379, 2019. DOI: 10.3390/plasma2030029.

[184] Y. Ito, Y. Fukui, K. Urabe, O. Sakai, and K. Tachibana, "Effect of Series Capacitance and Accumulated Charge on a Substrate in a Deposition Process with an Atmospheric-Pressure Plasma Jet," *Japanese Journal of Applied Physics*, vol. 49, no. 6, p. 066 201, 2010. DOI: 10.1143/JJAP.49.066201.

[185] E. Robert, T. Darny, S. Dozias, S. Iseni, and J. M. Pouvesle, "New insights on the propagation of pulsed atmospheric plasma streams: From single jet to multi jet arrays," *Physics of Plasmas*, vol. 22, no. 12, p. 122 007, 2015. DOI: 10.1063/1.4934655.

[186] I. Schweigert, D. Zakrevsky, P. Gugin, E. Yelak, E. Golubitskaya, O. Troitskaya, and O. Koval, "Interaction of Cold Atmospheric Argon and Helium Plasma Jets with Bio-Target with Grounded Substrate Beneath," *Applied Sciences*, vol. 9, no. 21, p. 4528, 2019. DOI: 10.3390/app9214528.

[187] L. Martinez, A. Dhruv, L. Lin, E. Balaras, and M. Keidar, "Interaction between a helium atmospheric plasma jet and targets and dynamics of the interface," *Plasma Sources Science and Technology*, vol. 28, no. 11, p. 115 002, 2019. DOI: 10.1088/1361-6595/ab4167.

[188] T. Darny, J.-M. Pouvesle, J. Fontane, L. Joly, S. Dozias, and E. Robert, "Plasma action on helium flow in cold atmospheric pressure plasma jet experiments," *Plasma Sources Science and Technology*, vol. 26, no. 10, p. 105 001, 2017. DOI: 10.1088/1361-6595/aa8877.

[189] L. B. Loeb, *Electrical coronas, their basic physical mechanisms*. University of California Press, 1965.

[190] R. S. Sigmond, "The residual streamer channel: Return strokes and secondary streamers," *Journal of Applied Physics*, vol. 56, no. 5, pp. 1355–1370, 1984. DOI: 10.1063/1.334126.

[191] Y. Kim, I. Jung, I.-Y. Oh, D.-S. Kim, and J.-G. Yook, "Time-Variant Microwave Absorption by Dielectric Barrier Discharge Plasma in Atmospheric Pressure Helium," *IEEE Transactions on Plasma Science*, vol. 46, no. 1, pp. 57–63, 2018. DOI: 10.1109/TPS.2017.2780293.

[192] M. Hofmans, P. Viegas, O. van Rooij, B. Klarenaar, O. Guaitella, A. Bourdon, and A. Sobota, "Characterization of a kHz atmospheric pressure plasma jet: Comparison of discharge propagation parameters in experiments and simulations without target," *Plasma Sources Science and Technology*, vol. 29, no. 3, p. 34 003, 2020. DOI: 10.1088/1361-6595/ab6d49.

[193] K. P. Arjunan, A. Obrusník, B. T. Jones, L. Zajíčková, and S. Ptasinska, "Effect of Additive Oxygen on the Reactive Species Profile and Microbicidal Property of a Helium Atmospheric Pressure Plasma Jet," *Plasma Processes and Polymers*, vol. 13, no. 11, pp. 1089–1105, 2016. DOI: 10.1002/ppap.201600058.

[194] A. M. Lietz, X. Damany, E. Robert, J.-M. Pouvesle, and M. J. Kushner, "Ionization wave propagation in an atmospheric pressure plasma multi-jet," *Plasma Sources Science and Technology*, vol. 28, no. 12, p. 125 009, 2019. DOI: 10.1088/1361-6595/ab4ab0.

[195] M. A. Ridenti, J. de Amorim, A. Dal Pino, V. Guerra, and G. Petrov, "Causes of plasma column contraction in surface-wave-driven discharges in argon at atmospheric pressure," *Physical Review E*, vol. 97, no. 1, p. 013 201, 2018. DOI: 10.1103/PhysRevE.97.013201.

[196] G. V. Naidis, "Simulation of streamer-to-spark transition in short non-uniform air gaps," *Journal of Physics D: Applied Physics*, vol. 32, no. 20, pp. 2649–2654, 1999. DOI: 10.1088/0022-3727/32/20/311.

[197] M. Černák, T. Hoder, and Z. Bonaventura, "Streamer breakdown: cathode spot formation, Trichel pulses and cathode-sheath instabilities," *Plasma Sources Science and Technology*, vol. 29, no. 1, p. 013 001, 2020. DOI: 10.1088/1361-6595/ab5051.

[198] F. X. Bronold, H. Fehske, M. Pamperin, and E. Thiessen, "Electron kinetics at the plasma interface," *The European Physical Journal D*, vol. 72, no. 5, p. 88, 2018. DOI: 10.1140/epjd/e2017-80512-0.

[199] T. Reess and J. Paillol, "The role of the field-effect emission in Trichel pulse development in air at atmospheric pressure," *Journal of Physics D: Applied Physics*, vol. 30, no. 22, pp. 3115–3122, 1997. DOI: 10.1088/0022-3727/30/22/009.

[200] F. Pechereau, Z. Bonaventura, and A. Bourdon, "Influence of surface emission processes on a fast-pulsed dielectric barrier discharge in air at atmospheric pressure," *Plasma Sources Science and Technology*, vol. 25, no. 4, p. 044 004, 2016. DOI: 10.1088/0963-0252/25/4/044004.

List of Publications

Peer-reviewed journal articles

- **Interaction of an atmospheric pressure plasma jet with grounded and floating metallic targets: simulations and experiments**
P. Viegas, <u>M. Hofmans</u>, O.J.A.P. van Rooij, A. Obrusník, B.L.M. Klarenaar, Z. Bonaventura, O. Guaitella, A. Sobota and A. Bourdon, *Plasma Sources Science and Technology, accepted for publication (2020)*

- **Characterization of a kHz atmospheric pressure plasma jet: comparison of discharge propagation parameters in experiments and simulations without target**
<u>M. Hofmans</u>, P. Viegas, O.J.A.P. van Rooij, B.L.M. Klarenaar, O. Guaitella, A. Bourdon and A. Sobota, *Plasma Sources Science and Technology, 29, 034003 (2020)*

- **Influence of targets on the electric field profile in a kHz atmospheric pressure helium plasma jet with the full calculation of the Stark shifts**
<u>M. Hofmans</u> and A. Sobota, *Journal of Applied Physics, 125, 043303 (2019)*

Conference contributions

Oral presentations

- 22nd Workshop on the Exploration of Low-Temperature Plasma Physics, Kerkrade, The Netherlands (November 2019)

- 3th PLAS@PAR Young Researcher Conference on Plasma Physics and Applications, Palaiseau, France (June 2019)

- 21st Workshop on the Exploration of Low-Temperature Plasma Physics, Kerkrade, The Netherlands (November 2018)

- 70th Gaseous Electronics Conference, Pittsburg, United States of America (November 2017)

Poster presentations

- 24th International Symposium on Plasma Chemistry, Naples, Italy (June 2019)

- 24th Europhysics Conference on Atomic and Molecular Physics of Ionized Gases, Glasgow, Scotland (July 2018)

- 5th PLAS@PAR Scientific Day, Paris, France (February 2018)

- 29th NNV-symposium on Plasma Physics and Radiation Technology, Lunteren, The Netherlands (March 2017)

- 19th Workshop on the Exploration of Low-Temperature Plasma Physics, Kerkrade, The Netherlands (December 2016)

Contributions of the Author

This thesis presents the original work of the author. Nonetheless, research is often a team effort and therefore the contributions of others to this thesis are outlined here.

The two-dimensional flow simulation model of which the results have been discussed in **chapters 4 and 7** has been developed and operated by dr. P. Viegas. The author has never operated the model, but has always been in close contact with dr. P. Viegas about adaptations to the model or the experiments to ensure better comparison. The description of the model and the discussion of results from the simulations in these chapters is largely attributed to dr. P. Viegas, but this has always been done in consultation with the author.

The Thomson and rotational Raman scattering setup and the corresponding fitting procedure, of which the results have been discussed in **chapters 4, 5 and 7**, have been developed by dr.ir. B.L.M. Klarenaar. In collaboration with dr.ir. B.L.M. Klarenaar, the measurements and the analysis have been performed by the author.

The COMSOL flow model of which the results have been discussed in **chapter 5** belongs to dr. A. Obrusník. The author has merely used the results.

Acknowledgements / Remerciements / Dankwoord

This thesis is the end result of three years of work that I have performed at Laboratoire de Physique des Plasmas (LPP) at École Polytechnique in Palaiseau, France, and at the group of Elementary Processes in Gas Discharges (EPG) at the Eindhoven University of Technology in the Netherlands. I am grateful for meeting many wonderful people during this time. I would like to thank all of them and this is also the right place to thank a number of them personally.

First of all, I would like to thank my supervisors Olivier Guaitella (Palaiseau) and Ana Sobota (Eindhoven) for the opportunity to perform my PhD research at the two labs. Although this increased the amount of administrative paperwork and the establishment of the joint agreement between the universities did not go smoothly, it has enabled me to use and explore more diagnostics than I could have imagined. You celebrated the ups with me, stood by me during the downs, and I could always count on your advice. It has been a great deal of fun to work with you in the lab, whether it was in Eindhoven or in Palaiseau. I learned a lot and I would not have wanted anyone else as supervisors.

Then, I would like to thank Gerrit Kroesen for being my first promotor and his help in establishing the joint agreement between the two universities. Richard Engeln, Svetlana Starikovskaia, Deborah O'Connell and Uroš Cvelbar: I would like to thank you for reading this thesis and being a member of the committee.

I thank everyone from EPG for the nice times, whether it was at the lab, at the streamer or group meetings, during coffee or lunch breaks, at the *Borrel* on Thursday or the annual barbecue in Gerrit's front yard. My thanks go to Eddy, Ab, Pieter and Jürgen for their technical support in the lab. Whether I needed a new bottle of helium (again), a high voltage cable or advice on which specific equipment to use in my setup: you were always there to help. For all administrative related help, I would like to thank Anita for her always swift replies. I am happy to have shared the office with Boy, Patrick, Siebe, Tim, Shariar, Zahra, Saman and Dmitri: thank you for all our conversations, whether they were physics related or not. The numerous tea breaks and lunch walks, as well as the games of table tennis, were a welcome break from the work in the office or the lab. I will also not forget the dinner nights, where everyone prepared a meal related to their home-country. Those were delicious! During the confinement period, which coincided with my thesis writing, the regular virtual coffee meetings with Boy, Patrick and Tim have certainly helped me to remain connected and feel less alone in my writing.

I have also had the opportunity during my PhD to supervise two master students on their graduation projects. Stefan and Olivier v.R.: you both did a great job. I think all three of us learned a lot and it makes me happy to see you now working on your own PhD projects.

Bart P.: thank you for your advice on RSI, because it has helped me to continue during the last stages of my thesis writing.

I would like to thank Marco for introducing me to the world of 3D printing. The jet mount (also know as the enterprise) we made is still in use in both labs. Since then, 3D printing has

been a new hobby to me, which I think has not gone unnoticed.

Bart K., as you can see our collaboration has been very fruitful for my thesis, so that one month of sunny days we spent in the dark lab was well worth it. Thank you for everything: it was a nice time and you gave me a lot of Matlab inspiration.

My PhD did not start at a lab, but at the Plasma School in Bad Honnef, which is where I first met my new colleagues and friends from LPP. I could not have wished for a better first week! Once at LPP, I joined the PhDarium with Antoine, Thomas, Florian, Ana Sofia, Abhyuday and later on Edmond. Thank you and the other LPPhDs for the tea breaks, the time we spent together at conferences and the movie nights − I am afraid I still owe you the Dutch movie night. You have also shown me that is was way nicer to live in Paris than in Bures sur Yvette, which made me move to Paris for my remaining stays. Thanking all people from LPP, I will also not forget the *apéros* (organized to celebrate the season or to welcome new interns) and the annual *Soirée Musicale*, with many people from LPP playing an instrument on one side of the room and a lot of raclette and cheese fondue on the other side of the room.

Elmar, Ana Sofia, Polina, Audrey and Olivier: thanks for the good times in the lab, whether we were working on experiments or having drinks in the mezzanine to celebrate good results or a published paper.

I would like to thank Pascal P. for his technical support in the lab and also for the language practice (my French and your English). My thanks also go to Cyril D. for his expertise on everything related to optical diagnostics and I will not forget that you are a sensitive person. Alexis, because of you I could continue my 3D printing hobby at LPP, for useful applications in the lab (mounts, tools and shields), the coffee room (puzzles) and at home (cookie cutters). Thank your for that.

Also, I would like to thank everyone from the Plasma Football team and in particular the team captains Abhyuday and Thomas for all the matches we played. Although some matches were more successful than others, I always had a lot of fun.

Florian and Audrey, you were always in for some activity. Together with Abhyuday and Thomas, we went hiking in Scotland, which was awesome except for the rain and the midges. In Italy we slept on a sailboat in the harbor, with a lovely view on Naples at night. You also came with Marine to my home, where we ate some typical Dutch winter food: *hutspot, zuurvlees, erwtensoep* and *pepernoten* (not together of course), and we visited Christmas markets in the caves.

Thank you also for everything else, Florian. You are an awesome friend and I am glad to have you as one of my seconds (*paranimfen*).

I am thanking Pedro for our collaboration, which has been very fruitful, since it has resulted in two publications and two chapters in this thesis. It was nice to work with you and I have learned a lot. With that I would also like to thank Anne for her help and work in this collaboration.

Performing my PhD at two universities in two different countries has been wonderful, but also difficult at times. Wherever I was, I would miss people and special occasions at the other lab and country. However, this also means that I was surrounded by awesome people at both places. Spending my time equally between the two universities meant that I switched lab (and thus country) roughly every six months. If I add it all up, I have moved eight times in the last three years, either by car (*bedankt pap!*) or by train.

During these last three years, and also the six years at the university before that, a few people have always been there for me, regardless of where I was. *Papa (Bob), mama (Louise) en ook Babette en Fabian (mijn tweede paranimf), ik ben zo blij met jullie als familie. Jullie hebben me altijd gesteund en geholpen waar mogelijk. Het was ook erg leuk om jullie Parijs te laten zien, en*

jullie zijn me iedere keer als ik naar Parijs vertrok komen opzoeken. Ik geloof dat ook jullie nu aan anderen kunnen uitleggen waar ik de afgelopen jaren mee bezig ben geweest. Oma Tiny, ik had heel graag gewild dat je bij mijn promotie aanwezig zou zijn, net zoals je bij het afstuderen van mijn master was. Helaas heb je alleen het begin van mijn PhD mogen meemaken, maar ik weet zeker dat je ook nu trots zou zijn geweest. Ik ben blij dat ik daarvoor ook jou nog Parijs heb kunnen laten zien.

Als laatste gaat mijn grootste dank uit naar Rion. Bedankt dat je er altijd voor me bent, of dat nu thuis is in Eindhoven of als ik op 400 km afstand in Parijs zit. Je bent me daar iedere keer komen opzoeken en anders spraken we halverwege in België af. Bedankt voor je steun, je vertrouwen en je goede ideeën. Zonder jou had ik het niet gekund.

I would like to end with a quote (from The Lego Movie):

"Everything is better when you are part of a team."

Thanks everyone! / Merci à tous! / Bedankt allemaal!

Curriculum Vitae

Marlous Hofmans
Born on May 16, 1993, in Zoetermeer, The Netherlands

2005 – 2011	Secondary education (Gymnasium) Bernardinuscollege, Heerlen, The Netherlands
2011 – 2015	Bachelor's degree (BSc) in Physics and Astronomy Radboud University, Nijmegen, The Netherlands
2015 – 2017	Master's degree (MSc) in Applied Physics Specialization in Plasma Radiation and Technology Eindhoven University of Technology, The Netherlands
Spring 2016	Research internship at Laboratoire de Physique des Gas et des Plasmas Université Paris-Sud, Orsay, France
2017 – 2020	PhD candidate in joint project between Institut Polytechnique de Paris and Eindhoven University of Technology, performed at: Laboratoire de Physique des Plasmas École Polytechnique, Palaiseau, France and Elementary Processes in Gas Discharges Department of Applied Physics Eindhoven University of Technology, The Netherlands

Titre: Caractérisation expérimentale de jets de plasma d'hélium

Mots clés: Jet de plasma, Pression atmosphérique, Hélium, Champ électrique, Densité et température électronique, Interaction plasma-surface

Résumé: Cette thèse porte sur l'étude d'un jet de plasma d'hélium à pression atmosphérique alimenté par des impulsions positives unipolaires à une fréquence de l'ordre du kHz. Des expériences sont effectuées pour caractériser la dynamique de propagation, la structure de l'écoulement et la température dans un jet en expansion libre, ainsi que l'influence d'une cible métallique sur le plasma. La spectroscopie à polarisation Stark indique un champ électrique axial d'environ 10 kV/cm dans le capillaire du jet et une augmentation jusqu'à 20 kV/cm dans la plume, qui est constante pour différentes amplitudes et durées de l'impulsion de tension appliquée. La diffusion Thomson et la diffusion Raman rotationnelle sont utilisées pour déterminer la densité électronique et la température électronique, à différentes positions axiales et radiales, ainsi que la température du gaz et la densité de N_2 et O_2 de l'air environnant qui sont mélangés dans le flux d'hélium. La comparaison quantitative de ces résultats expérimentaux avec les résultats d'un modèle fluide 2D montre une bonne concordance et permet une meilleure compréhension des résultats obtenus, à savoir que le champ électrique dans le front d'ionisation augmente avec la quantité d'air intégré au flux d'hélium au lond de la propagation. L'imagerie Schlieren révèle l'apparition de structures turbulentes à des débits élevés et lors de l'application des impulsions de tension. On constate que la température du gaz, mesurée par une sonde de température, augmente d'environ 12 °C quand le plasma est allumé et d'environ 25 °C lorsqu'une cible métallique est placée devant le jet.

Title: Experimental characterization of helium plasma jets

Keywords: Plasma jet, Atmospheric pressure, Helium, Electric field, Electron density and temperature, Plasma surface interaction

Abstract: This thesis studies an atmospheric pressure helium plasma jet that is powered by positive, unipolar pulses at a kHz frequency. Experiments are performed that focus on the propagation dynamics, flow structure and temperature in a freely expanding jet, as well as the influence of a metallic target on the plasma. Stark polarization spectroscopy yields an axial electric field of around 10 kV/cm in the capillary of the jet and an increase up to 20 kV/cm in the plume, which is constant for different amplitudes and durations of the applied voltage pulse. Thomson and rotational Raman scattering are used to determine the electron density and electron temperature, at different axial and radial positions, as well as the gas temperature and the density of N_2 and O_2 that are mixed into the helium from the surrounding air. Quantitative comparison of these experimental results with results from a 2D fluid model show a good agreement and allow for a better understanding of the obtained results, namely that the electric field in the ionization front depends linearly on the flow composition at that location. Schlieren imaging shows the onset of turbulent structures at high applied flow rates and at the application of the voltage pulses. The gas temperature, as measured by a temperature probe, is found to increase by around 12 °C when the plasma is ignited and by around 25 °C when a metallic target is placed in front of the jet.